Detector development towards axion searches with BabyIAXO

Dissertation
zur
Erlangung des Doktorgrades (Dr. rer. nat.)
der
Mathematisch-Naturwissenschaftlichen Fakultät
der
Rheinischen Friedrich-Wilhelms-Universität Bonn

von
Tobias Schiffer
aus
Troisdorf

Bonn, March 2025

Angefertigt mit Genehmigung der Mathematisch-Naturwissenschaftlichen Fakultät der Rheinischen Friedrich-Wilhelms-Universität Bonn

Gutachter/Betreuer:	Prof. Dr. Klaus Desch
Gutachter:	Prof. Dr. Matthias Schott
Tag der Promotion:	27.05.2025
Erscheinungsjahr:	2025

Meinen Eltern

Contents

CHAPTER I

Introduction

The search for the unknown is one of the driving forces of science. In physics, dark matter is a good example of this. As one of the major components of the universe, it can so far only be observed indirectly due to gravitational forces. Examples of these observations are the rotation curves of galaxies and gravitational lensing of galaxies. Despite these indirect observations, no constituent of dark matter is known. With theories on dark matter presenting very different possible compositions, a large field for the exploration of the unknown is opened.

In this field, one of the most interesting candidates for a dark matter particle is the axion. The axion was introduced in 1977 by Roberto D. Peccei and Helen R. Quinn as a solution for a completely different problem—the strong CP-problem. However, it was soon realised that it might solve multiple problems in physics, including dark matter. This origin makes it a very interesting candidate to search for since it not only solves one mystery of physics but potentially multiple.

The axion itself can interact with photons. This interaction leads to the production of axions from photons and vice versa. Consequently, the Sun would be a large source of axions. These axions would then arrive at the earth and can be measured. To measure axions arising from the Sun the most common experimental approach is the so-called helioscope. An axion helioscope consists of a magnet pointing towards the Sun followed by a detector system able to measure the photons emerging from axions converted in the magnet. Between the magnet and the detector system, a focusing optic can be introduced.

The specialised detectors needed to measure these photons have to be able to detect on the one hand very low energetic X-rays with high efficiency, and on the other hand, providing a very low background since the converted axion signals are very rare. A Micromegas detector is a proven solution for such applications. An enhanced version of a Micromegas detector is the GridPix detector.

In this thesis, the development of three GridPix detectors will be presented. After a short theory on axions and gaseous detectors in chapters 2 and 3 the GridPix will be introduced in chapter 4. The GridPix is a combination of a pixelised readout ASIC and a gas amplification stage. In this chapter also the differences between the GridPix —based on the Timepix ASIC— and the GridPix3 —based on the Timepix3 ASIC— are explained.

In chapter 5 the axion helioscopes CAST, BabyIAXO, and IAXO are described. For CAST in addition a short overview of the used detectors is given, and for BabyIAXO an overview of the proposed detectors is provided. After this, the vacuum system of BabyIAXO is described in detail in chapter 6.

Having set the scene, in chapter 7 the development and commissioning of ultra-thin X-ray windows will be described. These windows are necessary to allow the low energetic X-ray photons —converted axions— to enter the detector volume.

Such a window was used for the first time with the seven GridPix IAXO prototype detector described in chapter 8. In chapter 8 a focus is laid on the newly implemented veto systems to reduce the background. Due to the usage of seven readout ASICs a cooling device became necessary and will be described in detail. Then in chapter 9, the calibration measurements taken in the CAST detector lab are briefly discussed.

To further improve the GridPix detector a change of the readout from GridPix to GridPix3 was realised. For this, a completely new readout was developed. In chapter 10 the development of this readout is described as well as the commissioning of the resulting detector. To reach the anticipated background levels of BabyIAXO this detector is not sufficient since the intrinsic radiation levels of the used material are too high. Therefore, a completely new detector was designed using only materials known to be radiopure. The development of this detector is described in chapter 11. In order to test such a low background detector a detector test stand was developed reflecting the proposed detector housing of BabyIAXO. The test stand is described in chapter 12 showing that the construction started but could not be finished.

In chapter 13 the data reconstruction is described as well as the typical parameters used to monitor the stability of the detectors. Afterwards, the background rate of both GridPix3 detectors was measured. For this with each detector a long background run was performed and analysed. The results are shown in chapter 14. First the stability during the data taking is evaluated. Then the background rate is analysed using a likelihood approach. Here, five different methods are compared to examine the influence of the additional time measurement in the GridPix3 data.

Finally, an outlook presenting a new detector idea to measure X-rays with extremely low energies will be given in chapter 15. In this chapter also some ideas to further improve the BabyIAXO detector will be given before the thesis will be summarised in chapter 16.

CHAPTER 2

Axions

The axion is a hypothetical particle, originally arising from a solution for the strong CP problem (the Peccei-Quinn mechanism [PQ77b, PQ77a]). Only later it was realised that this mechanism would result in a new particle [Wei78, Wil78], the axion. However, nowadays multiple models use the axion to solve a variety of problems in physics, including dark matter, anomalous stellar cooling or the baryon asymmetry of the Universe. Following [GI22] a short introduction to the axion shall be given.

2.1 The strong CP problem

The Lagrangian of quantum chromodynamics contains a charge-parity (CP) violating term denoted as $\mathcal{L}_\theta$ given by:

$$\mathcal{L}_\theta = \theta \frac{g^2}{32\pi^2} G^\alpha_{\mu\nu} \widetilde{G}^{\mu\nu}_\alpha \,. \tag{2.1}$$

Here $G^{\mu\nu}_\alpha$ is the gluon field strength tensor, g is the coupling strength of the strong interaction, and θ is an angle. The angle θ not constrained by theory can have any value between 0 and 2π. A value of 0 would result in a vanishing CP violation within the strong interaction. Since so far no CP violation in the strong interaction is observed this seems to be the case. The strongest hint into this direction is the electrical dipole moment (EDM) of the neutron d_N given by

$$d_\mathrm{N} = (2.4 \pm 1.0)\,\theta \times 10^{-3}\,\mathrm{e\,fm}\,. \tag{2.2}$$

Measurements of the neutron EDM currently reach limits in the order of $1.8 \times 10^{-13}\,\mathrm{e\,fm}$ [NAG$^+$24]. Thus θ has to be smaller than 10^{-10}. This behaviour of the vanishing angle θ is called the strong CP problem.

2.2 The Peccei-Quinn mechanism

To solve this problem, Peccei and Quinn introduced another $U(1)$ symmetry spontaneously broken at the energy scale f_A. This symmetry replaces the θ term by the axion field A:

$$\mathcal{L}_\mathrm{A} \ni \frac{g^2}{32\pi^2} G^\alpha_{\mu\nu} \widetilde{G}^{\mu\nu}_\alpha \frac{A}{f_A} . \tag{2.3}$$

With $\theta \to A/f_A$ a dynamic replacement is done allowing to have different values for θ at different energy scales. Thus, the strong CP problem is solved. Due to the spontaneous symmetry breaking a new Nambu-Goldstone boson is required. However, the theory predicts a mass for this particle

$$m_A = (5.70 \pm 0.07)\ \mathrm{\mu eV} \left(\frac{10^{12}\mathrm{GeV}}{f_A} \right) . \tag{2.4}$$

Thus, one ends up with a pseudo Nambu-Goldstone boson called axion. The mass of the axion is nearly fully determined by QCD apart from the scale factor f_A. This also means that every axion coupling is proportional to the axion mass.

2.3 Couplings

Equation 2.3 shows that the axion will model independently couple to gluons. This implies further the possibility to couple to mesons like the neutral pion [IR18, Sik21]. Consequently, also a coupling to photons and hadrons occurs model independent. The coupling to photons described by the coupling constant $g_{a\gamma}$, can be described via [GI22]:

$$\mathcal{L}_{\mathrm{A}\gamma} = -\frac{g_{a\gamma}}{4} A F_{\mu\nu} \widetilde{F}^{\mu\nu} , \tag{2.5}$$

with $F_{\mu\nu}$ the electromagnetic field strength tensor. Thus, the axion will couple to electromagnetic fields. With this and the coupling to pions, it can be seen that the axion should, similar to the pion, mix with electromagnetic waves via the Primakoff effect. This leads to the experimentally interesting result that within a magnetic field the axion can couple to a virtual photon producing a photon, and vice versa.

As mentioned before the axion can also couple model independent to hadrons. Thus, a coupling constant to nucleons g_{aN} can be defined the coupling is given via the Lagrangian [DLGG+22]

$$\mathcal{L}_\mathrm{AN} = \sum_f -i g_{aN} A \bar{f} \gamma_5 f . \tag{2.6}$$

Here f denote the fermion fields. The axion-nucleon coupling arises model independent, however contributions from model dependent couplings can affect the axion-nucleon coupling.

The last coupling interesting within this thesis is the axion-electron coupling with its coupling constant g_{ae}. It is the only coupling mentioned that is model dependent, such that it does not necessarily exist in all models. The Lagrangian can be denoted as [Red13]

$$\mathcal{L}_{\mathrm{Ae}} = g_{ae} \frac{\partial_\mu A}{2m_{\mathrm{e}}} \overline{\psi}_{\mathrm{e}} \gamma^5 \gamma^\mu \psi_{\mathrm{e}} \,, \tag{2.7}$$

with ψ_{e} being the electron field. If the axion couples to the electron an interesting set of production mechanisms arises. This is specifically interesting for solar axions, meaning axions produced by the sun. However, as said before the axion-electron coupling is model dependent so a quick look at the two most popular models shall be taken.

2.4 Axion models

With the solution of the strong CP problem, the PQ mechanism will also affect other standard model (SM) particles. These extensions have of course to fulfill the observations available at the moment. This basically rules already out a lot of different axion models including the original one. For the original axion the coupling strength f_A was in the order of the electroweak scale, thus it should have been found already. A proper model needs to rescale this coupling to very low values allowing only a very weak interaction with matter. Consequently, a hard to detect axion with low mass will be produced, called the invisible axion. The two most popular models shall be briefly introduced in the following.

2.4.1 Kim-Shifman-Vainshtein-Zakharov (KSVZ) model

The KSVZ model [Kim79, SVZ80] is one of the simplest models reproducing the current observations within the SM. It introduces a scalar field and a non observable super heavy quark to the SM. By reducing the coupling strength f_A the KSVZ model allows for an invisible axion fitting current observation. The key point of the model is while allowing for axion-photon coupling, it does not allow for axion-electron coupling and therefore is sometimes called hadronic model.

2.4.2 Dine-Fischler-Srednicki-Zhitnitsky (DFSZ) model

The DFSZ model [Zhi80, DFS81] in contrast to the KSVZ model does not introduce a new quark but adds a coupling of the quarks to the PQ mechanism. Additionally, it introduces two new Higgs doublet fields allowing the decoupling of f_A from the electroweak scale, again getting an invisible axion. Due to the coupling to quarks, this model will affect on one hand the axion nucleon coupling and on the other hand allows for axion electron coupling in addition to the axion photon coupling.

2.5 Solar Axions

Since the core of this thesis is based on the detector development for a search for solar axions, the following will just look at the production mechanisms arising from the presented couplings and their implications for the solar axion flux. Thinking about the coupling of axions to photons within the magnetic field of an atomic core, called the Primakoff effect, a large source coming to mind would be the Sun. Due to the high density and the large photon flux inside the Sun, it might be the perfect source for axions. The solar axion flux will be made up by contributions of the axion-photon, the axion-nucleon, and model dependent of the axion-electron coupling. Since axion-electron coupling is not ruled out so far it shall be included in the further discussion.

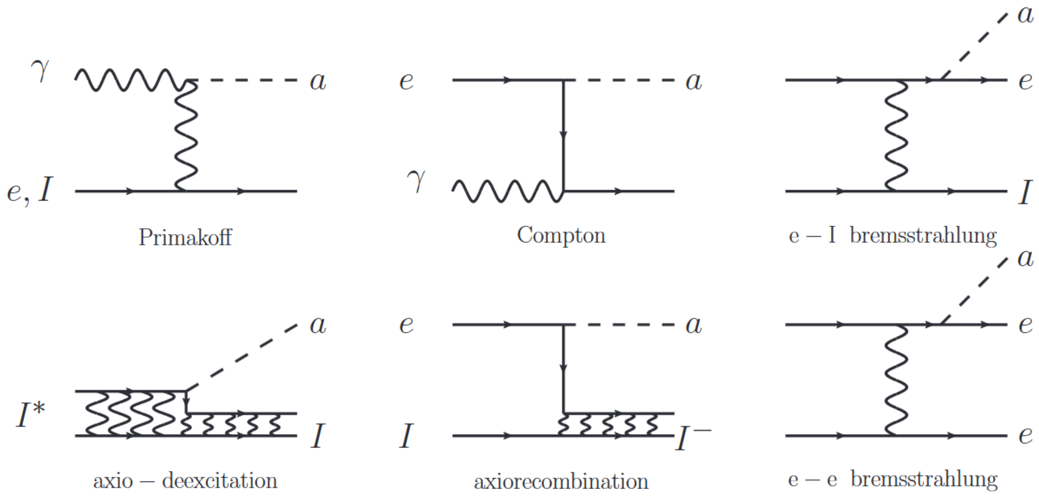

Figure 2.1: Feynman diagrams for the six dominant axion production mechanisms in the Sun. While the Primakoff effect is based on axion photon coupling the other five processes are based on axion-electron coupling. Taken from [Red13].

As shown in [Red13] the six dominating processes for the axion production within the Sun are:

- **Primakoff effect** A photon couples in the vicinity of the magnetic field of an atomic core to an virtual photon via a pion loop which can then produce an axion.
- **Compton scattering** A photon is absorbed by an electron and reemitted as an axion.
- **Electron-electron bremsstrahlung** An electron emitting axion bremsstrahlung in the vicinity of an electron.
- **Electron-ion bremsstrahlung** An electron emitting axion bremsstrahlung in the vicinity of an ion.
- **Axio-deexcitation** An ion de-excides by emission of an axion.
- **Axiorecombination** Electron capture by an ion emits an axion.

The Feynman diagrams of all six processes are shown in figure 2.1. Additionally, two further interesting contributions shall be mentioned. Firstly the axion-nucleon coupling producing axions from nuclear transitions. From the possible production channels the two strongest shall be presented. The strongest channel due to the high abundance of iron in the sun is ^{57}Fe which would lead to a peak at 14.4 keV. This is followed by ^{83}Kr peaking at 9.4 keV however the number of produced axions will be already reduced by a factor of $O(10^3)$ [DLGG+22]. Thus, a focus can be put on the ^{57}Fe transition.

Secondly, the plasmon-axion conversion. Here plasmons can convert into axions via axion-photon coupling [HJT21]. This process results in some resonances at low energies $O(100\,\mathrm{eV})$. These resonances exceed the peak flux from the Primakoff production. Consequently, they are an interesting candidate to search for.

With the scene set one can now calculate the solar flux of axions arriving at the earth, by integrating over the axion production rate per volume of the Sun [Red13]

$$\frac{d\Phi_a}{d\omega} = \frac{1}{4\pi R_{\text{Earth}}^2} \int_{\text{Sun}} dV \frac{4\pi\omega^2}{(2\pi)^3} \Gamma_a^P(\omega) \ . \tag{2.8}$$

Here Γ_a^P denotes the production rate of axions depending on the position in the Sun. It is a combination of the production rate for all mechanisms considered.

The result of this calculation is shown in figure 2.2. In black the total flux is shown. The flux is largely dominated by the axion-electron coupling. In order to differentiate this from the model independent fluxes from axion-photon and axion-nucleon coupling these fluxes are also plotted separately. To make the Primakoff and the plasmon conversion visible in figure 2.2 an enhancement by a factor of 25 was used. For the model independent fluxes the axion-nucleon coupling seems to be currently the most promising candidate. However, a detector capable of measuring X-ray energies in the range of the axion-plasmon conversions will profit from a large flux increase within the axion-photon coupling.

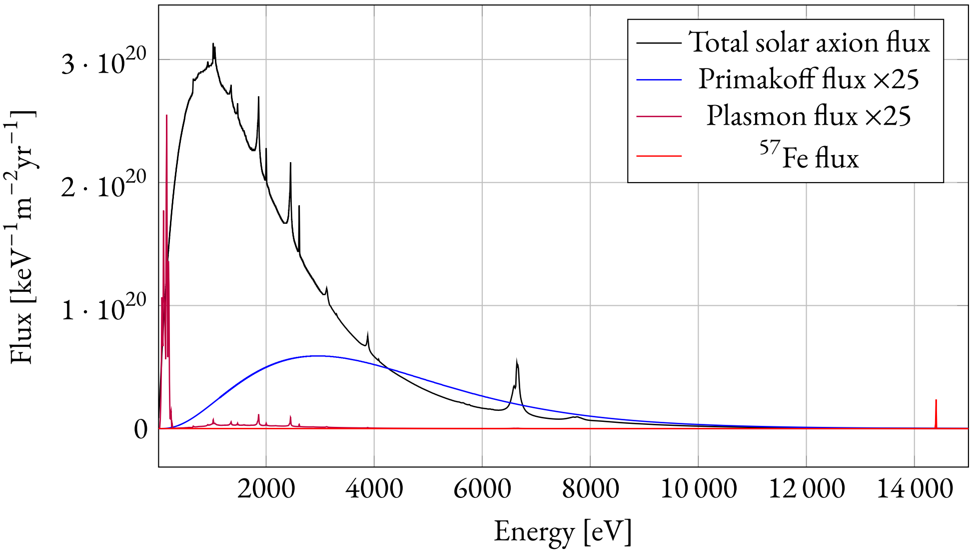

Figure 2.2: Solar axion flux at the earth using $g_{ae} = 1 \times 10^{-13}\,\text{GeV}^{-1}$, $g_{a\gamma} = 1 \times 10^{-12}\,\text{GeV}^{-1}$, and $g_{aN} = 1 \times 10^{-9}\,\text{GeV}^{-1}$. The Primakoff, the plasmon, and the ^{57}Fe flux are also shown separately. From [vO23].

2.6 Experimental approaches

In 1983 three experimental ways for axion searches were proposed [Sik83]. All three approaches use the axion-photon coupling to convert the axions to photons via their interaction with the magnetic field. These photons can then be measured. The major difference between the three approaches is the source of the axions.

The first approach has in situ axion production. This type of experiment is called light shining through the wall which uses two magnets separated by an optical barrier. Photons of an intense laser beam can interact with the magnetic field in the first magnet and convert to axions via the Primakoff effect. These axions can pass through the optical barrier and might convert back to photons in the second magnet. These photons then reproduce the wavelength of the initial laser radiation.

The second source of axions is the dark matter. If this assumption is true axions would be a part of the dark matter halo. These axions can be measured with cavity experiments in strong magnetic fields. If the resonance frequency of the cavity matches the axion mass the conversion probability will be enhanced, leading to a measurable signal. These experiments are called haloscopes.

The third source of axions is the Sun as described in section 2.5. Solar axions can be measured with an axion helioscopes. The axion helioscope contains a magnet mounted on a movable platform allowing

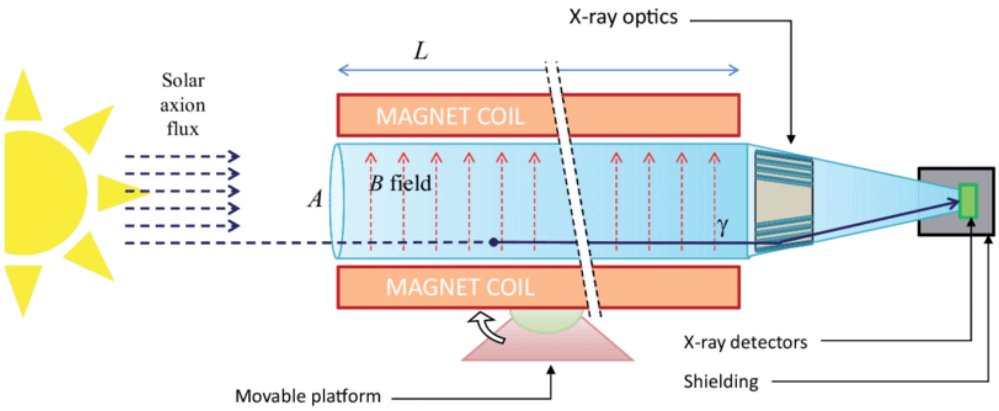

Figure 2.3: The enhanced axion helioscope. It includes an additional X-ray optic to focus the produced X-rays towards the detector. With this, higher signal to background rates can be achieved. Taken from [AAB+14b].

it to follow the position of the Sun. Inside the magnetic field axions might convert into photons by mixing with the virtual photons of the magnetic field. Behind the magnet, a detection system able to detect the converted axions (0.5 keV–8 keV) is placed. Depending on the size of the magnet bore additionally a dedicated X-ray optic might be introduced to focus the X-rays towards the detector and enable a better signal to background ratio at the detector. This combination is called the enhanced helioscope, shown in figure 2.3. In the figure, additionally a lead shielding is placed around the detector to further reduce the background induced by cosmic radiation. Since the energy of the photons is very low a vacuum is needed in order to transport the photons through the magnet bore and to the detector.

CHAPTER 3

Physics of gaseous detectors

The detectors developed for axion searches at the CERN Axion Solar Telescope (CAST) and the International Axion Observatory (IAXO) described in this thesis are micro pattern gaseous detectors (MPGDs). They are based on the interaction of particles with a gas. For solar axion searches the incident particles are X-ray photons at very low energies and muons as the main source of background. In the following the basic physics of these processes shall be described.

3.1 Interactions

When a particle enters a medium, in the following a gas, different processes depending on the energy and type of the particle will take place. Typically a particle entering the gas ionises one or more gas atoms (called primary ionisation) the electrons produced from the primary ionisation will then scatter with the gas atoms and produce further electron ion pairs. Within this thesis, all electrons from the primary and secondary ionisation will be called primary electrons.

3.1.1 Photons

For the low energetic X-rays originating from the conversion of the axions described in chapter 2. The main process is photo ionisation. The photon interacts with an electron of a gas atom and ionises it by transferring all its energy to the electron. This process is called primary ionisation. The electron obtained in this way will then create more electron ion pairs from the surrounding gas molecules by scattering. Depending on the gas and the pressure the track length of the primary electron varies drastically. For the search for axions, a gas is taken with a very short track length of the primary electron and thus the secondary ionisation will be almost stationary at the point of interaction. This leads to a quasi point like distribution for a photon. Within this process, the averaged energy W to create one electron-ion pair is given by [BRR08]:

$$W \langle N_\mathrm{I} \rangle = L \left\langle \frac{\mathrm{d}E}{\mathrm{d}x} \right\rangle , \tag{3.1}$$

with $\langle N_\mathrm{I} \rangle$ being the average number of ionisations taking place along a path of length L through the gas. For argon this value is [BRR08]:

$$W = 26.4\,\mathrm{eV}\,. \tag{3.2}$$

3.1.2 Cosmic muons

With respect to photons cosmic muons interact very differently within the gas since they, firstly are charged particles, and secondly arrive at much higher energies. Typically cosmic muons arriving at the earth's surface have on average an energy of 4 GeV [AMSM18]. From figure 3.1 it can be seen

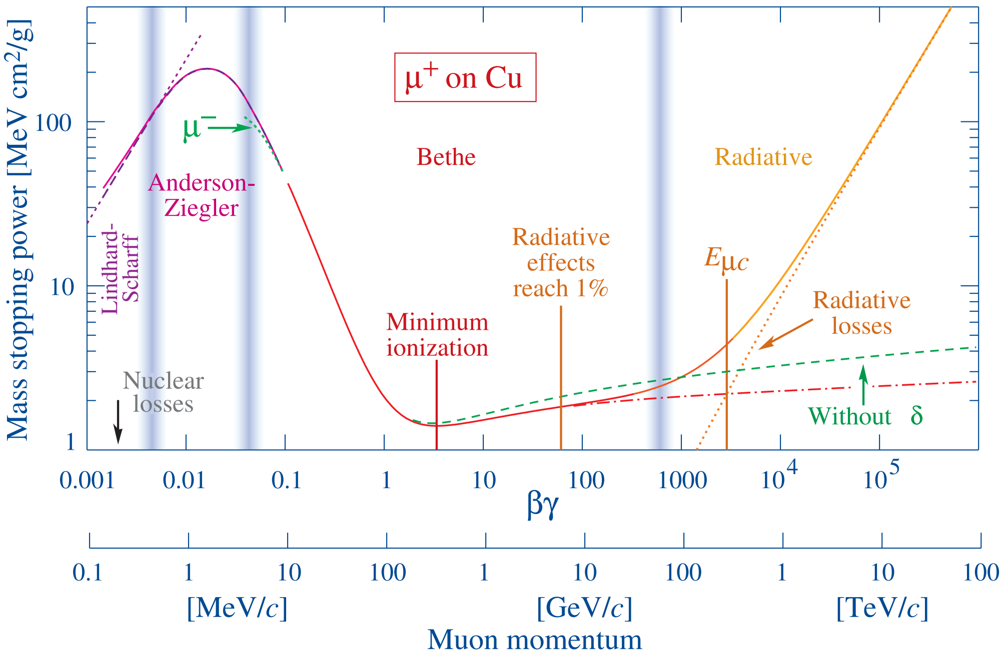

Figure 3.1: Stopping power for positive muons in copper. For the typical cosmic muon energies of 4 GeV [AMSM18] the muons are within the range of minimal ionising particles. Taken from [TGH+18].

that this is very close to the ionisation minimum. So the cosmic muons can generally be assumed to be minimally ionising. This means that the average energy loss in a medium is at its smallest value. For argon this value can be found in figure 3.2. The figure shows that for atomic numbers larger than $Z = 10$ the minimum ionisation follows a logarithmic law giving:

$$\left\langle -\frac{\mathrm{d}E}{\mathrm{d}x} \right\rangle_{\mathrm{min,Ar}} = [2.35 - 0.28\ln(18)]\ \mathrm{MeV\,g^{-1}cm^2} = 1.54\,\mathrm{MeV\,g^{-1}cm^2} \approx 2.75\,\mathrm{keV\,cm^{-1}} \tag{3.3}$$

for argon using a density of $1.784 \times 10^{-3}\,\mathrm{g\,cm^{-3}}$ at 20 °C and 1 bar(a). This shows that the energy of the primary ionised electrons is rather low, thus as explained in subsection 3.1.1 the secondary ionisation will happen very close to the muon path. Since the primary ionisation takes place as a statistical process the muon path will rather consist of multiple clusters than a single line shaped cluster. Due to the

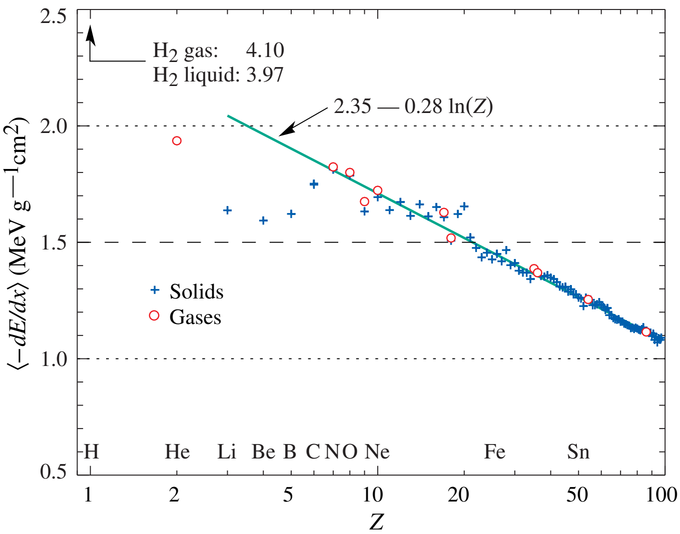

Figure 3.2: Energy loss of a minimal ionising muon in different media. Taken from [TGH+18].

point-like behaviour of the secondary ionisation isolated clusters on this track might mimic X-ray clusters.

3.2 Drift and diffusion

Following [BRR08] a short introduction of the drift and diffusion behaviour of the produced primary electrons shall be given. With an electrical field applied to the gas volume electrons and ions start to drift in different directions. Therefore, firstly they are separated so they will not recombine and secondly they will move according to the electric field. Due to the different masses of the ions and the electrons, the electrons will move much faster. For electrons the drift speed u in a homogeneous electrical field E is given by

$$u = \frac{eE}{m_\mathrm{e}}\tau\,, \tag{3.4}$$

with τ being the mean collision time.

While drifting through the detector the electrons will scatter on gas atoms or molecules. With each collision the electron will randomly change direction and lose some energy, this process leads to two types of diffusion, longitudinal and transversal. From the random nature of this process, it can be assumed that the resulting distribution starting from a point-like distribution will be gaussian. However, this is only true for the transversal diffusion. For the longitudinal diffusion, it is slightly different since the collision rate depends on the electron energy itself. This means that the leading edge of the electron cloud, has a higher collision rate than the trailing edge, resulting in a slight focusing in the longitudinal direction. Thus, the longitudinal diffusion will be slightly lower than the transversal diffusion. In order to calculate the mean width or length $\sigma_{\mathrm{t/l}}$ of a cluster typically the diffusion coefficients D_t and D_l for transversal or longitudinal diffusion are used via:

$$\sigma_{\mathrm{t/l}} = D_{\mathrm{t/l}}\sqrt{x}\,, \tag{3.5}$$

with x being the distance the electron drifted through the gas. The diffusion coefficients have to be either measured or can be simulated.

3.3 Amplification

If the strength of the electrical field in the gas is large enough that in between two collisions the electrons can gain enough energy to ionise a gas atom or molecule an electron avalanche will be created. From this one can define the so-called first Townsend coefficient α [KW16]:

$$\alpha = \frac{1}{\lambda_{\mathrm{ion}}} \propto \frac{1}{\lambda}\,, \tag{3.6}$$

with λ_{ion} being the mean free path between two ion productions, thus being proportional or identical (depending on the field) to the mean free path of the electron in the gas. The mean gain G being the number of electrons produced by one primary electron, over a path length s can then be defined as:

$$G = \mathrm{e}^{\alpha s} \propto \mathrm{e}^{\frac{s}{\lambda}}\,. \tag{3.7}$$

With the mean free path of an electron in a gas given by:

$$\lambda = \frac{1}{n\sigma}\,, \tag{3.8}$$

with $n = N/V$ being the number density of the gas and σ the cross section between the electrons and the gas. With the ideal gas law one can rewrite this to:

$$\lambda = \frac{V}{N\sigma} = \frac{k_{\mathrm{B}}T}{p\sigma}\,. \tag{3.9}$$

Here k_{B} is the Boltzmann constant, T is the temperature of the gas, and p the pressure. Plugging this into equation 3.7:

$$G \propto \mathrm{e}^{\frac{sp\sigma}{k_{\mathrm{B}}T}}\,. \tag{3.10}$$

Thus, the gain depends on the temperature and the pressure of the gas. Since the gas amplification is a random statistical process strongly depending on the electrical field geometry applied, a comprehensive theory is not available. Hence, in the following, two cases for the electrical field shall be discussed following again [BRR08].

In the case of a strong inhomogeneous field, e.g. in a wire chamber, it could be shown that to some extent the distribution of the gas gain follows a distribution, which can be described by a Pólya-distribution

$$P(x, \theta, k, G) = \frac{k}{G} \frac{(\theta + 1)^{(\theta+1)}}{\Gamma[\theta + 1]} \left(\frac{x}{G}\right)^{\theta} e^{-(\theta+1)\frac{x}{G}}, \tag{3.11}$$

where $\Gamma[z]$ is the gamma function, k is a scaling factor, θ determines the width of the function and G is the mean gas gain. The variance is given by:

$$\sigma^2 = \frac{G^2}{\theta + 1}. \tag{3.12}$$

The Pólya-distribution however does not occur from theory such that it is not based on a proper physical model. Nevertheless, it describes the gas gain distribution for strong inhomogeneous fields quite well. In the case of a strong homogeneous electrical field, e.g. within a parallel plate capacitor, the Pólya-distribution shows some differences to measured data. A model describing such data in a better way is the Legler model, however it has no closed form for fitting.

Finally, it shall be mentioned that none of these models will suit the amplification region of a GridPix (see section 4.2), since the field will be neither strongly homogeneous since holes, pillars, and the structure of the chip surface will obstruct the field, nor will it be strongly inhomogeneous, since the setup is still close to a parallel plate capacitor.

3.3.1 Jesse effect

The Jesse effect [JS55, Ino74] combines different mechanisms leading to a higher expected ionisation potential of a gas mixture. This includes subexcitation electrons [Pla55], where secondary electrons have an energy high enough to ionise an atom or molecule within the gas mixture, as well as the Penning effect. The Penning effect describes the transfer of energy from an excited atom or molecule A^* to another atom or molecule within a gas mixture. If the second atom or molecule has a lower W value then this energy might lead to an ionisation:

$$A^* + B \Rightarrow A + B^+ + e^-. \tag{3.13}$$

Thus the overall W value of the gas mixture will be decreased. Already small impurities (0.1%) in a gas can lead to a large increase in the ionisation potential of the gas (up to 40% [JS55]). Since so far no theory on the Jesse effect is available, the increase in the ionisation potential has to be measured.

3.3.2 UV-photons and quencher gases

An excited gas atom or molecule not transferring its energy to another atom or molecule, will typically lose the energy by emitting a photon

$$A^* \Rightarrow A + \gamma. \tag{3.14}$$

For noble gases these photons are in the energy range of ultra violet (UV) or extreme ultra violet (XUV). These UV photons can travel through the detector gas. If they hit a metal surface they can produce via the photoelectric effect an electron from the surface, which might lead to an additional avalanche in the detector. While single UV photons are not problematic large quantities can lead to gas discharges in the detector. To avoid this typically a so-called quencher gas is added to the gas mixture. A quencher gas (e.g. isobutane) is a molecular gas allowing to absorb the UV photon into vibrational modes, radiating off photons at much lower energies (infrared). With a larger amount of quencher gas more UV photons can be converted allowing a more stable operation.

3.4 Parameters of argon isobutane

In the following the relevant parameters for the used gas mixture of argon isobutane 97.7,2.3 shall be discussed. First of all this mixture is affected by the Jesse effect. For argon the energies of the excited states have a low energy ($\sim$ 11.6 eV) [JS55], so the impurity has to have an even lower ionisation potential. This is true for isobutane with an ionisation potential of 10.57 eV [LP92]. Hence, the ionisation potential will be larger than expected from pure argon. Sadly, no measurements for this mixture of argon isobutane are available such that the rate is unknown.

The UV-photons radiated from the mixture will be mostly in the energy range around 11 eV thus in the UV range. Since isobutane is added as a quencher gas the number of UV photons will be reduced but due to the low concentration of isobutane still affect the measurements.

The values for the drift velocity and the diffusion coefficient were simulated using Magboltz [Bia]. The values are summarised in table 3.1. As expected the longitudinal diffusion coefficient is smaller

D_t	$663.09\,\mu\mathrm{m}/\sqrt{\mathrm{cm}}$
D_l	$249.32\,\mu\mathrm{m}/\sqrt{\mathrm{cm}}$
u	$22.98\,\mu\mathrm{m/ns}$

Table 3.1: Parameters for argon isobutane 97.7,2.3 simulated with Magboltz [Bia].

than the transversal diffusion coefficient.

3.5 Paschen's law

Paschen's law describes the correlation between the electrical breakdown voltage between two conductors within a gas. It can be described via [LL05]:

$$V_\mathrm{B} = \frac{Bpd}{\ln(Apd) - \ln\left(\ln\left(1 + \frac{1}{\gamma_\mathrm{se}}\right)\right)}. \tag{3.15}$$

Here V_B is the breakdown voltage, p is the pressure, d is the distance, γ_se is a parameter determining the cathode material, and A and B are gas constants. The values used for Paschen's law can be found in table 3.2. While A and B are gas constants and tabulated in many books, γ_se seems to be problematic to determine since it strongly depends on the cathode material and surface quality as well as on the shape. The values listed here should be used with caution. Additionally, Paschen's law is also affected by the Jesse effect. This means that using a Penning mixture will lower the breakdown voltage drastically [Dun88].

Parameter	Helium	Argon
A	$2.8\,\mathrm{m^{-1}Pa^{-1}}$	$8.63\,\mathrm{m^{-1}Pa^{-1}}$
B	$57.75\,\mathrm{Vm^{-1}Pa^{-1}}$	$132\,\mathrm{Vm^{-1}Pa^{-1}}$
γ_{se}	0.01	0.02

Table 3.2: Parameters for helium and argon used within Paschen's law. A and B from [LL05], γ_{se} from [AGGB98]. It shall be mentioned that the value for γ_{se} is known to be hard to reproduce experimentally.

3.6 Working principle of the GridPix detector

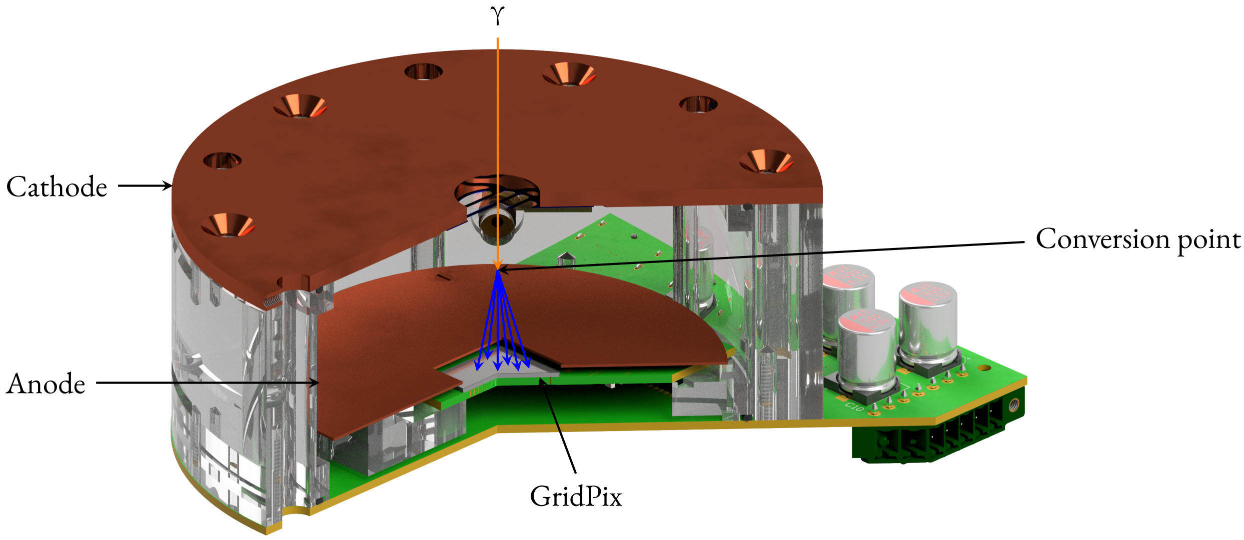

Figure 3.3: Principle of the photon detection in the GridPix detector. The photon (orange) enters the detector through a window in the cathode and reacts with the gas at a conversion point. There, first a photoelectron is produced, which then produces primary conversion electrons (blue) via scattering. The electrons drift towards the GridPix along the electrical field generated between the cathode and the anode/grid of the GridPix. Due to a much stronger electrical field between the Timepix surface and the grid gas amplification sets in, producing a signal measurable by the Timepix.

As a detector for a helioscope, the GridPix detector is a proven solution [Kri18, Sch24a]. The GridPix detector is an enhanced Micromegas detector using a pixelised readout application-specific integrated circuit (ASIC) with an integrated grid as described in chapter 4. The working principle is shown in figure 3.3. A photon enters the gas filled detector volume from the top, through a window in the cathode. Then the photon might interact with the detector gas (conversion point) producing a photoelectron. At this conversion point the photoelectron will produce further electrons by scattering along its track. The number of electrons is proportional to the energy of the initial photon. There is a possibility that not only a photoelectron, but also a fluorescence photon is created. This photon can leave the detector unnoticed —called escape photon— reducing the total number of electrons recorded by the GridPix. In an electric field —typically $O(500\,\mathrm{V/cm})$— between the cathode and the anode/grid the electrons drift towards the grid of the GridPix, where they pass through the holes into the amplification gap. Between the grid and the Timepix a much stronger electric field of $O(50\,\mathrm{kV/cm})$ is applied such that an electron avalanche takes place. This generates a signal that is measurable by the Timepix.

CHAPTER 4

GridPix

The GridPix is a combination of a Micromegas like structure built directly on top of a pixelised readout ASIC. The readout ASICs used are the Timepix and the Timepix3, described in section 4.1. Both ASICs feature 256×256 pixels with 55 µm pixel pitch. On top of the pixel a perfectly aligned aluminium grid, called InGrid (Integrated Grid) is produced via a photolithographic process. This grid is supported by insulating pillars 50 µm above the pixels. The process and details are described in section 4.2. It was developed originally for the Timepix ASIC (GridPix) and later also adapted for Timepix3 (GridPix3). The differences of the GridPixes will be discussed in section 4.3.

4.1 Timepix and Timepix3

The Timepix ASIC ([LBC+07]) is a 256 × 256 pixel CMOS ASIC developed by the Medipix collaboration ([Med]) in 2006. The Timepix ASIC was developed on the basis of the Medipix2 ASIC ([LCD+02]) therefore it shares many features with the latter. However, additions were made to make the ASIC suitable for particle physics experiments. The most important changes are the introduction of four different modes (pixel hit, particle count, Time over Threshold (ToT), Time of Arrival (ToA)) and the change to a 4-bit pixel threshold adjustment allowing for a more uniform threshold equalisation of the ASIC. In the following the key features of the Timepix ASIC will be described.

The Timepix ASIC provides a frame based readout without zero-suppression. Hence, if the shutter is closed the full chip is read out and the data is sent as one data stream containing the information of all 65536 pixels. The four readout modes work as follows. The particle counter mode can recognise if the charge on the pixel input pad was above the set threshold, implying the pixel was hit and count the number of hits for each pixel while the shutter is open. This mode is used for some calibration scans like the S-Curve Scan, and the equalisation. In this mode the pixel however will not time stamp the incoming hits so one does not know when within a frame the hit was registered. To save the data, each pixel contains a 14-bit register implemented as an Exclusive-Or pseudo-random-counter. This allows a maximum counter value of 11810. If this is reached the overflow logic is triggered and the counter will stop. The second mode is the ToT mode. Here, when a pixel is hit a counter is started until the drained charge is below the threshold. The drain speed can be adjusted via the Krummenacher current I_{krum} ([Kru91]). Here, instead of a feedback resistor to drain the pixel charge, a feedback path of two transistors is used with a biasing current I_{krum} working as an equivalent resistivity. Hence, a change of the biasing current will also change the equivalent resistivity. The lower I_{krum} the higher the resistivity leading to a slower drain. The adjustment of the drain speed is necessary to fit the expected amount of arriving electrons at the pixel to the length of the ToT counter, in order to get the best ToTcharge resolution. The third mode is the ToA mode. Here, a counter is started as soon as the charge in the pixel exceeds the threshold. Then the counter is incremented with the clock speed until it reaches its maximum value or the shutter is closed. For a clock speed of 40 MHz the 14-bit pseudo-random-counter allows a maximum time of 295.25 µs. Therefore, the time between the first hit and the shutter closing should not exceed this value since otherwise early hits might run into overflow being unusable for a later analysis. This can be achieved by either using a short shutter opening time or by using a trigger to close the shutter after an event is recognised. The last mode is the pixel hit mode. Here the Timepix will only count the first hit on a pixel within a frame. So when reading the frame it only shows if a pixel was at least once hit or not. Since this mode is giving less information than the particle counter mode, while providing the same type of data it is not used in the scope of the detectors described in this thesis.

To select these modes each pixel contains an 8-bit configuration register. It contains two bits, called `P0` and `P1`, for the selection of the mode, and additionally four bits for the pixel threshold, one bit to mask the pixel (for example if it is noisy), and one `test bit` to allow for external testing of the pixel. The four threshold adjustment bits can be used to equalise the pixel matrix in order to get a similar response of all pixels within a certain range. This is necessary due to minor differences in the pixels originating from the manufacturing process, meaning not every pixel has the exact same response to a signal. However with the four threshold adjustment bits controlling a 4-bit current digital-to-analog converter (DAC), those differences can be minimised. To minimise this distribution two steps have to be done first, the current source of the current DAC has to be set to a value, via the `THS` DAC, such that all pixels can be equalised to the same value by having the smallest possible steps in between the threshold adjustment DAC values. After this, the threshold DAC value for each pixel has to be determined (for the procedure see 10.3.1). The next part of the pixel configuration is the mask bit. With the mask bit a pixel can be switched off. This might be necessary if it is broken in the sense that it always has high count rates. The `test bit` allows to send a test pulse into an 8 fF capacitance to test the pixels. The `test bit` allows to select individual pixels in order to prevent cross talk. The voltage pulse for this has to be externally generated and connected via the `test in` pad to the ASIC.

The pixels are read out either parallel or in a serial way while in both cases several chips can be daisy chained leading however to increasing readout times. For the applications shown only the serial readout was used in order to avoid the need for 31 additional lines for the readout. To tell the ASIC what operation should be performed a set of 6 input pads is used (`M0`, `M1`, `Enable_In`, `Shutter`, `Reset`, `P_S`). They have to be set as shown in table 4.1 for the operations. Since the signals have to be set for the

M0	M1	Enable_In	Shutter	Reset	P_S	Operation
X	X	X	X	0	X	General reset
1	1	X	0	1	X	Counting
0	0	0	1	1	0	Serial readout
0	0	0	1	1	1	Parallel readout
0	1	0	1	1	X	Set Matrix
1	0	0	1	1	X	Write/Read FSR

Table 4.1: Input settings for the different operations of the Timepix ASIC. Adapted from ([Llo06])

full operation and must not be changed during the operation some of them can be set via slow control signals. Also a couple of other signals need only to be changed before an operation and therefore do not need a fast connection. Other signals like the `Shutter` or the `Enable_In` have to be sent fast in order to get the correct timing. These signals need to be timed with the input clock of the ASIC.

To control the DACs of the Timepix ASIC and to read the unique name (Chip ID) each ASIC has a Fast Shift Register (FSR) as part of the periphery. All 17 DACS can be changed with one command sending the values into the FSR. Additionally, the Chip ID will be send to the user while performing the operation. The DACs control different parts of the chip for example the overall threshold `THL` of the ASIC or the current drain of the pixels via the `IKrum` DAC. An overview of all DACS can be found in ([Llo06]).

In order to write any data to the chip two signals have to be sent to the chip, aligned with the `clock`, the `Data_In`, and the `Enable_In`. The number of clock cycles has to match the number of bits to be written to the chip (and some preload depending on the operation) and the first clock cycle has to match the first bit of data. Therefore the timing is very crucial for the Timepix ASIC. If the Timepix is used in the daisy chained mode then the number of clock cycles has to be multiplied by the number of ASICs.

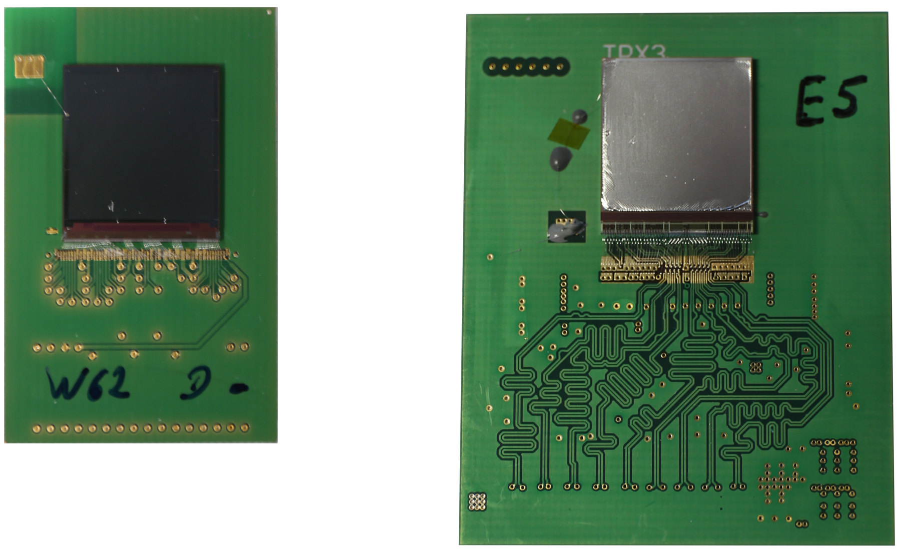

(a) (b)

Figure 4.1: Pictures of: (a) a GridPix on its carrier and (b) a GridPix3 on its carrier. It is visible that the GridPix3 carrier is larger than the carrier used for the GridPix. This is mainly due to the additional lines for the eight data links and the necessary time matching due to the high signal frequency.

With the Timepix3 ASIC [PPW+14] as the successor of the Timepix ASIC some major changes were introduced, while keeping the physical layout similar. The most interesting changes will be described in the following. Pictures of a GridPix (Timepix) on its carrier and a GridPix3 (Timepix3) on its carrier are shown in figure 4.1. First of all the Timepix3 offers three different operation modes, an only ToA mode, a combined ToT and ToA mode, and an event counter mode. Especially, the combined ToT and ToA mode is extremely useful, since it provides additional information. This mode will also be mainly used for the detectors developed in the scope of this thesis. In this mode each pixel has a 10-bit ToT counter and a 14-bit ToA counter. They both are measuring simultaneously. A special setting allows the ToA to have additionally a 4-bit fast ToA register (fToA) allowing for a resolution of 1.56 ns. The time resolution of the 14-bit ToA counter is 25 ns leading to a maximal readout time of 409.6 µs before the counter starts at zero again. The only ToA mode reduces the data amount to just the 14-bit ToA value with the possible extension by the 4-bit fast ToA extension. However the amount of data sent per pixel will be the same as in the other modes (the 10-bit of the ToT register will then contain no information), hence this mode gives no information not already included in the combined mode. The last mode is the event counter mode. This mode contains a 14-bit integral ToT counter and a 10-bit hit counter. This mode is used for certain calibrations 10.3.1.

The second major change concerning the Timepix is the readout of the ASIC. The Timepix3 can be read out in two different modes. A frame based mode like for the Timepix and a data driven mode where the data is sent when a pixel registers a hit. Therefore, nearly no dead time due to the readout will be introduced. Additionally, both versions of the readout use zero suppression, so only pixels that registered a hit will be read out, reducing the amount of data to be transmitted and saved. However, to make a zero suppressed output possible the amount of data per hit pixel rises due to the fact that in addition to the 28-bit of data each pixel needs to send its pixel address. The pixel matrix of the Timepix3 is divided into 128 double columns containing 64 superpixels each. A superpixel is a block of eight pixels in a double column. The unique 16-bit pixel address is organised in three fields; The 3-bit pixel number inside a superpixel, the 6-bit number of the superpixel inside a double column, and the 7-bit number of double column. The scheme of the address can be seen in figure 4.2.

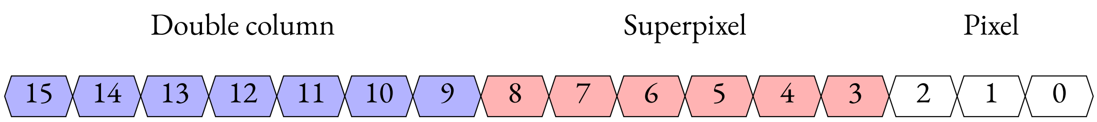

Figure 4.2: Format of the pixel address. The address is divided into three parts the double column number (blue), the superpixel inside the double column (red) and the pixel number inside the super pixel (white). With the zero suppressed output each pixel hit will send its address in this way with the data. Adapted from ([LP15])

The third major change is the way the Timepix3 is addressed with commands. Different to the Timepix, the Timepix3 has a command block decoding input commands. Therefore, all commands are just sent over the input line containing, at the beginning of the command, a header encoding the command type. In order to be able to talk to multiple chips with one data input line the chips can be addressed via their unique Chip ID, but also a broadcast is possible sending the same command to all Timepix3s on the line. A typical command is shown in figure 4.3. The package consists of four parts; The synchronisation header (40-bit) containing the information if the package is a broadcast or if it is for a certain Timepix3 ASIC. A 1-bit header telling the Timepix3 if the command is for the periphery or the pixel matrix, a 7-bit header defining the operation, and the last part containing the necessary data.

With these input packages the Timepix3 can be fully controlled. Depending on the setting of the ASIC and the input package the Timepix3 will send back one or more packages on up to eight output lines. The output lines are not daisy-chainable anymore, therefore each Timepix3 needs its own output line connections. One is free to choose on which and on how many of the lines the Timepix3 will return data.

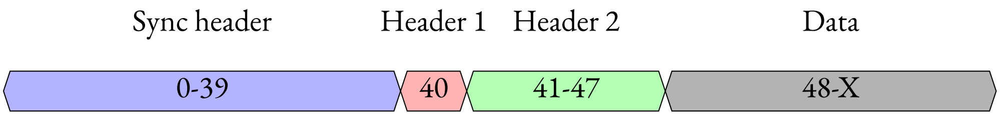

Figure 4.3: Typical input data package for the Timepix3 ASIC. The package consists of four blocks. The synchronisation block (blue) containing information if the package is broadcasted or only for a certain Timepix3, the first header (red) tells the ASIC if the package is for the periphery or the pixel matrix. The second header (green) tells the chip the specific command and the last block (grey) contains the necessary data.Adapted from ([LP15])

The important DACs stay functionally the same as for the Timepix, only the former `THS` DAC is called `Ibias_PixelDAC`. Additionally, there are two test pulse DACs `VTP_coarse` and `VTP_fine` to produce the test pulses directly on the ASIC. Therefore, no external test pulse generation is necessary for the Timepix3. In order to produce test pulses internally, a command can be called to specify the number of test pulses, the period of the test pulses, and the phase shift. The phase shift shifts the clock by one 16th of a clock cycle. This allows for timing corrections over the pixel matrix. If all this is selected and the test pulses are activated the generation will start as soon as the shutter is set to 1. Then a multiplexer will switch between the set levels of `VTP_coarse` and `VTP_fine`. The test pulse generation will be stopped when either the shutter is set to 0 or the set number of test pulses is produced.

4.2 InGrid production

In order to use the high granularity of a pixelised readout ASIC like the Timepix or the Timepix3 ASIC as good as possible for a Micromegas like detector the Integrated Grid (InGrid) technology was developed in 2007 ([vdG07]). Here, on top of the ASIC an aluminium grid structure with a distance of 50 µm to the pixels is built via photolithographic post processing, such that above every pixel there is a matching hole. The process was developed on single ASICs and then scaled up until complete wafers could be processed. Here, only the process for full wafers will be described since all new InGrids are produced on wafer scale. The process itself consists of several steps which will be explained in the following. An overview of the steps is also given in figure 4.4. For the GridPix and the GridPix3 those steps are the same, only the masks change due to the different layouts of the Timepix and Timepix3 wafers as also changes in the position and width of the dykes (a rim fixing the grid).

The first step of the production is the cleaning and inspection of the wafers. The cleaning is extremely important since debris on the wafer leads to inhomogeneities in the later steps resulting in low quality GridPixes (fig: 4.4(a)). After the inspection, the chip area containing the bond pads is covered with a thick (24 µm) thermal stable negative photoresist.

A photoresist is a material that changes its structure due to light exposure. For a negative photoresist, this happens either due to photocrosslinking or due to photopolymerisation. After this, the non-exposed part of the photoresist will be removed with a developer. To produce a layer, typically the resist itself is spin coated on the wafer. Then the wafer will be heated in order to remove solvents from the photoresist. After this, the exposure with light is performed. This either (for a positive resist) will break the structure of the photoresist or (for a negative resist) will start a polymerisation process. After this, in the case of the positive photoresist the exposed part can be chemically removed. In the case of a negative resist, a second baking needs to be performed in order to finalise the polymerisation. Afterwards, the unexposed parts can be removed.

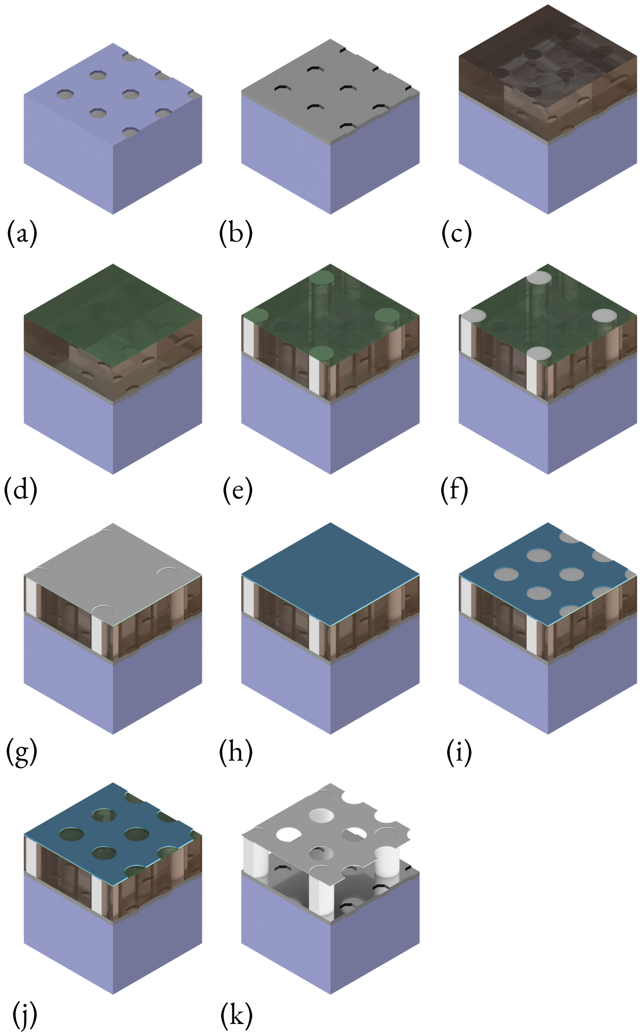

Figure 4.4: Production steps of the InGrid production on top of a Timepix or a Timepix3. (a) the cleaned and inspected wafer, the pixels are indicated as octagons; (b) application of the silicon nitride layer; (c) application of negative photoresist SU8; (d) application of positive photoresist; (e) exposure of photoresists pillars and dyke are formed; (f) removal of exposed positive photoresist; (g) sputtering of aluminium; (h) application of second positive photoresist; (i) exposure and removal of second positive photoresist to form grid structure; (j) wet etching of aluminium; (k) removal of positive photoresists and uneposed SU8.

In the next step a silicon rich silicon nitride layer is deposited on the wafer (fig: 4.4(b)). This layer is grown to 4–8 µm thickness. Here, the homogeneity of the layer is extremely important since it serves as a spark protection. Since the InGrid will be on a high potential, sparks might occur which could destroy an unprotected ASIC. With the protection layer, the charge from the spark will be distributed over a larger area of the ASIC and due to the high resistivity of the layer drained more slowly. Therefore, the layer should not contain any holes, defects, or thickness variations. Example images of a layer with defects and without defects can be seen in figure 4.5. It is clearly visible that in the image 4.5(a) there are lots of defects. This picture is taken from the production run `IZM6`, where the finished GridPixes showed bad spark protection. While the other image 4.5(b) is from the production run `IZM7`, showing a very good behaviour. Additionally, the silicon nitride layer needs to be conductive in order not to charge up and therefore lower the amplification field. After the layer is deposited the photoresist covering the bond pads is removed, leaving them uncovered so they can be contacted via wirebonds. After this, the wafer is inspected again to control the quality of the layer.

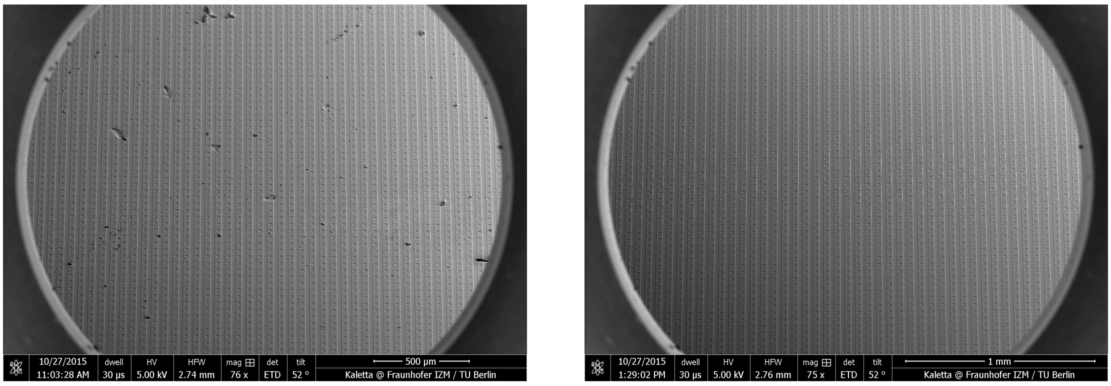

(a) (b)

Figure 4.5: Electron microscope images of the silicon nitride layer of two wafers from different production runs. In image (a) the layer shows lots of large defects resulting in a bad protection layer. The layer of image (b) looks very homogeneous with nearly no defects. ([fZuMI])

In the next step, a 50 µm thick layer of a negative photoresist (SU8-50) is added on top of the the silicon nitride layer from which a pillar and dyke structure to support the grid will be produced (fig: 4.4(c)). On top of this layer a thin 1 µm layer of a positive photoresist is coated (fig: 4.4(d)). This thin additional layer is necessary to allow for an easier later removal of the unexposed SU8. After this, the two layers are exposed through a mask containing the pillar and dyke pattern creating the desired structure (fig: 4.4(e)). The pillars are needed to hold the grid above the pixels at a fixed height. The dyke at the outer rim of the grid structure stabilises the grid and makes the GridPixes easier to handle. Additionally, it provides a stable surface to fix the high voltage connection to the grid needed for operation. After this, the exposed part of the positive resist is removed (see figure 4.4(f)). Then the layers are baked in order to finish the polymerisation of the SU8.

Then a 1 µm thick layer of aluminium is deposited via sputtering (fig: 4.4(g)). From this layer, the grid is produced in the next two steps. First again a layer of a positive resist is spin coated on top of the aluminium to produce a mask with the later hole locations(fig: 4.4(h)). After the exposition and the development (fig: 4.4(i)) of the layer the not covered aluminium is removed by wet chemical etching (fig: 4.4(j)).

Now the InGrid is produced and the wafer will be diced into single GridPixes. After the dicing, the two positive resists (below and above the Grid) and the unexposed SU8 are removed (fig: 4.4(k)). The finished GridPix will be inspected again and depending on the result some additional cleaning in a plasma oven may be necessary.

The structure of a GridPix3 can be seen in figure 4.6. In this image part of the grid is removed to show the pillars. At the part where the grid is visible the good alignment between the holes and the pixels can be seen. This makes it possible to later measure single electrons arriving at the grid holes with

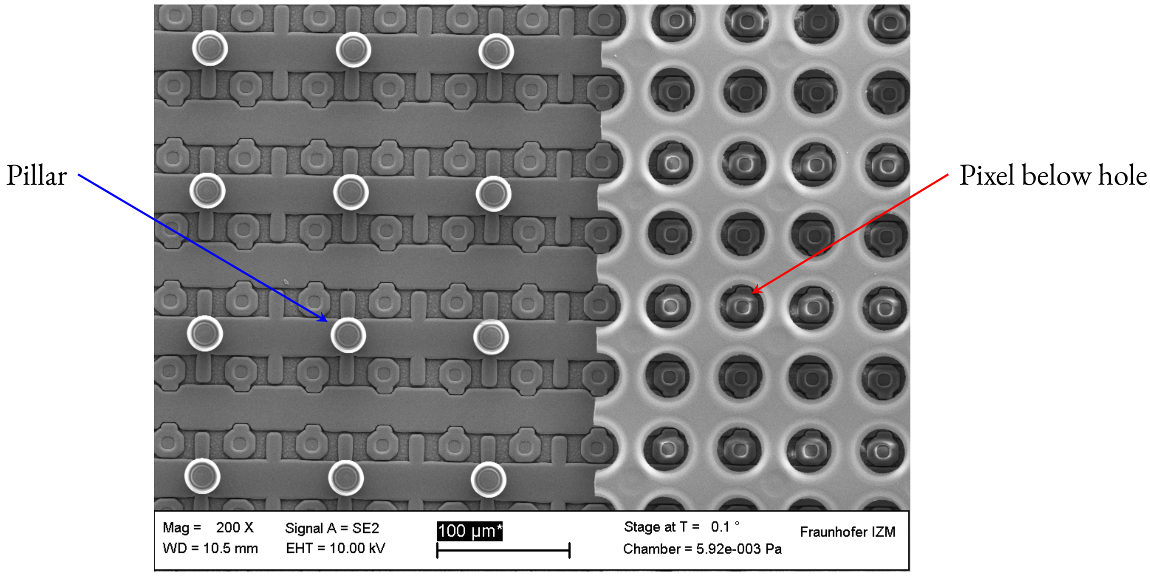

Figure 4.6: Electron microscopy image of the GridPix3. The Grid is partly removed revealing the pillars underneath. The alignment of the grid holes to the pixels can be nicely seen on the right of the image (indicated in red). The pillars are only in every second row and column as seen on the left side of the image (indicated in blue). [fZuMI]

single pixels. The pillars are only placed in every second row and column of the matrix. This amount of support is enough to fix the grid, however height differences of the grid were measured in the order of 4 µm due to sagging. As seen in figure 4.7(a) the grid is at nominal height at the pillars and then bending downwards towards the middle positions between the pillars. A comparison with a FEM simulation using only gravity as the acting force showed no significant deformation.

Only by adding an additional pressure of 50 kPa, the behaviour could be reproduced. In figure 4.7(b) one can see that the way the grid is bending follows the scheme except that at the pillar tops a smooth surface can be observed while in reality the grid is slightly bending upwards. A calculation of the force per area from the electrical field when a high voltage (300 V) is connected to the grid leads only to $F_{el}/A = 160$ Pa. So the electrical force is also too small to explain the deformation. However due to the 1 µm layer of photoresist on top of the SU8 a certain sagging of the grid is expected. Additionally, the removal process of the SU8 includes the movement through the developer liquid acting as an additional force on the grid. The combination of this force and the sagging could explain the 4 µm deviations. Also, the height deviation on top of the pillars is explained by the additional photoresist since at the edges of the hole above the pillars more aluminium will be deposited.

4.3 Comparison of GridPix and GridPix3

Comparing the GridPix with the GridPix3 will show how and on what parts the GridPix3 is changed with respect to the GridPix. In the end, it will be discussed how those changes affect the performance for rare event searches. Since the GridPix is based on the Timepix and the GridPix3 is based on the Timepix3 the differences and similarities of those shall be summerised first. An overview is given in table 4.2.

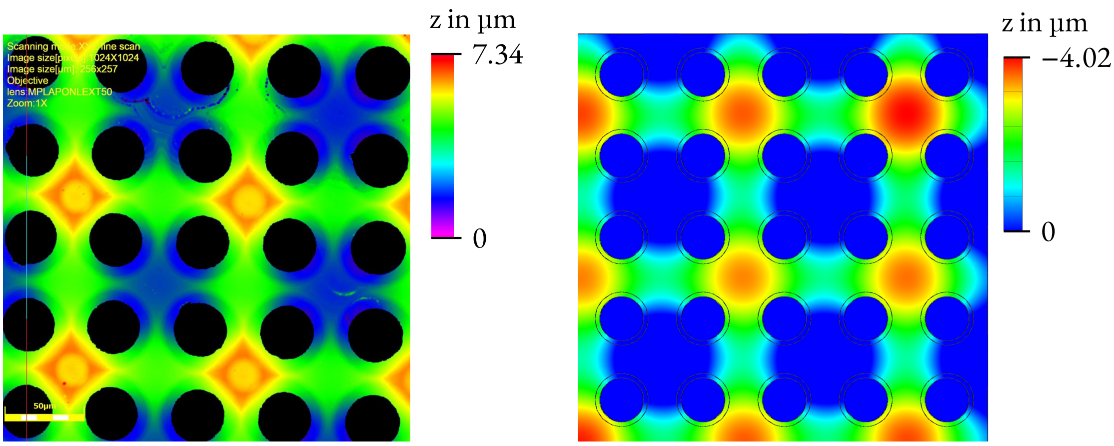

(a) Microscopy image (b) FEM simulation

Figure 4.7: Deformation of the grid measured with a Microscopy (a) showing a deformation of about 4 µm from the pillar top (orange) to the lowest point in between the pillars (blue). In (b) a FEM simulation of the grid is shown where gravity pulls the grid downwards. To reach a similar deformation gravity on its own is not sufficient an additional pressure of 50 kPa needs to be added to the top of the grid. With this configuration the difference is again about 4 µm (the colour scale here is inverted, blue is the pillar top).

	GridPix	GridPix3
Chip size	$14.1 \times 16.1\,\mathrm{cm}^2$	$14.1 \times 16.2\,\mathrm{cm}^2$
Pixel	256×256	256×256
Pixel pitch	$55 \times 55\,\mu\mathrm{m}^2$	$55 \times 55\,\mu\mathrm{m}^2$
Pixel size, open	Octagon $20 \times 20\,\mu\mathrm{m}^2$	Octagon $12 \times 12\,\mu\mathrm{m}^2$
Pixel size, metal	Octagon $30 \times 30\,\mu\mathrm{m}^2$	Octagon $18 \times 18\,\mu\mathrm{m}^2$
Readout	Frame-based, full frame	Frame-based or data-driven, zero suppressed
Readout modes	ToT	ToT and ToA
	ToA	ToA
	Hit count	Hit count and iToT
Time resolution	10 ns	1.56 ns
Min. detectable charge	$> 750e^-$	$> 500e^-$
Pixel below dyke	9.90%	2.34%

Table 4.2: Comparison of GridPix and GridPix3 properties important for a low rate detector

Both chips offer 256×256 pixels with a pitch of $55 \times 55\,\mu\mathrm{m}$. The pixel openings of the Timepix3 ($137\,\mu\mathrm{m}^2$)([Llo]) are about half of the Timepix pixel openings ($350\,\mu\mathrm{m}^2$)([Llo06]). The outline of both chips is very similar: $14.1\times16.2\,\mathrm{mm}^2$, with the pixel matrix occupying a square of $14.1\times14.1\,\mathrm{mm}^2$ the rest is occupied by the analog periphery and the wire bond pads. The most important differences are the data-driven zero-suppressed output of the Timepix3 and the ability to measure ToT and ToA at the same time for each pixel. Also, the number of input signals is reduced for the Timepix3 due to the command block. For multi-chip boards the ability of the Timepix3 to react only on data packages containing its chip name, the number of necessary data lines is further reduced. The Timepix3 offers a

ToA resolution of 1.56 ns which is about 10 times better timing than the Timepix (10 ns). A drawback of the Timepix3 is the reduction of the ToT register to 10-bit, leading to less accurate results or a smaller measuring range. The minimal threshold (minimal detectable charge) of the Timepix is around 750e$^-$ while for the Timepix3 500e$^-$ can be achieved.

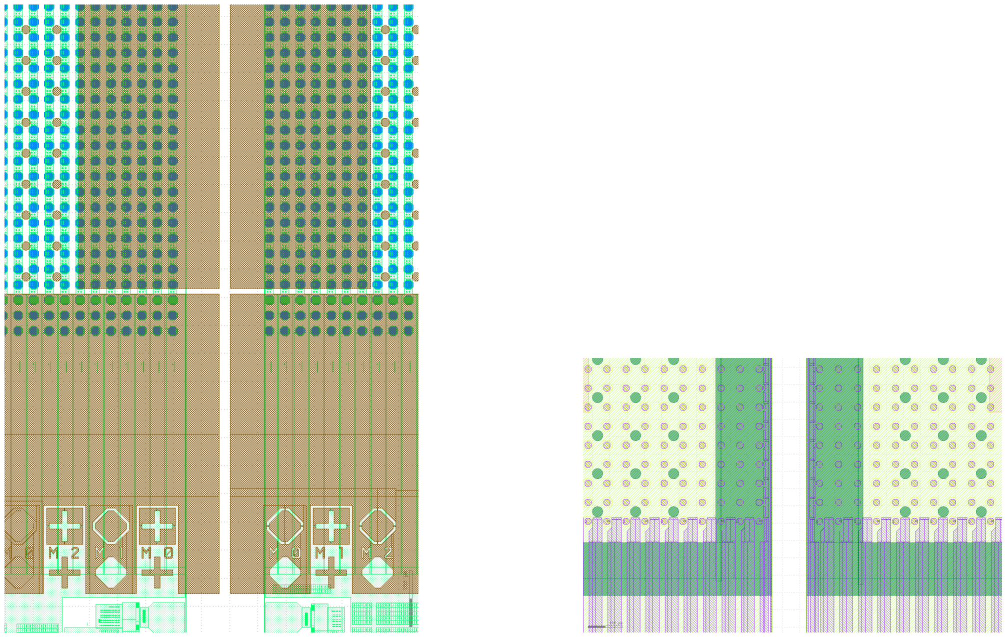

(a) (b)

Figure 4.8: Comparison of the masks for the dyke and pillar structure of the GridPix and the GridPix3. In image (a) the setup for the GridPix is shown. Here, one can see the corner close to the wire bonding pads. It can be seen that the dykes cover three rows of pixels at the bottom and seven columns on the sides of the Timepix. The pixels under the dyke are not usable since they are fully covered with SU8. Not shown in the image is that at the top nine rows are covered. In (b) the same is shown for the GridPix3. It can be seen that on the bottom of the Timepix3 no rows are covered. The same holds for the top. On the sides only three columns are covered by SU8 making them unusable.([Bil])

Regarding the InGrid, on the Timepix3 the number of unusable pixels due to the dyke structure on the outline of the pixel matrix is reduced from 9.9% to 2.3%, due to the development of smaller dykes as shown in figure 4.8. The figure shows the bottom corners of the dykes for the GridPix (fig.: 4.8(a)) and the GridPix3 (fig.: 4.8(b)). The number of covered pixels for the left and right side of the chip is reduced from seven to three columns and in the bottom, a reduction from three to zero covered pixel rows was achieved. For the not shown top row the reduction was from nine rows to zero rows. With 97.6% the GridPix3 offers a bigger active readout surface and less dead space if multi-chip setups are used.

For the usage in a rare event search detector the GridPix3 is an advance compared to the GridPix. With the data-driven zero-suppressed readout it allows for a basically dead time free measurement for very long times. However, since the clock will overflow after 409.6 µs, an additional clock extension via the readout system is necessary. The simultaneous measurement of ToA and ToT allows for efficient event and energy reconstruction, therefore helping to discriminate background events from signal events. For the signal efficiency, the smaller pixels will reduce the collected charge by 25% (see section 13.6). This is partly abrogated by the lower threshold but still implies that a higher gas gain is needed to reach a high efficiency. With the chip itself being the same size as its precursor, due to a better layout of the grid, the available active area is increased. This is also important when a multi-chip detector will be set up since the dead area between the chips is reduced allowing better reconstruction of events. However, two drawbacks need to be mentioned, on one hand, the lower ToT register size allows only for a less precise measurements or a decreased measurement range and on the other hand a higher power consumption leading to even more heat dissipation making cooling of the detector more important. For a single chip detector this will not be a major issue, however for multi-chip setups it was already observed with GridPix and due to the higher power consumption will be an issue for GridPix3.

CHAPTER 5

CAST, BabyIAXO, and IAXO

The axion will be produced, if existent, by the Sun. In the past, three axion helioscope experiments have successfully been operated, achieving upper limits on the coupling constants for axions. The first setup was built in Brookhaven [LSC+92] and was not movable, so the Sun tracking time was very limited ($\approx 2000\,\mathrm{s}$). This first helioscope did only run for about two hours during one sunset. After this, the Tokio Axion Helioscope experiment was set up. It consisted already of a movable magnet. The experiment did run for about five days, tracking the Sun for about half of the time [MMN+98]. After these two rather short running experiments, the next big step was the CERN Axion Solar Telescope (CAST) [ZAA+99], which did perform axion searches for more than 20 years at CERN. A description of CAST will be given in section 5.1. Including CAST, all the mentioned experiments repurposed magnets not intentionally built for an axion helioscope and therefore not optimised for this type of experiments. So naturally, the next step towards an axion discovery is an experimental setup specifically built for this purpose. The first realisation of such an experiment will be BabyIAXO (see section 5.2) [AAAC+21]. BabyIAXO will from the beginning follow the scheme of the advanced axion helioscope (see figure 2.3) and besides its discovery potential will prepare for the International Axion Observatory (IAXO). IAXO as described in section 5.3 will be another big step in discovery and post discovery potential. To compare the experiments in section 5.4 a figure of merit for the experiments will be given and discussed.

5.1 CAST

The CERN Axion Solar Telescope (CAST) started data taking in 2003 and ended data taking in 2022. CAST was using an LHC prototype dipole magnet. As an early prototype, this magnet's bores were straight and therefore suitable for an axion experiment. The magnet was mounted on a movable platform to follow the Sun. First, a description of the experimental design is given followed by a review of the various detectors used in CAST over the 19 years of data taking. The operation can be divided into two different phases, one with a vacuum inside the magnet bore and one with helium as a buffer gas inside the bore (called CAST phase II). Phase II was performed from 2005 to 2012 in order to aim for higher axion masses (see [VBMMR89]). For high axion masses, the conversion probability in vacuum will drop due to the loss of coherence between the axion and the photon. To recover this coherence condition a gas can be introduced into the magnet. This coherence condition only holds for a narrow mass range, such that multiple pressure steps are necessary to cover a range of axion masses.

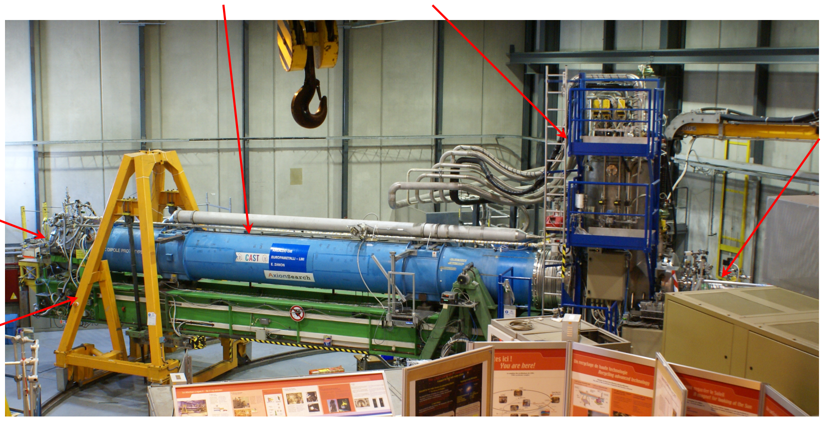

Figure 5.1: Picture of the CAST experiment in 2016. The main parts are labeled. The magnet (blue) was a LHC prototype dipole magnet with straight bores. The sunrise detectors are hidden on the right in the picture behind the magnet's power converter.

In the following, a short overview will be given with some details on the detectors relevant to this thesis. After the description, a short overview of the obtained results is given.

5.1.1 The experimental design

The CAST experiment can be seen in figure 5.1. The experiment consists of an LHC prototype dipole magnet mounted on a movable platform (drive system) to follow the Sun at sunrise and sunset for about 1.5 hours each per day. On both sides of the magnet the mounting of detectors was possible, however on the side for the sunset tracking the space was very limited. On the side for the sunrise tracking additional X-ray optics were mounted in order to focus the X-rays on the detectors to allow for smaller readout areas and better signal to background ratios.

The used magnet is a superconducting dipole magnet with two 9.26 m long magnet bores with a cross section of $A = 14.5\,\mathrm{cm}^2$ [KBC⁺07] per bore and a field of approximately $B = 9\,\mathrm{T}$. The bores have a distance of 180 mm [BRW⁺94] limiting the available space for the upstream systems. As the magnet prototype was built for accelerator purposes, it was never intended to be tilted by large angles. Therefore, construction-wise, it can only be tilted by $\pm 8^\circ$ allowing only 1.5 hours of tracking at sunrise and sunset. The rest of the time the experiment was in a horizontal position and the detectors took background data. At the sunrise tracking side of the experiment, over time, two X-ray optics were mounted. The optics were both Wolter Type 1 [Wol52] optics, consisting of nested systems of parabolic mirrors followed by hyperbolic mirrors.

The first one was a spare optic from the ABRIXAS space mission [KBC⁺07]. Due to the small size of the magnet bore as seen in figure 5.2(a) only a small part of the optic was used. Therefore, the image was not of a circular shape but more of an hourglass shape. As shown in figure 5.3(a) the efficiency of the telescope is very high in the energy range between 500 eV and 2.5 keV. Then it drops sharply by about 50%. Between 2.5 keV and 7 keV, it then stays more or less constant until it drops towards higher energies. The focal length of the optic is 1600 mm. The second optic was a custom made pathfinder for the IAXO experiment based on the optics for the NuSTAR mission [HCC⁺13].

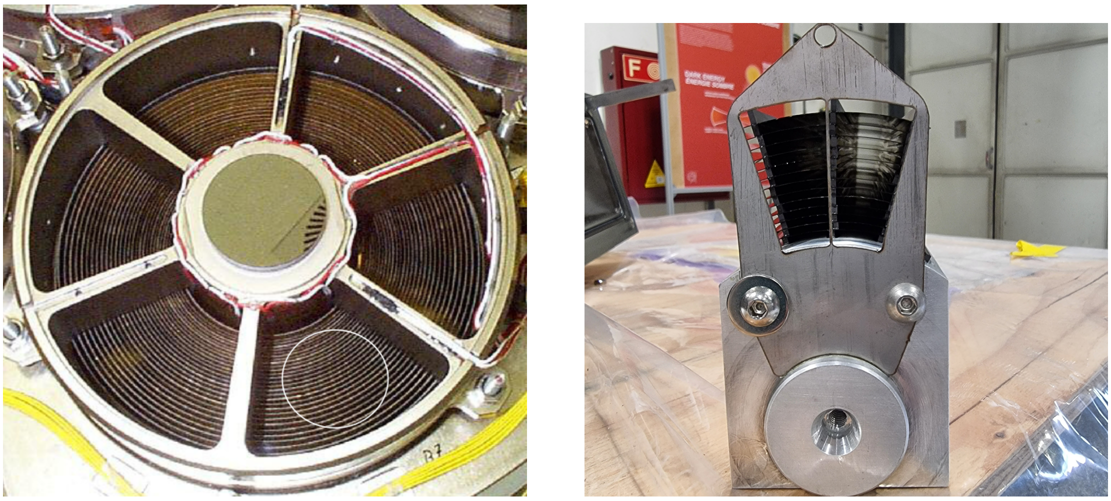

(a) (b)

Figure 5.2: Pictures of the two X-ray optics used at CAST. (a) The ABRIXAS optic with the beam pipe position indicated. [KBC+07] (b) The custom optic, which due to the small beam pipe diameter only consists of one wedge of a full optic [C.].

It was custom built for CAST. Here, again due to the small size of the magnet bore, only 1/12 of the optic was built as seen in figure 5.2(b). Therefore, the image on the focal plane is hourglass shaped. Regarding efficiency, as shown in figure 5.3(b), the optic performs better at low energy, especially at very low energy (< 500 eV) and at high energies (> 4 keV) worse than the ABRIXAS optic. The focal length of this optic is 1500 mm.

In the focal plane of the X-ray optics, the detectors are mounted in housings of radiopure lead. The lead thickness depends on the X-ray optics since the focal planes and therefore the available space differs. The detectors, X-ray optics, and the magnet bores are connected via a vacuum system to avoid absorption of the low energetic X-ray photons.

The whole system is mounted on a movable platform allowing for $\pm 8^\circ$ inclination and $\pm 40^\circ$ rotation. The movement of the stage reaches a precision of better than 0.01° [ZAA+05].

5.1.2 The detectors

Over the years of operation seventeen different detectors have taken data at CAST to search for new physics like the axion. In this section, an overview will be given. In the first data taking period of CAST three different detectors were mounted, a time projection chamber (TPC), a Micromegas detector (MM), and a charge coupled device (CCD). While the TPC was mounted on both bores of the sunset side of the experiment, the other two were mounted on the sunrise side, each covering one of the bores. Since only the ABRIXAS optic was available, only the CCD detector could make use of a focused beam.

The TPC was mounted on the sunset side where not a lot of space is available, hence the capability to place a proper shielding was quite limited. However, a multi-layer shielding of copper, lead, cadmium, and polyethylene surrounded the detector. The TPC itself had a drift length of 10 cm and a multi-wire readout plane. In order to allow the X-ray photons to enter the TPC, thin windows made from 3 µm

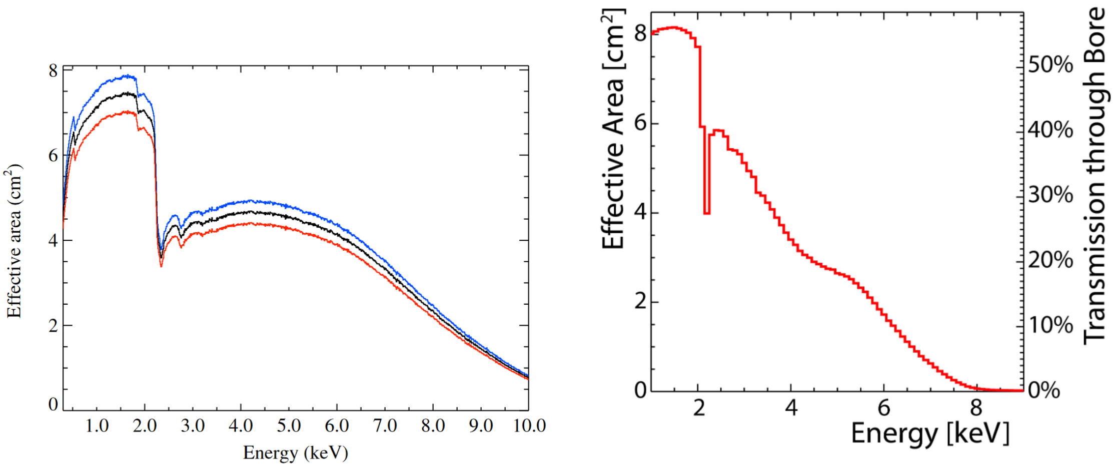

(a) (b)

Figure 5.3: Effective area (a measure for the efficiency of an optic) of the two CAST X-ray optics. (a) The ABRIXAS spare optic's effective area. The three curves show the behaviour for different positions between the magnet bore and the optics (for an infinitely far away source (black and blue)) and for the axion sun (red) at the position corresponding to the positioning leading to the black line. The fast decrease at about 2.5 keV can be seen as well as the decrease at energies beyond 7 keV. [KBC+07] (b) The efficiency of the IAXO pathfinder optics at CAST. Here, the good efficiency at low energies and the loss of efficiency towards high energies can be seen [ACC+15].

and 5 µm Mylar® foil with a coating of 40 nm aluminium were used. During operation the TPC was filled with an argon(95%)-isobutane(5%) mixture at atmospheric pressure [ABC+07].

The MM detector on the sunrise side was set up from a MircoMegas readout behind a 2.5 cm or 3 cm drift volume. The used gas was also argon(95%)-isobutane(5%). As a window, here a combination of two 4 µm polypropylene windows was used. While the one between the gas volume and the vacuum of the beamline is glued on a strongback to withstand the pressure difference, the second one was used to allow for differential pumping since the leak rate of the detector window itself was too big. The MM detector was operated until 2006 without any shielding [AAA+07a, ADF+09].

The CCD detector was mounted behind the ABRIXAS optic and inside a vacuum, therefore no window was necessary. It was a fully depleted pn-CCD cooled to $-130\,^{\circ}$C. The shielding around the detector was made of copper and lead [KBC+07].

All three detectors reached background rates in the order of 4×10^{-5} counts cm^{-2}keV^{-1}s^{-1} to 8×10^{-5} counts cm^{-2}keV^{-1}s^{-1}. The detectors took data during the first phase with the magnet bore under vacuum (2003-2004) and a second phase (2005-2007) with the magnet bore filled with ^{4}He to reach higher axion masses (up to $m_a = 0.4$ eV).

After this, the TPC showed signs of degradation and was replaced by two new Micromegas detectors. Also, the other Micromegas detector was replaced.

These three MM detectors were designed with a smaller outline, allowing for better shielding to reduce the background. Later one of them was replaced by a microbulk Micromegas detector reducing the background even further. These detectors reached background rates in the order of 1×10^{-5} counts cm^{-2}keV^{-1}s^{-1} [ADF+09].

Additionally, behind the sunrise MM detector a calorimeter was placed to search for axions from nuclear decays. The converted X-ray of these processes would result in mono-energetic lines in the order of MeV [AAA+10].

With this detector setup now consisting of four detectors from 2008 to 2012 a data taking campaign with ^{3}He inside of the bores was performed to reach for even higher axion masses (up to $m_a = 1.2\,\mathrm{eV}$). The ^{3}He was necessary since due to the very low temperature inside the magnet bore and the high pressures needed to reach these high axion masses ^{4}He would condense.

After this, the bores were evacuated again and a new set of detectors was mounted. The new detectors included a silicon drift detector (SDD), and a GridPix detector. Both detectors were installed to search for solar chameleons (a dark energy candidate). Additionally, the best performing Micromegas detector was used for an axion search with a second X-ray optic. At the sunset side, two new MM detectors were mounted. Data taking took place between 2013 and 2015.

The SDD detector was only used for a short period (9 days) at the beamline where normally the ABRIXAS optic was mounted. But, the optic was dismounted for recalibration purposes. The SDD detector was mounted directly inside the vacuum with a radiopure copper shielding. Around the vacuum pipe an additional shielding of 6 cm lead was mounted. The detector was cooled to $-30\,^\circ\mathrm{C}$. However, it performed not very well and reached only a background of 1.43×10^{-3} counts $\mathrm{cm}^{-2}\mathrm{keV}^{-1}\mathrm{s}^{-1}$ [AAA+15].

When the ABRIXAS optic was mounted again, the first GridPix detector was mounted to search for chameleons. It used a 2 µm thick entrance window made from Mylar® and was shielded with 5 cm of lead. The detector was built as a small projection chamber with a 3 cm drift volume filled with an argon(97.7%)-isobutane(2.3%) mixture. This detector reached a background in the order of $\sim 2.9 \times 10^{-5}$ counts $\mathrm{cm}^{-2}\mathrm{keV}^{-1}\mathrm{s}^{-1}$ [Kri18].

At the other magnet bore the new IAXO pathfinder optic was mounted and behind that an updated MM detector. Additionally, two MM detectors were used on the sunset side. All three MM detectors used the microbulk technology as a readout and a 4 µm thick Mylar® entrance window. They were covered in a passive copper and lead shielding with an added active shielding using 5 cm thick plastic scintillators. With this combination, all three detectors reached backgrounds in the order of 1×10^{-6} counts $\mathrm{cm}^{-2}\mathrm{keV}^{-1}\mathrm{s}^{-1}$ [ACC+15] [AAB+17].

After those detectors the sunset side was not operated as a helioscope anymore. With the insertion of cavities into the bores CAST was converted partly into a haloscope (searching for axions from a potential dark matter halo). On the sunrise side, an improved GridPix detector was mounted behind the IAXO pathfinder optic, besides an experiment to search for the direct coupling of chameleons to matter called KWISP (Kinetic WISP detection).

The cavity experiments inserted into the two bores of the CAST magnet were called the CAST-CAPP experiment and the RADES experiment. CAST-CAPP used four $23 \times 25 \times 390\,\mathrm{mm}^3$ rectangular cavities with a tuning mechanism made of sapphire strips to be sensitive to axion masses between 21 µeV and 23 µeV [AAA+22]. The RADES experiment used a mechanically coupled system of five rectangular ($22.9 \times 22.9 \times 10.2\,\mathrm{mm}^3$) [MCC+18] cavities without a tuning mechanism to access a mass of 34.67 µeV [ÁMACB+21].

The KWISP experiment searched for the direct chameleon coupling with a 100 nm membrane inside of a Fabri-Pérot cavity. If a chameleon interacts with the membrane it would displace it leading to a change in the resonance frequency of the cavity, thus being measurable [KCG+16].

The improved GridPix detector is described in detail in chapter 8. It was placed within a lead shielding behind the new X-ray optic and took data between 2017 and 2018. With all improvements the detector reached a background rate in the order of 8×10^{-6} counts cm^{-2}keV^{-1}s^{-1} [Sch24a].

From 2019 to 2021 finally again a MM detector was mounted using argon(97.7%)-isobutane(2.3%) at 1.4 bar(a) and later xenon(48.85)-neon(48.85)-isobutane(2.3%) at 1.05 bar(a). This detector reached background levels in the order of 1.5×10^{-6} counts cm^{-2}keV^{-1}s^{-1} [AAAC+24].

5.1.3 Results

The detectors described before produced new limits on axion and chameleon couplings. Here, the most stringent limits on the axon-photon coupling $g_{a\gamma}$ and the axion-electron coupling g_{ae} achieved with helioscopes (CAST) shall be discussed.

The limit for the axion-photon coupling comes from the CAST data taking campaign of the Micromegas detectors from 2019 to 2021. The limit reached was $g_{a\gamma} < 0.58 \times 10^{-10}\,\mathrm{GeV}^{-1}$ at 95% CL for axion masses up to $m_a = 0.02$ eV. [AAAC+24] Limits for masses up to $m_a = 1.17$ eV were set during the helium phases 2005 to 2010 and are in the order of $g_{a\gamma} < 3.3 \times 10^{-10}\,\mathrm{GeV}^{-1}$ at 95% CL [AAB+14a].

For the axion electron coupling, due to the shifted energy spectrum, the best limit was produced with the improved GridPix detector described in this thesis. The limit for axion masses up to $m_a = 0.02$ eV was determined to $(g_{ae}g_{a\gamma}) < 7.35 \times 10^{-23}\,\mathrm{GeV}^{-2}$ at 95% CL [Sch24a]. The limit can only be given as a combination of g_{ae} and $g_{a\gamma}$ due to the reconversion via the Primakoff effect inside the magnet.

Note that the discussed limits are for solar axions. Other experimental approaches lead to different limits. However, these limits are only comparable to a limited extent, since for example the limits from haloscopes depend on the assumption that axions are part of the dark matter. The same holds for astrophysical and cosmological bounds, which are strongly model dependent. For the axion-photon coupling the current limits are shown in figure 5.10. It can be seen that the limits produced by CAST are weaker than the astrophysical bounds.

5.2 BabyIAXO

The successor of the CAST experiment will be a precursor version of the International Axion Observatory IAXO called BabyIAXO. It will provide a 2 T magnet offering two 10 m long bores with an open diameter of 70 cm being 160 cm apart from each other. Behind both bores an X-ray optic will be placed. In the focal plane, a detector inside a combination of an active and a passive shielding will be placed. The system will be placed on a movable platform allowing for 360° rotation and ±25° inclination. This allows the system to follow the sun for 12 h per day. The experiment will be set up in an underground hall at the DESY facility in Hamburg. In the following, a detailed description of the experimental setup will be given as well as an overview of the proposed detectors and the physics potential of the experiment.

5.2.1 The experimental design

The BabyIAXO experiment as shown in figure 5.4 consists of five major parts: the drive system, the magnet, the beamlines, the optics, and the detectors. While the latter will be described in section 5.2.2, here the other parts shall be explained. A detailed description of the experiment can be found in [AAAC+21].

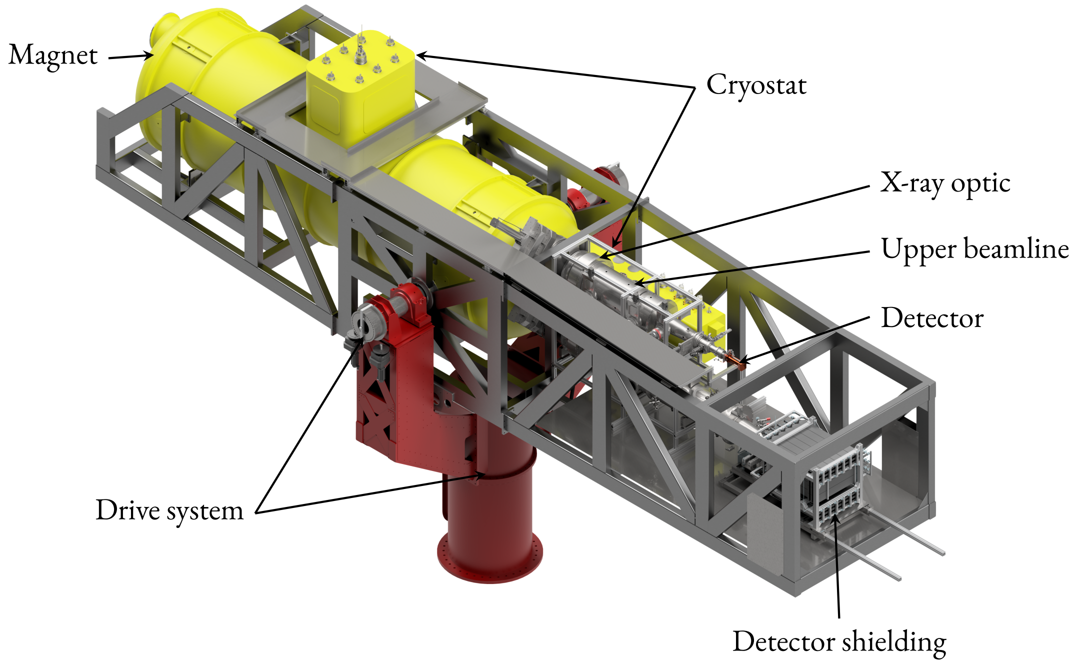

Figure 5.4: Computer aided design (CAD) view of the BabyIAXO experiment. The main parts are labeled. In yellow the magnet and its cryostat can be seen, the drive system is shown in red. The detector shielding of the upper beamline is not shown. For the lower beamline, the detector shielding is shown. The experiment is overall 11 m high, 21 m long and 7.6 m wide. It can rotate fully around its vertical axis and incline to $\pm 25^{\circ}$.

The drive system

In order to build a helioscope it is necessary to have a magnet that is able to follow the Sun for a period of ideally 12 h per day. While longer tracking times will not improve the physics potential of the experiment due to a lack of background data taken, shorter tracking times would decrease the performance. To reach such tracking times in Hamburg (Germany), a system capable of $\pm 25^{\circ}$ inclination and 360° of rotation is sufficient. In order to reach this, a modified Medium Sized Telescope (MST) positioning tower (4.3 m high) from the Cherenkov Telescope Array (CTA) will be used. On the tower the inclination system with the mounting frame is set up. The frame is 21 m long and the first beamline will be positioned at a height of 7 m above ground. The rotation system is taken from the MST and facilitates a pointing resolution better than 0.01°, being able to rotate the system at a maximum speed of $\omega_{\mathrm{rot}} \approx 6^{\circ}/\mathrm{s}$. The inclination system has to be fully redesigned and will provide a pointing resolution better than 0.01° and a maximum movement speed of $\omega_{\mathrm{inc}} \approx 2^{\circ}/\mathrm{s}$. The system has to move a total weight of around 100 t for the inclination and 120 t for the rotation. Therefore, acceleration and deacceleration times have to be carefully taken into account, to reduce stress on the system. The precision of the pointing is very important since a misalignment in the order of 0.05° would already lead to a significant signal loss on the detectors. This can be seen in figure 5.5. If the system is pointing approximately 0.05° away from the sun either in rotation or in inclination, this would lead to a signal loss of 50%. With the planned pointing accuracy of 0.01° the signal loss is in the order of 1% which is sufficiently low.

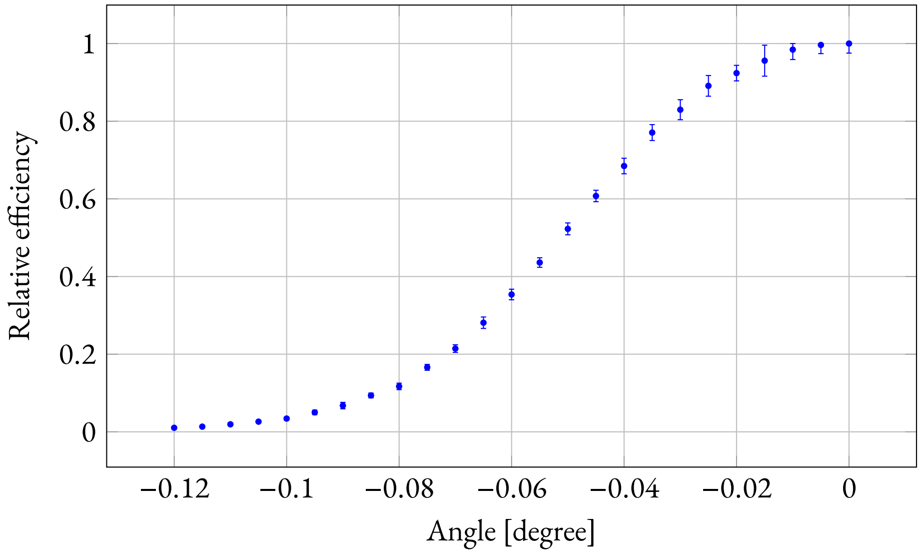

Figure 5.5: Simulation of the efficiency loss if the experiment is, rotation wise, not pointing towards the Sun. It can be seen that already small angular displacements have a strong impact on the efficiency. Data provided by [vO].

The magnet

The magnet is the most important part of the helioscope since the axions convert within its magnetic field. The magnet planned for BabyIAXO is a superconducting magnet with two racetrack coils between which two magnet bores of 70 cm diameter are located. The bores will be operated at room temperature. However, without additional heating, the walls of the magnet bores will reach temperatures in the order of 150 K. To keep the magnet movable, the whole cryogenic system is mounted on the magnet so no external liquid helium lines are necessary. The magnet needs to be inclinable to $\pm 25^{\circ}$ leading to a special design of the cryostat and the cold mass of the magnet. A typical setup for such a magnet is shown in picture 5.6. Inside the vacuum vessel of the cryostat the racetrack coils are fixed with wires and rods around the magnet bores. To reduce the heat load on the cryostat the mechanical connections between the cold mass (the coils of the magnet) and the cryostat vessel (outer vacuum vessel and the magnet bores) should have a high thermal resistance. This can be done by a choice of material or by elongating the fixations. Typically, long cables are used for this. The magnet bores will be fixed in the end caps of the vacuum vessel and therefore will not necessarily need additional supports. The coils forming the cold mass are fixed to each other by stiff rods to counter the repelling force of the two coils when powered. Not shown in the picture are the thermal shields put between the walls of the cryostat vessel and the cold mass. The coils for the BabyIAXO magnet will be made of an aluminium clad Rutherford cable. In order to produce a Rutherford cable multiple superconducting strands are arranged in a helix structure and pressed into a rectangular shape. The superconducting strands are then cladded with aluminium [ABC+85]. For BabyIAXO these superconducting strands are made from Ni-Ti/Cu. The Rutherford cable is then wound in multiple layers into the shape of the racetrack coils. In order to cool the coils to superconducting temperatures, a closed loop cooling system is envisioned, which is positioned on the top of the magnet and in an extension on one of the end caps. The extension is necessary to allow the placement of for example vacuum pumps outside of the stray magnetic field. The

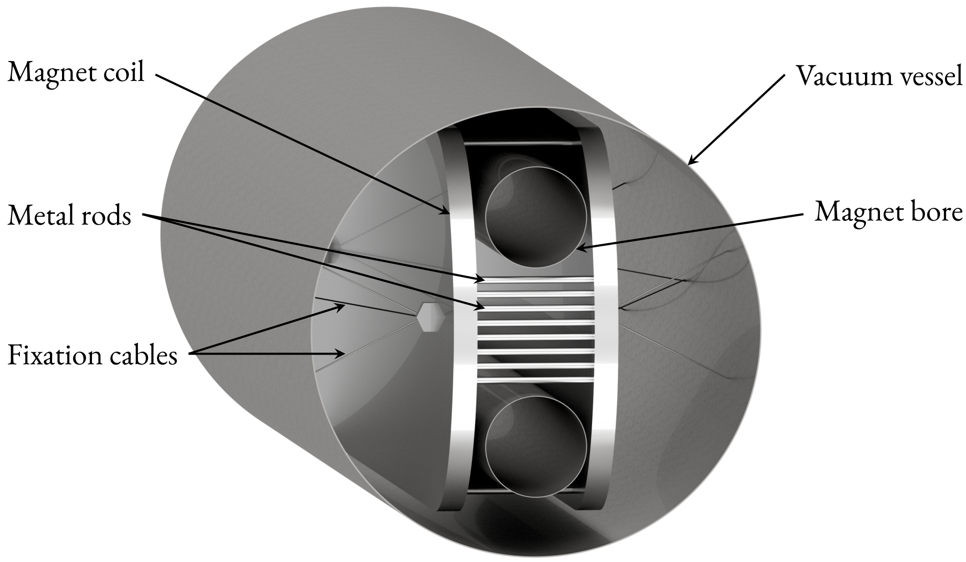

Figure 5.6: Mock-up of a superconducting magnet setup as planned for BabyIAXO. Inside the cryostat vessel (cryostat tank and magnet bores) the cold mass (basically the coils) is fixed to the walls with cables. The coils themselves are fixed to each other with metal rods.

part on top of the magnet contains the reservoir for liquid helium. The position on top of the magnet is necessary to ensure that also in the tilted position the coils are below the reservoir. The current to the coils is provided through so-called bus-bars connecting the coil electrically to the power supplies which need to be placed away from the experiment. The bus-bars need to be thermally isolating while at the same time highly conducting to allow for the high currents (some kA) to flow into the coils. This can be done with copper or aluminium rods and so-called high temperature superconducting (HTS) tape.

The optics

Behind the magnet bores separated by gate valves, the X-ray optics will be mounted. For BabyIAXO two different Wolter Type 1 optics are planned. One is a flight spare of the XMM Newton space mission [SGRK+22] while the other one will be custom built using two different techniques as a pathfinder for IAXO. Additionally, there might also be the possibility to have a third type of optic built as an additional pathfinder for IAXO.

The optic from the XMM Newton space mission is a flight spare that was stored after the mission was launched. It has a diameter of 70 cm with a focal length of $\approx$ 7.5 m [JLA+01] and is therefore well suited for BabyIAXO. The optic consists of 58 nested shells made of gold coated nickel. The shells are produced as full cylinders with the parabolic and hyperbolic mirrors produced as one part. The diameter of the innermost shell is 306 mm, hence approximately 19% of the X-ray flux is lost. An additional loss will come from the rim of the shells and from the structure holding the shells which is called spider (see figure 5.7(a)). In total, the losses due to geometry are approximately 25%. The radius

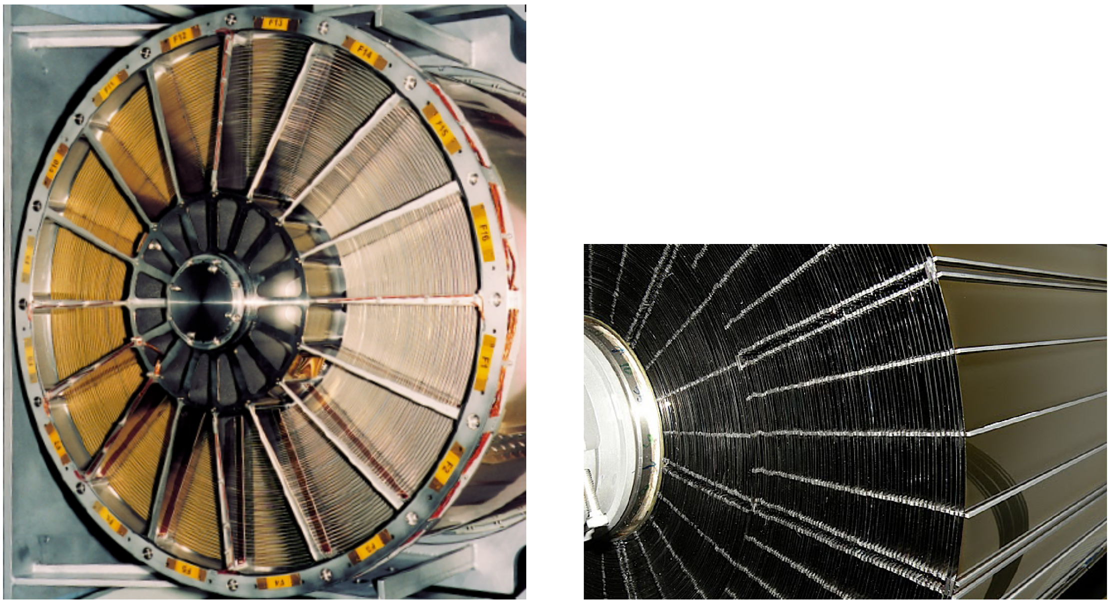

(a) (b)

Figure 5.7: Pictures of the two X-ray optics proposed for BabyIAXO. (a) The XMM optic, in the front the spider structure can be seen holding the mirror shells [DCLVKK99]. (b) The NuSTAR optic, used as the core of the custom optic for BabyIAXO. The two different parts of the NuSTAR optics can be seen. The inner part (65 layers) is made of six segments (divided by two white spacers close to each other) per layer and the outer part (65 layers) is made of twelve segments per layer [CAB+11].

of the focal area where 50% of the energy is collected (half energy width HEW) of the optic at best focus is in the order of 8 mm [vO]. This means, that the entrance window of the detector needs to be at least the same size, to not cut away an additional part of the signal. The overall efficiency of the XMM optic is shown in figure 5.8. It reveals that for low energies the highest efficiency is reached. A first drop can be observed at approximately 2 keV where the efficiency drops by 30%. At 7 keV the efficiency starts to drop again and is constantly dropping towards zero which is reached at about 10 keV. Thus, the optic is well suited for solar axion searches.

The second optic planned for BabyIAXO consists of two different setups, an inner part with a diameter D ($10 \leq D \leq 38$ cm) and an outer part $50\,\text{cm} \leq D \leq 70\,\text{cm}$. The inner part will be based on the optics of the NuSTAR mission and uses multilayer coated segmented glass mirrors. Here, in order to make the production easier the module is produced in a conical approximation for the parabolic and hyperbolic shapes [KAB+09]. The optic consists of 97 layers (less than the original NuSTAR optic depicted in figure 5.7(b)) glued with spacers onto each other. As seen in figure 5.7(b), the layers can be divided into two sets, the first layers are produced from six glass segments per layer while the outermost layers have twelve glass segments per layer. In between are a few intermediate layers built from six segments with more spacers. The coating so far is planned to be of the same type as for the IAXO pathfinder optic used at CAST (see figure 5.3(b)). With this, the search for axion-nucleon coupling producing axions at 14.4 keV can not be performed. Thus, investigations on the coating to achieve efficiency at this energy is ongoing. The innermost mirror shell has a diameter of 108.8 mm, hence the geometrical cutoff is much smaller than for the XMM optic. The outermost shell will have a diameter

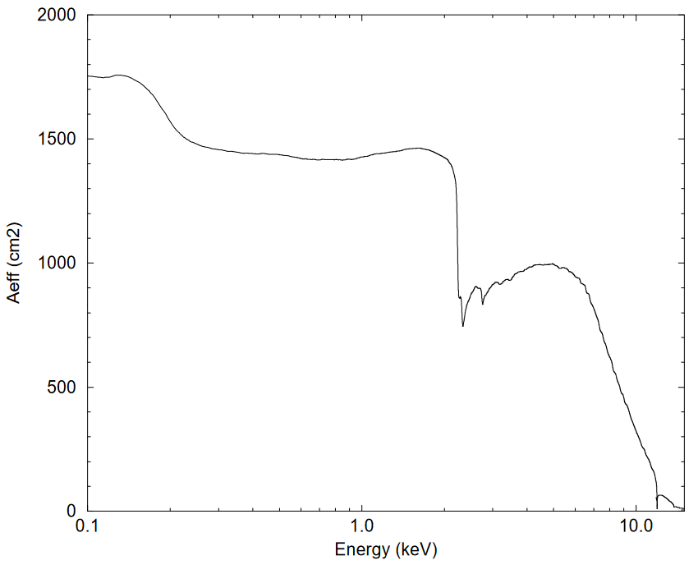

Figure 5.8: Effective area of the XMM optics. With a good performance at low energies a first drop (30%) appears at approximately 2 keV. Then at 7 keV the effective area starts to drop towards 0 which is reached at about 10 keV. Adapted from [JLA+01].

of 382.4 mm, determined by the reused machines from the production of the NuSTAR optic. The focal length is adapted to 5.2 m, so shorter than for the XMM optic. This is important since a shorter focal length will reduce the total length of IAXO.

The outer part of the optics is built in a different way. The CSGO corona optic will be produced from very thin flat glass sheets in a cold slumping process. The thin and bendable glass is pressed into a mold to give it the desired shape. Then they are glued with ribs to the mounting structure to hold their shape. In order to avoid building two separate molds for each of the 33 layers (a parabolic and a hyperbolic), the molds are reused for several layers. This will lead to a broadening of the focal point. However, the reduction of the image quality is not critical for BabyIAXO. The coating for the optic will be produced similarly as for the inner core. Also, the focal length needs to be adapted to the focal length of the inner core. However, since the optics cannot be mounted inside each other, a slight modification of approximately 50 cm is necessary, so the overall focus is on one spot. This is necessary since both optics have a length of approximately 450 mm with a mounting structure between them. The inner optic (NuSTAR) and the outer optic (CSGO) have to be mounted behind each other. Additionally, they should be movable inside of the vacuum vessel in order to be aligned with the optical axis of the experiment. To do so, multiple ideas have been studied. All of them are based on the same ideas. Both optics are fixed to a common frame where the movement system will be attached. A sketch of this can be seen in figure 5.9. Following the X-rays, first the inner optic will be mounted and after that with a shorter focal length the outer optic. This is necessary to avoid shadowing effects and therefore efficiency losses. The whole custom optic will reach a length of about 1 m and with the movement system (e.g. hexapod) a diameter of more than 800 mm. The geometric loss due to not equipped radii of the optic is approximately 24%. The other geometric losses can not be determined at the moment since there is no full design available, however they will be larger than for the XMM optic. Regarding the weight of the optics the custom optic outperforms the XMM optic (420 kg [DCLVKK99]). The original

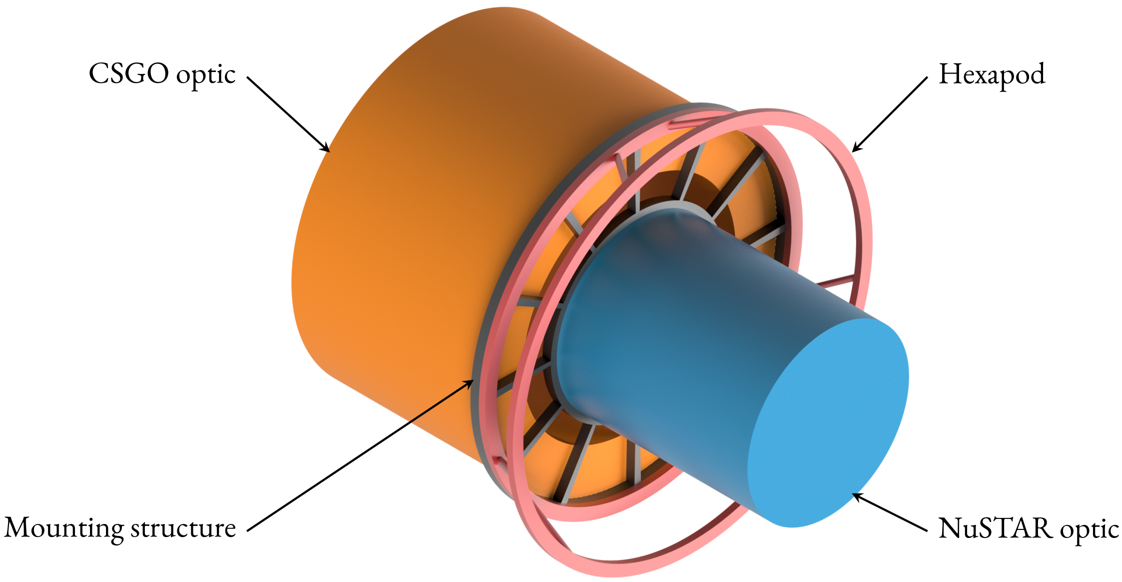

Figure 5.9: Sketch of the custom optics mounted together. At the mounting structure (black) a hexapod (red) is fixed for mounting to the vacuum vessel. This allows for aligning the optics. The X-rays pass the picture from right to left. Hence first the NuSTAR optic (blue) is passed and then the CSGO corona (orange).

NuSTAR optic only weights 38 kg [CAB+11] and since the corona optic is built in a similar way the total weight of the custom optic including the mount will be ≈ 100 kg. This allows for moving the optic inside the vacuum chamber and therefore a very good adaption and alignment to the optical axis. This might reduce losses from misalignment which can be, as shown in figure 5.5, problematic even for small deviations. For the custom optic another approach for the inner optic is also under investigation, a XRISM-like [T+20] core optic. The XRISM space mission was launched in 2023 with a so-called foil optic on board. This optic is built from thin gold coated aluminium foils and similar to the optics of the ASTRO-H mission [OSH20]. This kind of optic would be a good addition to the BabyIAXO custom optic since its design parameters fit very well. It has a focal length of 5.6 m and is built as a soft X-ray optic, therefore focusing X-rays in the range of 300 eV to 12 keV. Also, the outer diameter is 450 mm and therefore fitting as an exchange for the NuSTAR optic [TKM+16]. It is, as the NuSTAR optic, a conical approximation of a Wolter Type 1 optic. The 203 nested shells consist of aluminium foil quadrants. The aluminium foils are shaped for this on a mandrel and then gold coated in a special process [SS96]. This results is a low mass optic suitable for BabyIAXO and would be also a good candidate for the final IAXO experiment.

The beamline

The different focal lengths of the two optics lead to the setup of the beamlines as seen in figure 5.4. The XMM optic will be used in the lower beamline and the custom optic will be used for the upper beamline in order to not obstruct the space for detectors more than necessary.

The beamlines themselves are an important part of the experiment since they transport the X-ray photons to the detectors. The beamlines are necessary since the low energetic X-rays would be absorbed in air within less than 1 m [Gul]. Hence, a vacuum system is required to get a sufficient transmission towards the detectors. The beamline consists of vacuum pipes as a connection between the optic vessels and a gate valve, behind which the detector systems are mounted. Since the optic vessels and the beamline are connected without a differential window, the vacuum requirements for both parts need to be fulfilled. To these pipes, the vacuum pumps and measurement devices are connected. A detailed overview of the beamline vacuum system will be given in chapter 6. After the experimental phase using a vacuum inside the bores also a phase with gas inside of the bores is foreseen to aim for higher axion masses. For this additional ports at the beamline need to be foreseen.

The detector systems

The detector systems consist of dedicated vacuum systems in order to reach at least the same vacuum level as in the beamline. Each detector system might vary vastly for the different detector technologies, therefore here only the setup for the GridPix3 detector (see chapter 11) will be discussed. However, this setup is very similar to the one of the Micromegas detector.

The detector beamline for the GridPix3 detector consists of a vacuum system as described in chapter 6. The roughing pump is mounted with an additional needle valve in between the pumping line, so the pressure change at the ultra-thin detector window is slow, reducing the risk of failure. Additionally, a movable calibration source will be mounted at this part. The calibration source is either a ^{55}Fe source or an X-ray tube. The calibration source will be mounted on a linear stage able to move it into the centre of the beamline. If it is taken out of the beamline, great care has to be taken that no radiation will enter the beamline. After this part, an extension tube made of radiopure copper will be used to position the detector in the focal plane of the corresponding optic. Inside the tube a radiopure polytetrafluoroethylene (PTFE) tube will be mounted to absorb the fluorescence photons from the copper. Around the copper tube and the detector a passive shielding made from lead, copper, and PTFE is foreseen to shield the detector from cosmic background radiation. In order to also remove background events induced by muons, an active scintillator shielding will be mounted around the passive shielding, tagging events in which a muon entered the shielding. Those events will then be removed in the later data analysis. The GridPix3 detector itself is then mounted inside the shielding and is also only composed of radiopure material (for a detailed description see chapter 11). For the other detectors, the shielding may vary depending on the setup. The foreseen detectors will be described in the following.

5.2.2 Proposed detectors

For BabyIAXO currently five different detector technologies are under development. The detectors used at BabyIAXO should have a background level in the order of 10^{-7} counts cm^{-2}keV^{-1}s^{-1} to reach the required sensitivity to the axion couplings. Hence, a good background reduction hardware- and software-wise will be necessary.

The Micromegas detector

The baseline detector is an improved version of the Micromegas detector (MM), already successfully used at the CAST experiment. The detector is built as a small time projection chamber with a 3 cm drift cylinder made of radiopure copper and a microbulk Micromegas readout, $6 \times 6\,\text{cm}^2$ in size. Inside of the drift cylinder a Kapton® field cage is mounted, surrounded by a PTFE layer to absorb the copper fluorescence photons. The cathode of the detector contains a 4 µm Mylar® entrance window which is metalised on one side. The window is glued on a metal strongback to withstand the pressure difference between the vacuum of the beamline and the gas pressure inside the detector. The detector is fully sealed with PTFE seals. For operation two different gas mixtures are taken into account, on the one hand, a mixture of argon(98%)-isobutane(2%) at 1.4 bar(a), and on the other hand a mixture of xenon(50%)-neon(48%)-isobutane(2%) at 500 mbar(a). The xenon mixture has two benefits, one being the higher X-ray absorption of the gas and therefore a lower pressure inside of the detector allowing for thinner windows and on the other hand no fluorescence line in the region where the axion signal is expected. A detector built in that fashion reached background levels in the order of 1.5×10^{-6} counts $\text{cm}^{-2}\text{keV}^{-1}\text{s}^{-1}$ above ground and 1×10^{-7} counts $\text{cm}^{-2}\text{keV}^{-1}\text{s}^{-1}$ in the Canfranc underground laboratory [ACD+14] where muons are absent. So with a proper muon veto system, similar backgrounds should be achievable.

The GridPix detector

The second detector will be a radiopure built GridPix detector. The GridPix detector is also built as a small time projection chamber and will be described in detail in chapter 11.

The silicon drift detector

The third detector is a silicon drift detector (SDD). The detector is based on the TRISTAN detector [TRI22] [MBK+20] for the KATRIN experiment [AAA+21]. The TRISTAN SDD is built to measure electrons with a high energy resolution at very high rates. For this purpose, the SDD has a very thin entrance window in form of a 10 nm SiO_2 layer. This allows to measure low energetic X-rays since they are not absorbed in this layer. In order to develop the detector towards BabyIAXO, additionally a readout was implemented on the SDD, which allows to move the readout electronics far away from the SDD. The whole setup can be produced from radiopure materials allowing for the required low background. As shielding, a combination of copper and lead is foreseen with a scintillator muon veto. Furthermore, a high purity germanium detector might be set directly around the SDD to measure fluorescence X-rays coming from the copper and lead shielding. With the prototypes so far a background rate of 5.6×10^{-6} counts $\text{cm}^{-2}\text{keV}^{-1}\text{s}^{-1}$ was reached in the Canfranc underground laboratory [BBE+24]. Despite being able to measure over most of the range of the Axion spectrum starting at about 0.5 keV [Wie], the energy resolution is very good ($\sim 130\,\text{eV}_{\text{FWHM}}$ at 6 keV). Another advantage is the possibility to operate the SDD in a vacuum, not requiring a window in front of the detector and therefore increasing the signal.

The metallic magnetic calorimeter

The fourth detector proposed is a metallic magnetic calorimeter (MMC). A MMC is a calorimeter working at temperatures in the order of 100 mK. Typically, a paramagnetic metallic absorber (e.g. gold)

Detector	Energy range in keV	Energy resolution at ~ 6 keV	Achieved background in counts $\mathrm{cm^{-2}keV^{-1}s^{-1}}$
Micromegas	1–10	$\sim 780\,\mathrm{eV_{FWHM}}$	1.5×10^{-6}
GridPix	0.2–10	$\sim 540\,\mathrm{eV_{FWHM}}$	1.1×10^{-5}
SDD	0.5–50	$\sim 130\,\mathrm{eV_{FWHM}}$	5.6×10^{-6}
MMC	0.1–≥ 10	$1.6\,\mathrm{eV_{FWHM}}$	$\sim 10^{-4}$
TES	0.05–≥ 10	$\sim 3\,\mathrm{eV_{FWHM}}$	$\sim 6 \times 10^{-5}$

Table 5.1: Comparison of the five detector technologies. The three most interesting values regarding the discovery potential are selected.

weakly coupled to the thermal bath is placed in an external magnetic field. If the temperature of the absorber is changed also the magnetisation of the absorber will change leading to a signal in a pick-up circuit. The signal is then amplified and can be read out [FLB+09]. MMCs can measure over the whole range of axions produced by the Sun with high efficiency. However, they suffer from infrared radiation (IR) and therefore need an IR-blocking window in front despite being operated in a vacuum. They also reach a very good energy resolution ΔE_{FWHM} of a few electron volts. This would allow to measure specific features of the axion spectrum after discovery. For BabyIAXO a prototype based on the maXs30 detector chip, originally developed for applications at FAIR [HKS+15], was set up and tested. The chip consists of 8×8 pixels covering an area of $4 \times 4\,\mathrm{mm}^2$. So far, the prototype detector only reached a background level of $\sim 10^{-4}$ counts $\mathrm{cm^{-2}keV^{-1}s^{-1}}$ [UAE+21].

The transition edge sensor

The fifth detector is a transition edge sensor (TES). A TES is based on the principle of the transition between the normal and the superconducting state of a material. The resistivity drops in that region very fast with the temperature. This can be used in the way that small temperature changes will induce large resistivity changes. The TES will be then voltage biased and coupled to a very sensitive current amplifier. This makes it possible to measure the change in resistivity by a change in the current [IH05]. With this technology, large array detectors with more than 1000 pixels have already been realised. The benefits of the TES detector are again a very low energy threshold $\sim 50\,\mathrm{eV}$, the possibility to mount it in a vacuum, and a very good energy resolution of $\sim 3\,\mathrm{eV_{FWHM}}$ [IH05]. However, they need a very stable cryogenic temperature to be operated. The biggest challenge here is to reach the goal in the background rate. The development of low background TES detectors so far reached a limit of $\sim 6 \times 10^{-5}$ counts $\mathrm{cm^{-2}keV^{-1}s^{-1}}$ [PG17].

5.2.3 Comparison of the detectors

A comparison of the key parameters of the five detector technologies is given in table 5.1. The three most interesting parameters are chosen to be the energy range the detector can efficiently measure, the energy resolution in order to resolve the structure of the axion spectrum, and the background rate to increase the chance to find the axion. While the Micromegas, the GridPix, and the SDD perform very well regarding the aim for a low background, the MMC and the TES have an incredibly good energy resolution, however, they perform badly regarding their background rate so far. This makes the first mentioned detectors a good choice for the beginning since they are further developed for the case of

BabyIAXO and have a higher possibility of being sensitive enough to find the axion. The latter two detector technologies might be added at a later stage since they would be able to resolve the solar axion spectrum and therefore allow the investigation of the different axion couplings. Further important differences like the necessity of a window and its properties are problematic to compare since they are very dependent on the energy of the X-ray photons. However, it can be stated that for very low energies ($E_\gamma \leq 1\,\mathrm{keV}$) a window influences the signal. At those energies detectors with very thin (both sides in vacuum) or no windows, might outperform the other detectors even when not reaching the anticipated background rates.

5.2.4 Specialised detectors

In this section, other more specialised detectors proposed for BabyIAXO shall be discussed. First a specialised detector for the axion emission from the axion-nucleon coupling at 14.4 keV shall be discussed and second a calorimeter in order to measure axions appearing from supernovae.

The emission line from the axion-nucleon coupling at 14.4 keV is challenging for most of the mentioned detectors since the efficiency of the detector drops (technology dependent) drastically towards higher energies. Only the SDD has shown good performance in this aspect so far. Other possibilities would be a gaseous detector with a higher pressure or a denser gas like xenon to increase the absorption. Additionally, the drift distance could be extended. A combination of these three methods could lead to a detector able to measure those energies. However, this is achieved at the price of reducing the capability for low energies (diffusion, absorption by a thicker window). Other possible technologies might be semiconductor detectors based on cadmium-zinc-telluride, which due to the heavier elements have good efficiencies at higher X-ray energies [TKK21].

Also, a calorimeter for measuring axions from supernovae is under investigation. Here, the photons will have energies in the range of 10 MeV to 100 MeV [GHI+20]. Those X-rays cannot be measured with the so far proposed detectors. Hence, a calorimeter optimised for this energy range might be used if feasible. Since the supernovae events need to be close by ($\lessapprox 300\,\mathrm{pc}$) [CPG+25] in order to have a measurable axion flux arriving at the experiment, such events are quite rare. Thus, the calorimeter should not block one of the two experimental stations. A good way would be to place them on the other side of the magnet in front of the magnet bores. If a supernova is upcoming, this can be determined some hours before the core collapse [MLTZ20], giving time to point BabyIAXO towards the supernova. However, the position error is quite large in the beginning and gets smaller over time. For Betelgeuse as an example, the position one hour before the supernova can be narrowed to a circle of about 45°. This would contain four possible candidates. In the best scenario two minutes before the circle narrows to 20° to 30° enclosing only one or two possible candidates. Therefore, a good chance for observation is given, especially considering the fast movement of $\sim 2^\circ/\mathrm{s}$ in inclination and $\sim 6^\circ/\mathrm{s}$ in rotation possible with BabyIAXO. Even within a minute pointing to a new close-by candidate might be possible.

In a later stage, it is also planned to insert cavities into the magnet and therefore to use BabyIAXO as a haloscope [AÁMAC+23]. For this, a cryostat will be fitted into the magnet bore. Into the cryostat then a cavity or multiple cavities will be inserted. A single cavity (10 m long, 60 cm diameter) would benefit from an easy readout and would be sensitive to a mass of 1.2 µeV. However, such large cavities are complicated to manufacture and very hard to tune in order to measure not only at a single axion mass. Hence, a multi-cavity approach might be more feasible. Here, the complicated part is the coupling of the different cavities in order to get the maximum signal out. A last approach might be to have multiple cavities tuned to different axion masses but running for a longer time.

5.2.5 Physics potential

With the BabyIAXO helioscope, the physics reach is already given and with the setup and the planned detectors, the detection of axions is possible by reaching into a yet unexplored part of the parameter space. For the axion-photon coupling $g_{a\gamma}$ the current limits and the projection for BabyIAXO are

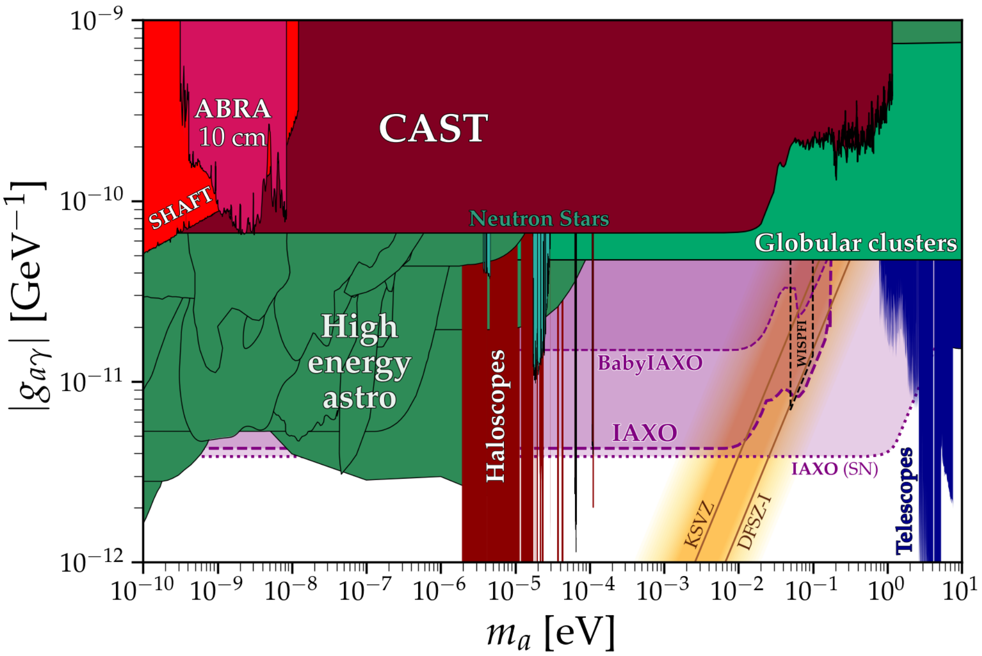

Figure 5.10: Current limits and projections for the axion-photon coupling $g_{a\gamma}$.Shown is the for helioscopes relevant mass range from $m_a = 10^{-10}$ eV to $m_a = 10$ eV. Cosmological limits are shown in green, and exclusions from haloscopes are in dark red. The projections for BabyIAXO and IAXO are shown in purple as well as the projection for a measurement of axions from a supernova with IAXO. Plotted with [O'H20].

shown in figure 5.10. It can be seen that BabyIAXO will already access previously unexplored parts of the parameter space. Further, the cosmological limits are always model dependent and therefore cannot fully exclude an axion. The same holds for the haloscope exclusions. For the measurement of axions from supernovae no limit is calculated for BabyIAXO, however it might also extend the limit since the conversion process reaches towards higher axion masses. This can be seen in the supernova projection for IAXO. Regarding the axion-electron coupling g_{ae}, which can with BabyIAXO and IAXO only be measured as a combination of $g_{ae} \times g_{a\gamma}$, a new part of the parameter space can be investigated. The same holds for the chameleon. In the later stages with cavities inserted, limits on the axion-photon coupling using BabyIAXO as a haloscope will be achieved [AÁMAC+23].

Additionally, the setup can also be used to measure ultrahigh-frequency gravitational waves, here the magnetic field and the bore are used to convert gravitational waves via the inverse Gertsenshtein effect [Ger62, FMM22, EEC+19]. Those gravitational waves are of interest since they could be produced by primordial black holes (PBMs). PBMs are one of the other dark matter candidates. Additionally, measurements of ultrahigh-frequency gravitational waves would increase the understanding of the early universe. With IAXO especially primordial black holes, the cosmic gravitational microwave background (CGMB) and exotic compact objects could be discovered [AAB+21, RSET21].

Via the inverse Gertsenshtein effect, an electromagnetic wave will be produced inside the magnet bore. This wave can depending on the frequency of the gravitational wave, in the X-ray regime and therefore be measurable with the proposed detectors. For later stages also more dedicated detectors can be explored towards their physics potential. However, the key facts for those detectors are again the background level and the energy range since lower frequencies result in lower energies.

5.3 IAXO

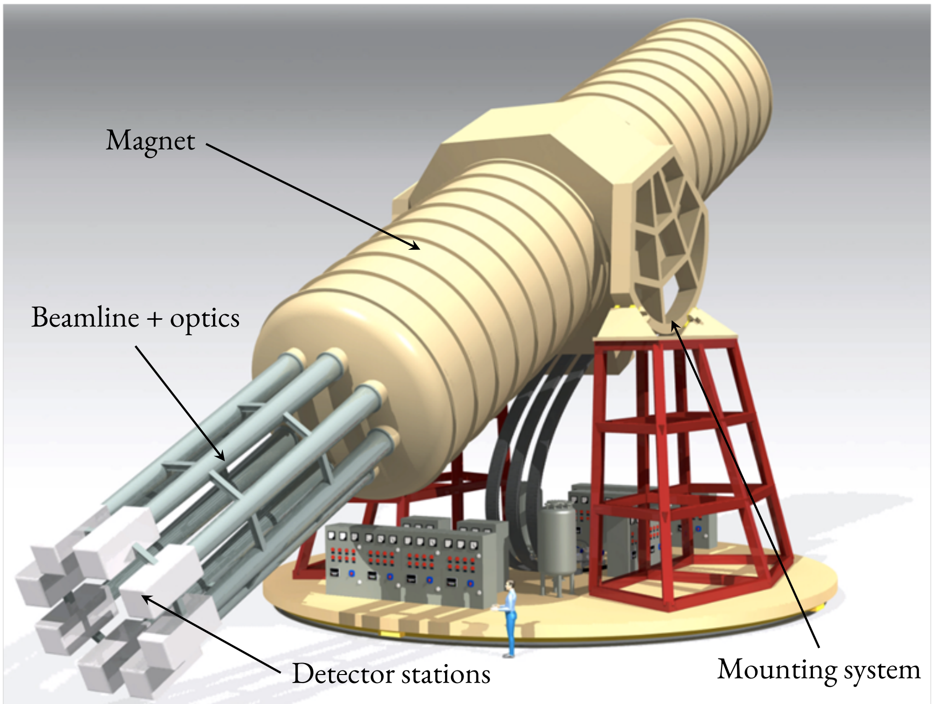

Figure 5.11: Envisioned setup of the IAXO experiment. A 20 m long magnet, with eight magnet bores of 60 cm diameter equipped with different detector stations at the end. To focus the X-rays towards the detectors, between the magnet and detector stations beamlines with focusing X-ray optics will be mounted. The experiment will be able to track the sun for around 12 h per day. IAXO will be located on the DESY campus, either completely outside or covered with a lightweight hall. Picture from [IAXa].

The International Axion Observatory (IAXO) will be a larger and enhanced version of the BabyIAXO experiment described in section 5.2. The principle of the experiment stays the same, however the experiment will be much larger allowing a higher conversion rate and more detectors. In the following the changed parts shall be shortly discussed as well as their impact on the discovery potential. The chapter is mainly following the conceptual design report of IAXO [AAB+14b].

The biggest change from BabyIAXO to IAXO will be the magnet. The magnet of IAXO will contain eight 20 m long magnet bores with a diameter of 60 cm each. The average magnetic field in the bores is supposed to be 2.5 T. Behind each magnet bore a beamline and a detector station can be set up. The beamline will, like in BabyIAXO, consist of an X-ray optic and a vacuum system in order to focus and transport the X-ray photons to the detector stations. The vacuum setup will be similar to the setup chosen for BabyIAXO. The bores will be also prepared for a filling with a buffer gas to reach for higher axion masses. For this, the BabyIAXO system will be very helpful since the challenges observed there will influence the setup of IAXO.

The design of the X-ray optics will follow the experience from the BabyIAXO prototype optics, from the techniques described in section5.2.1. However, due to the large number of beamlines also optics optimised for certain energies (e.g. optimised for the 14.4 keV or optimised for very low energies $\leq$ 500 eV) or even detectors might be used. For example, if a detector showed good performance at BabyIAXO an X-ray optic might be optimised for this specific detector. This optimisation can be done for the focal spot size and the reflectivity for certain energies or energy bands leading to a signal enhancement.

Each detector station will be then equipped with a detector, these might be the same type of detector at some bores, but the possibility exists to have eight different detectors mounted. Thus, at the same time, multiple detectors can measure for different parts of the axion spectrum enhancing the discovery potential. For the detectors of IAXO the background level is supposed to be one order of magnitude better than for BabyIAXO (10^{-8} counts $\mathrm{cm}^{-2}\mathrm{keV}^{-1}\mathrm{s}^{-1}$).

The experiment will be mounted on a movable platform, which will be able to follow the sun for at least 12 h per day. Therefore, an inclination of $\pm 25^\circ$ and a rotation of 360° is foreseen. It needs to reach at least the same precision as BabyIAXO. Since the IAXO system will be two times larger and much heavier than the BabyIAXO system the reusability of the design of the moving system is not given, hence a completely new system has to be developed. Depending on the success of BabyIAXO, there might be also the possibility of an upgraded version of IAXO referred to as IAXO+. This version consists technically of a better magnet with a length of 22 m and an average field of 3.5 T. The optics are considered to be the same while the detectors are presumed to be an order of magnitude better than for the standard IAXO scenario [AAAC+21].

5.4 Comparison of CAST, BabyIAXO, and IAXO

To compare CAST, BabyIAXO, and IAXO a figure of merit (FOM) (f) was defined in order to have a single comparable number. The FOM connects the most influential parameters referring to the axion discovery potential and is defined via [AAB+19]:

$$f = f_\mathrm{M} \cdot f_\mathrm{DO} \cdot f_\mathrm{T} \tag{5.1}$$

$$= B^2 L^2 A \cdot \varepsilon_\mathrm{d} b^{-1/2} \cdot \varepsilon_\mathrm{o} \alpha^{-1/2} \cdot \sqrt{\varepsilon_\mathrm{t} t}\,. \tag{5.2}$$

Here $f_\mathrm{M} = B^2 L^2 A$ is the magnets figure of merit with the magnetic field B, the length of the magnet bore L, and the aperture A of the magnet bores. The figure of merit of the optics and the detector is defined as $f_\mathrm{DO} = \varepsilon_\mathrm{d} b^{-1/2} \cdot \varepsilon_\mathrm{o} \alpha^{-1/2}$. It consists of the detector efficiency ε_d, the normalised detector background level b, the efficiency of the optic ε_o, and the focal spot size of the optic α. The last term is the time figure of merit $f_\mathrm{T} = \sqrt{\varepsilon_\mathrm{t} t}$, with the tracking time fraction ε_t and the run time of the experiment t. This FOM can now be used to compare the four described setups CAST, BabyIAXO, IAXO, and IAXO+. The parameters of CAST and the design parameters of BabyIAXO, IAXO, and IAXO+ are shown in table 5.2.

With these parameters one can now calculate the FOM for the different helioscopes. Apart from the design parameters given in table 5.2, two modified scenarios shall be discussed. The first one changes the

Parameter	CAST	BabyIAXO	IAXO	IAXO+
B in T	9	2	2.5	3.5
L in m	9.26	10	20	22
A in m^2	0.003	0.77	2.3	3.9
ε_d	0.6	0.7	0.8	0.8
b in counts cm^{-2}keV^{-1}s^{-1}	1×10^{-6}	1×10^{-7}	1×10^{-8}	1×10^{-9}
ε_o	0.3	0.35	0.7	0.7
α in cm^2	0.15	2×0.3	8×0.15	8×0.15
ε_t	0.12	0.5	0.5	0.5
t in a	1	1.5	3	5

Table 5.2: The parameters of CAST and the design parameters of BabyIAXO, IAXO, and IAXO+. The values for CAST show the IAXO pathfinder setup using the NuSTAR like optic and a Micromegas detector. Data taken from [AAAC+21].

FOM	CAST	BabyIAXO	IAXO	IAXO+
Design	3356	266 791	36 000 694	591 035 362
Scenario 1	3356	217 834	20 785 011	264 319 049
Scenario 2	3356	217 834	20 785 011	83 585 022

Table 5.3: Figure of merit (FOM) of the CAST experiment and the design values for BabyIAXO, IAXO, and IAXO+. As Design, the FOM with the parameter values from table 5.2 is shown. Scenario 1 uses the same parameter but the measurement time t is for all setups set to $t = 1$ year. In Scenario 2 additionally, the background rate of IAXO+ is set to the value used for IAXO.

measurement time t for all setups to $t = 1$ year, this leads to a better comparison since the measurement time is easy to adapt if the experiment shows good performance. For the second scenario, also the detector background rate for the IAXO+ setup will be reduced to the values assumed for IAXO. This leads in principle to a comparison of f_M and is a more realistic approach since a background rate of 10^{-9} counts cm^{-2}keV^{-1}s^{-1} seems very optimistic regarding the current detector developments. The FOM of those scenarios can be found in table 5.3.

From the data, it can be seen that the FOM of CAST is rather low with respect to the planned experiments. Already BabyIAXO is nearly two orders of magnitude better than CAST, while looking at IAXO or IAXO+ the FOM rises by four or five orders of magnitude. For all the mentioned designs and scenarios a comparison is shown in table 5.4. From this, it is easily visible that BabyIAXO will be already a factor 80 better than CAST referring to the design values. From BabyIAXO to IAXO the factor will be even larger (135).

However, the measurement time still has some impact on those values so a comparison for scenario 1 will give a better feeling for the upgrade of the experiment. Here, the factors are a little bit smaller but still between one and two orders of magnitude. Since either IAXO+ or IAXO will be built, an upgrade seems unlikely, here a comparison between those two seems to be most relevant.

For the baseline design and scenario 1 the factor is 16 or 13, hence the measurement time increase has no big impact. However, looking to scenario 2, IAXO+ will perform four times better than IAXO. This is only due to the design of the magnet since all other parameters are the same. This means that the improved magnet of IAXO+ on its own improves the FOM and therefore the sensitivity by a factor of

	BabyIAXO	IAXO	IAXO+
CAST	80	10 732	176 185
CAST 1	65	6196	78 792
CAST 2	65	6196	24 916
BabyIAXO	1	135	2215
BabyIAXO 1	1	95	1213
BabyIAXO 2	1	95	384
IAXO		1	16
IAXO 1		1	13
IAXO 2		1	4

Table 5.4: Comparison of the figures of merits shown in table 5.3. Each field shows by which factor the FOM of the experiment is better(e.g. the first field states that the design BabyIAXO is 80 times better then CAST). The design values and the scenario values (indicated by 1 and 2) are only compared within the design/scenario values.

four. Hence, for the design of IAXO the magnet is the most important part since it later can also not be changed, while the optics and the detectors will be evolving elements as seen in the CAST experiment over its 19 years of data taking.

CHAPTER 6

The BabyIAXO vacuum system

In order to transport photons converted in the magnet of BabyIAXO to the detectors a vacuum beamline is needed, since the low energetic X-rays will be absorbed otherwise. The vacuum beamline will connect the magnet with the optics as well as the optics with the detectors. An overview of the planning of the vacuum system will be given in the following.

6.1 Setup of the vacuum system

In this section, the vacuum system for BabyIAXO will be discussed. The vacuum system consists of the magnet bore, the optics, and the beamline, thus connecting the whole experiment. The following calculations are shown for the larger 7.5 m beamline. The same setup can then be used for a 5 m beamline. The needed pumping power to reach a final pressure of 10^{-7} mbar will be given, as well as a scheme how to distribute the pumps. Additionally, the vacuum measurement system will be briefly discussed.

6.1.1 Size and surface of the beamline

The beamline and the magnet can be seen in figure 6.1. It consists of the following parts: end cap, magnet bore, connection between magnet and optic, gate valve, bellow, optic, and the connection tube to the detector. From the CAD model of all parts one can calculate and measure the inner surfaces and the volume. The results can be found in table 6.1. It should be noted that the values are only rough estimates and that the beamline is still in development. However, the estimates can be used for calculations, since the total surface and volume will not change by more than $\approx 10\%$. Keeping this in mind one can calculate the necessary pumping capacities.

6.1.2 Suction capacity of pumps

To develop the vacuum system the first step is to calculate what suction capacity the vacuum pumps need to provide. For this an overall pumping time needs to be defined. Following [Pfe13] the overall pumping time can be split into three different time intervals t_1, t_2, and t_3. The first interval t_1 will be the time for pumping until a level of 0.1 mbar is reached. This pressure is reached with roughing pumps like membrane or rotary pumps. The second interval t_2 is the time to reach a level 10^{-4} mbar. Here

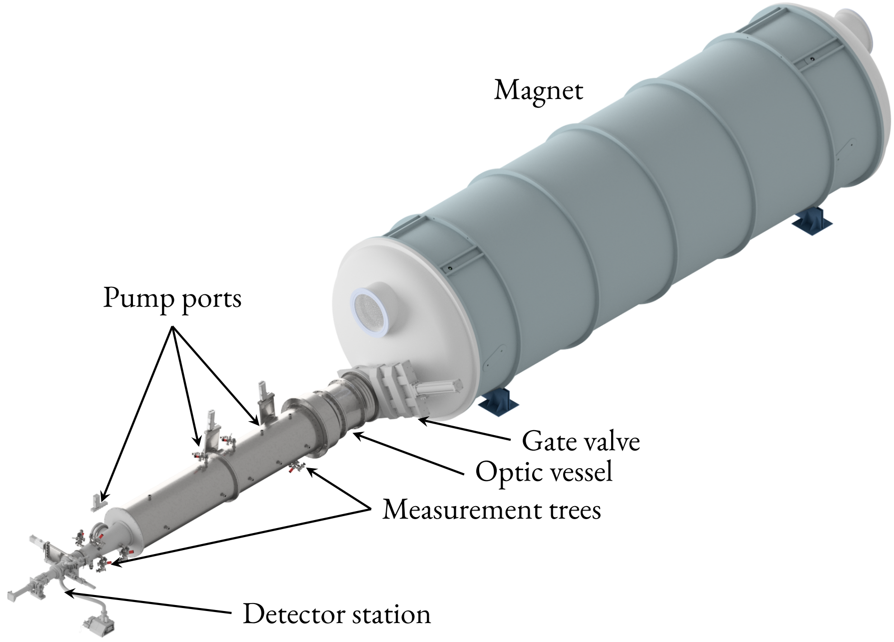

Figure 6.1: CAD image of the 7.5 m beamline and the magnet. The 5 m beamline would be positioned at the second magnet bore above the 7.5 m beamline.

Part	Surface in m^2	Volume in m^3
End cap	0.503	0
Magnet bore	21.991	3.85
Connection	0.754?	0.15
Gate valve	0.553?	0.11
Bellow	0.6?	0.21
Telescope	100?	0.25?
Connection tube	10.930	1.73
Total	135.311	6.55

Table 6.1: Surfaces and volumes of the different parts of the 7.5 m beamline of BabyIAXO measured from the CAD model. Values marked with a question mark are estimates.

turbomolecular pumps (TMP) are used. The time t_3 is mainly the desorption time of the stainless steel surface which is important for the pumping to 10^{-7} mbar. It shall be mentioned that t_1 defines the needed suction capacity of the roughing pumps and $t_2 + t_3$ defines the suction capacity of the TMP.

First, the suction capacity for the roughing pumps shall be determined. For this, we set $t_1 = 1$ h. A short time constant here is beneficial to speed up leak detection. The necessary suction capacity

S_{roughing} can be calculated via [Pfe13]

$$S_{\text{roughing}} = \frac{V}{t_1} \cdot \ln \frac{p_0}{p_1}, \tag{6.1}$$

with the volume V, the starting pressure $p_0 = 1000$ mbar, and the final pressure of the roughing pump $p_1 = 0.1$ mbar. Calculating this leads to a pumping speed of $S_{\text{roughing}} = 60.3\,\text{m}^3\text{h}^{-1}$.

As mentioned above, t_2 and t_3 are defining the TMP suction capacity. It shall be mentioned that typically $t_2 \ll t_3$. Consequently, to choose the time one has to keep in mind that a pressure of $\mathcal{O}\left(10^{-4}\,\text{mbar}\right)$ will be reached fast and then a decrease in the pumping speed will be observed due to desorption. To calculate time t_2 one can use formula 6.1 rearranged for time t_2:

$$t_2 = \frac{V}{S_{\text{TMP}}} \cdot \ln \frac{p_1}{p_2}. \tag{6.2}$$

Here $p_2 = 10^{-4}$ mbar is the pressure before the pumping is mainly working against the desorption. For the pumping against desorption, one can define time t_3 as follows [Pfe13]:

$$t_3 = \frac{q_{\text{des}} A t_{\text{des}}}{S_{\text{TMP}} p_3}. \tag{6.3}$$

Here we use the desorption rate for stainless steel q_{des}, the surface of the system A, the desorption time constant t_{des}, and the desired pressure $p_3 = 10^{-7}$ mbar. So combining the t_2 and t_3 will lead us to the necessary suction capacity S_{TMP}:

$$t_2 + t_3 = \frac{V}{S_{\text{TMP}}} \cdot \ln \frac{p_1}{p_2} + \frac{q_{\text{des}} A t_{\text{des}}}{S_{\text{TMP}} p_3} \tag{6.4}$$

$$\Leftrightarrow S_{\text{TMP}} = \frac{1}{t_2 + t_3} \left(V \cdot \ln \frac{p_1}{p_2} + \frac{q_{\text{des}} A t_{\text{des}}}{p_3} \right). \tag{6.5}$$

The overall pumping of the system to reach the desired pressure should be on the order of 14 days hence $t_2 + t_3$ need to be set accordingly. With the desorption rate of stainless steel $q_{\text{des}} = 2.9 \cdot 10^{-4}\,\text{Pa}\,\text{m}^3\,\text{s}^{-1}\,\text{m}^{-2}$ [GC17] and a desorption time constant $t_{\text{des}} = 3600$ s we can now give an estimate on the needed suction capacity $S_{\text{TMP}} = 10.91\,\text{m}^3\text{s}^{-1}$. This suction capacity seems very large, however TMPs with suction capacities of $\approx 2\,\text{m}^3\text{s}^{-1}$ are available. Additionally, it shall be mentioned that the errors especially on the desorption rates are very large [GC17]. For this reason, also desorption rates for other materials like the gold coating of the X-ray optic are not taken into account for the estimate. The needed suction capacity S_{TMP} should be divided into at least four pumps. This is necessary since at the low pressure regimes where molecular flow dominates the gas transport the efficient suction capacity depends on the distance from the pump to the volume (see 6.1.3). Therefore, the pumps should be distributed over the vacuum system. In particular the optics will be a barrier for the molecular flow due to the nested shells. Consequently, TMPs on both sides of the optics are needed.

6.1.3 Effective pumping speed for a distant pump

Due to the setup of the beamline, the TMPs cannot be distributed equally over the beamline (e.g. the magnet bore is not accessible). Additionally, TMPs cannot be mounted in strong magnetic fields, hence they have to be moved to some distance from the magnet. The tube connection between the vacuum system and the pump will reduce the suction capacity S of the pump to an effective suction capacity S_{eff}. In order to calculate the reduction through a straight tube of diameter d one has to see if the flow is laminar or molecular. The rough barrier between the two flow mechanisms (even if there is no sharp barrier) is at the point, where the Knudsen number is $Kn = 0.5$ [Pfe13]. The Knudsen number is given by [Jou18]:

$$Kn = \frac{\overline{l}}{d}. \tag{6.6}$$

Here $\overline{l}$ is the mean free path. The values for $\overline{l} \cdot p$ are shown in table 6.2 for air and nitrogen at ambient temperature. With those values, one can calculate the pressure p where the molecular flow dominates

Gas at $0\,^\circ$C	$\overline{l} \cdot p$ in m mbar
Air	6.65×10^{-5}
N2	5.9×10^{-5}

Table 6.2: Mean free path for air and nitrogen at ambient temperature [Jou18].

the gas transport

$$p = \frac{\overline{l}}{dKn}. \tag{6.7}$$

The results for the diameter of a connection tube $d = 0.2$ m and the magnet bore $d = 0.7$ m are listed

p in mbar	$d = 0.2$ m	$d = 0.7$ m
Air	6.65×10^{-4}	1.9×10^{-4}
N2	5.9×10^{-4}	1.68×10^{-4}

Table 6.3: Pressures for $Kn = 0.5$.

in table 6.3. From this one can extract that below 10^{-4} mbar molecular flow dominates. Thus, it is important to understand how much efficiency one loses, since this will increase the necessary suction capacity if the pumping time should be maintained. The effective suction capacity for a tube is given by [Pfe13]

$$S_{\text{eff}} = \frac{SC_{\text{mol}}}{S + C_{\text{mol}}}, \tag{6.8}$$

with the suction capacity S and the conductance of a tube for molecular flow C_{mol}. For a round tube this can be calculated via [Pfe13]

$$C_{\text{mol}} = \frac{\bar{c}\pi d^3}{12l}, \tag{6.9}$$

with $\bar{c}$ being the mean thermal speed of the gas molecules. This leads to

$$S_{\text{eff}} = \frac{S\bar{c}\pi d^3}{S12l + \bar{c}\pi d^3}, \tag{6.10}$$

for round tubes with diameter d and length l. The results of this calculation can be found in figure 6.2.

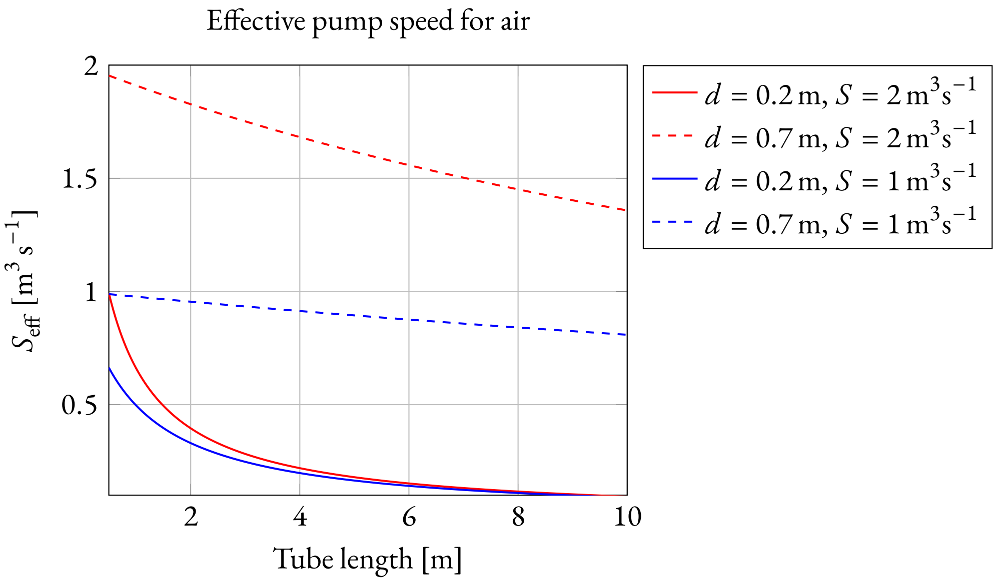

Figure 6.2: Effective suction capacity for different setups pumping air in the molecular case.

For the smaller diameter, it can be seen that for long distances the effective suction capacity is dropping significantly. For lengths beyond 2 m it basically does not matter how large the suction capacity of the pump is. For a tube with the diameter of the magnet bore one can also observe a significant drop over distance. Hence, the distribution of pumps should be as homogeneous as possible. For the magnet bore, if only pumped from one side for example, the suction capacity needs to be raised by 50% to maintain the pumping time.

6.1.4 The vacuum system

With the knowledge of the necessary suction capacity one can start to plan the distribution of pumps as well as the setup of the vacuum system. The first step for this is the positioning of valves in order to separate the system in cases of maintenance or if components should be changed. For BabyIAXO the beamline will contain two main valves. A large valve (VO) between the magnet and the optics and a smaller valve at the end of the beamline (VD). VO is installed in order to allow the exchange of parts at

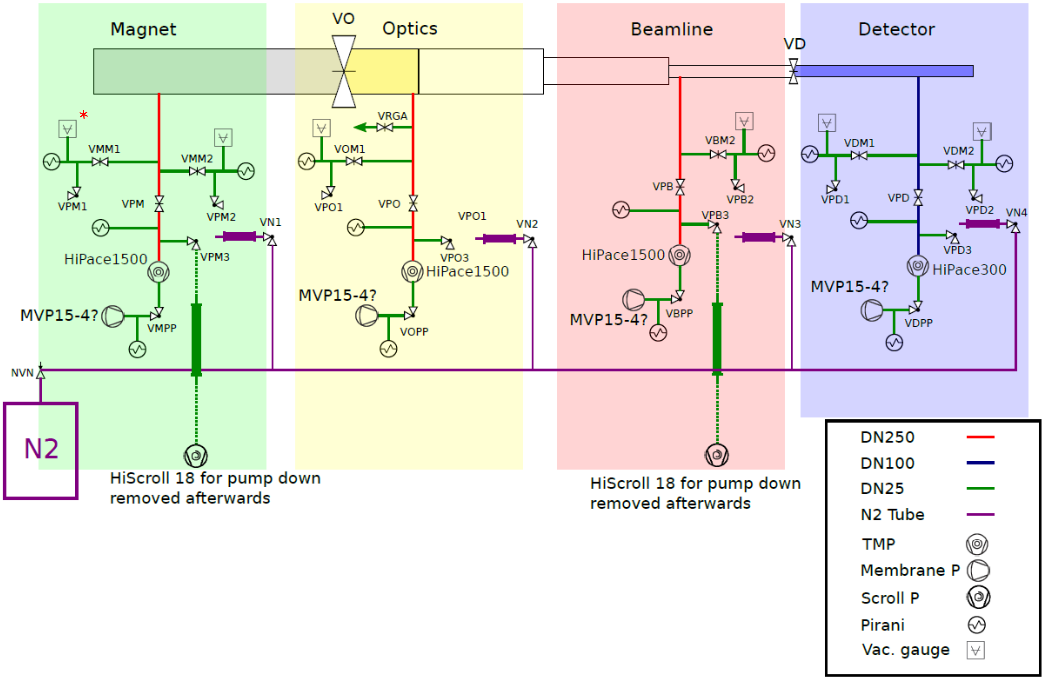

Figure 6.3: Schematic of the vacuum system. The whole beamline is divided into four parts. Each part has a TMP and a set of measurement devices. The measurement devices are planned such that a redundant set is available for each part separable by the two main valves VO and VD. Additionally, a nitrogen system (purple) will be mounted to allow venting with dry nitrogen.

the magnet and the magnet end cap without venting the optics. This might be the case if for example calibration devices (e.g. X-ray sources) need to be mounted at the end cap of the magnet. VD is used to define the end of the beamline. Everything behind VD will be the detector system. Hence, this valve is important to allow for detector maintenance and exchange. An overview of the system is given in figure 6.3. At the top, the beamline is depicted. The system is separated into four parts. The Magnet system (green) is defined from the magnet end cap to VO it contains a TMP with a baking pump as well as a so-called measurement tree.

The measurement tree contains vacuum gauges to measure the pressure inside the beamline. It is set up such that every gauge can be individually exchanged without impacting the beamline itself. For example, if the gauge marked with the red star in figure 6.3 needs to be replaced valve VMM1 can be closed and nitrogen can be flushed into the system via valve VPM1. After this, the gauge would be replaced and a vacuum pump is connected to VPM1 until the pressure of the beamline is reached, then VPM1 will be closed and VMM1 can be opened again.

Within each section separable by either VO or VD a redundant setup of these measurement trees is installed. This way if a gauge has to be replaced one always knows the pressure in the beamline, or in a part of the beamline. The vacuum pumps are also connected via a valve (e.g. VPM) to the beamline. Here in every stage also a vacuum gauge will be mounted to not allow undefined pressures between two valves.

The Optics system (yellow) connects as closely as possible to the optics. It is similar to the Magnet system but the measurement tree is not set up redundantly, since redundancy is automatically reached with the measurement tree of the Beamline system (red). In contrast to all others, the optics system contains an additional valve VRGA to connect a rest gas analyser to the optics to monitor that no harmful gases, like hydrocarbons, spoil the optics. The Beamline system (red) is a copy of the Optics system without VRGA.

The Detector system (blue) is set up similarly to the Magnet system but contains a smaller TMP.

To allow venting of the system or parts of the system with dry nitrogen a nitrogen distribution system is planned. From a reservoir, a central nitrogen line will lead to the beamlines. Here for each subsystem a branch is installed ending at a flexible tube to reach all input valves.

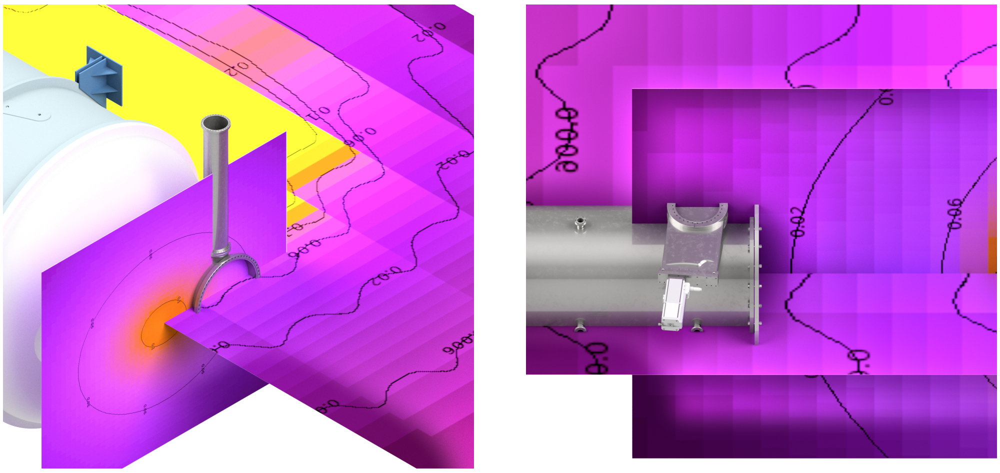

(a) End cap

(b) Beamline

Figure 6.4: The magnet stray field at the positions of the vacuum pumps at the end cap (a) and at the beamline valve closest to the optics (b). The wavy structure of the field lines are artifacts of the interpolation between the data points. Field values in Tesla. Field data from [IAXb].

Since TMPs cannot be mounted in magnetic fields $T \geq 6\,\text{mT}$ a study of the magnetic field at the pump positions closest to the magnet was performed. The outcome is shown in figure 6.4 for the position at the magnet end cap and for the position closest to the optic. The study reveals that for the position at the end cap an extension tube of around 1–1.5 m is needed. To shorten this extension as much as possible a magnetic shielding can be mounted to the pump, thus giving a threshold of $T \geq 60\,\text{mT}$. Then the tube can be shortened to $\approx 0.5\,\text{m}$. For the position close to the optics an extension tube is not necessary. However, if pumping directly at the optics vessel is desired an extension tube will become inevitable.

CHAPTER 7

The ultra-thin silicon nitride windows

For the search for axions and ALPs with helioscopes, the detector has to be mounted to a vacuum system, hence for a gas filled detector a barrier between the gas volume and the vacuum is necessary. In order to get the low energetic X-rays (100–3000 eV) into the detector an entrance window is needed allowing the X-rays to pass while retaining the barrier between the vacuum and the gas volume. Thus, the pressure difference to be withstood by the window is in the order of 1000–1200 mbar. For this purpose thin Mylar® foils were a proven solution and used for example at CAST ([KKLD17], [AAA+07b]). However, those windows perform not very well at the lowest energies 100–1000 eV, therefore in the case of the axion-electron coupling a lot of the signal will be partially lost. To improve this, a new type of windows with ultra-thin silicon nitride membranes were developed in collaboration with Norcada [Nor] and successfully used [Sch24a]. In the following, first an overview of the windows and their performance will be given (section 7.1). Before in section 7.2 the results of a measurement campaign at the synchrotron radiation source SOLEIL [SOL] will be presented.

7.1 Ultra-thin silicon nitride windows

In order to get a good transmission of low energetic X-rays into the detector volume while at the same time keeping the gas inside, thin films on strong-back structures are a typical choice. For the GridPix detector at CAST or IAXO, those windows need to withstand a pressure difference of 1.2 bar while sustaining an open diameter big enough to not cut off the focused beam from the X-ray optics. This results, depending on the optics, in open diameters between 8 and 14 mm as described in section 5.2.1. These restrictions and the fact that the window needs to be vacuum tight narrows the available materials. Widely used are thin foils of polypropylene (PP) or Mylar®. However, they need to have a certain thickness $O(\mu\mathrm{m})$ to reach a reasonable vacuum tightness. To circumvent those problems silicon nitride (SiN_x where $0 \leq x \leq 1.33$) thin films are a potent solution [LSC91, TSM+13, TKS+14], being on the one hand vacuum tight while on the other hand having a good mechanical stability in very thin $O(100\,\mathrm{nm})$ configurations. Albeit the properties of those membranes strongly depend on the way of production, for example, the density can vary over a range of $2.0\,\mathrm{g/cm^3}$ to $3.44\,\mathrm{g/cm^3}$ [KPGA20] or Young's modulus which varies over a range of 65 GPa–360 GPa [KPGA20]. While the density has a direct impact on the transmission of the X-rays, Young's modulus impacts the maximum strain the membrane can withstand. So the way the windows are manufactured and their composition are strongly impacting the usability.

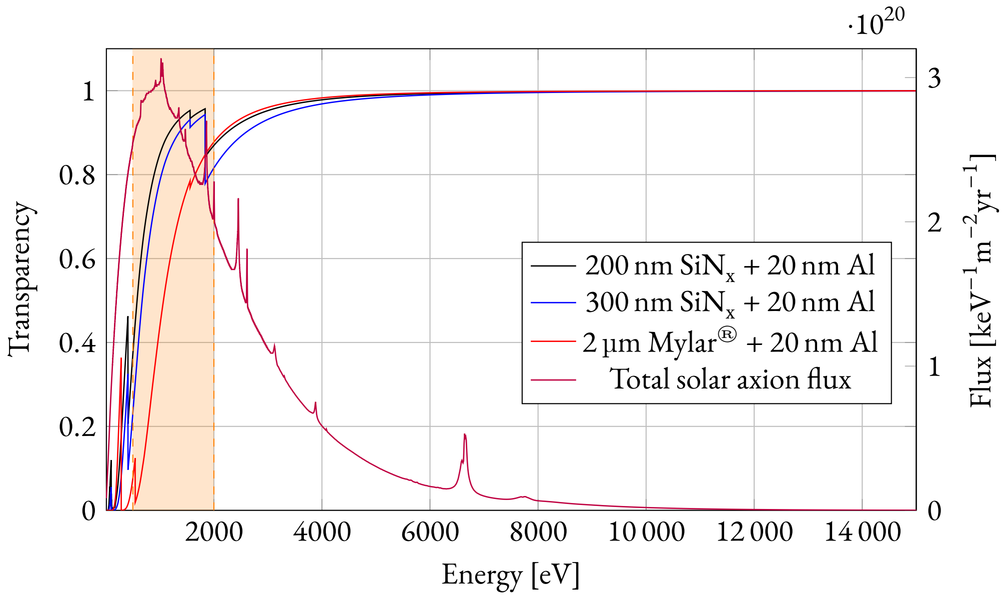

Figure 7.1: Expected transparency of the ultra-thin silicon nitride windows for a mixture of Si_3N_4 and a material density of $\rho = 3.44\,\mathrm{g\,cm^{-3}}$. For comparison reasons also the transmission of a Mylar® window is shown. The assumed solar axion flux ($g_{ae} = 1 \times 10^{-13}\,\mathrm{GeV^{-1}}$, $g_{a\gamma} = 1 \times 10^{-12}\,\mathrm{GeV^{-1}}$) is also added. It can be clearly seen that in the energy range where the most axions are expected (shaded in orange) the SiN_x windows perform much better than the Mylar® windows. Transparency data from [Gul], axion flux from [vO23].

A variety of detector windows produced as a combination of a silicon strong-back and a SiN_x thin film membrane have been tested, resulting in a design with 300 nm thick membranes and an open diameter of 14 mm, coated with a thin (20 nm) aluminium layer. The testing included helium leak tests to specify the vacuum tightness, as well as multiple cycles from ambient pressure to 1.5 bar overpressure to ensure the quality of the window. In this development process also 200 nm windows were tested, however only one window could be found to survive multi-cycle overpressure tests to 1.2 bar. The expected transparencies for the three types of windows are shown in figure 7.1. For energies above 4 keV all windows show approximately the same transmission very close to 100%. In the, for the axion-electron coupling, interesting energy range between 500 eV and 2 keV the SiN_x-windows perform a factor 2–3 better than Mylar® windows. The performance of the SiN_x-windows decreases, as expected, with the window thickness.

7.1.1 Design of the windows

To produce a reliable window with the thinnest possible membranes a variety of strong back structures (see figure 7.2) have been investigated and tested. The window structures made of silicon nitride on a silicon strong back were produced by the company Norcada [Nor]. Since the windows are also part of the cathode the side pointing to the gas volume is coated with 20 nm of aluminium. After gluing the window into the cathode no direct connection is necessary to the aluminium coating since it will charge up statically due to the surrounding field. With this, the influence of the entrance window is very small. To find the best and most reliable windows, a testing schema with 5-6 pressure cycles from

Figure 7.2: Drawing of the three different window strong back designs. The window opening always has a diameter of 14 mm. From left to right: double rib, double cross, quad rib. The squared outer shape was later changed for the quad rib windows to a round shape.

Strong back	Membrane thickness in nm	Tested windows	Passed
Double cross	200	5	0
	300	1	0
Double rib	200	5	0
	300	3	0
Quad rib	200	9	1
	300	21	11

Table 7.1: Results from the overpressure tests of the silicon nitride windows. The strong back designs are shown in figure 7.2.

0 bar(g) to 1.5 bar(g) and back was performed for all designs. Afterwards, they were put on a vacuum test bench to measure the leak tightness. During these tests, one cycle was always performed to stay at 1.5 bar(g) over several hours.

Table 7.1 shows the result of the tests and the yield of the different membrane and strong back combinations. It is clearly visible that the best design is the quad rib strong back with a 300 nm membrane. This quad rib strong back was chosen early so most of the tested windows were produced in this way. The 200 nm membrane thickness was tested to be not reliable. Therefore, the final design was a quad rib structure with a 300 nm membrane. A batch of eight windows was produced and a yield of 75% was reached.

7.1.2 Vacuum testing

Windows that survived the overpressure tests were set onto a vacuum test bench to be helium leak tested. For this, a small vacuum test stand was set up consisting of a turbo-molecular pump (TMP) connected to a flange to mount the windows. To reach the low vacuum regime necessary to start the TMP a membrane pump is used. The pump is connected via a valve to the TMP and has a bypass with a needle valve in order to slowly reduce the pressure. This is important since fast pressure drops might weaken the windows which could lead to failure. When the pressure reaches the level necessary to start the TMP ($O(1\,\mathrm{mbar})$) the needle valve is closed and the membrane pump is used as the backing pump for the TMP. The tests were performed with several windows until the detection limit of the leak tester was reached or a leak was found. Since this limit depends on the pressure inside the test stand, the values differ depending on the duration for which the test stand was pumped. To reach the very low pressures necessary to measure limits below 1×10^{-8} mbar l s^{-1} it takes a long time due to desorption of gases from the walls of the test stand. However, for one window with a 300 nm membrane, a limit of better than 3.0×10^{-9} mbar l s^{-1} was reached. Also, no window tested so far showed any leakage in the tested range so there are only lower limits, meaning those windows can be considered leak tight. This was also shown by other studies [TSM+13, TKS+14]. Additionally, one window with a 200 nm membrane was stable enough to be tested, showing a leak rate below 8.0×10^{-9} mbar l s^{-1}. Hence, it can be stated that the leak tightness does not seem to decrease with the thickness significantly.

Other windows, for example windows provided by CEA Saclay with membranes made of 2000 µm PP or Mylar® foil with a honeycomb structured strong back made of aluminium or copper were also tested. Regardless of the strong back none of those windows reached the detection limit of the helium leak tester. Since the leak tightness dropped with the size of the membranes the leakage is presumably coming from the foil membrane itself. Since the foils are additionally much thicker they are not considered as an option.

7.2 Transparency measurements

The transparency of the entrance windows of the detector is a crucial value for the data analysis of CAST or the upcoming IAXO experiment data, since it influences the expected signal. Hence, different transparencies of the windows will change the resulting limits on the coupling to the axion. Therefore, a measurement of the transparency over a wide energy range covering the expected X-ray energies is important. Such measurements have been performed at the MÉTROLOGIE beamline [M′] at the synchrotron radiation source SOLEIL.

7.2.1 SOLEIL

The synchrotron radiation source SOLEIL is a research facility hosting 27 synchrotron radiation beamlines for different purposes. The synchrotron is set up as an electron storage ring with a two stage injector consisting of a 100 MeV linear accelerator (LINAC) as an injector stage followed by a booster synchrotron accelerating the electrons to their nominal energy of 2.75 GeV. These are injected into the storage ring until a beam current of 450 mA is reached. After reaching the expected current the storage ring is operated in a top-up mode, so if the beam current drops below a certain threshold an injection from the booster synchrotron is initiated. This results in a sawtooth like pattern of the beam current in the storage ring. The total power of the synchrotron radiation $P_{\text{total,sync}}$ is proportional to the beam current I [Sch14]

$$P_{\text{total,sync}} = \frac{eL}{6\pi\varepsilon_0} \frac{I}{(m_0 c^2)^4} \frac{E^4}{R^2}, \tag{7.1}$$

with L being the circumference of the storage ring, ε_0 the vacuum permittivity, m_0 the mass of the electron, E the energy of the electrons, and R the radius of the bending magnets. Thus, the intensity of the synchrotron radiation at the beamlines will also show the before described sawtooth pattern. The storage ring provides the beamlines with radiation from three different synchrotron radiation sources: undulators, wigglers, and bending magnets. The equation above only holds for bending magnet radiation as used for the MÉTROLOGIE beamline. However, also for undulators and wigglers the linear proportionality to the beam current is given. The energy spectrum for the three sources of synchrotron radiation varies from line spectra in the case of undulators to broadband spectra for wiggler and bending magnet radiation.

For the MÉTROLOGIE beamline, this means that a broadband spectrum is emitted which has to be filtered in order to produce small band emission lines. To achieve this two systems of gratings and X-ray monochromators are installed. They are called soft X-ray branch (energy range 30 eV to 2000 eV) and hard X-ray branch (energy range 3000 eV to 38000 eV).

For the soft X-ray branch, the setup consists of a focusing mirror, a monochromator, and a second mirror in order to return the light parallel to the horizontal plane. The monochromator used consists of a plane grating inside a concave spherical mirror [IMMD06]. To get a bigger energy range three interchangeable gratings (75, 300, and 1200 lines per mm) are installed for different wavelength bands. This type of monochromator typically reaches a line width smaller than 1 eV [KSB22, Pea18]. Behind the monochromator, a set of filters and a low order sorter (to remove higher order X-rays from the grating) are mounted to further reduce the line width. After this, the beam enters a vacuum chamber with a goniometer installed in order to place and move the samples. Behind the goniometer, a choice of four diodes is installed to measure the flux. At the end of the vacuum chamber, a flange is available to mount other devices for data taking.

For the hard X-ray branch the setup consists of a double crystal monochromator followed by two mirrors, a focusing elliptical mirror, and a flat bendable mirror. The double crystal monochromator uses Si(111) crystals. The spectral pursuit here is determined by the higher harmonics which can be drastically reduced by slightly detuning the alignment of the crystals [ML11]. This leads to a reduction of the harmonics to 1% of the power spectrum. The line width after a double crystal monochromator depends on the crystal type, its orientation, and on the energy E. For Si(111) crystals, the line width ΔE can be expressed as $\Delta E/E = 10^{-4}$ [Wil19]. Here, a vacuum chamber with a goniometer and an array of diodes for measurements is mounted. The setup except for the goniometer is basically the same as for the soft X-ray branch. The difference in the goniometer is the size and the maximum available movement.

7.2.2 Data taking at the MÉTROLOGIE beamline

For the measurement campaign data was taken at the soft and the hard X-ray beamline. In order to do so the windows had first to be mounted inside the vacuum chamber in a way that the window membranes can be centred to the beam. For the soft X-ray branch, it was due to the movement range of the goniometer possible for all four windows at the same time as shown in figure 7.3(a). Here all four membranes can be seen. It is also important to have one spot without any device in the movement range to measure the nominal flux arriving from the monochromator. This spot was on the bottom of the goniometer in between the two lower windows. For the preparation of the scan, first a x-y-scan over the membranes of all four windows was performed. This was necessary to find an optimal position in the middle between the strongback in order to later just measure the transparency of the membrane. After this was performed for the four windows also a position for the nominal flux measurements was fixed.

For a measurement first the energy is set. This happens mostly automatised, however eleven settings (D2-1 to D10) for eleven different energy ranges are available in order to produce a small line width and a high flux. The settings change the monochromator grating, the filter, and the low order sorter.

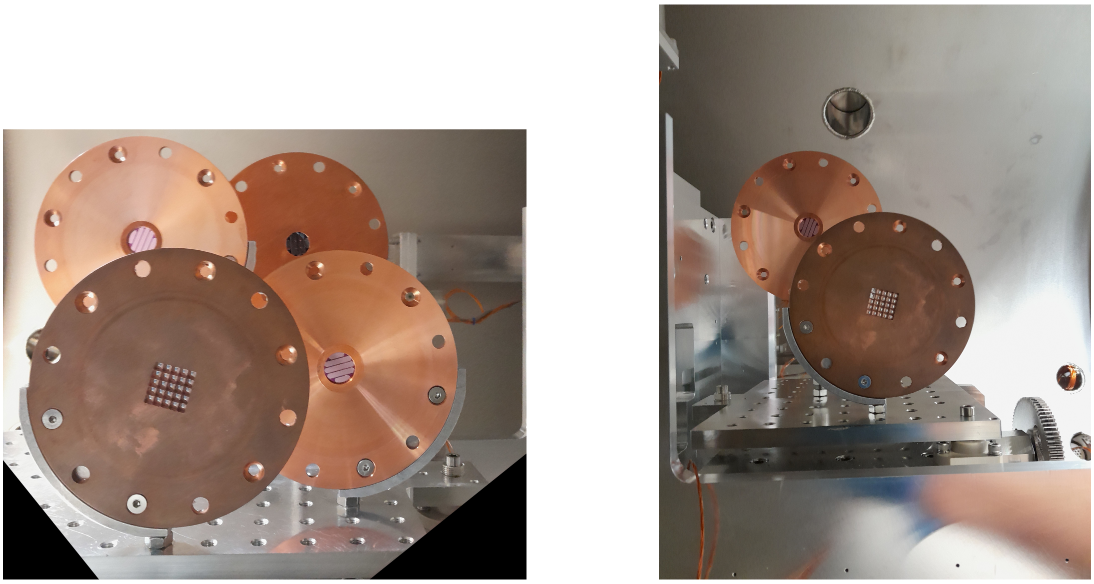

(a) (b)

Figure 7.3: Setup of the windows in the two beamlines. (a) The setup of the windows in the vacuum chamber of the soft X-ray branch. All four Windows mounted on a goniometer. They are mounted such that all windows can be reached by the beam. (b) The setup of two windows in the vacuum chamber of the hard X-ray branch. Due to the limitations of the goniometer, a setup with all four windows was not possible.

After finishing the setup the desired energy can be selected and the monochromator is automatically set to the according angles. For a full measurement at one energy, six sets of data are taken. In the beginning, the nominal flux, then the flux through the four windows, and at the end the nominal flux again in order to take long term drifts in the incoming flux into account. The measurement time for one measurement was one minute and for the measurements a photodiode (`IRD AXUV100` [OPT]) was used. An example of such a measurement can be seen in figure 7.4, with the mean value and its standard deviation indicated. The current fluctuations are small, hence short measurement times are possible. With the time the goniometer needed to move to the positions a full measurement cycle took about 20 minutes. Those measurements were taken at a total of 32 different energies ranging from 50 eV to 2000 eV.

A longer measurement as shown in figure 7.5 reveals the top-up pattern of the synchrotron as described in subsection 7.2.1. To avoid jumps in the data taken the measurements were only taken in between two top-ups. However, depending on the starting point on the slope each measurement is slightly offset to the other. Since no time-stamped data of the top-up cycle is available the error is taken into account as a systematic error. The percental error $E_{\text{top-up}}$ is given with the mean $\overline{x}_{\text{top-up}}$ and the standard deviation $s_{\text{top-up}}$ via

$$E_{\text{top-up}} = \frac{s_{\text{top-up}}}{\overline{x}_{\text{top-up}}} = 0.157\%. \tag{7.2}$$

For the soft X-ray branch additionally one of the settings (D9) was not producing proper results. This

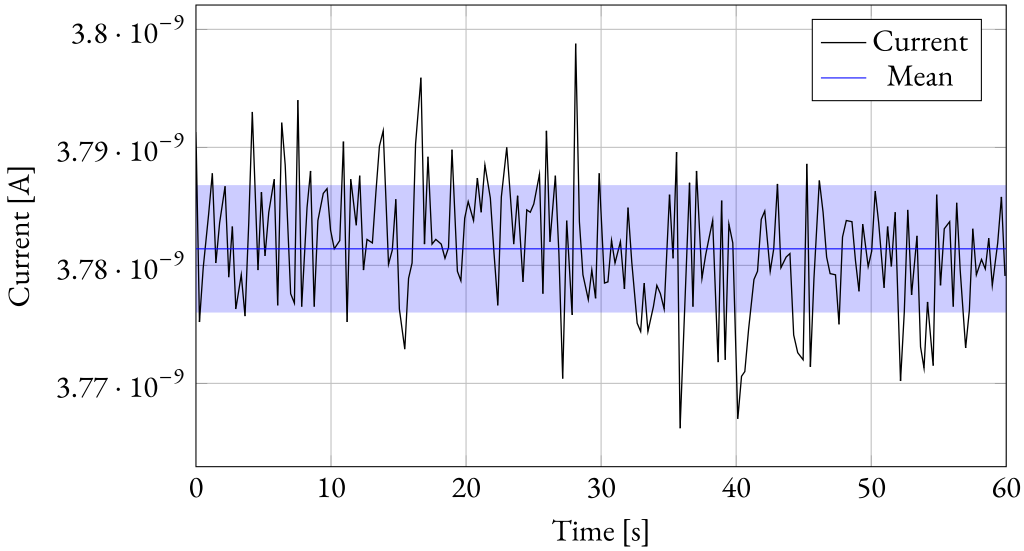

Figure 7.4: Example of a measurement taken at the soft X-ray branch at an energy of 700 eV. The 200 nm window was inside the beam. The mean ($\overline{x}_D = 3.7814 \times 10^{-9}$ A) and the standard deviation ($s_D = 5.4002 \times 10^{-12}$ A) used for the transparency calculations are indicated.

set was designated for the energy range 910 eV to 1090 eV affecting only the measurement at 1000 eV. This seemed very low, so the measurement was repeated with the setting (D10) giving proper results. A scan with the settings (D9) at 950 eV and 1050 eV also showed incorrect and non-conclusive results. Most interesting, the results from the SiN_x membranes show the behaviour while the results from the Mylar® window does not. Therefore, a good explanation could be a change in the spot size or a position change.

For the hard X-ray beamline, the setup had to be changed. Due to the smaller movement range of the goniometer, only two windows could be mounted at the same time inside the vacuum tank as shown in figure 7.3(b). For the measurement, the procedure was again very similar, after finding the best measurement positions for the two windows and a good spot for the measurement of the nominal current, again four measurements of one minute were performed per energy. First the nominal flux, then the two windows, and at the end again the nominal flux. After all energies were measured the vacuum tank was opened and the windows were exchanged in order to measure the other two windows. Then the procedure described before was repeated.

A longer measurement at high energies (above ≈ 6 keV) as shown in figure 7.6 reveals a constant slope of the flux. The source of this slope is not known, it might be a thermal behaviour of the beamline or it might come from the calibrated diode or the ampere meter. However, the error is included in the calculations by construction due to the mean calculation of the two measurements of the nominal flux. The top-up pattern can be slightly seen in the data, only adding minor changes to the slope. An additional systematic uncertainty comes from the harmonics of the crystal monochromator as described in subsection 7.2.1. At the hard X-ray branch measurements at fifteen energies ranging for 3 keV to 15 keV were taken.

As seen from the energy ranges, between the two beamlines there is a gap from 2 keV to 3 keV. Therefore, no data could be taken in this energy range. Here other beamlines of SOLEIL like the

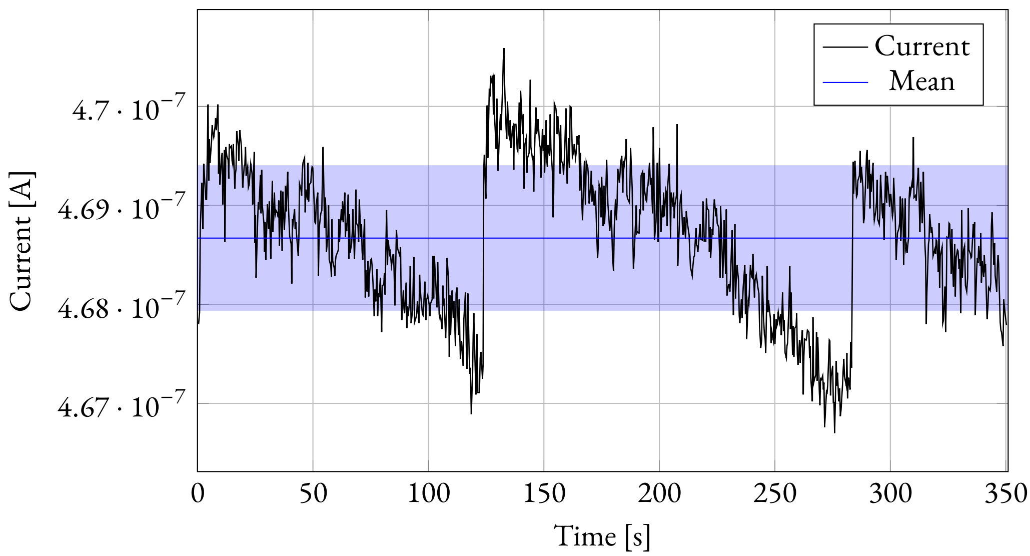

Figure 7.5: Measurement taken over 350 s without a window at the soft X-ray branch. The top-up cycle of the accelerator can be seen. The mean ($\overline{x}_{\text{top-up}} = 4.6867 \times 10^{-7}$ A) and the standard deviation ($s_{\text{top-up}} = 7.3604 \times 10^{-10}$ A) used for the transparency calculations are shown.

SIRIUS beamline [SIR] might be helpful offering a monochromator in the range from 1.4 keV to 4 keV.

7.2.3 Results

The data taken during the measurement campaign was analysed and compared to the expected transparency curves. The systematic errors described in subsection 7.2.2 are included in the analysis. After all means and standard deviations were computed, in a fist step the average mean $\overline{x}^{n\,\text{eV}}_{\text{diode}}$ and the average standard deviation $s^{n\,\text{eV}}_{\text{diode}}$ of the diode measurement is calculated. With those values and the corresponding values for the windows $\overline{x}^{n\,\text{eV}}_{\text{window i}}$, $s^{n\,\text{eV}}_{\text{window i}}$ the transparencies and their errors can be calculated.

$$t = \frac{\overline{x}^{n\,\text{eV}}_{\text{window i}}}{\overline{x}^{n\,\text{eV}}_{\text{diode}}}, \tag{7.3}$$

$$\delta t = \sqrt{\left(\frac{1}{\overline{x}^{n\,\text{eV}}_{\text{diode}}} s^{n\,\text{eV}}_{\text{window i}}\right)^2 + \left(\frac{\overline{x}^{n\,\text{eV}}_{\text{window i}}}{\overline{x}^{n\,\text{eV}\,2}_{\text{diode}}} s^{n\,\text{eV}}_{\text{diode}}\right)^2}. \tag{7.4}$$

After this, the systematic errors are added to the corresponding data point. Here, the effect from the top-up pattern is treated as a linear independent error and therefore added orthogonal to the statistical error. The error from the higher harmonics can only increase the measured transparency and is therefore added to the lower limit. The result for the SiN_x windows can be seen in figure 7.7. It can be seen that due to the behaviour shown in figure 7.6 the error bars for the data points above 6 keV are getting bigger. The decrease of the diode current also explains why transparencies above 1 are possible. The

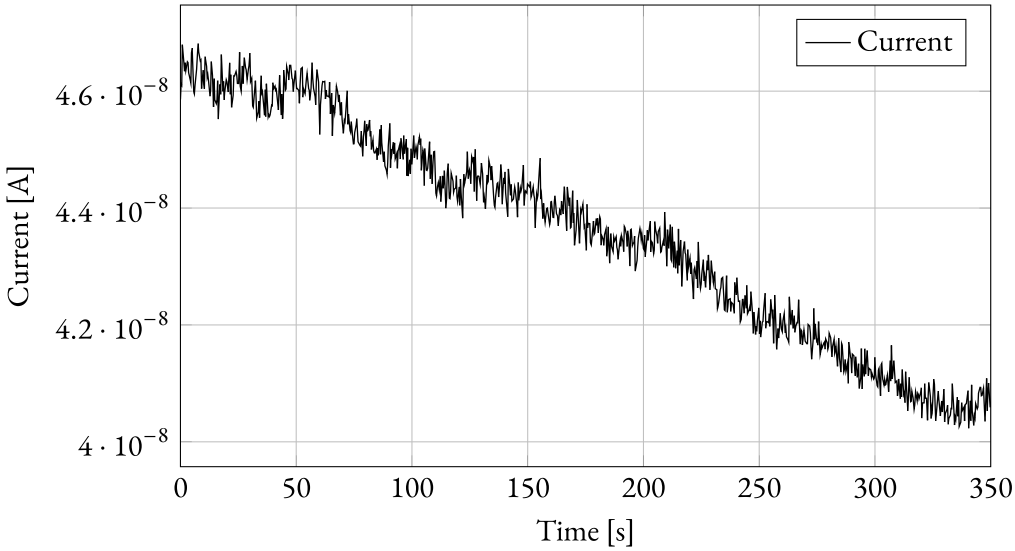

Figure 7.6: Measurement taken over 350 s without a window at the hard X-ray branch at an energy of 15 keV. At energies above ≈ 6 keV a constant slope was observed during the measurement. On the slope the top-up cycle of the accelerator can be seen, however the slope is the dominant factor.

overall picture shows that the data fits well with the expectation, however a look into the low energy part of the measurements (up to 3.5 keV) as shown in figure 7.8 reveals that all of the data points are above the expectation. Therefore, either the thickness of the membranes is thinner than expected or the composition and density is different. Since the manufacturing tolerances are too small to explain the behaviour, the latter is the more likely explanation. Since silicon rich silicon nitride thin films can be produced in a huge variety of compositions and densities no real selection can be made. However, for a slightly reduced density, from $\rho_{\text{nom}} = 3.44\,\text{g/cm}^3$ to $\rho_{\text{new}} = 3.0\,\text{g/cm}^3$ the data agrees much better with the expectation. As described in subsection 7.2.2 the data taken with the setting D9 showed non-conclusive results. The data points from those measurements are marked and should not be taken into account.

For the case of the Mylar® window, the data and the expected transparency fit very well. There is only one exception at 2 keV where the data point is not fitting. Due to time restrictions it was not possible to do more measurements close to this energy. A different measurement of another Mylar® window performed shortly after this measurement campaign revealed the same behaviour at 2 keV [Qui]. Hence, it is unlikely that it's just a flux variation. Also the measurements with the SiN_x windows don't show this behaviour. Due to the energy restriction of the beamlines, no data could be taken between 2 keV and 3 keV, therefore it is unclear if there is an absorption edge or not. This should be investigated in another measurement campaign since it would impact the analysis of data taken with a Mylar® window in the region between 2 keV and 3 keV which has a high expectation for axions produced via the Primakov effect.

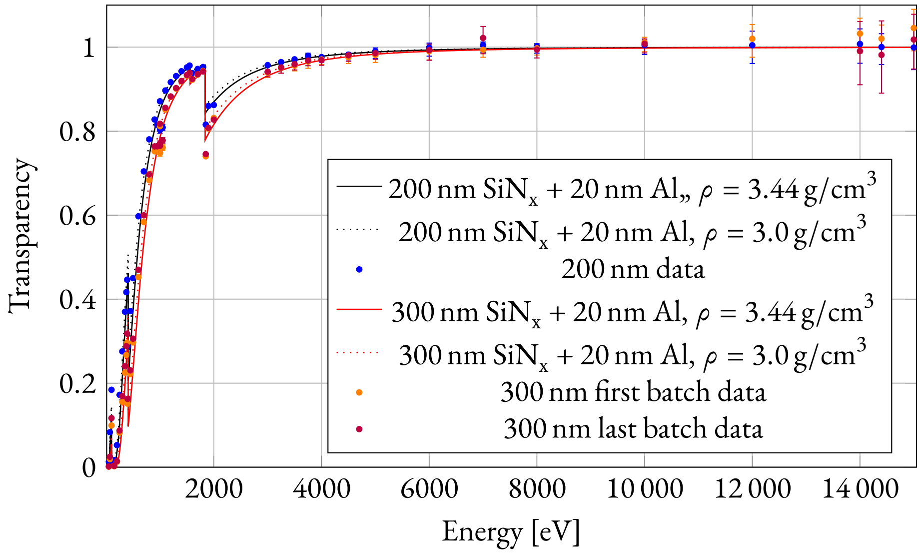

Figure 7.7: Transparencies of the SiN_x windows for an energy range from 10 eV to 15 000 eV. The data and the expected transparencies are shown. Expected transparencies from [Gul].

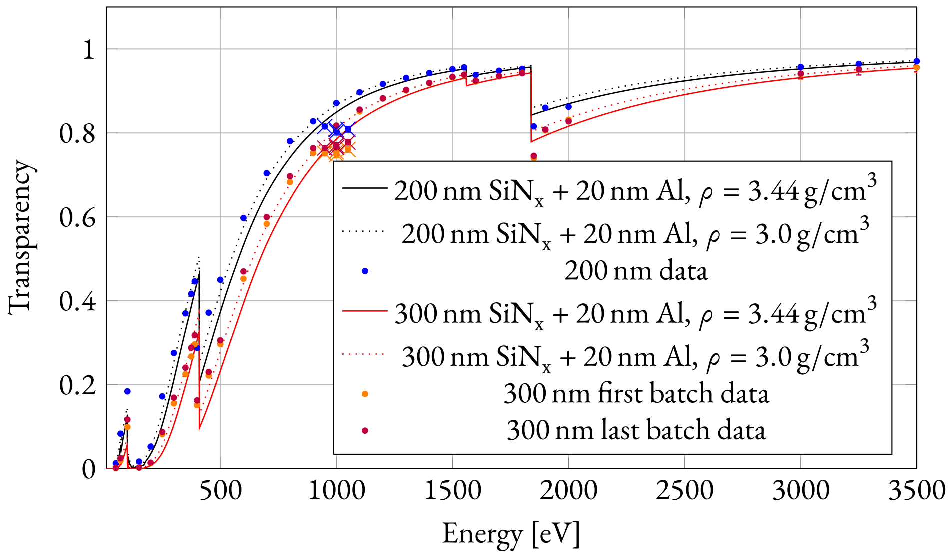

Figure 7.8: Transparencies of the SiN_x window over an energy range from 10 eV to 3500 eV. It is clearly visible that the measured data is always above the expectation. Therefore the composition of the silicon nitride membranes is supposed to be different. Data points taken with setting D9 showing non-conclusive results are marked with crosses. Expected transparencies from [Gul].

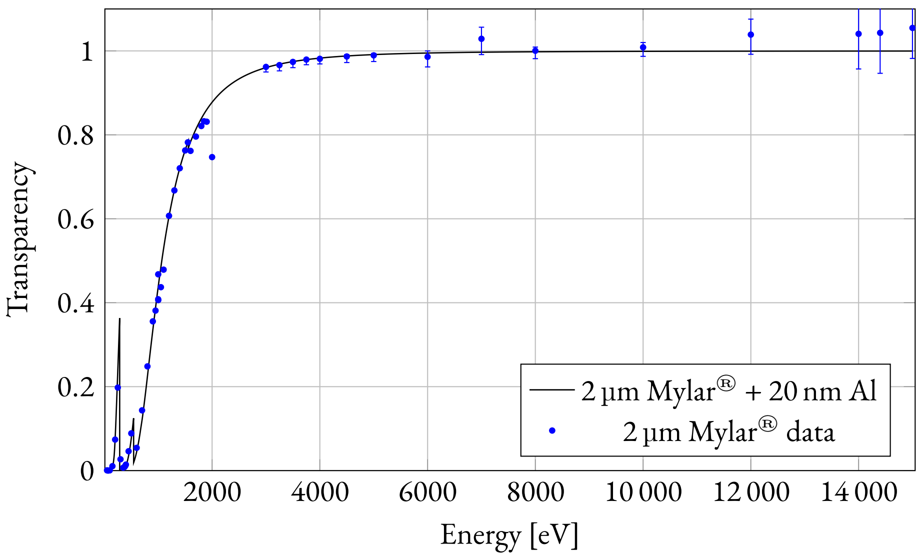

Figure 7.9: Transparencies of the Mylar® windows for an energy range from 10 eV to 15 000 eV. The data fits very well with the expectation, except for one point at 2000 eV. This difference is unclear and was also observed for a measurement of two other Mylar® windows [Qui]. It is also unlikely to be an error since the data for the SiN_x windows is not showing the behaviour. Expected transparencies from [Gul].

CHAPTER 8

The seven GridPix detector

Based on the developments for the first GridPix detector used at CAST [Kri18, KKLD17, KKVD18], a detector with additional features that aim to further reduce the background level and therefore increase the axion sensitivity. The main additional features are two scintillator vetoes and a ring of six GridPixes around the central one to better determine muon tracks and fluorescence induced by them. Implementing those features requires a redesign of the detector, the firmware, and the software. In the following, the improved detector is described in section 8.1 with a deeper insight into the cooling of the detector (section 8.2). Finally, a description of the firmware and the necessary changes is given in section 8.3.

8.1 Detector layout

The full setup of the detector can be seen in figure 8.1. The detector consists of a small gas volume defined by an ultra-thin entrance window within a cathode, a drift ring with a field cage, and the anode with the readout underneath. Thus, a homogeneous field inside the gas volume is achieved. The readout consists of the Septemboard carrying the seven GridPixes and the Intermediateboard. The Intermediateboard contains all the connections to the field-programmable gate array (FPGA)-based readout and also the connection of the temperature readout to the readout computer. In between the Intermediateboard and the Septemboard a cooling device is mounted. The cooling device is necessary to keep the GridPixes in a working temperature range. Below the Intermediateboard a small scintillator is mounted to veto perpendicular incoming muons, which could mimic an X-ray photon. A closer look at the parts will be given in the following subsections.

8.1.1 Cathode with ultra-thin window

The cathode with the ultra-thin window is the connection between the beamline of the experiment and the detector. It serves on the one hand as the barrier between the detector gas and the vacuum of the beamline and on the other hand as the entrance for the low energetic X-rays. The cathode is produced from copper and connected to the high-voltage via a small screw on its rim. In the centre of the cathode, the ultra-thin window described in chapter 7 is placed.

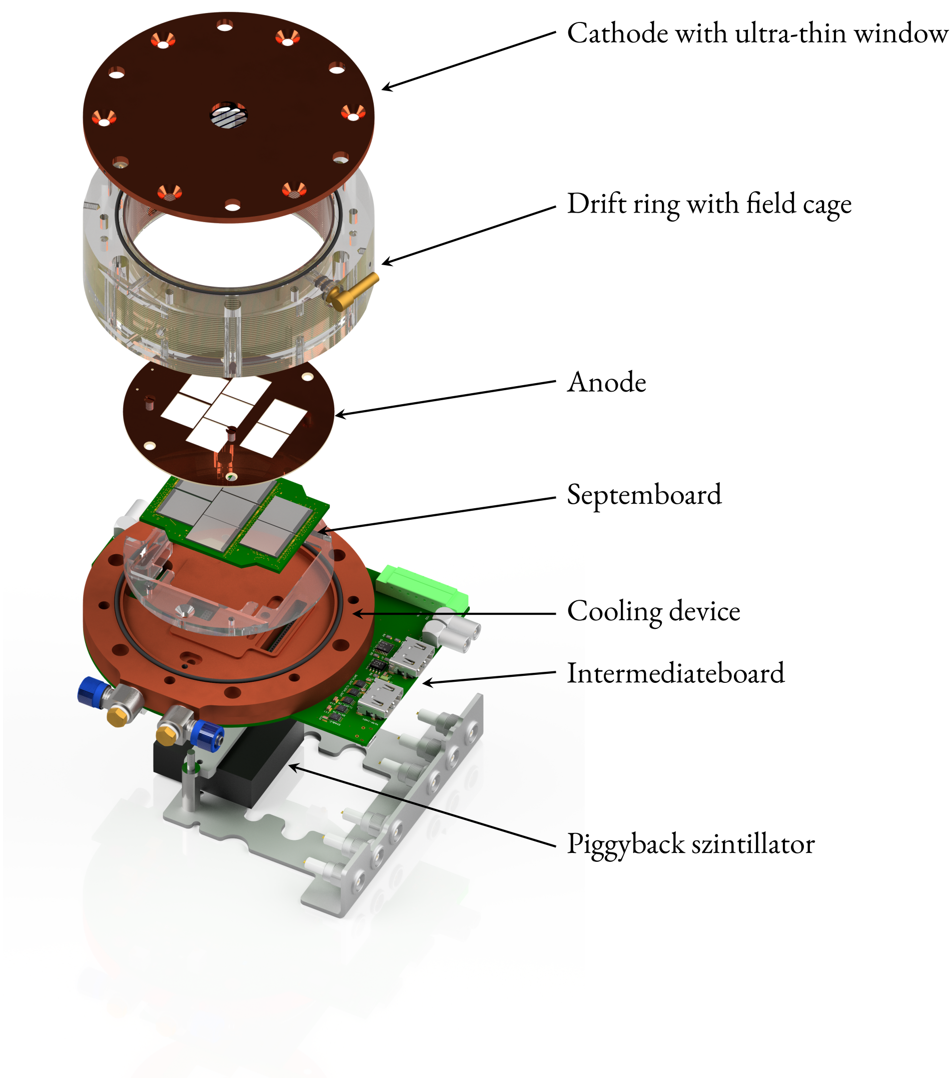

Figure 8.1: Exploded CAD view of the seven GridPix detector. The main parts are labeled.

8.1.2 Drift ring and field cage

The drift ring is the central part of the detector. It contains the active volume of the gaseous detector. The drift ring is made from Polymethylmethacrylate (PMMA) and has on its sides two holes for the connection of the gas in- and out-let. The drift ring has a height of 31 mm, it is sealed on one side to the cooling plate and on the other side to the window. The seals are standard rubber O-rings made from Viton®. The inner diameter of the field cage is 79.8 mm, which defines a gas volume of about 0.15 l. The angled connectors for the gas connection are made of two brass parts soldered together and sealed with two rubber O-rings each. Due to the not perfect leak tightness, it is necessary to have a constant gas flow through the detector and to operate the detector on a slight overpressure. Here a

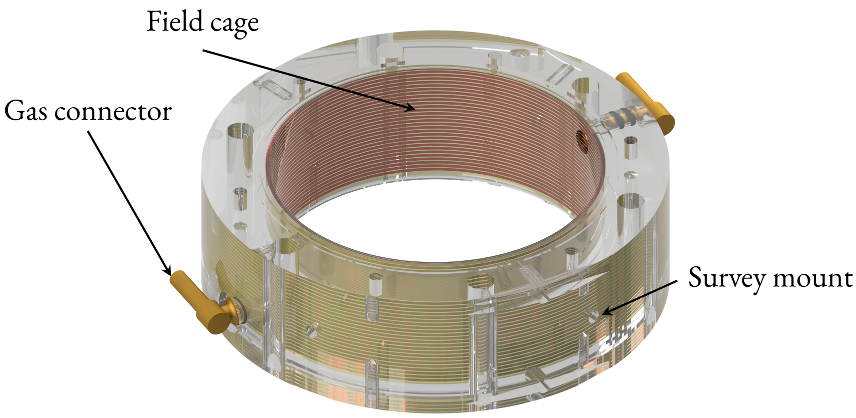

Figure 8.2: CAD view of the field cage. The field cage and the gas connectors can be seen. Also one of the four holes for the survey targets is marked.

pressure of 1050 mbar(a) is used. The drift ring also contains two holes on one side where wires are glued in, connecting the field cage. The field cage is necessary to shape the drift field inside the detector to avoid disturbances of the event shapes on the six outer GridPixes. The field cage itself is made from a polyimide printed circuit board (PCB) containing 29 conducting copper rings of 0.7 mm width and a spacing of 0.3 mm. To get the ring shape necessary for the field cage, the PCB is bent so both ends touch and each ring is soldered together. Each ring is connected to its neighbouring ring via a resistivity of 10 kΩ. Then, to the first and the last ring a wire is soldered, which is then glued into the drift ring. These wires are used to set the field cage to the appropriate high-voltages. In combination with the resistivities connecting the field cage rings a homogeneous field in the gas volume is achieved.

8.1.3 Septemboard and anode

The Septemboard with the seven GridPixes is the main component of the detector. The Septemboard holds and connects the seven GridPixes to the Intermediateboard. In addition close to the GridPixes a temperature sensor (PT1000) to monitor the inside temperature of the detector is mounted on the Septemboard. The temperature sensor is mounted on the backside of the Septemboard as shown in figure 8.3. The further readout electronics are on the Intermediateboard. The GridPixes are glued to the front side of the Septemboard and then connected via wire bonds. Also, the InGrids are connected via wire bonds to the Septemboard. Therefore, between the middle row and the bottom row a gap of 3 mm is required for the wire bonds. The second and smaller gap (0.75 mm) between the two GridPixes in the top row is necessary for the high-voltage (HV)-connection of the InGrid of the central GridPix.

To have, in particular close to the GridPixes, a homogeneous field inside of the detector, a field-shaping anode is essential. The field-shaping anode consists of 0.8 mm copper-clad PCB material. A drawing of the anode is shown in figure 8.4. The two sides are connected with two through-contact rivets. While the bottom side is at most parts milled out, to allow for very low placement without touching the wire bonds of the GridPixes, the topside just shows the seven cutouts for the GridPixes. A placement of the top surface of the anode as close to the surface of the grid is important to shape the field close to the GridPix's edge, preventing a distortion of the event shape. On the bottom side where the copper is not removed a connector is soldered to the anode to connect it with a HV line on the

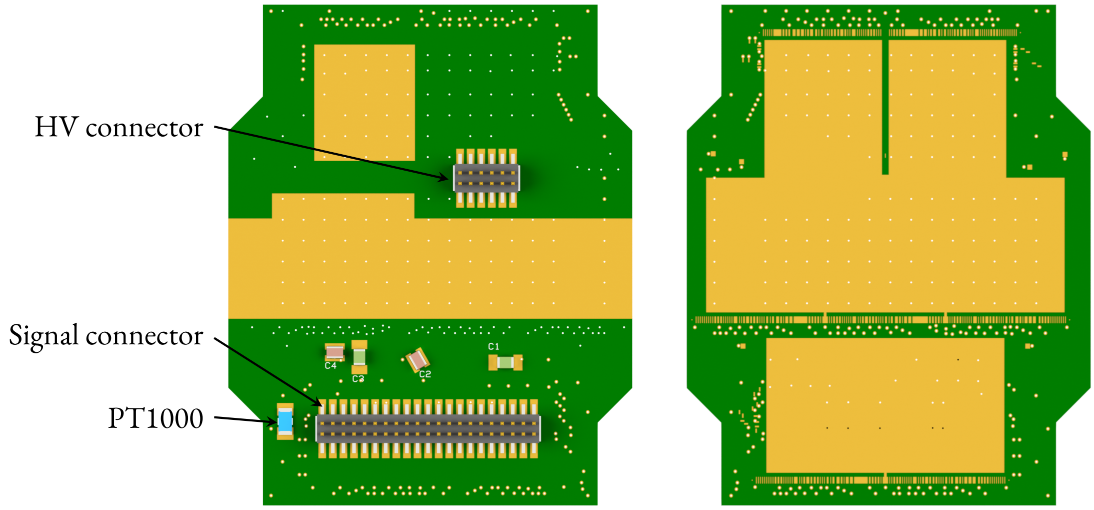

Figure 8.3: CAD model of the Septemboard. Both sides are shown. On the bottom side (left) the connectors for the high-voltage (HV) and the electronic signals are indicated. Also, the position of the temperature sensor (PT1000) can be seen. Additionally there are four capacitors to stabilise the powering of the GridPixes. On the top side (right) the places for the 7 GridPixes are visible as well as the rows of bond pads for the connection of the GridPixes.

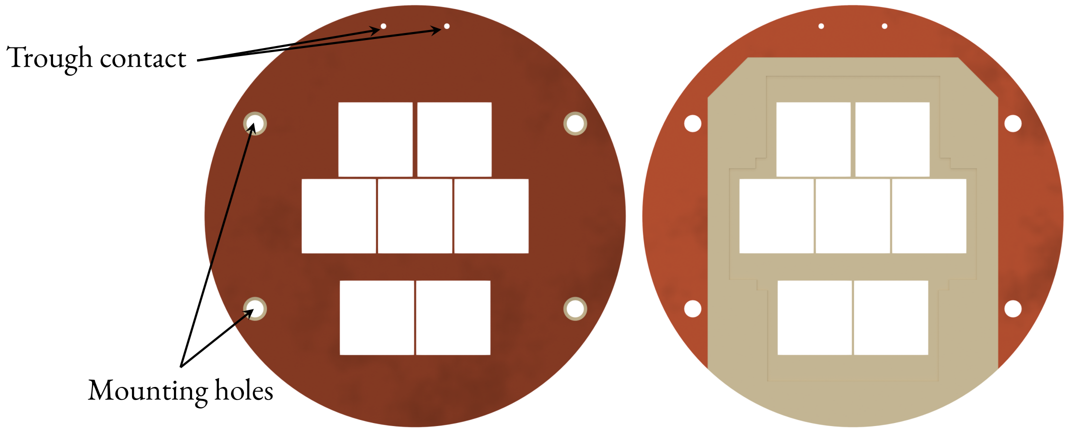

Figure 8.4: CAD model of the anode. Both sides are shown. The bottom side (right) is milled out around the position of the GridPixes to make a very low mounting position possible. Also, the through contact holes on the top are visible. Here rivets connect the top and the bottom side.

Intermediateboard. The anode is held in place by four copper screws. To avoid electrically connecting the anode with the cooling device a spacer made from PMMA is mounted on the cooling device on which the anode is fixed. This spacer also defines the height difference between the anode and the grid of the GridPixes.

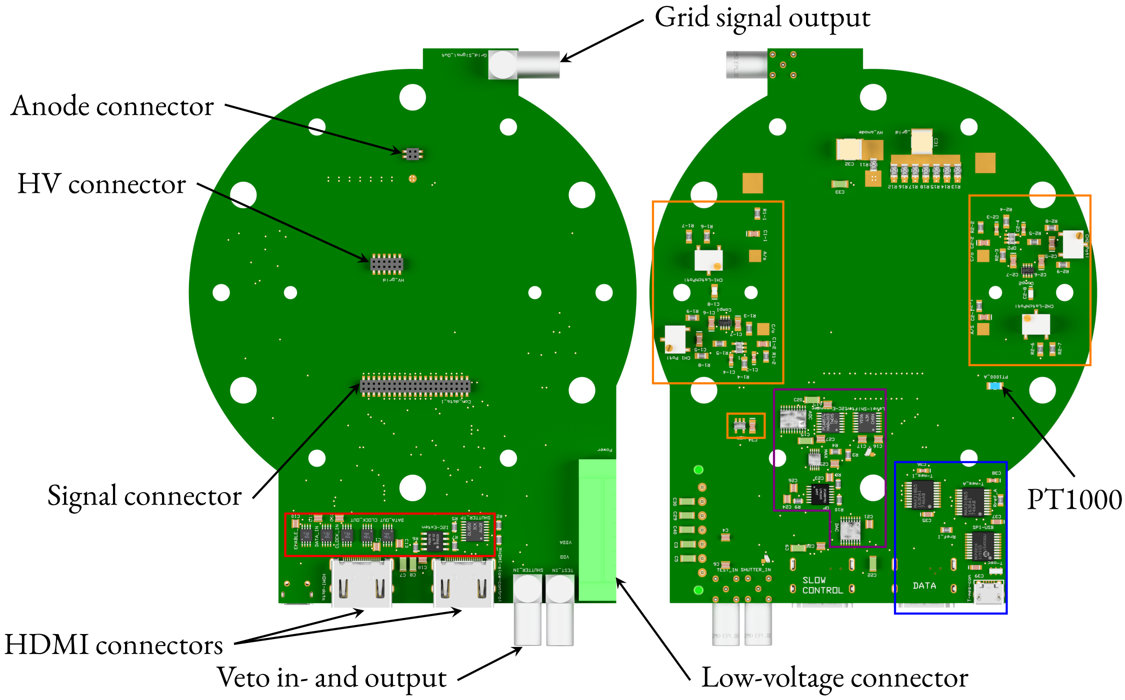

Figure 8.5: CAD model of the Intermediateboard. Top (left) and bottom (right) side is shown. The most important connectors are indicated. Also, the important groups of electronics are marked with coloured boxes. In red the LVDS-extenders and the I^{2}C-extender are marked. They are needed to use long HDMI cables for the detector connection to the FPGA board. In violet the parts for the test pulse generation are marked, here also an I^{2}C-expander is mounted to produce the slow control signals for the Timepix. The blue rectangle marks the temperature readout consisting of the two readout ICs and the USB interface with connector. In orange the electronics for the readout of the piggyback scintillator is marked. The three LEMO 00 connectors are used for the input of the veto from the FPGA board, for the output of the signal from the piggyback scintillator, and the output of the Grid signal.

8.1.4 Intermediateboard

The Intermediateboard is the main detector PCB and serves different tasks, the most important one being the connection and powering of the Septemboard. It also contains the electronics for the temperature measurement, the readout of the piggyback scintillator, the HV distribution, test pulse generation, and the grid signal decoupling. A rendering of the board with the different blocks of electronics can be seen in figure 8.5. In the following, the different parts of the Intermediateboard will be explained.

To power the Intermediateboard an external power supply is connected to the low-voltage connector providing all necessary voltages.

The Septemboard connects via a 42-pin connector to the Intermediateboard. There most of the signal lines are forwarded via signal extenders to the HDMI connectors in order to connect to the FPGA readout board. Since the two HDMI cables offer not enough signal lines to connect all necessary signals, some of the slow control signals are transmitted as an inter-integrated circuit (I^{2}C) stream and then split in an I^{2}C I/O expander to produce the slow control signals (see section 8.3.2). All signals going and coming from the HDMI cables are amplified at both ends via LVDS or I^2C extenders to allow proper signal transport over long cables (< 15 m).

Also, the test pulses necessary to calibrate the GridPixes are generated on the Intermediateboard and sent through the connector to the Septemboard. The pulses are generated via a DAC controlled by the I^2C signals. The DAC sets two voltage levels which are then switched via a multiplexer in order to produce the test pulses. The number of test pulses can be set by the software and is sent via the FPGA directly to the Intermediateboard.

The second Septemboard connector connects the high-voltage for the seven GridPixes via twelve pins. Close to this connector another four-pin connector is used to connect the field-shaping anode to the high-voltage. The high-voltages themselves are fed into the Intermediateboard via LEMO HV connectors soldered with short cables to the board. In each line, a 10 MΩ resistor is mounted to prevent damaging of the detector due to sparks. The high-voltage connection of the central GridPix also contains a capacitor decoupling the induced analog signal from the InGrid to a LEMO 00 connector. This signal is read out via a Flash ADC (FADC) and used for two purposes: as a trigger in order to read out the GridPixes if a signal is measured on the central GridPix and as an additional veto for perpendicular muons mimicking an X-ray (see [Sch24a] for details).

The piggyback scintillator is read out via two silicon photomultipliers (SiPM), these are connected to discriminators to digitise the signal. The inverted pulses from the discriminator are then sent into a NOR gate to produce a veto signal from the scintillator if both SIPMs have sent a coincident signal. This is again necessary to reduce noise. This signal is then forwarded to the LEMO 00 connectors which are connected to the FPGA board.

The temperature readout consists of two platinum resistance temperature detectors (RTDs) which are read out by a resistance-to-digital converter. This converter compares the temperature dependent resistance of the RTD with a reference resistance and sends the results via a serial peripheral interface (SPI) to an SPI host. The SPI host is then connected via a USB interface to a computer. The resistance-to-digital converter can handle up to eight devices. In this case two devices are installed for the two temperature sensors. One of the RTDs is mounted on the Intermediateboard itself to measure the surrounding temperature while the other one is mounted on the Septemboard (see section 8.1.3).

8.1.5 Veto scintillators

The veto scintillator setup contains two scintillators, a small one ($40 \times 40 \times 10\,\mathrm{mm}^3$) mounted to the detector and a big one ($800 \times 400 \times 50\,\mathrm{mm}^3$) above the detector setup. They are used to veto cosmic muons.

The small one (piggyback) is used to avoid the misinterpretation of muons which are traversing the central GridPix perpendicular and therefore giving a X-ray-like event shape. A muon like this will traverse the detector and therefore also the scintillator, which then produces a signal sent to the FPGA.

The big scintillator is mounted above the lead shielding of the detector and covers the shielding and parts of the copper tube used to mount the detector to the beamline. Here, a muon could likely produce either fluorescence photons inside the detector or the tube or it could produce neutrons inside the lead which can lead to a cascade of other particles [RC20]. So if a muon is registered by the big scintillator, the signal will be handed to the FPGA.

8.2 The cooling device

The cooling device is a water-cooled copper plate. It is coupled with a thermally conductive pad to the Septemboard. The Septemboard has 168 vias for thermal coupling between the GridPixes and the cooling device. The cooling device has a round cooling channel of 3 mm diameter for the water to flow through. The water is cooled via a closed loop chiller with a 120×240 mm radiator equipped with two 120 mm fans, a water pump, and a reservoir. The system has a cooling capacity of approximately 175 W/10 K[1]. With an ambient temperature at CAST hall between 15 °C and 27 °C, the water will, due to the air-cooled chiller gain the same temperature as long as the dissipated heat is not higher than the cooling power of the chiller. In the case of the CAST detector, this is not the case, since the measured peak power consumption and therefore dissipated heat is not higher than 14 W. However, the maximum peak power seven chips could reach is around 23 W (approximated from a single GridPix measured at full noise (3.3 W)). Since both values are peak values the average power consumption will be lower. The following calculations will be performed for 14 W as a conservative estimate.

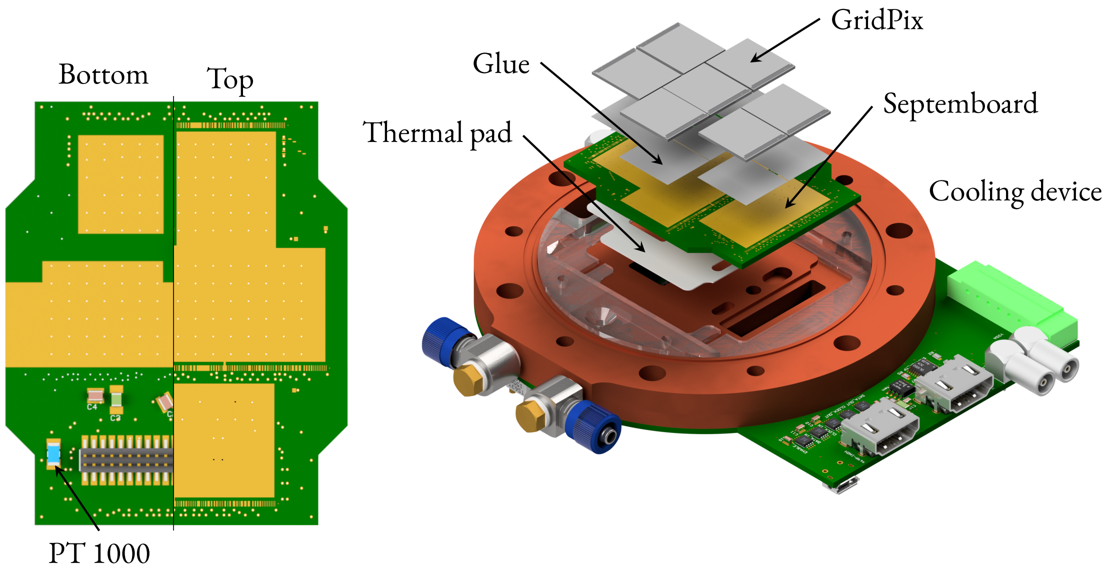

(a) (b)

Figure 8.6: (a) The Septemboard split in top and bottom side, the vias for heat conduction as well as the PT 1000 for temperature measurements are visible. (b) The materials between the GridPixes and the cooling device.

8.2.1 Necessity of the cooling device

During the first test runs of the newly built CAST detector containing seven GridPixes multiple problems occurred, which were not known from the in 2014/15 used detector, specifically high sparking rates, a runaway of the threshold, and very atypical noise patterns on the chip as seen in

[1] The cooling power of the system was estimated with test results from (https://www.xtremerigs.net/2015/02/10/alphacool-nexxxos-xt45-360mm-radiator-review/4/) the tested model is the 360 mm instead of the here used 240 mm version and the fan speed is only 1200 rpm fitting none of the tested speeds, therefore the results are modified to better suit the used model.

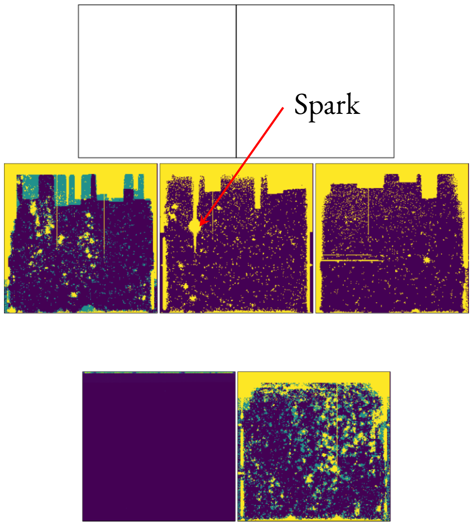

Figure 8.7: Occupancy plot of the uncooled Septemboard with only five GridPixes mounted. It can be seen that on four GridPixes many sparks occur. The reason for the rectangular shape of most of the features is that the readout of the GridPix only processes the first 4096 pixels, while the rest is discarded. A major spark is marked on the central chip. They typically lead to a change in the chip setting, therefore a stable operation is not feasible.

figure 8.7. After the implementation of temperature sensors on the Intermediateboard as well as on the Septemboard the temperature inside the detector was investigated. The temperature sensor of the Septemboard can be seen in figure 8.6(a). It is visible that the temperature measurement is neither taken on the same side nor directly below the GridPixes. Therefore, the temperature at the GridPixes will be even higher than the measured temperature. However, the measurement showed that the temperatures inside the detector did rise to very high levels. At high temperatures, on the one hand the gas gain is dropping for higher temperatures, on the other hand, the noise and therefore the needed threshold of the chip rises. Hence, the detector performance is decreased. A first approach for cooling with a fan reduced the temperature and the sparking behaviour. This was further investigated in a master thesis [Sch19a] mentored in the scope of this thesis. The results showed that above a threshold temperature of around 70 °C the sparking behaviour starts to occur. First sparks seem to be only on the dyks of the InGrid structure, while at temperature above 90 °C also sparks on the active surface occur. With this knowledge, a cooling device had to be mounted beneath the Septemboard.

8.2.2 Mechanical layout

The copper cooling plate consists of two half plates hard soldered together. The half plates consist of oxygen-free copper in order to be able to solder them in a vacuum soldering process. To cool the cooling device with water, channels are milled into the copper which after the soldering form a circular cooling channel. While planning the cooling device some restrictions had to be fulfilled. They mostly occurred from the fact that the detector was built and planned without cooling and only later it was found to be necessary. Therefore, the cooling plate is designed around all existing features limiting the thickness of the plate and also introducing pockets and holes for specific parts. In figure 8.8 one of the half plates is depicted. The through holes for the Septemboard and anode connection can be seen as

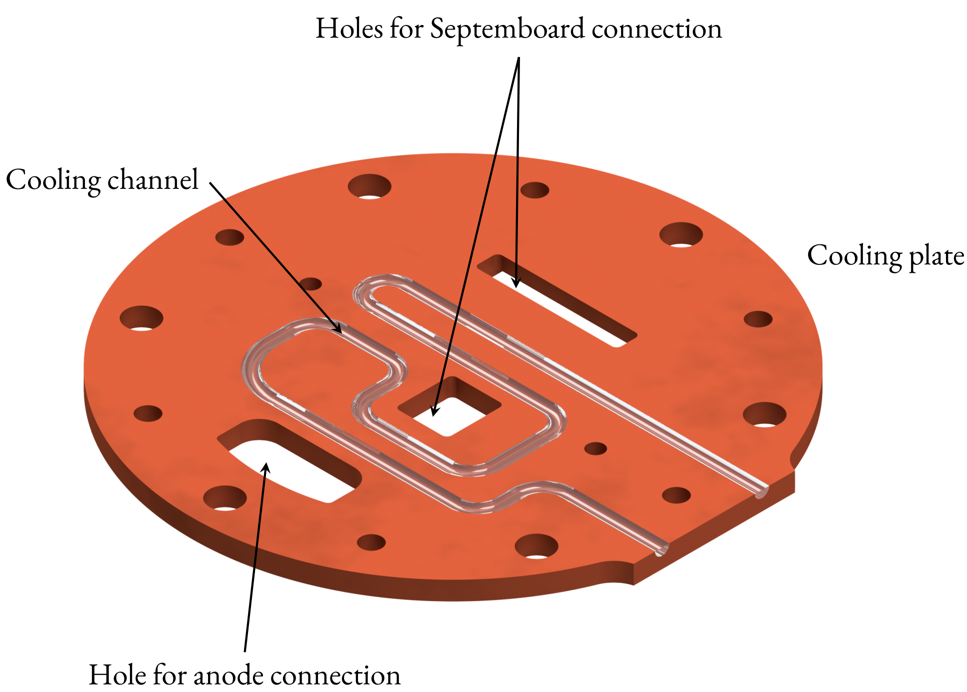

Figure 8.8: CAD model of one half plate of the cooling device. The soldering side is shown to reveal the water channel. Also, the through holes for the connections of the Septemboard to the Intermediateboard are visible and how the cooling channel is designed around them to allow for good heat collection.

well as the cooling channel. The water channel is designed in a way that at least 1 mm wall thickness is maintained, to reduce the possibility of leaks. Also, it was tried to have the channel pass under all seven chips as homogeneously as possible while avoiding sharp corners, which would lead to additional turbulences. To produce the cooling device in a first step the rough shape of the half plates is milled out. Then the plates are annealed to release all stress from the material. After this the shape and thickness is finalised and the surfaces for soldering are flattened to ensure an absolutely watertight soldering. After soldering the cooling plate is milled to its final design and tested for water tightness.

8.2.3 Heat transport

The first step, to determine if the cooling is sufficient, is to calculate the heat transfer from the copper to the water. For this one has to calculate or measure the total surface area of the cooling channel. This is measurable from the CAD model and results in 0.002856 m^2. Secondly, the flow through the cooling device has to be known and was measured to be $q_{\text{water}} = 0.3\,\text{l/min}$. With this one can now determine the Reynolds number $Re(T)$ to determine whether the flow is laminar or turbulent. The following calculations are following [LKLT20]:

$$Re(T) = \frac{c_{\text{water}} d}{\nu_{\text{water}}(T)} = \frac{4 q_{\text{water}}}{\nu_{\text{water}}(T) \pi d} . \tag{8.1}$$

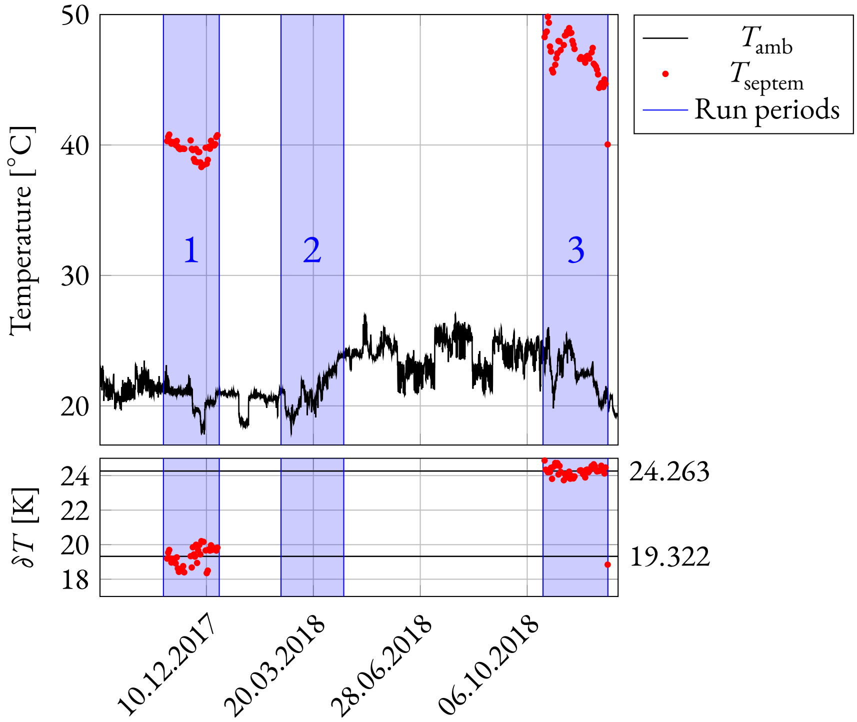

Figure 8.9: Hourly averaged temperatures measured in the CAST-hall T_{amb} (black) shown together with the temperatures measured at the Septemboard T_{septem} (red). In blue the the run periods of the detectors are indicated. At the second run period the temperature measurement was not working due to a broken USB port. This was fixed for the third run. It is visible that the Septemboard temperature is following the ambient temperature with a certain offset $\delta T = T_{septem} - T_{amb}$. This offset is shown in the lower plot. It is visible that the offset was lower for the first run period. The fitted values for both runs are indicated on the right, revealing that the offset between the runs is ≈ 5 K. This can be an effect of air gaps due to the remounting of the Septemboard or due to a reduced water flow.

The onset value for turbulent flow is not a clear point; a lot of different numbers between typically 1700 and 2300 can be found in literature. Therefore, a slightly higher number was chosen than the one determined in [AMDL+11]. Also, due to the bends turbulent flow will probably set in for lower values of $Re(T)$. The results of the calculations for different temperatures can be seen in figure 8.10. The temperature band, indicated in red, shows the ambient temperatures in the CAST hall during data taking. Here, it can be seen that the result tends to the turbulent behaviour. However, it is in the transition region so both cases need to be investigated. The values for the kinematic viscosity $\nu_{water}(T)$ are taken from [KW19].

Now one can calculate the Nußelt number for turbulent and laminar flow inside a tube, the Nußelt number is the dimensionless coefficient connecting the heat transport between a fluid and a solid. In

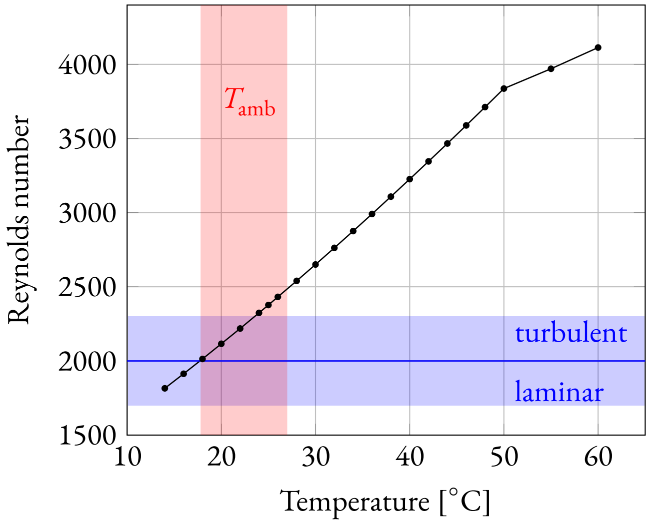

Figure 8.10: Reynolds numbers $Re(T)$ for water temperatures of $T = 14\,^\circ\mathrm{C}$ to $T = 60\,^\circ\mathrm{C}$. The area where the flow would change from laminar to turbulent is indicated in blue, as well as the area of the ambient temperature at CAST T_{amb} is indicated in red. The graph reveals that a turbulent flow is most likely. However, a laminar flow cannot be completely excluded.

this case between water and copper. For turbulent flow one finds

$$Nu_{\mathrm{turb}}(T) = \frac{\frac{\xi(T)}{8} \cdot (Re(T) - 1000) Pr(T)}{1 + 12.7\sqrt{\frac{\xi(T)}{8}}\left(Pr(T)^{\frac{2}{3}} - 1\right)} \cdot \left(1 + \left(\frac{d}{L}\right)^{\frac{2}{3}}\right), \tag{8.2}$$

with $Pr(T)$ as the Prandtl number (values from [KW19]), L the length of the cooling channel and $\xi(T) = \left(1.82 \log\left(Re(T)\right) - 1.64\right)^{-2}$. If the flow is laminar the Nußelt number can be determined by

$$Nu_{\mathrm{lam}}(T) = \left(49.37 + \left[1.615\left(Re(T)Pr(T)\frac{d}{L}\right)^{\frac{1}{3}} - 0.7\right]^{3}\right)^{\frac{1}{3}}. \tag{8.3}$$

The results are plotted in figure 8.11. For laminar flow, the number is basically constant while for turbulent flow it rises with the temperature. With the Nußelt number one can derive the heat transfer coefficient

$$\alpha(T) = \frac{Nu_{\mathrm{turb/lam}}(T)\lambda_{\mathrm{water}}(T)}{d}, \tag{8.4}$$

with $\lambda_{\mathrm{water}}(T)$ as the thermal conductivity of water (values from [KW19]). With this, finally over Fourier's law the heat flow rate $\dot{Q}(T)$ from the copper to the water can be calculated as

$$\dot{Q}(T) = \alpha(T) A \left(T_1 - T_2\right). \tag{8.5}$$

Since the heat flow rate necessary is known to be $\dot{Q}(T) = 14\,\mathrm{W}$, one can rewrite Fourier's law in order

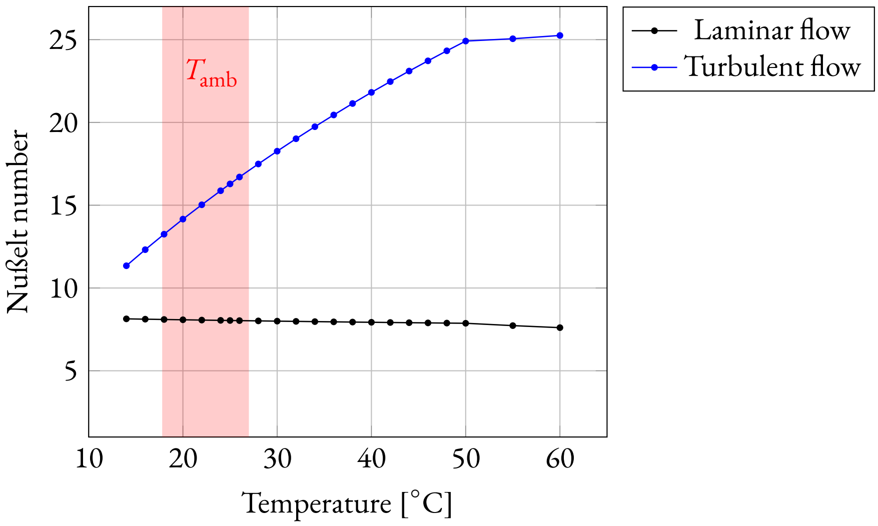

Figure 8.11: Nußelt numbers for laminar and turbulent flow. it can be seen that the Nußelt number for the laminar case is basically constant.

to calculate the heat difference $\Delta T = T_1 - T_2$ between the copper and the water

$$\Delta T = \frac{\dot{Q}(T)}{\alpha(T)A}\,. \tag{8.6}$$

The result is shown in figure 8.12. It is visible that the temperature difference in both cases, laminar and turbulent behaviour, is low. In the more likely case of turbulent flow, it will be, depending on the ambient temperature, between 1.5–2 K. This shows that the cooling device is sufficient for the Septemboard at full power. With the cooling device to be sufficient the next step is to calculate the temperature difference between the water and the chips in order to find the expected temperature at the chips. Here, one has to calculate the thermal resistance of the materials between the water and the chips. Since the materials are flat connected to each other one can easily follow the stack of materials consisting of copper, thermal tape, FR4 (PCB), and the glue used to fix the GridPixes. The stack and the different sizes of the surfaces can be seen in the exploded CAD view in figure 8.6(b). All areas have been measured from this CAD model. However, the Septemboard itself has some vias underneath the GridPixes to have a better thermal coupling. For all seven GridPixes there are in total 168 vias. They have a diameter of 0.2 mm and a wall thickness of 15 µm and consist of copper. The thermal resistivity $R_{\mathrm{th}}(T)$ for a flat surface of Area A and thickness d is defined by

$$R_{\mathrm{th}}(T) = \frac{d}{\lambda(T)A}\,. \tag{8.7}$$

The results for the different layers are shown in table 8.1.

In contrast to water, the heat transfer coefficient for the materials listed in table 8.1 does not change much in the temperature range needed for the cooling device so the calculated heat resistivity values

[3] The measured thermal conductivity of FR4 varies (0.29–0.343) W/mK [AG96] [SPW90], a value of 0.3 W/(mK) is often used by manufacturers.

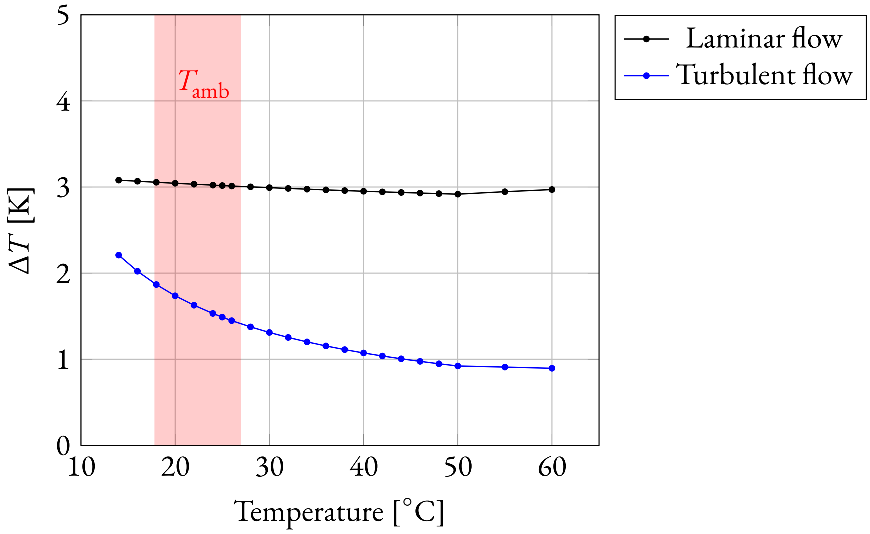

Figure 8.12: Necessary temperature difference ΔT to reach a heat flow rate $\dot{Q}(T) = 14$ W for laminar and turbulent flow from the copper to the water. It can be seen that the temperature difference needed for a sufficient heat transfer is very low. Therefore, the copper cooling plate will only heat up around 1.5–3 K depending if the flow is laminar or turbulent and on the surrounding temperature.

Layer	$\lambda(T)$ in W/(mK) at 20 °C	A in m^2	d in m	$R_{\text{th}}(20\,°\text{C})$ in KW^{-1}
Copper	393 [BS18]	1.61×10^{-3}	4.0×10^{-3}	0.0063
Thermal pad	0.9 [Aka]	1.61×10^{-3}	0.3×10^{-3}	0.2070
FR4	0.3 [3]	1.56×10^{-3}	1.6×10^{-3}	1.3846
Vias	393	3.04×10^{-6}	1.6×10^{-3}	3.4080
Glue	1.3 [Com20]	1.56×10^{-3}	0.2×10^{-3}	0.1475

Table 8.1: Thermal resistivities for the material layers of the thermal coupling between the GridPixes and the water channel.

can be used independent of the temperature for this case. With these numbers one can compute, via the stack of materials, the total heat resistivity. Here materials stacked are simply added up

$$R_{\text{th}} = \sum^{i} R_i\,, \tag{8.8}$$

while materials in the same layer are treated like parallel electric resistivities:

$$R_{\text{th}} = \frac{1}{\sum^{i} \frac{1}{R_i}}\,. \tag{8.9}$$

With this, finally, the total thermal resistivity can be calculated as

$$R_{\mathrm{th}}^{\mathrm{total}} = R_{\mathrm{th}}^{\mathrm{copper}} + R_{\mathrm{th}}^{\mathrm{heat\ pad}} + \frac{1}{\frac{1}{R_{\mathrm{th}}^{\mathrm{via}}} + \frac{1}{R_{\mathrm{th}}^{\mathrm{FR4}}}} + R_{\mathrm{th}}^{\mathrm{glue}} = 1.273\,\frac{\mathrm{K}}{\mathrm{W}}\,. \tag{8.10}$$

With the thermal resistivity, the temperature difference between the GridPixes and the water of the cooling device can be calculated:

$$\Delta T_{\mathrm{diff}} = R_{\mathrm{th}}^{\mathrm{total}} P_{\mathrm{dis}}\,, \tag{8.11}$$

where P_{dis} is the dissipated power of the GridPixes. Now one can calculate the temperature difference between the water in the cooling device and the copper temperature close to the water $\Delta T_{\mathrm{diff}} = 17.8\,\mathrm{K}$. From this and the results of figure 8.12 one can see that the cooling device is able to transport the heat away from the chips. This means that the minimum temperature of the chips will be $\Delta T = 19.5\,\mathrm{K}$ higher than the ambient hall temperature at CAST. Thus, the dimensions of the cooling plate are sufficient. Comparing these results with the measured data shown in figure 8.9 one can see that there is an agreement with the data from the first run being around 19.3 K above the ambient hall temperature. However, in run 3 the temperature is far off, compared to the calculated value. This can be explained due to a reassembly of the detector. Since the cooling power of the cooling plate and the chiller is way above the maximum dissipated power, the major temperature difference between the surrounding temperature and the chip's temperature is given by the thermal resistance. During run 3 the temperature was around 24.3 K higher than the ambient temperature, meaning that probably the thermal resistance changed to a slightly higher value. This might come from small air gaps and air pockets between the different layers of the material stack since air has a very low thermal conductivity of $\lambda = 0.026$ [Spa19]. So even very small air pockets have a significant effect. For example, an additional 0.02 mm air gap in the stack would lead to an additional temperature difference $\Delta T_{\mathrm{add}} = 6.7\,\mathrm{K}$.

8.3 Firmware

To allow communication between the GridPixes and the computer an FPGA is necessary. For the seven GridPix detector, a Virtex®-6 evaluation board (ML605) was used. The existing firmware for a single chip readout used VHDCI cables, not offering much flexibility in cable length. Due to this, the electronics were changed to HDMI cables which were already used for the GridPix TPC [Lup16]. However, the readout of this project was using FECv6 FPGA boards (see section 10.1.1) which contain a different version of the Virtex®-6 and also different electronics aboard. In the following, the structure of the firmware, as well as the necessary changes will be described. Additionally, the veto implementation of the scintillators and the analog grid signal will be introduced.

8.3.1 General overview

The firmware is set up from three major blocks, the Ethernet block, which receives and sends packages from and to the readout computer, the $\mathrm{I^2C}$ block, which controls the $\mathrm{I^2C}$ interface and the Timepix control block, which transceives the Ethernet packages and converts them to signals for the Timepix and also receives the answers from the Timepix and forwards them as packages to the Ethernet block.

The Ethernet block is substituted from the Virtex-6 Embedded Tri-Mode Ethernet MAC wrapper. It provides the communication with the physical Ethernet layers. The block is split into two major sub-blocks, the client side first in, first out (FIFO) and the serial gigabit media-independent interface (sgmii)-block. The latter provides the communication to the physical Ethernet layer, while the client side FIFOs provide the communication to the rest of the firmware. The communication with the client side FIFO works via a set of instruction variables (`EoF`, `SoF`, `data`, `src_rdy`, `dst_rdy`). As shown in figure 8.13 a typical data package in the transmitter is produced by setting the `src_rdy`-signal and the `dst_rdy`-signal to `0`, only when both of them are set to `0` dataflow from source to destination can be achieved. First, the `SoF`-signal is set to `0` and back to `1` indicating the start of a frame, and then the `data` is written to the frame. Once this is finished the `EoF`-signal is set to `0` and back to `1` indicating the end of the frame.

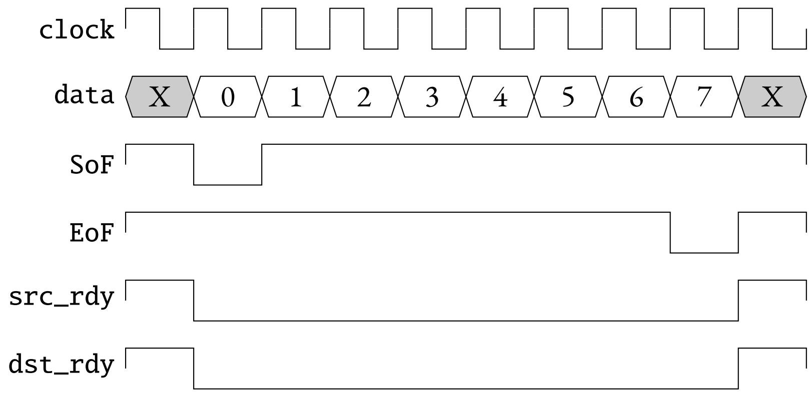

Figure 8.13: Timing diagram of the transmitter. The diagram shows the transmittance of an 8-byte data[7:0] package. The grey bytes marked with X will not be transmitted since they are before the `SoF`-signal or behind the `EoF`-signal. The same would happen if one of the signals (`src_rdy`, `dst_rdy`) would not have been `0`.

The I^2C block produces the I^2C signals. They are necessary due to the limited number of connecting wire pairs in the two HDMI cables. Therefore, some of the slow control pins of the Timepix are not connected directly to the FPGAs. In order to produce those signals on the Intermediateboard an I^2C expander is used. The signals for this have to be generated as a serial I^2C-signal.

The Timepix control block is the operating block for the Timepix, it gets the information from the computer software via the Ethernet receiver and produces the input for the Timepix and for the I^2C block and in the end, produces the packages to be sent back to the computer. It is divided into 33 different operations, called via a two-byte code (01 to 22) by the Timepix operation software (TOS). The software sends a data package with the code and the necessary data for the operation. In the following, the operations will be shortly discussed:

`01` reset

Resets the Timepix by setting the necessary signals on the I^2C expander. Then the clock to the Timepix is activated to perform the reset. After a few clock cycles the I^2C-expander is set back to a default state.

`02` start counting

Opens the shutter to start counting with the Timepix.

`03` stop counting
Closes the shutter to stop counting with the Timepix.

`04-06` serial readout
Reads the data from the Timepix. This is divided into three operations, the initial one `04` starts the readout. It sets the necessary signals to the I^2C expander and sets the enable and clock signals to the chip and reads back the first data package containing the information on the total length of the data stream. The software will ask for operation `05` until the second to last package. For the last package, the software will ask for operation `06`, which will send the last package and stop the readout.

`07` I^2C reset
This function sets all I^2C devices into a default state such that no operation is performed.

`08` I^2C expander
A test function in order to test the functionality of the I^2C expander. Each I^2C expander pin can be set to 0 or 1.

`09` I^2C DACs
A function to test the I^2C DAC channel and voltage can be chosen freely via the software.

`0A-0C` set matrix
Here, the matrix is set. This is again divided into three operations called consecutive by the software. First `0A` is called to start setting the matrix. Here again, the necessary I^2C expander signals are generated and the Timepix enable is set to 1 so the Timepix accepts data. With the first package, the clock is sent and stops at the end of the first matrix package. Then by calling `0B` all except of the last package are sent to the chip. The clock has to be started and stopped with each package. For the last package `0C` is called. Here the last package is written to the matrix and then the enable is set back to 0, so the Timepix is not accepting any more data.

`0D` set DAC write FSR
With this operation the DACs on the Timepix are set to the values set and the FSR is written to the Timepix. This is necessary to set the Timepix into a defined usable state after powering it. Also, in order to change a specific DAC this operation is called.

`0E` readout ADC
This command reads the value of a selected channel of the ADC back. With the ADC the DACs of the Timepix can be read out. Each ADC channel corresponds to one Timepix. To select a DAC the FSR has to be written to the chip with the proper setting.

`0F` test pulses
Here test pulses are produced with the test pulse generating circuitry (see section 8.1.4) on the Intermediateboard. Two channels of the I^2C DAC are set to the chosen voltages and sent to a multiplexer whose output is connected to the test pulse input of the Timepix. Then the multiplexer is directly driven by the FPGA so the number and frequency can be chosen.

`10` external testpulses on
This command enables the test pulses input so test pulses from an external pulser can be fed into the chip.

11 external testpulses off

This command disables the external test pulse input.

13 start counting

The start counting function allows the user to start a data taking by opening the shutter for a set time. The time is dependent on a number between 1 and 256 chosen by the user which is then multiplied with a factor of 46 to fit the maximum range of the ToT/ToA register. This maximum number is 11810. To know how long the shutter is open, the calculated number has to be multiplied by 25 ns since the clock runs, in this case, at 40 MHz. Hence, a shutter opening time between 1.15 µs and 294.4 µs can be chosen. In this function also the readout for the two veto scintillators is implemented (see section 8.3.3).

14 start counting with fast clock

This function works in the same manner as function 13 except that it uses a faster (80 MHz) clock. This allows for a more precise measurement of the ToA or ToT. However, since inside the FPGA still a 40 MHz clock is used, the possible shutter opening times stay the same. Also, the veto scintillators are not implemented for the fast clock.

15 start counting long

This function works in the same manner as function 13 except that it uses an additional factor of 256 for the shutter opening time. This allows for longer shutter opening times and therefore, since the readout time is always the same, for a higher duty factor. The selectable shutter opening times are between 294.4 µs and 75.37 ms.

16 start counting very long

This function works in the same manner as function 13 except that it uses an additional factor of 65536 for the shutter opening time. This allows for much longer shutter opening times and therefore, since the readout time is always the same, for a higher duty factor. The selectable shutter opening times are between 75.37 ms and 19.29 s. In this function also the readout for the two veto scintillators is implemented (see section 8.3.3).

17 start counting with external trigger

This function also opens the shutter for a defined time similar to function 13. But different to this the shutter is not opened directly but after an external trigger signal. In order not to wait infinitely long if the trigger signal is not arriving, the function stops waiting after 15000 clock cycles (375 µs).

18 start counting with external trigger and fast clock

This function works in the same manner as function 17 except that it uses a faster (80 MHz) clock.

19 set I^2C addresses

In this function, the I^2C addresses can be set to communicate with the I^2C components on the Intermediateboard. By default, the addresses are set to match the components on the Intermediateboard of the seven GridPix detector.

1A–1C readout chip zero suppressed

The zero-suppressed fast readout is again a block of three functions. The first function 1A assigns all necessary signals to read the data from the chip. This data is then processed in order to suppress all pixels which are 0 and writes the data to the RAM block on the board. Thus, only active pixel data is stored. This procedure is done for all connected Timepixes. However, only the first 4096 active pixels of each Timepix are processed, so if more non-zero data is received from the Timepix, it is lost. After the data has been stored function `1B` is called, which starts the sending of zero suppressed data to the computer. The computer asks for the data of one chip and the function sends all the data for that chip to the computer. Then the computer might ask for the next chip. `1C` is a combination of `1A` and `1B`. It reads data from the chips to a RAM block while at the same time sending the data of the previous readout stored in a different RAM block to the computer. When the data readout is finished it will send a package to the software.

`1D` count with external shutter
This function is used to control the shutter of the detector externally.

`1E` start counting long with fast clock
This function works in the same manner as function `15` except that it uses a faster (80 MHz) clock. This allows for a more precise measurement of the ToA or ToT. However, since inside the FPGA still a 40 MHz clock is used, the possible shutter opening times stay the same.

`1F` start counting very long with fast clock
This function works in the same manner as function `16` except that it uses a faster (80 MHz) clock. This allows for a more precise measurement of the ToA or ToT. However, since inside the FPGA still a 40 MHz clock is used, the possible shutter opening times stay the same. Also, the veto scintillators are not implemented for the fast clock.

`20` FADC trigger closes shutter on
This function allows an external trigger signal to close the running shutter window. The shutter is not closed immediately but a selectable number of clock cycles later to allow the full ToT to be measured. When this is used the time the shutter was open is saved. This time is sent to the computer as well as the times since the last trigger of each of the two scintillators (see section 8.3.3). The function receives an input for an additional amount of clock cycles the shutter will be kept open to allow for the charge to properly drain, so a proper ToT measurement is possible.

`21` FADC trigger closes shutter off
This function switches the external trigger function `21` off, so the shutter will always run until it reaches its desired time.

`22` count with external shutter with fast clock
This function works in the same manner as function `1D` except that it uses a faster (80 MHz) clock. This allows for a more precise measurement of the ToA or ToT. However, since inside the FPGA still a 40 MHz clock is used, the possible shutter opening times stay the same.

Most of those functions had to be changed to fulfill the changes necessary for the seven chip readout via HDMI cables. Additionally, functions `20` and `21` were added to enable or disable the veto system and to allow the usage of the FADC as a trigger for the shutter. A summary of the most important changes regarding those two topics will be given in the following sections.

8.3.2 Implementation of multi-chip HDMI-readout

In order to use a multi-chip readout via HDMI cables, some changes had to be implemented. This includes the implementation of I^2C in order to set multiple slow control signals (M0, M1, TRESET, Polarity, EnabelTestpulse) to high or low. For this an I^2C core was implemented in the firmware the I^2C-block was taken from [Lup16] and had to be implemented in the firmware of the ML605 readout board. In order to use the block in each function all signals controlled over I^2C have to be assigned to the required state, then these states are written into the I^2C block and sent to the expander. The timing of the fast control of the chip has to be adjusted to wait until the I^2C block finishes the operations and the signals are set on the expander. Additionally, issues like missing bits in the Ethernet packages were fixed. They were not a major issue with a single chip read out but accumulated for seven chips.

8.3.3 Implementation of the veto

The veto consists as explained in section 8.1.5 of two scintillators and the decoupled grid-signal which is recovered by a FADC. In order to get data with the correct timestamps from the scintillators the scintillator signals are discriminated and then fed into the ML605 FPGA board. Here, also the trigger signal from the FADC is connected to see if a signal is induced on the grid, meaning that an event was registered by the central GridPix, passing the threshold for the analog signal.

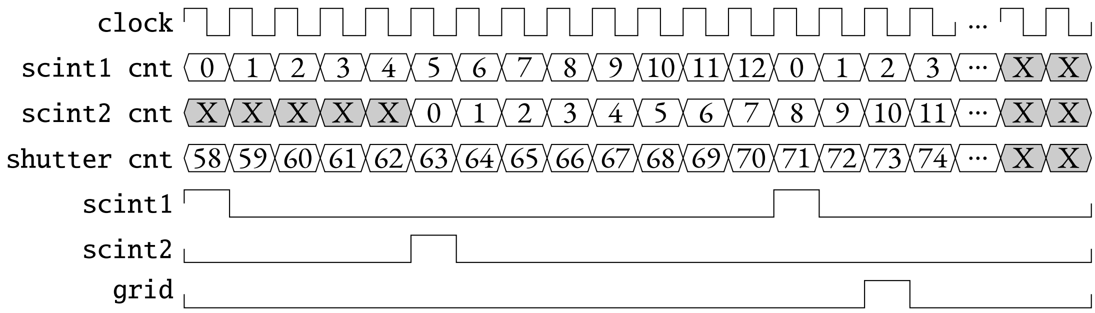

Figure 8.14: Timing diagram of the veto implementation. When the shutter opens a counter is started in order to close the shutter after the desired time. If, while the shutter is open, one of the two scintillators (`szint1`, `szint2`) registers a hit the respective counter (`szint1 cnt`, `szint2 cnt`) is set to 0 and the counting starts with the 40 MHz clock. This counter will count for a maximum 100 µs. If the scintillator triggers a second time the counter is set to 0 again (see `szint1 cnt`). If on the grid a signal is detected (`grid`), a routine is started to close the shutter and to send the counter values of the two scintillators as well as the time the shutter was open (`shutter cnt`) to the readout computer. All three values will be saved and sent after the shutter is closed. In order to allow the current in the pixels to flow out and therefore to get proper ToT values, the routine waits a selectable amount of time before closing the shutter and reading the chip out.

If the veto function is activated via the command (`20`) on the FPGA it can be currently used in functions `13` or `16`. If for example `16` is used first all necessary counters are initialised to 0. Then, if one of the scintillators registers a hit the respective counter is started and can in principle run for 100 µs (this results in a counter value of `4000`). If in this time neither another hit on the scintillator nor a trigger from the FADC is registered the counter is stopped and set to a value of `4095` meaning it reached overflow. The time of 100 µs is chosen since a muon hit will produce a signal on the grid earlier and fluorescence induced by muons will extremely unlikely last longer ($\tau \leq \mathcal{O}(\text{ps})$) [DH82] in the detector. However, if another signal reaches the scintillator then the counter is set back to `0` and the counting starts again. This can be seen in figure 8.14 as an example for `szint1`. During the measurement with very long open shutter times this may even happen several times to both scintillators. If at some point the FADC trigger arrives while the shutter is open, a routine is started to save the scintillator times and the time the shutter was open, and send this information to the computer. For this, first of all, a veto signal is set so the counters of the scintillators cannot be set back by a newly arriving signal. Then the time the shutter was open as well as the times between the last hit in each scintillator and the time the shutter closes are saved. Then a number of clock cycles, defined via TOS (the default is `200`), is waited in to allow for the drift of the electrons through the detector and for the charge to be drained by the pixels to get a proper ToT count. After this, the values are sent as a 56 bit package to the computer where it is handled by the TOS. The order of the package is shown in figure 8.15. Then the chip is normally read out. If no grid signal triggers the readout to be stopped earlier then the trigger points of

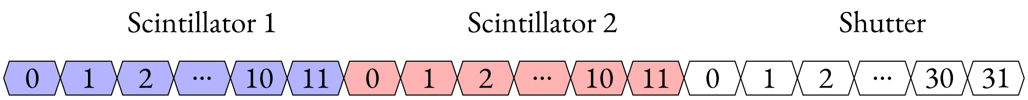

Figure 8.15: Data structure of the 56 bit containing the timing information of the scintillator vetos. The 32 bit shutter time contains the time the shutter was open in clock cycles. The two 12 bit scintillator times contain the time between the last scintillator trigger and the closing of the shutter.

the scintillators are not written and therefore not sent to the computer. However, in order to know if the scintillator is triggering at all, the overflow value of `4095` is, if reached, saved and written back to the computer. Hence, for long shutter times, this is a good handle to see if the scintillators are set up correctly and working as expected.

CHAPTER 9

The CAST detector lab

9.1 Measurements at the CAST detector lab

In order to measure the properties of the detector over a wide range of energies a variable X-ray source is necessary. Such a system is provided within the CAST detector lab (CDL). The X-ray source is set up in a vacuum system with a valve at the end in order to mount a detector for tests. The source can then be set to different energies. For measurements with the presented detector eight energies in a range from 0.277 keV to 8.04 keV were selected. This range is relevant for the detector's purpose of searching for axions at CAST. The data was analysed within a master thesis [Sch19b] and a PhD thesis [Sch24a]. In the following a brief overview of the CDL and the results shall be given.

9.1.1 The CAST detector lab

Figure 9.1: Picture of the CDL. Main parts are labeled. Taken from [Sch24a].

The CAST detector lab (CDL) shown in figure 9.1 is a variable X-ray source providing beams of X-rays at different energies by using a system of different target and filter combinations and an electron source with an adjustable high voltage. By combining a target and a filter with a fitting high voltage, certain fluorescence lines of the targets can be selected to get a more or less mono-energetic X-ray beam by filtering out lower energies using an appropriate filter material. The whole X-ray generator is mounted in a vacuum system to allow for very low energetic X-rays. The detector is positioned at the end of the vacuum system sealing it with the entrance window. In order to allow for the necessary slow pumping while using the ultra-thin window, an additional bypass was added to the vacuum system of the CDL containing a needle valve.

9.1.2 Measurements

After the setup of the detector the eight voltage target filter combinations shown in table 9.1 were used for the data taking. The selected energies span the energy range interesting for the searches for axions.

Voltage	Target	Filter	Fluorescence line	X-ray energy
0.6 kV	Carbon (C)	EPIC	C K$\alpha_{1,2}$	0.277 keV
0.9 kV	Copper (Cu)	EPIC	O K$\alpha_{1,2}$	0.525 keV
2 kV	Copper (Cu)	EPIC	Cu L$\alpha_{1,2}$	0.93 keV
4 kV	Aluminium (Al)	Aluminium (Al)	Al K$\alpha_{1,2}$	1.49 keV
6 kV	Silver (Ag)	Silver (Ag)	Ag L$\alpha_{1,2}$	2.98 keV
9 kV	Titanium (Ti)	Titanium (Ti)	Ti K$\alpha_{1,2}$	4.51 keV
12 kV	Manganese (Mn)	Chromium (Cr)	Mn K$\alpha_{1,2}$	5.89 keV
15 kV	Copper (Cu)	Nickel (Ni)	Cu K$\alpha_{1,2}$	8.04 keV

Table 9.1: Voltage, target, and filter combinations, and the resulting fluorescence line energies used for the detector calibration in the CDL. (The filter material EPIC was developed for the XMM-Newton space mission and is a combination of polyimide and aluminium [BGS+16])

Thus, with this data set the detector can be calibrated to a sufficient level. After the data was taken, cuts were applied to every data set to only select events reproducing the energy of the selected fluorescence line (for details see [Sch24a]). With the obtained data set one can now calculate properties of interest. Here, the behaviour of the energy resolution shall be discussed first. The determination of the energy resolution is described in section 13.5. The results for the different energies can be seen in figure 9.2. The plot shows that the energy resolution is roughly following as expected a $1/E$ distribution. However, larger discrepancies can be observed towards lower energies. Also, the spread within different data sets taken at single energies shows that the detector was not working stably over the data taking. This might be an effect due to changes in the ambient temperature during the data taking.

For the lowest energies, the resulting energy resolution is $\epsilon_{0.277\,\mathrm{keV}} \approx 30\%$ while for larger energies its getting closer towards $\epsilon_{8\,\mathrm{keV}} \approx 7\%$. This is compatible with the results obtained in [Kri18].

Finally, the data later used to calculate the likelihood in order to estimate the background of different detectors (see chapter 14) shall be briefly discussed. To calculate the likelihood probability distributions at different X-ray energies are necessary (called reference distributions). For the likelihood three cluster properties are used and their probability distributions are shown in figure 9.3. It can be seen that for the selected properties all distributions show a similar behaviour of getting narrower with rising energy. At low energies, especially for the property called `fractionInTransverseRMS` it can be noticed that the distribution is not very smooth anymore and shows even some prominent peaks (e.g. at 0) occurring from the integer nature and very low number of electrons.

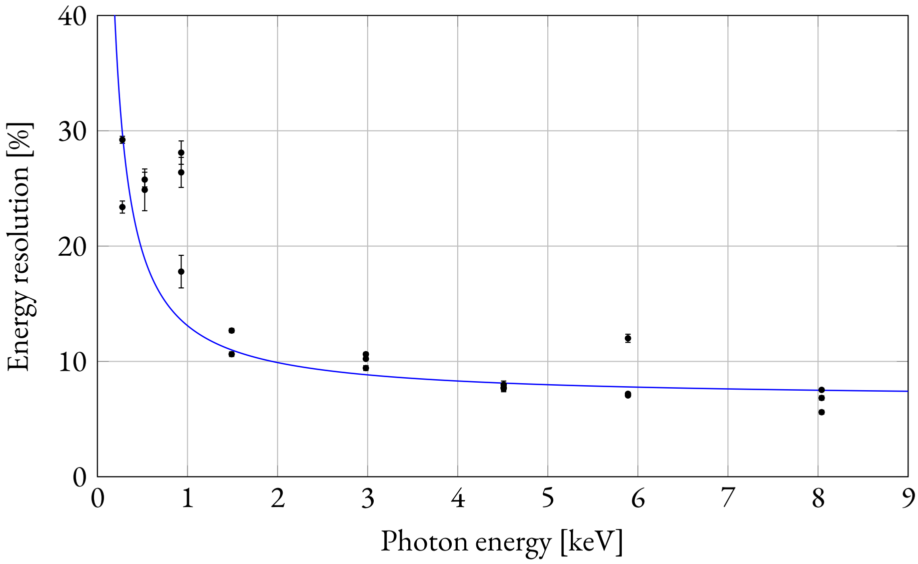

Figure 9.2: Energy resolution obtained from the CDL measurements. The data follows roughly the expected $1/E$ behaviour indicated in blue, albeit larger discrepancies can be observed at low energies. Also seen from the multiple data sets taken for some energies a large spread can be observed not reflected by the error bars. Data taken from [Sch24a].

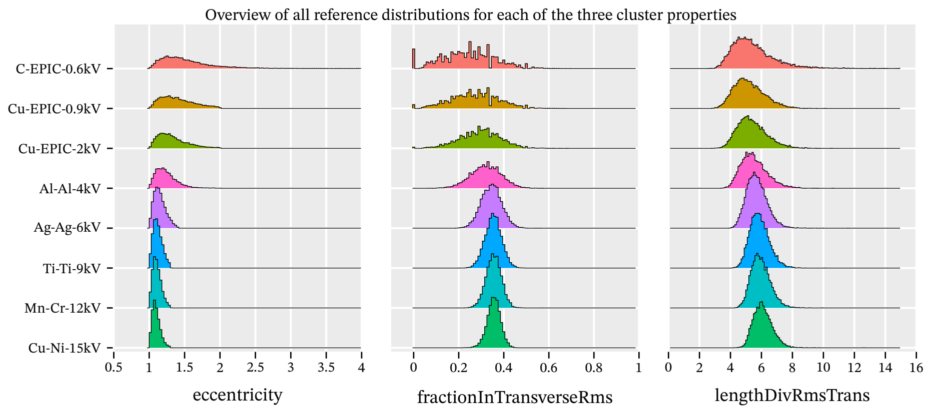

Figure 9.3: Distribution of all properties used for the likelihood method. Taken from [Sch24a].

CHAPTER 10

A versatile Timepix3 readout system

In order to build a GridPix3 detector for IAXO first a versatile readout platform for Timepix3 needed to be developed. For this, a simple GridPix3 detector was developed to test the readout. The design of the detector is similar to the design of the CAST detector and therefore multiple parts can be reused. The detector, developed as a general purpose detector is currently used for general tests and verifications as well as for X-ray polarimetry. First, the hardware of the detector shall be introduced in section 10.1 before a brief introduction to the firmware will be given (section 10.2). After that, in section 10.3 the software will be described focusing especially on the features of the user interface (UI) and how it interfaces with the scan functions. Finally, in section 10.4, a validation of the system will be performed showing its reliability.

10.1 The hardware

The detector consists of two major parts, the electronics to operate the Timepix3 or GridPix3, and the detector housing or mechanical design, necessary to use it with a GridPix3. In the following first the electronics will be described and then the mechanical design.

10.1.1 Electronics

The readout for the chip consists of four different electronic components. The first is the front-end concentrator (FECv6) [TME+11]. The FECv6 is a multipurpose FPGA board with a PCI outline slot to support different readout systems. It has two 1-GBit Ethernet connections for communication with the readout computer. Plugged into the PCI slot of the FECv6 the adapter card is the next part of the readout electronics. The adapter card features three DisplayPort (DP) connectors and connects them via low-voltage differential signaling (LVDS) signal drivers to the FPGA pins. Hence, the adapter card is only forwarding the signals from PCI to the DP connectors and vice versa. The next stage would then be connected via three DisplayPort cables (one data in and two data out) to the Intermediateboard. On the Intermediateboard the DP connectors are then routed to the connector for the chip carrier. Here the groups of LVDS input line pairs and output line pairs are each time-matched to keep the clock and data synchronous. This is separately done for the Intermediateboard and the chip carrier. This allows for easier changes on the PCBs since as long as it is matching on the new PCB the full system is matched. Additionally, in the output lines LVDS signal drivers are implemented to allow

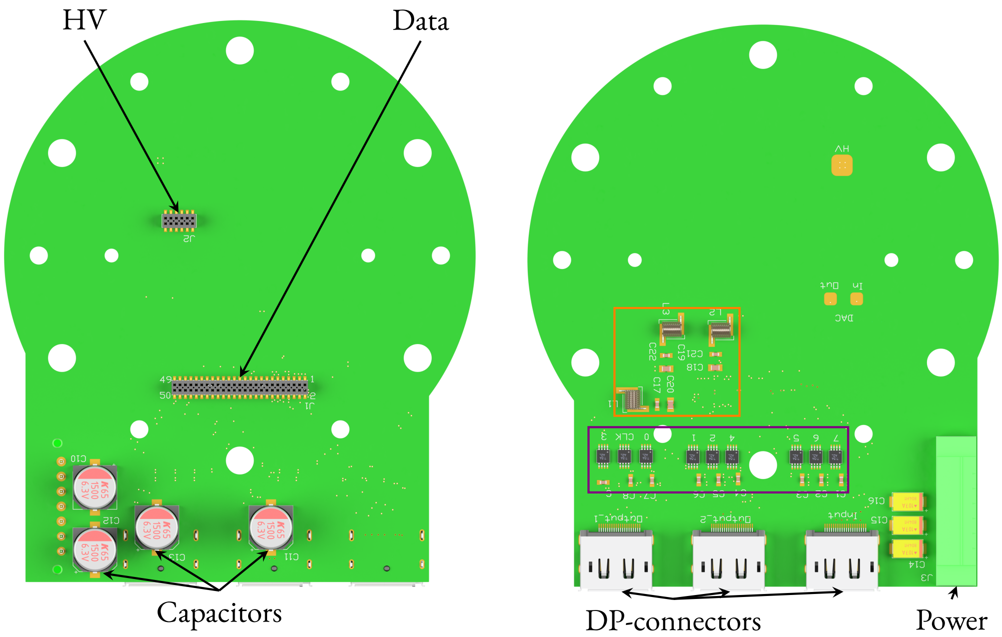

(a) Top (b) Bottom

Figure 10.1: The top (a) and the bottom (b) side of the GridPix3 Intermediateboard. On the top side, only the connectors for the chip carrier (data, HV) can be seen as well as four large capacitors for buffering the input power. On the bottom side, the three DP-connectors for connection to the FPGA, the power connector, the LVDS signal drivers (purple box), and the passive filters (orange box) can be seen.

for long distances between the detector and the adapter card/FPGA. As shown in figure 10.1 the Intermediateboard serves as a connector between the adapter card and the chip carrier. At the same time, it is also part of the detector volume for the GridPix3 detector as it serves as the bottom of the gas volume. The Intermediateboard also contains the voltage supply lines for the Timepix3 and the high-voltage supply lines for the GridPix3. For the power supply seven large capacitors and three passive filters are implemented. The main purpose of the large capacitors is to buffer large current changes from the chip carrier. This is required in particular if long connection lines between the power supply and the Intermediateboard are used. Therefore, the two 1.5 V power lines for the Timepix3 (VDD (digital part), VDDA (analog part)) contain two 1.5 mF and one 100 µF capacitors each. This will stabilise the voltage over a wide range for ´slow´ changes in the current drawn by the Timepix3. For the auxiliary power (3.3 V), needed to power the signal drivers on the Intermediateboard, a 100 µF capacitor is implemented. After the buffering capacitors the power line for the phase-locked loop (VDDPLL) on the Timepix3 is split from VDDA. Into all three power lines for the Timepix3 a low-pass filter as shown in figure 10.2 is implemented. These filters have a cutoff frequency of $f_{\mathrm{cut}} \approx 160\,\mathrm{kHz}$ and therefore reduce high frequencies coupled into the power lines. Here, it shall be mentioned that the large capacitors in front of the filter will have nearly no impact since the circuit is driven by a voltage source having a very low impedance. On the other side, the capacitors and inductances on the chip carrier will influence the filter depending on the load of the Timepix3. The chip carrier as seen in figure 10.3 contains the Timepix3 on top and on the bottom side 21 capacitors (9 for VDD[$C_{\mathrm{total}} = 148.8\,\mathrm{nF}$], 9 for VDDA[$C_{\mathrm{total}} = 148.8\,\mathrm{nF}$], and 3 for VDDPLL[$C_{\mathrm{total}} = 23.36\,\mathrm{nF}$]) for the compensation of

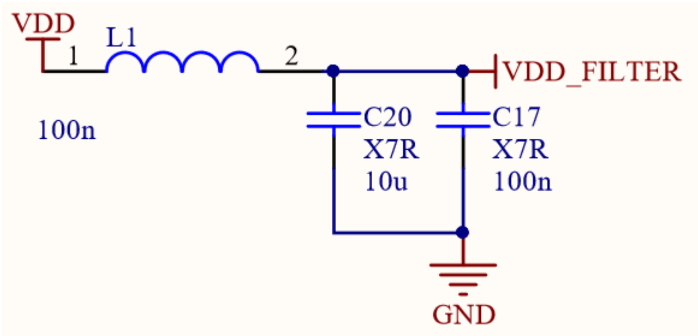

Figure 10.2: Schematic of the passive filter design. Three of these filters are implemented in the power supply for the Timepix3.

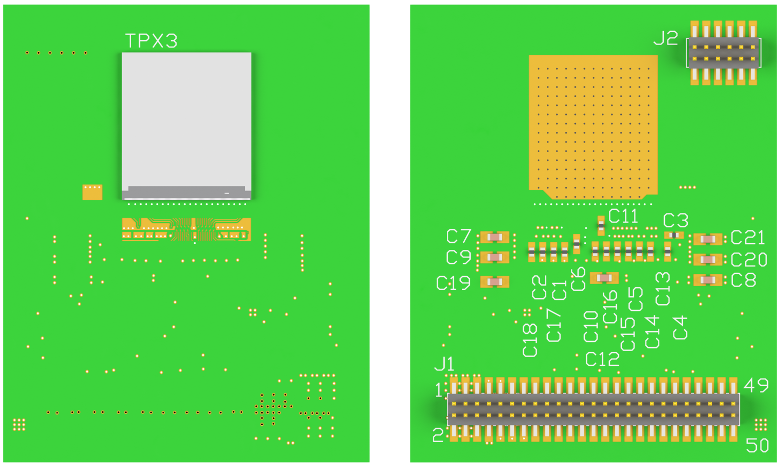

(a) Top

(b) Bottom

Figure 10.3: The top (a) and the bottom (b) side of the Timepix3 chip carrier. On the top side, only the chip is mounted to avoid additional components making it more versatile for mounting in detectors (e.g. placement of parts on chip level). On the bottom side, capacitors and the connectors for data + power (50 pin connector) and for high-voltage (12 pin connector) (only needed for GridPix3) can be seen.

current spikes drawn by the different power networks. Of course, also the two plugs (data, HV for GridPix3) to connect to the Intermediateboard are on the bottom side. As mentioned before these capacitors will add to the filter, but since they are very small compared to the 10.1 µF of the filter, the change is in this case negligible. A difference might come from the bond wires of the Timepix3 since they introduce an additional inductance to the filter. The inductance of a bond wire can be estimated, as a rule of thumb, via [GGC81]:

$$L[\mathrm{nH}] = 5.08 \times 10^{-3} \cdot 39.37 \cdot l \left(\ln \left(\frac{4l}{d} \right) - 1 \right), \tag{10.1}$$

with l as the length of the bond wire and d as the diameter of the bond wire in mm. With this a 5 mm long bond with a bond wire diameter of 25 µm has an inductance of 5.68 nH. For VDD fifteen bond wires are connected to the chip and for VDDA sixteen, hence the inductance for those lowers to 0.38 nH and 0.36 nH respectively. Since these values are also small compared to the 100 nH filter inductance the change of the cut-off frequency is again negligible. Hence, the design values for the filter seem reasonable.

To conclude the electronics, reasonable choices for power buffering and filtering have been made and the system showed no problems so far. With these electronics a basic detector with the Timepix3 can already be operated.

10.1.2 Mechanical layout

To use the electronics in combination with a GridPix3 and therefore as a gaseous detector a mechanical setup needs to be built atop the Intermediateboard. The mechanical layout is developed closely to the design presented in [Kri18]. This was done to allow the reusage of different parts as well as to be able to compare results. As seen in figure 10.4 there are some differences to the detector described in chapter 8. However, the working principle of the detector is similar. The base of the detector is the Intermediateboard serving as the readout board and the bottom of the gas volume. Onto this, a holder made from polymethylmethacrylate (PMMA) is mounted in such a way that the chip carrier fits right into it and the anode can be mounted on top. The anode is important for the usage as a gaseous detector since it reduces the field distortions between the grid and the cathode. Thus producing a homogeneous drift field above the GridPix3. The anode is produced from 0.8 mm thick FR4 covered with a layer of copper. In the centre of the anode, a hole slightly larger than the active surface of the GridPix3 is milled. From the bottom side the area where the bond wires of the GridPix3 are the material is thinned as much as possible in order to mount the anode as close to the grid as possible. However, the leftover material still needs to insulate the bond wires from the anode. Around the anode mounted on the Intermediateboard, the drift ring made from PMMA defines the gas volume of the detector. The drift rings are exchangeable to match different use cases. Typically, as the height of the drift volume 3 cm is chosen. For this height and only a single GridPix3 mounted in the detector a field cage is not necessary, simplifying the detector. The drift ring also contains the gas connections to provide a constant gas flow through the detector. The gas connectors made from brass are pushed in the holes in the drift ring and are sealed with two O-rings each. On top of the drift ring the copper cathode is mounted containing a thin but conductive window (see chapter 7) in the middle above the GridPix3. The drift ring is sealed to the cathode and the Intermediateboard with a standard O-ring. Additionally, two O-rings are used to seal the two screws fixing the anode holder to the Intermediateboard. The final detector can also be seen in figure 10.5 with the cathode removed, in this view the connection of the anode to the high-voltage supply line can be seen. The red cable is soldered to the top of the anode and connected to a feedthrough glued into the drift ring. The high-voltage can then be connected from the outside of the drift ring.

10.2 The firmware

The connection between the Timepix3 and the readout computer is done via an FPGA. To use the FPGA a firmware is needed to take care of sending and receiving data to the Timepix3, as well as sending and receiving data via Ethernet from or to the readout computer. The data received has to be rearranged to fit the data format expected by the receiver. The firmware used for the Timepix3 readout is based on `Basil` [SiL] and therefore very different from the firmware described in section 8.3. A block diagram of the firmware is shown in figure 10.6. The communication via Ethernet to the computer is controlled

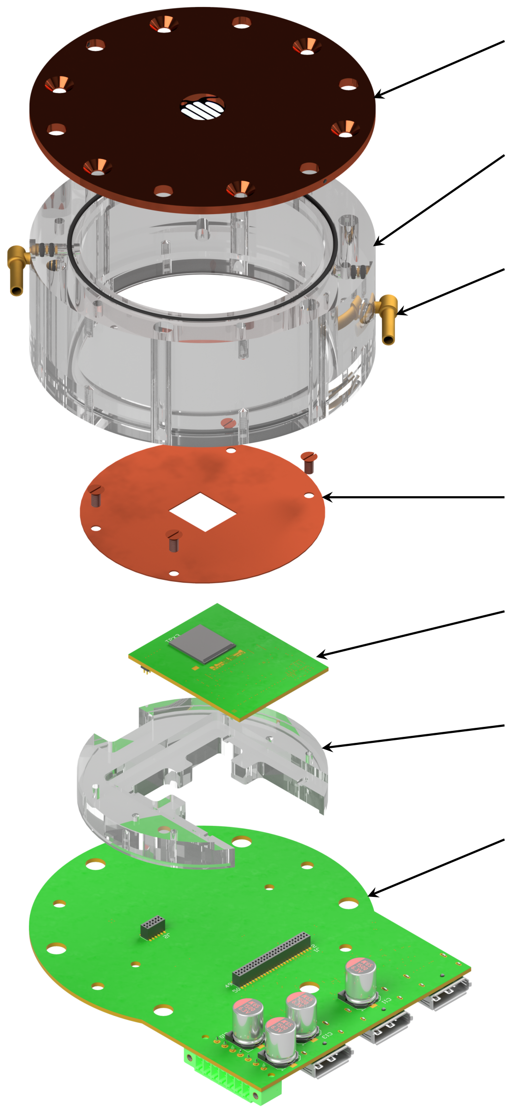

Figure 10.4: Exploded view of the multi-purpose detector design. The design is very similar to the design presented in [Kri18]. The Intermediateboard builds the bottom of the gas volume whereupon the anode holder, the chip carrier, and the anode are mounted. Defining the gas volume the drift ring is mounted to the Intermediateboard and closed with the cathode containing the X-ray entrance window.

by a TCP core handling transmitted and received data. If data is received, first the TCP core looks in the header if the data is for the Timepix3 or if it is control data for the FPGA control block. Data for the Timepix3 is collected until the full data package is collected (see chapter 4) and then sent synchronised with the clock to the Timepix3. The clock (40 MHz) is produced by a clock generator (Clk gen) on the FPGA and is constantly sent to the Timepix3. If control data is received the data is processed in the control block. There, either slow control pins (e.g. reset) are set or for example, a time stamp extension is activated.

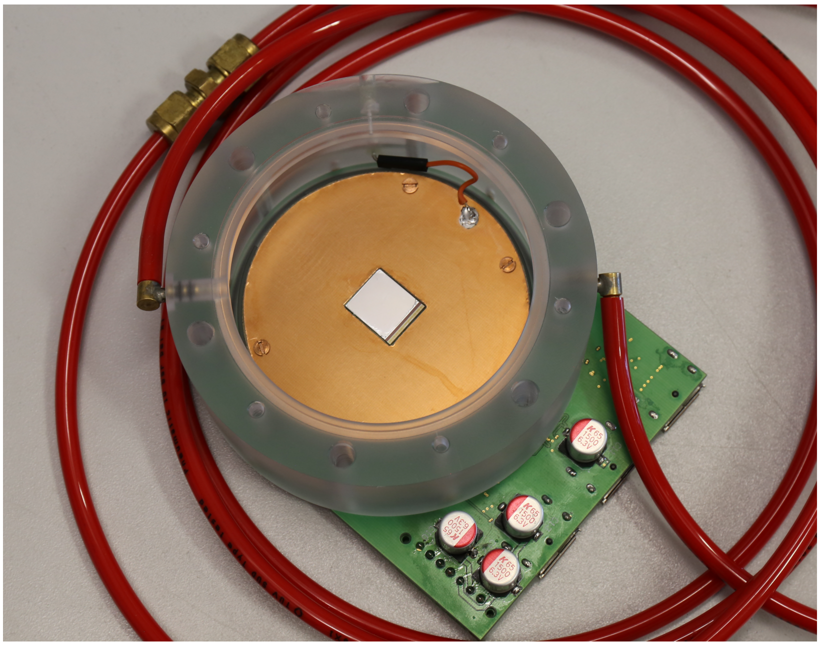

Figure 10.5: Picture of the detector with the cathode removed; the GridPix3 can be seen in the middle. On the right of the anode, the high-voltage connection can be seen. Gas would be connected via the red tubing entering the drift ring from left and right.

The time stamp extension is needed since the time stamp (ToA) of the Timepix3 is only a 14 bit register and therefore at a clock frequency of 40 MHz the overflow is reached after 409.6 µs. Albeit this being sufficient for most cases where a triggered readout is used, if the data is read data-driven one can quickly run into problems differentiating clusters. Therefore, on the FPGA a synchronous 48 bit counter can be activated and added to the data stream via an arbiter extending the time stamp to a period of 81 days. To reduce the amount of data sent, the time stamp extension is only added to the data stream about every 100 µs.

The Timepix3 will then send data on up to eight links to the FPGA. This data is first processed by a 8 bit/10 bit decoder and then buffered by the link first in first out buffer (FIFO). For each link one FIFO is available. Here a data synchronous clock is provided by the FPGA. This is necessary since the output data of the Timepix3 is sent with up to 320 MHz double data rate provided by a clock generated via a phase-locked loop on the Timepix3. To sample this data a clock with at least double the frequency is necessary. In the scope of the presented readout, only 160 MHz double data rate is implemented and used. From the link FIFO the data is sent in 8 bit words into a clock domain crossing FIFO where the data is synchronised to the FPGA clock. From this FIFO the data is sent to the output buffer. If the time stamp extension is activated an arbiter adds the extensions to the data stream. The TCP core then takes the data from the output buffer and sends it to the readout computer. If errors occur in this chain(e.g. a FIFO reaches its size limit and data gets lost) an error is raised to the control block. These errors are then sent to the readout computer for further processing by the software.

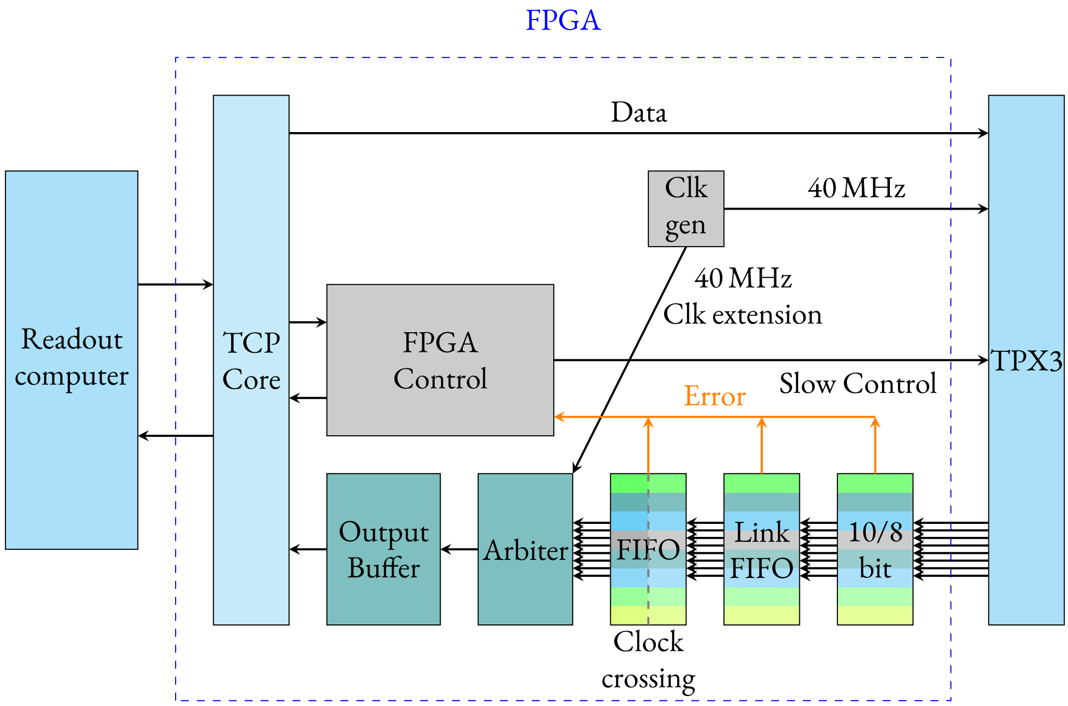

Figure 10.6: Block diagram of the firmware. The Timepix3 firmware has a TCP core to communicate with the readout computer. This core takes care of all Ethernet data and forwards them to their destination. The Timepix3 can send data through up to eight links. First, each link is 8 bit/10 bit decoded and then buffered in the Link FIFO. After that, the data crosses the clock domain from the clock synchronous to the chip output to the internal FPGA clock. Depending on the settings then an arbiter adds an additional time stamp before the data is stored in the output buffer, ready to be sent to the readout computer. If problems within the data processing happen, the impacted block reports errors to the control block, to be sent to the computer.

10.3 The software

The software, similar to the firmware is also based on `Basil` [SiL]. From `Basil` the base communication with the FPGA is used. In order to communicate with the Timepix3 everything chip specific had to be implemented. A block diagram of the software is shown in 10.7. To communicate with the FPGA (with the Timepix3) the `tpx3 class` is used. The `tpx3 class` contains all low-level communication functions needed for the Timepix3 as well as functions to handle the data received from the FPGA. This data contains Timepix3 data as well as communication data from the FPGA (errors etc.). The data received from the FPGA is processed, as an intermediate step between the FPGA and the `tpx3 class`, within a `FIFO reader`. The `FIFO reader` pulls the data from the FPGA when the computer is ready to receive the data and stores them in a data queue. The `tpx3 class` reads them from this queue and divides the data into errors and Timepix3 data. The errors are provided for further use by the scans, while the Timepix3 data is further processed. First, the data packages received from the FPGA (two network packages per Timepix3 data package) are stripped so only the Timepix3 data is left over and then combined back to the original 48 bit word produced by the Timepix3. In the next step, the data needs to be decoded depending on the type of data (data, commands). The type of data is encoded in a

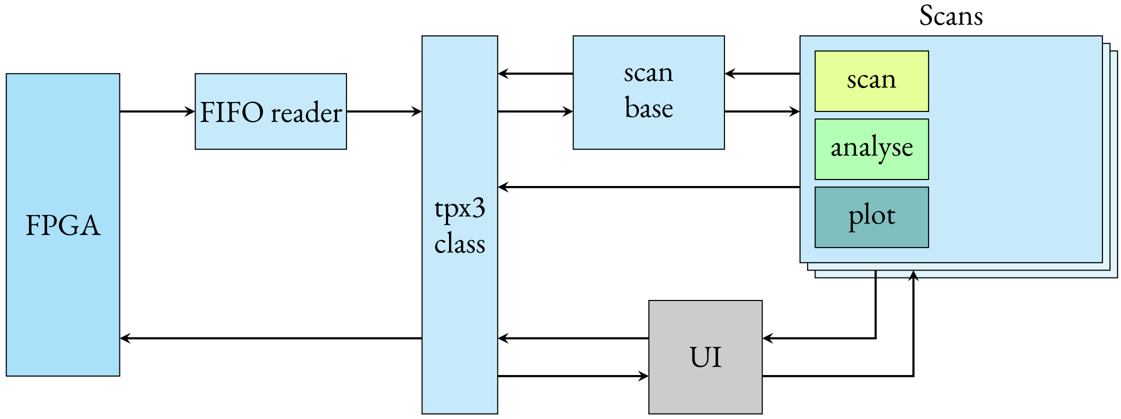

Figure 10.7: Block diagram of the software. The operation software consists of three main blocks, the `tpx3 class` preparing the base communication with the chip, the scans, and the `UI`. The scans so far contain nine different scans containing calibrations as well as the initialisation of the chip and the data taking. All scans communicate via the `scan base` with the `tpx3 class`. The `scan base` contains general functions to save data and functions used by multiple scans. The scan base is then communicating with the `tpx3 class` sending and receiving data from the FPGA. The `UI` as the user backend allows to start and configure scans as well as to change settings of the FPGA.

3 bit header (see [LP15]), after reading this the data can be decoded depending on its type. For pixel data for example this is the pixel address, the ToT value, the ToA value, and if activated the fToA value. The decoded data is then further processed within the active scan. For data to be sent to the Timepix3 the `tpx3 class` produces the necessary headers, commands, and adds the data. A typical input data package is shown in figure 4.3. According to this scheme the data stream is produced, sent to the FPGA and from there forwarded to the Timepix3.

The data needed for the input packages and the further procession of the data received from the Timepix3 is done by the `scans`. The `scans` are communicating via the `scan base` with the `tpx3 class`. The `scan base` takes care of saving data into HDF5 files, processing errors from the FPGA and providing functions generally used by multiple scans like producing mask files for scans or controlling the shutter. The scans themselves are subdivided into three steps each, first the `scan`, then the `analysis` of the results, and last the `plotting` of the results. So far nine different scans have been implemented and a description is given in section 10.3.1. In the `scan` phase, a scan is communicating with the `scan base` to set the Timepix3 according to its needs and taking the necessary data. The taken data is then analysed and the results are saved as an HDF5 file. Then the data is plotted.

To control the Timepix3, start scans, and take data all necessary functions are interfaced by a user interface (UI). The user interface is separated into a command line interface (CLI) and a graphical user interface (GUI). Both interfaces allow for full control over the Timepix3, hence it connects to the `scans` as well as to the `tpx3 class`. The UI and its functions are described in 10.3.2

10.3.1 Scans

The scans were implemented in the scope of [Gru]. There are nine scans implemented including the initialisation of the chip and the data taking command (called run). In the following, the functionality of all scans shall be discussed shortly. All scans except for the initialisation take initial parameters defined by the user. Within the parameters of all scans using test pulses one parameter is called `iterations`. This parameter sets how many steps are needed to scan every pixel in the matrix. For each step then a chip mask is created using a subset of pixels for the scan (e.g. for a value of 64 each eighth pixel by row and column is used, and the rest is masked). Using this is necessary for scans with the test pulse source for two reasons: First, the internal test pulse source cannot supply all pixels with equal test pulses at the same time. Second, there can be crosstalk between neighbouring pixels, especially when the test pulses are high. Hence, values below 64 are not a good choice for a trustworthy calibration. The scans shall be now shortly described in the typical order they would be performed to start a data taking campaign.

- **Init** The initialisation is the first scan called to start up a Timepix3. The scan first checks if the FPGA is properly connected and if a Timpix3 is connected. For the Timepix3 it is then checked how many of the eight links are connected and the clock for the data receival is adjusted to the incoming data. This adjustment is made using the standard pattern the Timepix3 is sending on all active links when running in idle mode. For each link then a configuration is saved and all proper working links are activated. After that, the Chip-ID is read from the Timepix3, by sending the E-Fuse read command (reading back the Chip-ID), and assigned to the links (important in preparation for a multi-chip readout). The Chip-ID and the number of active links is then provided to the UI for display.

- **Pixel DAC opt** The pixel DAC optimisation is needed to allow for a proper equalisation of the pixel matrix. The pixel DAC sets a current source supplying the pixels threshold DAC. Since the pixel threshold DAC only has 4 bits the supplied current has to be matched with the threshold spread of the pixel matrix. This can be done by measuring the response of the pixel matrix at the pixel thresholds of 0 and 15 respectively. To measure the response a number of test pulses is sent to every sixteenth pixel for a set of global thresholds. Then, for each used pixel the response is fitted with a z-curve function in the form of

$$z(x, A, \mu, \sigma) = -0.5A \cdot \operatorname{erf}\left(\frac{x-\mu}{\sqrt{2}\sigma}\right) + 0.5A\,. \tag{10.2}$$

  Here A is a scaling factor, erf() is the error function, μ is the slope centre and σ is the steepness of the z-curve. By taking the μ value for all used pixels for either the pixel thresholds of 0 or 15, one gets two gaussian distributions. For the ideal pixel DAC value these distributions should overlap so the pixels with the highest threshold response at a pixel threshold of 0 are overlapping the pixels with the lowest response at a pixel threshold of 15. Then, over the full range, all pixels can be equalised. This overlap is defined in the scan to be at $3.3 \cdot \mathrm{rms}$ to reduce the influence of extreme outliers. This is done by iterating over different pixel DAC values. To calculate the next step for this the difference between the means and the sum of the rms values of the gaussian distributions are used:

$$n_{\text{next pixel DAC}} = n_{\text{pixel DAC}} + \eta \cdot 3.3\left(\mathrm{rms}_0 + \mathrm{rms}_{15}\right) - \eta\left(\mathrm{mean}_{15} - \mathrm{mean}_0\right)\,, \tag{10.3}$$

  with η being the relative change of the difference of the means with respect to the pixel DAC value calculated from the previous iteration. These calculations are done until $n_{\text{next pixel DAC}} = n_{\text{pixel DAC}}$, hence the value is found. After the scan the value is forwarded to the UI and directly set to the Timepix3.

- **Equalisation** The equalisation is performed in order to set the pixel threshold DAC such that the response of every pixel is as similar as achievable. This is important since small differences in the pixels are not avoidable. To perform this, two approaches are possible and implemented. A noise-based approach and a charge-based approach. For the charge-based approach, similar to the pixel DAC optimisation, a number of test pulses are injected into the pixel over a range of thresholds. This is done for each pixel for pixel thresholds set to 0 and 15. Then all the z-curves are fit and the resulting μ values are again used to find the means of the resulting distributions. Since the pixel DAC optimisation already has shifted both distributions such that they overlap, one can simply map the range of the pixel thresholds to the distance of the two means and then calculate the pixel threshold for each pixel via

$$\mathrm{THR}_{\mathrm{pixel}} = 8 - \left(\mu_0 - \mathrm{mean}_0 \frac{16}{(\mathrm{mean}_{15} - \mathrm{mean}_0)}\right). \tag{10.4}$$

  After this calculation values lower than 0 and higher than 15 will be clipped to 0 or 15 and saved. The equalisation is saved as an HDF5 file and the path of the equalisation is set so it will be loaded when needed. The noise-base approach is similar to the charge-based approach, just instead of calculating the threshold mean values from the injected charge, the noise peak is used.

- **Noise scan** The noise scan scans over a given range of the global threshold to find the lowest global threshold value at which the chip operates mostly noise free. To scan this for each threshold in the set range the shutter of the Timepix3 is opened for a given time of 10 ms. Then the pixels are read out and the number of active pixels as well as the number of total hits are saved. Then two plots are produced showing the number of active pixels per threshold and the number of total hits per threshold. The plots are saved and the user has to decide what threshold value fits the application. One may also decide to mask pixels showing constant noise.

- **Threshold calibration** The threshold calibration is necessary to convert a set global chip threshold into the corresponding number of electrons. For this, a number of test pulses are injected into the pixels. This is typically done for five different test pulse heights. These injections are then performed over a range of global thresholds. For each pixel and test pulse height a z-curve is fitted to the data to get the mean threshold. The mean thresholds per pixel are then put in a histogram and a gaussian distribution is fitted. The mean and the standard deviation are then defining the threshold corresponding to the injected pulse height. The results from all pulse height iterations are then fitted with a linear fit to get a calibration curve.

- **ToT calibration** The ToT calibration is needed in order to assign a charge to a measured ToT value. To perform this a range of test pulse heights is sent to the chip and the responding ToT values are analysed. For each test pulse height, ten test pulses are sent to each pixel. For the analysis first the mean ToT value per pixel is calculated. Then, all pixels which detected less than ten test pulses are discarded. After this, it is checked if for the given test pulse height more than 60% of the pixels are active. If this is the case the mean over all active pixels is built. Thus, giving the ToT value corresponding to the injected test pulse height. After performing this for all scanned test pulse heights a fit of the form

$$f(x, a, b, c, t) = ax + b - \frac{c}{x - t} \tag{10.5}$$

is performed to these results. The fit consists of a linear part towards large ToT values (a,b) and a curved part for small ToT values (c,t). However, the curved part (c,t) is not very distinct within the data for Timepix3. The results and the data are then saved as a HDF5 file for further use as well as plotted for monitoring.

For the usage within the analysis, the test pulse heights have to be converted from a voltage to the number of injected electrons. Since the test pulses are always injected via a test pulse capacitance $C_{\mathrm{test}} = 3\,\mathrm{fF}$ into the pixel, one can calculate the corresponding number of electrons via

$$Q_{\mathrm{pulse}}[e^-] = \frac{C_{\mathrm{test}} U_{\mathrm{pulse}}}{\mathrm{e}} . \tag{10.6}$$

- **Threshold scan** The threshold scan is used for validation of the equalisation and the pixel DAC optimisation. For the scan for each global threshold value a given number of test pulses are injected into the pixels. The z-curve is fitted to the data for each pixel and the means from the z-curve are plotted as a histogram. This histogram shows above which threshold the pixels see the test pulses. Additionally, an occupancy map is generated showing the distribution of the threshold values over the Timepix3. This can be helpful to investigate areas with a in general lower or higher threshold.
- **Test pulse scan** The test pulse scan works similarly to the threshold scan. Only instead of changing the global threshold it uses the set threshold and iterates over a set of test pulse heights. Then, the data is again fitted but this time a s-curve is used (inverted z-curve). Similar plots are produced as for the threshold scan. From these one can see how many electrons are needed to see a signal above the set threshold and how this is distributed over the pixel matrix
- **run** The run command starts the data taking. After the chip is fully set up, the scan sets all DACs and loads the calibrations and the mask file to the Timepix3. Then, the shutter is opened for a given time or until stopped by the user (if 0 as time is set). During the run, the data is constantly written into an HDF5 file.

With those scans the Timepix3 is operational.

10.3.2 User interface (UI)

To use the system described so far a user interface is needed. The user interface combines all scans and settings of the chip with functions easy callable by the user. This is done in two different ways. A command line interface (CLI) and a graphical user interface (GUI). Both interfaces support the same functions. However, a few differences in the usage exist. Both the CLI and the GUI also use a backup system for all settings so if the system is accidentally closed or is closing due to a fault all settings can be automatically recovered. There are two types of backups possible, the temporary backup which is stored every time a scan is started. These backups are saved in a separate folder and are automatically deleted if they are older than two weeks. The other type of backups are permanent backups they can be saved by a user command and they are produced if the GUI or the CLI are closed at the end of a data taking. These backups are not deleted automatically and can be loaded to the system at any time by the user. Each backup contains all information necessary to run the chip (Chip ID, DAC settings, paths to mask and equalisation files, etc.).

In the following, the CLI and the GUI will be described in detail working out the characteristic features.

Command line interface (CLI)

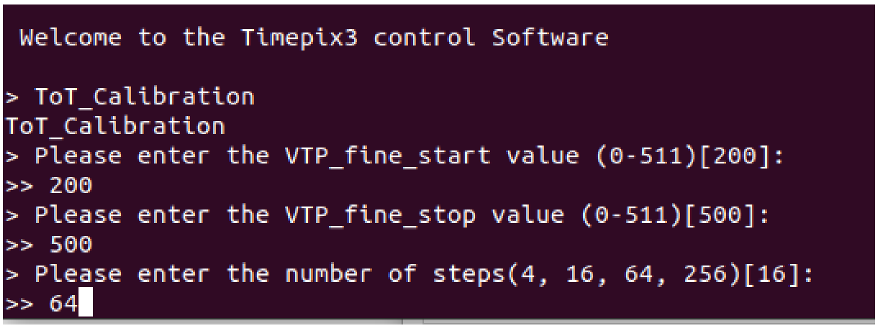

Figure 10.8: The Timepix3 CLI interface with the inputs for a ToT calibration. Behind every needed input there is a suggestion in square brackets which is typically a useful value. If the last value had been entered the scan would have started, showing a progress bar and what operation is currently running.

The command line interface (CLI) can be started in the shell and uses no graphic backend, hence it can also be operated remotely using low bandwidth connections. The CLI itself can be operated via commands given by the user. In the CLI 38 commands are implemented allowing for full control. For each command there is a subset of different spellings as well as short forms implemented (e.g. the ToT calibration can be started via [ToT, ToT_Calibration, tot_Calibration, or tot]). To get an overview of the implemented commands, there is also a help implemented showing the user one command per possible operation. If an operation is selected the CLI will ask for the necessary parameters. Here for each parameter the possible range will be given and the input will be checked to match the requirements. For the ToT calibration first the starting pulse height will be asked then the stopping pulse height and finally the number of (mask) steps(`iterations`) to be performed on the Timepix3. This can be seen in figure 10.8. After that the scan will be started by calling the scan via a multiprocessing approach. This is necessary to keep the CLI usable while the scan is running.

Since the CLI allows the user to change all chip settings and shows the commands in a help context, a small subset of operations is only available within an expert mode. The expert mode can be accessed from the CLI by typing `expert` this allows the user to six additional settings. However, for normal operation, these settings don't need to be changed.

A characteristic feature of the CLI is the possibility of scripting commands. This can be used to run sets of scans or runs on the detector without supervising them. To script a command the CLI is started with the set of commands as an option. For each command, the command itself as well as all necessary parameters have to be given separated by spaces. Multiple commands are concatenated with the + character. For example, run two ToT calibrations after each other, the following command needs to be written to the shell:

```
python tpx3_cli.py init + ToT_Calibration 200 500 64
+ Set_DAC 7 1338 + ToT_Calibration 200 500 64
```

This command would first start the CLI and run the `init` to initalise the readout and load all necessary data. Then, with the settings loaded from the backup a ToT calibration is performed. After this, the `Set_DAC` command would change the threshold DAC to a new value and after that, the ToT calibration is performed again with the changed DAC setting. After everything is performed the CLI will automatically be closed.

To sum up, the CLI offers good potential for remote operation of a detector, allows for full control on the Timepix3, and offers the possibility to script sets of scans or runs so operation without supervision is possible.

Graphical user interface (GUI)

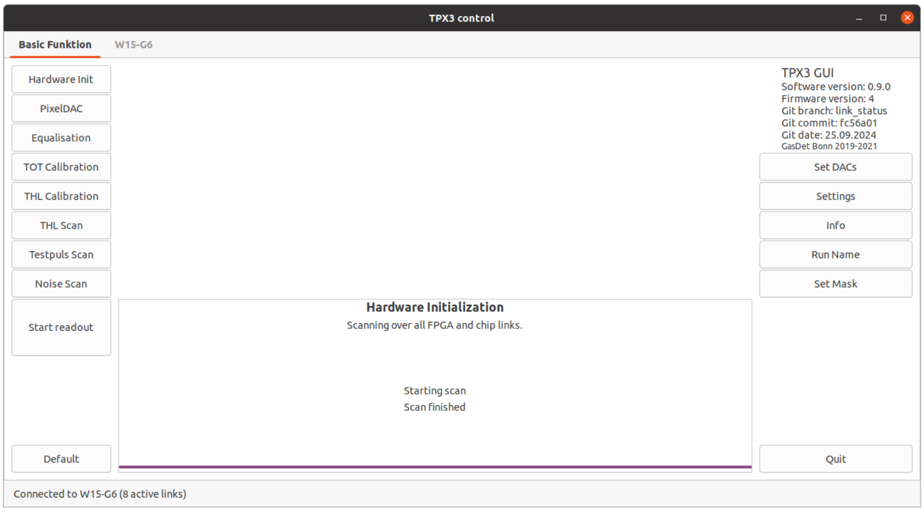

Figure 10.9: The main window of the GUI. On the left, buttons for the scans can be found. In the middle, an output shows what scan is performed or was last performed (Hardware Initialisation). Below information on the scan and its steps are given as well as a progress bar (purple). On the right first, an information block shows the currently used version of the software and firmware. Below there are buttons for settings, and the Quit button used to stop a scan or if no scan is running to quit the GUI. After initialisation the footnote of the window shows the Chip ID and the number of active links. On the top next to the tab Basic Functions, a second tab is shown with the chip name. It will show a live view of the chip data.

The graphical user interface should be the main interface for the users to the detector. The GUI is set up within the GTK-framework [Thea] as a graphic backend. If the GUI is started a window is generated (fig. 10.9) showing buttons for the most important scans and settings. Starting from the top of the window first a separation in two tabs can be seen. The figure shows the Basic Functions tab allowing for all operations. In the Basic Function tab on the left buttons for each scan are visible. They are ordered from top to bottom in the order they typically would be performed to calibrate the Timepix3, ending with start readout which would start a `run`. In the central part of the window an output is implemented showing information on the current (running) or the last finished scan. On top, the name of the scan is shown (e.g. Hardware Initialization). Below that first, a short description of the scan is given and then information on the current step the scan is performing. On the bottom of the output a progress bar (purple) can be seen to have a hint on the scan progress. On the top right, some information on the currently used software and firmware version is given. Below buttons for all important settings can be found. At the bottom right a Quit button is shown which either quits the

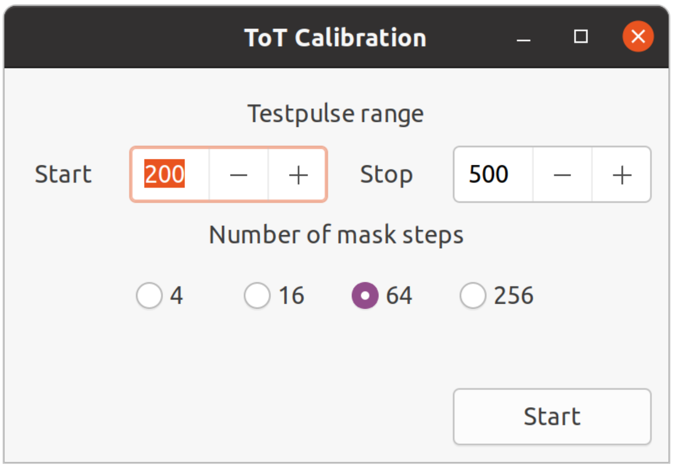

Figure 10.10: Dialog window for the ToT calibration. All needed parameters are shown and can be changed. When the window is opened the settings are at default state. After everything is set the Start-button would start the scan and close the window.

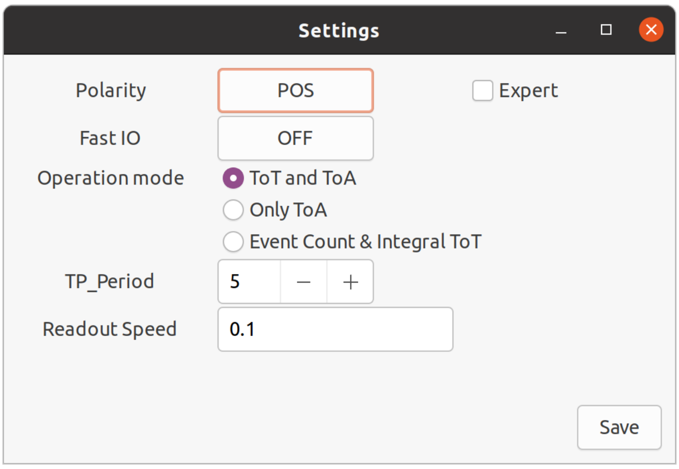

Figure 10.11: Dialog window for the settings. Here the typical setting for the Timepix3 can be changed. More advanced settings are hidden and will only be shown if the Expert check box is activated.

current running scan or if no scan is running closes the GUI. After the initialisation is performed in the footnote of the window the chip ID as well as the number of active links is shown. If one of the scan buttons is clicked a dialog window for the selected scan is opened as shown in figure 10.10. In the window, all parameters necessary for the scan can be changed and with clicking on the start button the scan will be started. If the scan is started as its own process, the dialog window is automatically closed and the output in the main window will show the scan and the current progress. Within the window, it is not possible to set unreasonable numbers. For example, it would not be possible to set the starting value for the test pulse height higher than the stopping value. Regarding the chip settings two parts will be discussed in the following. First, the Settings window as shown in figure 10.11 and then the Set

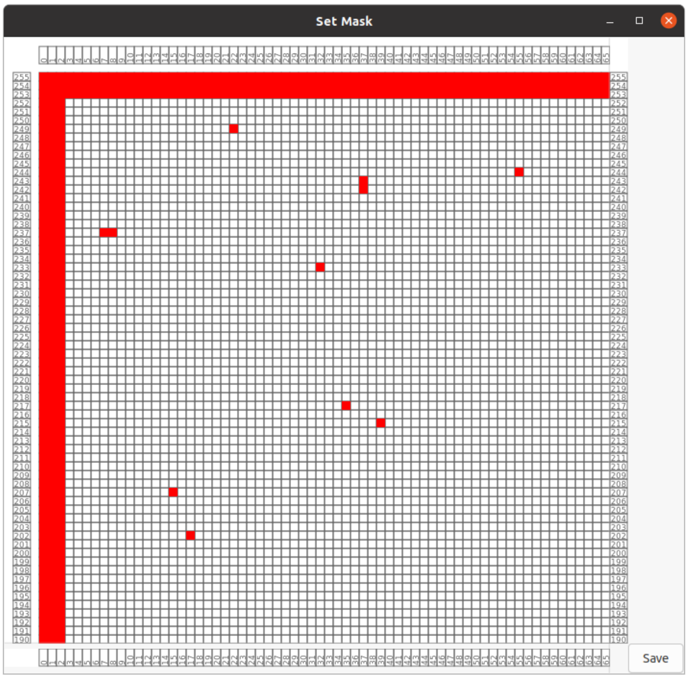

Figure 10.12: Dialog window for masking pixels. A full matrix of 256×256 squares, representing the pixels of the Timepix3, is generated with row and column numbers on both sides. Pixels coloured in red will be masked on the chip. If a pixel is clicked it changes colour and masks (red) or unmasks (white) the pixel. If row or column numbers are clicked the whole row or column will be masked or unmasked ignoring already masked pixels.

Mask window (fig. 10.12). In the Settings dialog window typical chip settings can be performed like changing the readout mode or changing the polarity. More advanced settings are hidden from the user but are easily reachable by clicking on the Expert check box. If a setting is changed and the save button is clicked the changes will be applied to the next scan started after the change. The Set Mask dialog window, as in figure 10.12, is very special with respect to the other windows since it works differently. All windows presented so far are working on window gadgets from GTK. However, this was not an option for the full pixel matrix. First, the buttons are too large and second creating 256×256 buttons will make the GUI extremely slow (non-operational). To circumvent this, a generator was written producing a picture of the pixel matrix and additional pictures of the row and column numbers. They are then arranged to a window as shown. To allow the masking by clicking into a specific pixel, the clicked coordinates are read out and transformed into the pixel coordinates. These coordinates are saved to the mask file and a new picture is produced with the clicked pixel marked in red. If a mask file is loaded, before the dialog window is opened, this file will be also loaded into the generation of the picture showing the masked pixels directly to the user. In order to allow for the masking of full rows or columns it is possible to click on the row or column number then the whole row or column will be masked regardless of already masked pixels within. If the number of a fully masked row or column is clicked again the whole row or column will be unmasked. As a last addition it shall be mentioned that there is also the possibility to mask/unmask the full chip by clicking in the top left space between the column and row numbers.

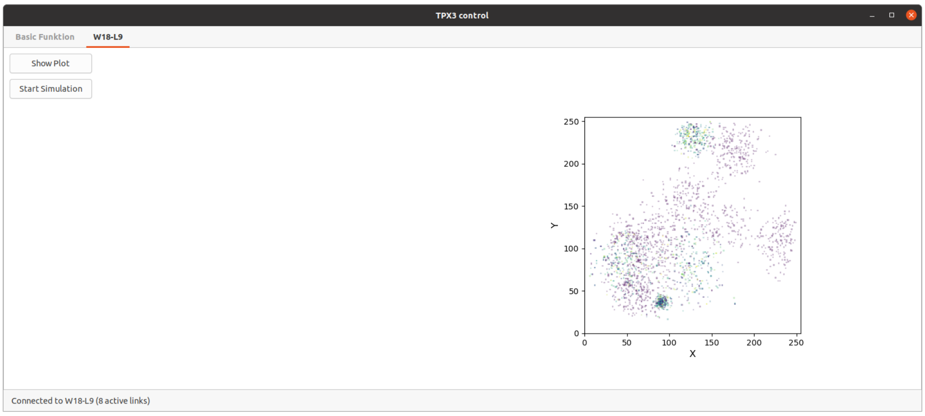

Figure 10.13: Second tab of the GUI window. This tab is named with the chip ID and will show a live plot of the data on the Timepix3. If the Show Plot button is clicked the plot will be set to a separate window so the user can start other scans while observing the data. The Start Simulation button allows to read in an old data set and viewing the data again.

The second tab of the main window is named with the Chip ID. It allows for a live view of the data. A picture is shown in figure 10.13. The plot on the right shows the data currently taken with the chip. If the Show Plot button is clicked the plotting is separated in a new window so the tab can be switched again to start new scans or change settings. Additionally, a simulation is built into the GUI. It can be accessed with the Start Simulation button. With this, a data set can be loaded and viewed again.

The idea of having a separate tab for the plotting is based on the future plans to extend the readout towards multiple chips. Then for each Timepix3, a tab will be generated, allowing for individual chip settings and of course showing the data of the chip.

With the GUI finally, the readout system is completed and can be used.

10.4 Validation of the system

After having the system fully set up the next step is to validate the readout and the detector. For the validation of the detector, the system was set up and the detector was powered. Then the readout was started and the initialisation connected 8 links of the chip. Then the detector was filled with gas to a pressure of 1050 mbar(a) and the high-voltage was slowly ramped up. The test showed no gas leaks and no sparks were observed, hence the detector can be used for data taking. Before that a proper set of DAC settings for the Timepix3 had to be found and the implemented scans had to be tested to run stable. This means that the same scan with the same settings on the same Timepix3 always produces the same result. In the following, we will first look into the scan stability (see section 10.4.1) and then the investigations on the DAC settings (sec. 10.4.2) will be presented.

10.4.1 Scan stability

To validate the scan stability each scan was run ten times and the results were compared. No scan showed large differences, only values in the range of typically ±1 were observed. As an example, the results of the pixel DAC optimisation and the ToT calibration will be discussed.

Run	1	2	3	4	5	6	7	8	9	10
Value	82	82	83	83	83	82	83	84	84	83

Table 10.1: Results of ten pixel DAC optimisations.

Run	a in 1/mV	b	c in mV	t in mV
1	0.66 ± 0.00	−7.55 ± 0.17	6.13 ± 1.73	23.24 ± 0.52
2	0.67 ± 0.00	−7.72 ± 0.17	5.60 ± 1.66	23.32 ± 0.52
3	0.66 ± 0.00	−7.63 ± 0.17	5.96 ± 1.78	23.21 ± 0.56
4	0.66 ± 0.00	−7.65 ± 0.16	5.37 ± 1.63	23.34 ± 0.53
5	0.66 ± 0.00	−7.68 ± 0.17	5.48 ± 1.69	23.29 ± 0.55
6	0.66 ± 0.00	−7.58 ± 0.17	6.05 ± 1.78	23.16 ± 0.57
7	0.66 ± 0.00	−7.61 ± 0.17	5.87 ± 1.73	23.27 ± 0.53
8	0.66 ± 0.00	−7.66 ± 0.17	5.95 ± 1.73	23.24 ± 0.53
9	0.67 ± 0.00	−7.65 ± 0.16	5.84 ± 1.69	23.25 ± 0.53
10	0.66 ± 0.00	−7.68 ± 0.17	5.33 ± 1.67	23.33 ± 0.55

Table 10.2: Results of ten ToT calibrations. All fit parameters are compatible with each other within the error margins.

For the pixel DAC optimisation the resulting pixel DAC values can be found in table 10.1. Out of the ten scans, three showed a result of 82, five of 83, and two of 84. No scan failed or showed large differences to the others, hence a result of 82.9 ± 0.7 shows that the scan runs stable. As a second example, the results for ten ToT scans can be seen in table 10.2. From the resulting fit data, it can be observed that all values fit to each other within their error margins. Also, the important value a giving the slope of the fitted curve is only varying by 0.01 mV^{-1}. This shows that also the ToT scan is producing stable results. To give a better comparable number for the ToT calibration one can calculate the number of electrons for a ToT value of 100. Calculating the mean from this leads to a result of 7604.6 ± 46.5 e^-. From this it can be seen that the difference in the number of electrons for a given ToT value produces an error smaller than 1% from one calibration to the other. The results for the other scans are similar. For the equalisation also the results for each pixel can be compared. For this, the difference for all ten runs is almost never larger than ±1, only very few pixels showed larger differences. This is probably coming from pixels with defects (e.g. very noisy pixels) that can not be equalised.

10.4.2 DAC settings

After having verified that the scans are stable the next step is to find a useful set of DAC settings to operate the detector. This has to be optimised for the application therefore in the following a set for a GridPix3 operation will be determined. For the determination of the DAC setting for each DAC, a set of values was chosen and then all scans were performed to find the best value. For this all relevant DACs have been evaluated, however the results are mostly influenced by two (`Ibias_IKrum` and `Vfbk`). These DACs control the Krummenacher current and the dynamic range of the pixel. For the `Ibias_IKrum`, since it influences the ToT measurement, first a very rough scan was performed to get an idea of the interesting range. The higher the value set for the `Ibias_IKrum` DAC the faster the charge is drawn from the pixel. The scan showed that for the low charges ($\mathcal{O}(10000\,\mathrm{e}^-)$) only the lowest values are interesting. Hence, the scan was performed on DAC values from 1 to 6. The most interesting numbers to compare are the threshold of the chip and the number of electrons per ToT clock cycle. While the first one sets the lowest detectable charge and therefore the efficiency of the detector, the second value gives the energy resolution of the detector. As shown in table 10.3 for the `Ibias_IKrum` DAC the lowest two values can be ruled out since the threshold rises. For the other four values, it can

`Ibias_IKrum`	1	2	3	4	5	6
Threshold[e^-]	Chip noisy	1818	1234	1167	1186	1259
ToT[e^-] at 100 clock cycles		7200	8553	10060	11128	12658

Table 10.3: Results of the `Ibias_IKrum` DAC scan. For the lowest value the chip was too noisy to get any results.

be seen that the charge necessary to reach 100 clock cycles in the ToT measurement is getting larger with every DAC step as expected. However, even for the lowest values, the GridPix3 will not use the full range of the ToT (1021 clock cycles). Comparing the threshold and the ToT clock cycles the best values for operation are 4 and 5.

The next DAC to be evaluated is the `IPreamp` DAC. For this DAC the full range was scanned in steps of 50 and with `Ibias_IKrum` = 5. The scan shows that for lower values both the threshold and the number of electrons per ToT clock cycle are lowered slightly, however it could be observed that the spread in the pixel response is growing larger (the result from the pixel DAC optimisation rises), making the response over the full chip more unequal. Hence, low values should be omitted. Since we found two values for `Ibias_IKrum` also a test with `Ibias_IKrum` = 4 was performed. This test showed the best result for a value of 150. Therefore `Ibias_IKrum = 4` and `IPreamp = 150` were chosen for further usage. The next DAC scanned was the `Vfbk` DAC also here some pretest led to a narrowing of the range so the DAC was only scanned between 122 and 192 in steps of ten. The results of the scan are shown in figure 10.14. A minimum can be observed at a value of 172 for both parameters. Also, the other scans show proper results at this point so a value of 172 for the `Vfbk` DAC should be chosen. However, for the shown measurements, the `Vfbk` was accidentally set to 132.

The next DACs to be examined are the two DACs `Disc_S1` and `Disc_S2`. They influence the frontend discriminators. Both showed no influence on the threshold or the number of electrons per ToT clock cycle. Since the `Disc_S1` current influences the pixel DAC current, higher values of `Disc_S1` raise the result of the pixel DAC optimisation, and for the `Disc_S2` the behaviour is vice versa but less significant. The main influence of these two DACs will be on the time jitter of the ToA, which was not included in the validation parameters. If usage of the fast ToA is needed, these DACs should be reviewed. With this knowledge, the value for the `Disc_S1` DAC was chosen to be 100. For `Disc_S2` since nearly no influence could be measured the value was set to 128 being the centre of the DAC range. The last DAC to be tested is `VPreamp_NCAS` the DAC should influence the noise by affecting the preamplifier. However, this behaviour could not be observed. Only towards a value below 100 the noise and therefore the threshold rose. Thus, the DAC is set to 128.

After having all necessary DACs tested and set with the new set of parameters the `Ibias_IKrum` DAC is scanned again to see if the behaviour is different. The results are shown in table 10.4. A clear trend towards lower thresholds and lower numbers of electrons per ToT clock cycle for lower DAC values is observed. For the setup, one can still use `Ibias_IKrum` values of 4 or 5 as the best values for the GridPix3. In cases where the ToT resolution is very important a value of 3 could be used. This is a

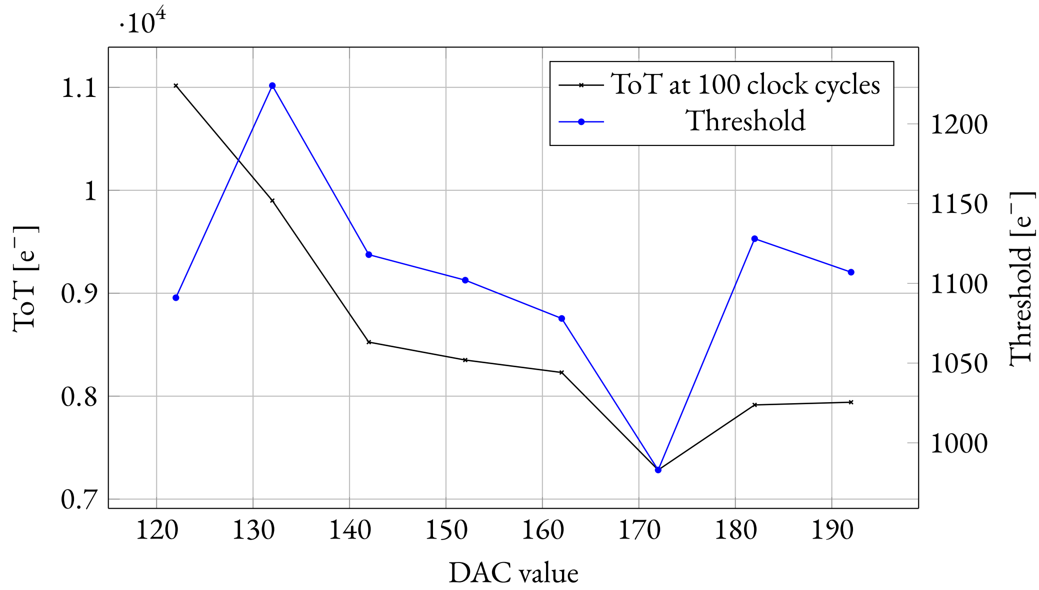

Figure 10.14: Result of the scan of the `Vfbk` DAC. A minimum can be observed for both parameters at a value of 172.

`Ibias_IKrum`	1	2	3	4	5
Threshold[e⁻]	Chip noisy	1433	939	774	770
ToT[e⁻] at 100 clock cycles		6118	6803	7406	8404

Table 10.4: Results of the final `Ibias_IKrum` DAC scan. For the lowest value, the chip was too noisy to get any results.

good result showing that a proper set of DAC parameters will improve the efficiency and the energy resolution of the detector. As a baseline for the GridPix3 detector, the determined values will produce proper results and will be used for the rest of the thesis.

10.5 Summary

A versatile Timepix3 detector was developed and built including the readout electronics and a mechanical design for the usage of a gaseous detector with a GridPix3. For this a firmware and software was developed implying all necessary scans and functions and a graphical and non-graphical user interface. The detector was then mechanically and electronically validated, showing no problems. With the detector, the scans were validated and a set of DAC settings for a GridPix3 detector was determined for further usage. In figure 10.15 the set up detector is shown in the picture the gas supply and the high-voltages are not connected. With the full system later background data was taken (see chapter 14) and the detector was used for polarisation measurements (see [Gru]).

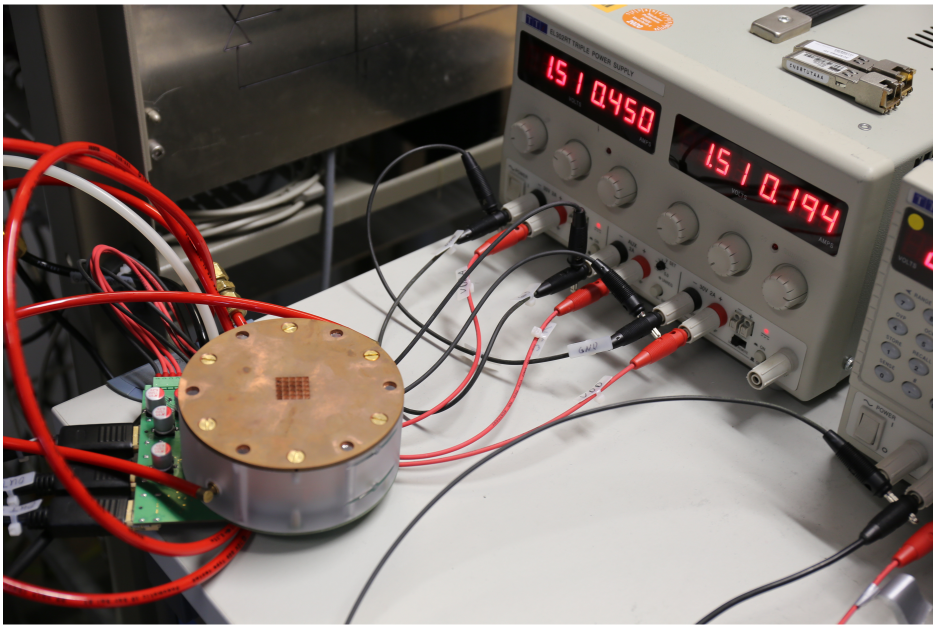

Figure 10.15: The GridPix3 detector setup in the lab used for the presented scans.

CHAPTER 11

A prototype detector for BabyIAXO

For the upcoming BabyIAXO experiment, a prototype detector was developed such that it can be built out of materials known for low background applications. As described in chapter 5 a background rate in the order of 1×10^{-7} counts $\mathrm{cm}^{-2}\mathrm{keV}^{-1}\mathrm{s}^{-1}$ is envisaged. To reach this goal the intrinsic background of the detector needs to be lowered compared to the detector described in chapter 8. This intrinsic background occurs from radioactive isotopes in the materials used. When they decay they produce different types of radiation, which might end up in the sensitive volume of the detector. Through this radiation also X-ray photons can be produced inducing a signal into the detector. These signals can not be distinguished from photons stemming from axion conversion leading to a non-suppressible background. To reduce this background, materials can be chosen which are known for their low amount of radioactive isotopes. An overview of materials known to be radiopure will be given in section 11.1. After knowing what materials can be used for the detector the setup of the prototype detector will be presented in section 11.2. At the end, a validation of the detector will be presented showing that the detector is operational. It shall be mentioned that the presented detector is only built from materials known to be radiopure or manufacturable to be radiopure. For the presented prototype still standard versions of these materials, which are not yet the most radiopure versions, have been used.

11.1 Radiopure materials

Radiopure materials are commonly used in rare event searches. From these experiments, a database with a lot of tested materials was set up [LCC+16]. The database is accessible via [J.C]. From this database, a lot of materials can be compared and those most suitable for the detector setup will be explained in the following:

- **Copper:** Copper is a very radiopure material since there are no radioactive isotopes of copper occurring naturally. Therefore, pure copper would be absolutely radiopure, however due to the refining process other materials, like cadmium and lead, will spoil the radiopurity. Hence, for the copper a very pure alloy needs to be used. For this typically an alloy consisting of 99.99% copper will be used. This can still be further refined if necessary but for experiments on the surface like BabyIAXO these steps are not required, since cosmic radiation will activate the material again [EAA+23].

- **Lead:** Lead is naturally not a radiopure material as it always contains small amounts of radioactive isotopes. Of those ^{210}Pb is the most problematic since it has a half-life time of ≈ 22 years leading to a slowly decaying background. However, lead is commonly needed as a shielding material to reduce the background emanating from the environment. Since it is very hard, if not impossible, to remove the ^{210}Pb, two possibilities are left. The first one is to search for lead ore with a low content of ^{210}Pb. The other option is to simply wait, since after a few hundred years the lead will be very radiopure. To avoid such long times one can use lead which was already produced hundreds of years ago. The best source for this is lead used as counterweights in ancient ships.
- **PTFE:** Polytetrafluoroethylene (PTFE) is commonly known as Teflon™. PTFE is an isolator and therefore very useful for the detector setup. Polymers are typically not very radiopure since they are produced from petroleum products containing pollutants. PTFE is also produced from petroleum products, however it is produced from light distillates. Therefore, the pollution is much lower than for heavier distillates. For PTFE it is important that only pure, non-filled PTFE can be used since otherwise, the filling material may spoil the radiopurity.
- **Polyimide:** Polyimide is commonly known as Kapton®. Typically used as a printed circuit board (PCB) material polyimide is to some extent radiopure. The radiopurity mostly depends on the manufacturing hence testing the material is necessary. This is even more important for PCBs since for the production of the PCBs adhesives are used, which are often not radiopure.
- **Epoxy:** Epoxy glues are needed to build the detector. There are epoxies available with a reasonable radiopurity.

Based on this, a detector was designed using only these materials. Some components like the final epoxies used or the PCB were tested already within the prototype version while materials like copper and PTFE were used in their non-radiopure versions for the prototype. However, all materials have been sourced and the radiopurity is being tested, so after the prototype is successfully tested, a radiopure version can be produced. For the production of the radiopure version, it is very important that the materials are not contaminated during the machining, hence all tools and machines need to be cleaned. Also, the lubricants used for the machining might contaminate the material, therefore only specific lubricants like ethanol can be used. After the machining, all parts have to be cleaned by etching to remove the surface layers.

11.1.1 Radiopurity of materials for the radiopure detector

In order to get an idea if materials are suitable for building a radiopure detector they need to be screened. Screening of such materials is mostly done in specialised underground laboratories with germanium detectors. For the materials shown in the following, these measurements were performed at the Canfranc Underground Laboratory [MBC+05] with the germanium detector Paquito [CDFR+11] and analysed with the methods described in [BFA+11]. The results of the measurements are shown in table 11.1. The table shows that, except for the PCB and the lead, for all materials only upper limits could be determined. The large variances in the upper limits occur mainly from the amount of material available for screening and from different measurement times. For the PCB however, excesses for two radioisotopes could be determined. For a PCB this was expected and the activity lies within the typical range. However, for the final detector PCB a screening of the material should be repeated and maybe

	Material activity in mBq/kg					
Isotope	SiN	PCB	Epoxy	Copper	PTFE	Lead
^{228}Ac	< 515	< 70	< 51	< 3.9	< 7.0	< 3.1
^{228}Th			< 21	< 3.0	< 4.0	< 2.4
^{212}Pb	< 217	< 43				
^{208}Tl	< 354	< 54				
^{234}mPa	$< 19 \times 10^3$	$< 2.9 \times 10^3$	$< 1.7 \times 10^3$	< 136	< 289	< 94
^{226}Ra			< 38	< 5.3	< 8.7	< 4.0
^{214}Pb	< 389	68 ± 27				
^{214}Bi	< 455	< 89				
^{235}U	< 151		< 14	< 2.4	< 2.9	
^{40}K	$< 2.7 \times 10^3$	227 ± 94	< 160	< 15	< 26	< 8.1
^{137}Cs	< 110	< 20	< 12	< 1.3	< 1.8	
^{60}Co	< 119	< 13	< 10	< 0.91	< 1.7	< 0.54
^{210}Bi						$(38 \pm 11) \times 10^3$

Table 11.1: Results of the radiopurity screenings of the materials needed for the detector. SiN is the material for the ultra-thin windows. The epoxy tested is Araldite Ay 103-1Hy 991. For the copper and PTFE multiple samples have been tested and here only the worst results are shown. Most materials only show upper limits for all common radioisotopes. Only the PCB made of polyimide shows excesses for ^{214}Pb and ^{40}K. This is comparable with other results from polyimide PCBs. For the lead, not being ancient, it was expected to have a high activity of ^{210}Pb, which was measured via the decay of its daughter nucleus ^{210}Bi. Data from [CG].

other suppliers should be tested since other polyimide substrates might show better results. The lead tested was bought from a lead supplier and is standard commercial lead. The manufacturer was selected as they offered lead with a low activity compared to the average activity of natural lead in the order of hundreds of Bq/kg [D.]. Since the lead will be used for the test stand (see chapter 12) and is not part of the detector this result is sufficient. The results for the most common materials in the detector (copper and PTFE) are comparable with the results known from other low-background experiments.

11.2 The detector design

To produce a detector only from the materials mentioned in section 11.1 a complete redesign of the detector presented in chapter 10 was necessary. In figure 11.1 the redesigned detector can be seen. It is clear that it still contains all of the components discussed for the other detectors (see chapters 8 and 10), however every part had to be newly constructed, and new methods for building and connecting parts had to be developed. The detector consists of a three-part housing (base plate, drift ring, and cathode) building the gas volume. On the base plate, the PCB is positioned and fixed in the region where the GridPix3 is placed. The GridPix3 is then directly glued on the base plate to allow for good thermal contact in order to cool the chip. Into the drift ring the field cage is mounted and connected via contact springs to the PCB. The drift ring with the field cage inside is mounted on the base plate. Then the anode is screwed to three PTFE mounts fixed in the base plate. It connects to the PCB via a push

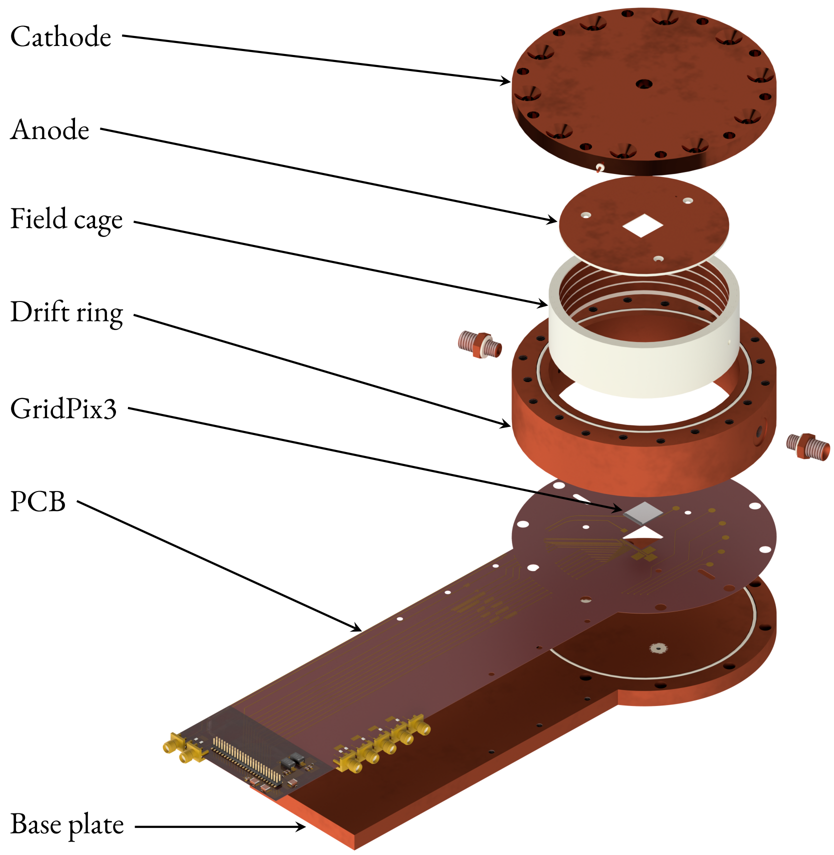

Figure 11.1: Exploded view of the radiopure detector prototype. The prototype only consists of copper, PTFE, polyimide, and some epoxy. All electronic components are away from the active volume of the detector. The main parts are indicated. Since the outer body of the detector is conductive and on ground potential, a field cage is necessary even with a single GridPix3.

contact. Finally, the cathode closes the gas volume. To seal the detector, a new concept was developed since standard rubber gaskets cannot be used. For this, PTFE and lead gaskets were tested and finally, PTFE gaskets were chosen for the detector. The lead gaskets might be a good candidate for the upstream vacuum flanges. In the following, all parts will be discussed in detail.

11.2.1 The printed circuit board (PCB)

The PCB for the radiopure detector is made from polyimide. It was developed in cooperation with the University of Siegen using the designs presented in section 10.1.1. However, the PCB contains only the chip carrier, thus the Intermediateboard is still needed for the readout. Figure 11.2 shows the PCB already mounted on the base plate with the GridPix3 bonded. All electronics are moved far away from the active volume. This is necessary since most electronic components and also solder are not radiopure. Hence, soldering should be avoided close to the active volume. To reach this goal the power lines to

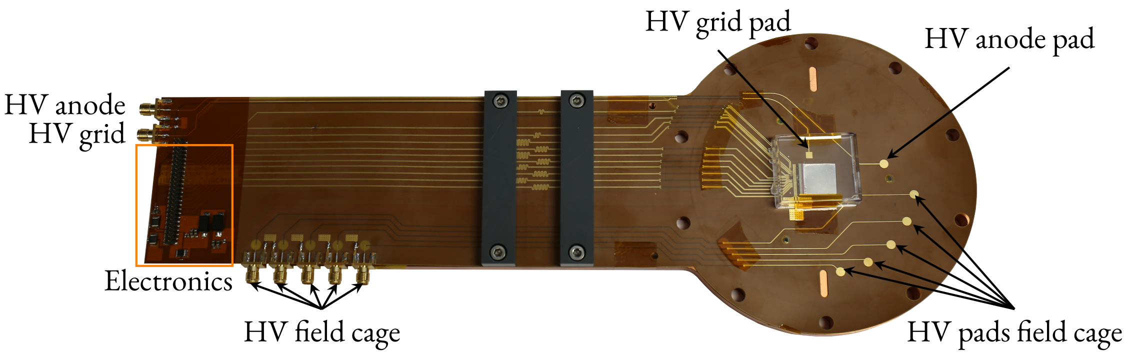

Figure 11.2: Picture of the detector PCB already mounted with the GridPix3 on the base plate. The grey bars are not part of the detector and are only fixing the PCB to the base plate. They will be replaced with a copper shield for the final detector. The electronics are moved far away from the active volume of the detector (orange box). The high-voltage connectors (bottom left) are also moved away from the detector. They are connected to pads inside the active volume. In the active volume of the detector (right part) only the GridPix3 remains.

the GridPix3 are designed with a large width to have a low resistivity to avoid capacitors close to the GridPix3. Also, all high-voltage connectors are moved to the far end of the PCB. They are connected to power pads in the active volume, where contact springs connect the anode and the field cage to the high-voltage lines. For the GridPix3 a hole is cut into the centre of the PCB so the GridPix3 can be glued directly to the base plate. Then, the GridPix3 is bonded to the PCB. For this, the part of the PCB containing the bond pads is glued to the base plate as well. At the active volume, the PCB contains five additional holes, two slots for faster degassing of the trapped air between the base plate and PCB, and three holes surrounding the GridPix3 for fastening the anode. Around the active volume, a circle can be seen where no conducting paths are visible on the surface since the conductive paths are routed through the inner layer of the PCB. This is the part where the drift ring is mounted. Since the drift ring is made from copper it would otherwise connect all conducting paths.

11.2.2 Base plate and drift ring

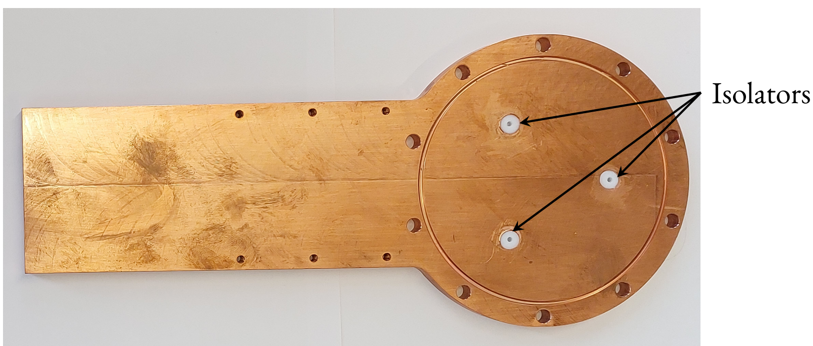

Figure 11.3: Picture of the base plate of the detector. The PTFE isolators to mount the anode can be seen as well as the groove for the seal. The GridPix3 will be glued directly onto the copper. The base plate is uncleaned and showing stains from handling which need to be avoided for the radiopure detector.

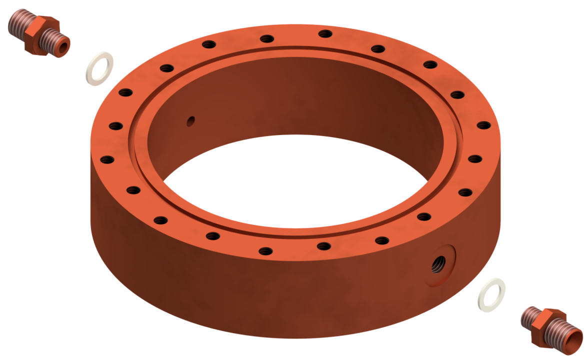

Figure 11.4: Exploded view of the drift ring. The gas connectors and the PTFE gasket are visible. The two circles of threaded holes can also be seen. One is to fix the cathode and the other one is to mount the detector. The groove visible will contain the seal for the cathode.

The base plate is the lower part of the detector. It consists of copper with three PTFE inserts needed to fix the anode to the base plate while electrically isolating these parts from each other. A picture of the base plate is shown in figure 11.3. The three PTFE isolators are screwed into the base plate with epoxy to fix them. After the epoxy is cured the isolators will be milled over until they are planar with the copper surface. For the radiopure detector, the whole part would be cleaned a second time to avoid contamination from the process. To the base plate, the PCB would be fixed by glueing only the part containing the bond pads. This is done to allow for the exchange of the PCB on the base plate in case of a failure. After the GridPix3 is glued and bonded, the drift ring will be mounted, fixing and sealing the base plate, the PCB, and the drift ring to one unit.

The drift ring is made entirely of copper and defines the gas volume. To allow for gas flow two gas connectors produced out of copper are fixed to the drift ring. As shown in figure 11.4 the gas connectors (clamp connection for 6 mm tubes) are sealed with a PTFE gasket to the detector. The drift ring contains two circular patterns of threaded holes (fixing the base plate, fixing the cathode, and fixing the detector to the beamline) and two grooves for gaskets on the bottom side to seal to the top of the PCB and on the top side to seal to the cathode.

11.2.3 Field cage

In difference to the detector described in chapter 10 the drift ring of the radiopure detector consists of copper and is connected to ground potential. Thus, a field cage is necessary for the detector, since the electric drift field would be extremely disturbed otherwise. As mentioned in section 13.2, most selection criteria for the background reduction are based on geometrical properties, therefore these properties need to be preserved as good as possible. For this, a homogeneous electric field above the grid is crucial since all inhomogeneities in the field will disturb the shape of the events. The behaviour of the field without a field cage is shown in figure 11.5. It can be seen that the field is strongly disturbed. The disturbances would change the electron paths leading to a changed geometry of the events. A classical field cage as used for the seven-chip detector (see section 8.1.2) cannot be used since it contains resistors soldered to the field cage PCB inside of the active volume. Hence, a new concept had to be developed. First, the number and size of the field cage rings need to be determined. Thus, different versions of the field cage were modelled and simulated with the finite element method (FEM) software ANSYS [Ans]. First, the necessary number of field cage rings had to be determined by comparing the

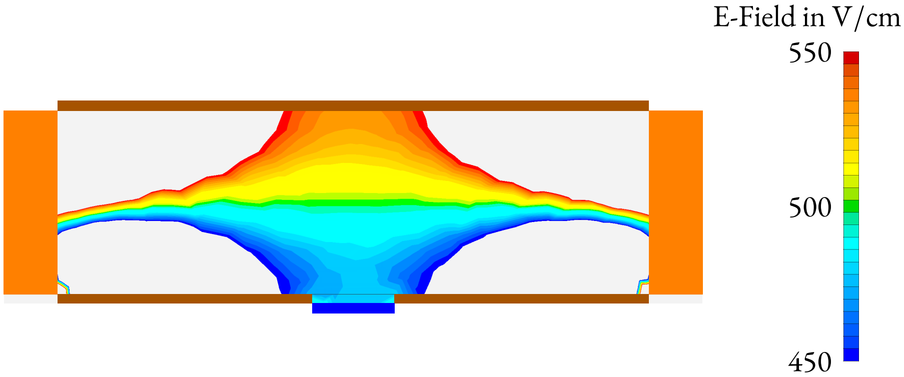

Figure 11.5: Simulation result of the detector without any field cage. The GridPix3 (blue) is located in the centre at the bottom. Grounded side walls are indicated in orange, cathode (top) and anode (bottom) are coloured in a darker orange. The GridPix3, the anode, and the cathode are set to voltages that produce an E-field of 500 $\frac{\mathrm{V}}{\mathrm{cm}}$. The colour scale indicates differences up to 10%. Larger differences are not coloured. Simulated with ANSYS [Ans].

homogeneity of the electrical field in the sensitive volume. Example-wise results of this simulation are shown in figure 11.6. It can be seen that for the setup with only two rings the field above the detector is still slightly disturbed. For the cases with five or ten rings, this is not the case anymore. However, in preparation to house seven GridPix3s in the detector to allow for a better background discrimination as shown in [Sch24a], the homogeneity of the field needs to be preserved over a larger area. In figure 11.6 this is indicated by four horizontal lines. From those, it can be seen that for the two ring field cage, the disturbances are large especially close to the edges of the position of the outer GirdPix3s. Between the results of the five and the ten ring field cage, the change is not very large. Consequently, a field cage with five rings was chosen.

The next step was to see how the sizes of the rings influence the results. For this, three different models of a field cage with five rings were simulated. The results are shown in figure 11.7. It can be seen, that field cages with wider rings produce a more homogeneous field. Especially, for the 2 mm wide rings the results are showing that the field would not be uniform. For a potential setup with seven GridPix3s, as indicated again with black lines, it can be clearly seen that the field would be disturbed above the outer GridPix3s. Hence, the gap between the field cage rings should be as small as possible to reach the best result for a given number of rings. Nevertheless, since the rings will be on different electrical potentials in the end, a minimal distance must be kept between the rings. This distance grows with the voltage between the rings and therefore grows with a lower number of rings. Resulting from these simulations a good choice for the field cage is a model with five rings of 5 mm width each. To verify that the simulated results are not strongly influenced by the cell size of the simulation with the chosen field cage the influence of the cell size was tested. This study showed that the homogeneity rises the smaller the cell size of the simulation is, however the differences are marginal.

To produce this field cage from radiopure materials two different setups were evaluated. A field cage made from copper rings embedded with epoxy and a version made from copper rings and PTFE. In the following both versions will be explained, starting with the epoxy version. For the epoxy version, a mould was built where the copper rings were fixed to their height with the central part of the mould. Then the rings were wired by knotting the wires to holes drilled into the rings and fixing them with a

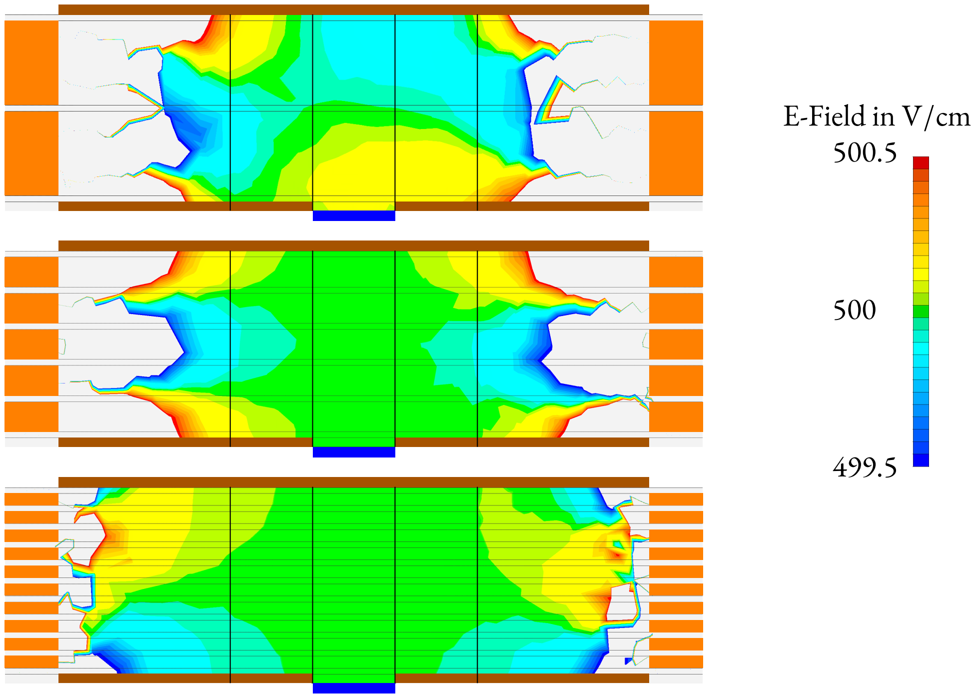

Figure 11.6: Simulation result of the detector with different field cages. From top to bottom 2 rings, 5 rings, and 10 rings. The gap between the rings is kept constant. The GridPix3s (blue) are located in the centre at the bottom of each setup. The rings of the field cages are marked in orange, and the cathodes (top) and anodes (bottom) are coloured in a darker orange. All voltages are set such that an E-field of 500 $\frac{\text{V}}{\text{cm}}$ is produced. The colour scale indicates differences up to 0.1%. Larger differences are not coloured. The horizontal black lines indicate the borders of a setup with one or three GridPix3s in the detector. The later one would indicate a usage for a setup with seven chips as described in chapter 8. Simulated with ANSYS [Ans].

copper dowel. Then the wires were fixed at the top of the mould, such that they later would be fitting to the PCBs HV-pads. This can be seen in figure 11.8(a). Since the wires from the lower rings have to pass other rings, polyimide tape was used to electrically isolate them. After the rings are wired, the outer shell is mounted. It was figured out that a shell made from three equal parts is the best setup for the outer shell. The splitting up of the shell is necessary for the removal after the epoxy is cured. In order to avoid the epoxy from leaking, all slits were sealed with hot glue. Then the epoxy was added and after curing the field cage could be taken out of the mould. Afterwards, the inner and outer surfaces were machined to the needed diameters. As a last step, the contact springs for the electrical connection to the PCB needed to be added to the field cage. It was figured out that this task is problematic since the epoxy has to be removed around the wires without damaging the wires. Following this, grooves have to be produced 1.5 mm deep allowing for knotting the contact springs to the wire and filling the grooves with epoxy again. After that, the surface has to be machined flat. The result of this is shown in figure 11.9. In the figure it can be seen that the positioning of the contact springs is not very accurate, hence to have them match the pads on the PCB they need to be bent slightly without breaking the epoxy. The other even worse problem is trapped air between the field cage ring. Due to this, air pockets are created in which during the milling of the inner surface copper dust gets trapped, electrically connecting the

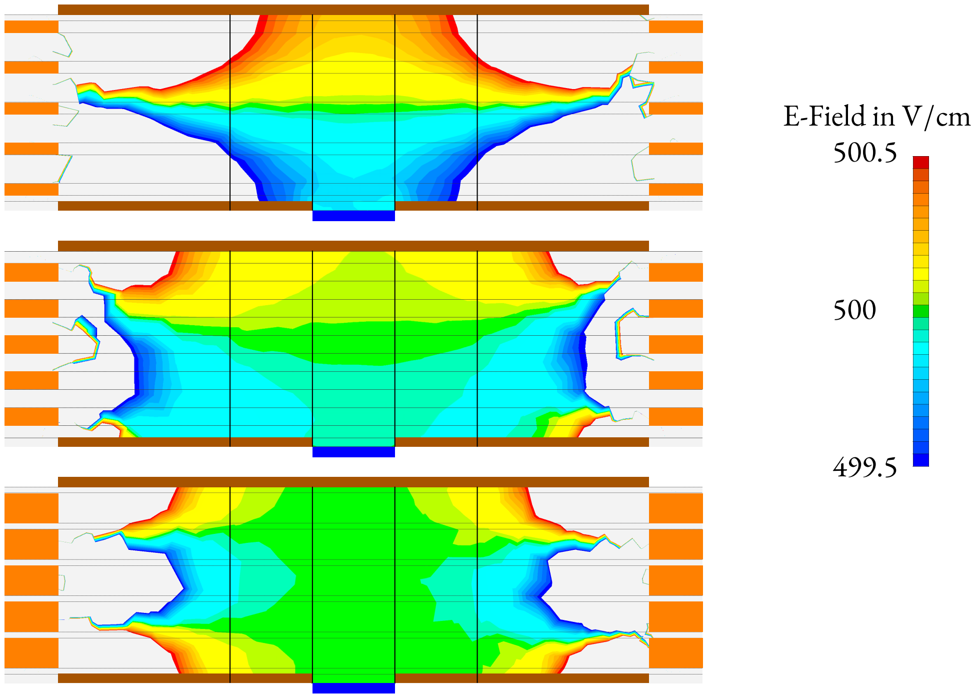

Figure 11.7: Simulation result of the detector with different field cages with five rings and different sizes of the rings. From top to bottom 2 mm wide rings, 3 mm wide rings, and 5 mm wide rings. The gap width is chosen accordingly to keep the height of the field cage identical. The GridPix3s (blue) are located in the centre at the bottom of each setup. The rings of the field cages are marked in orange, and the cathodes (top) and anodes (bottom) are coloured in a darker orange. All voltages are set such that an E-field of 500 $\frac{\mathrm{V}}{\mathrm{cm}}$ is produced. The colour scale indicates differences up to 0.1%. Larger differences are not coloured. The horizontal black lines indicate the borders of a setup with one or three GridPix3s in the detector. The later one would indicate a usage for a setup with seven chips as described in chapter 8. Simulated with ANSYS [Ans].

rings, making the field cage unusable. If these pockets are shallow, there is the possibility to clean them out later and fill them with epoxy. However, two pockets could not be cleaned, hence the rings could not be used with high-voltages. With the remaining rings successful tests were made showing that the field cage, despite the manufacturing problems, would work. Due to the described problems though, the field cage was not used for the detector.

The second field cage is produced only from PTFE and copper. No glue is involved in the setup, hence it can be disassembled at any time if a failure is found. The field cage consists of three shells of PTFE and the copper rings inside. A cut view of the field cage can be seen in figure 11.10. The shells are numbered in the following from the inside. The first shell consists of two half circles. They are manufactured such that they separate the copper rings and hold them in place. The second shell (indicated in yellow in fig. 11.10) will on one hand hold the first shell and the rings together and on the other hand support the contact springs. To place them at the correct angles, five small grooves are added at the envisaged positions. The third shell is then used to isolate the field cage contact springs and wires from the drift ring. To connect the copper rings to the contact springs in the first and second shell small holes are drilled for the wires. In figure 11.10 the path of the wire can be seen through the

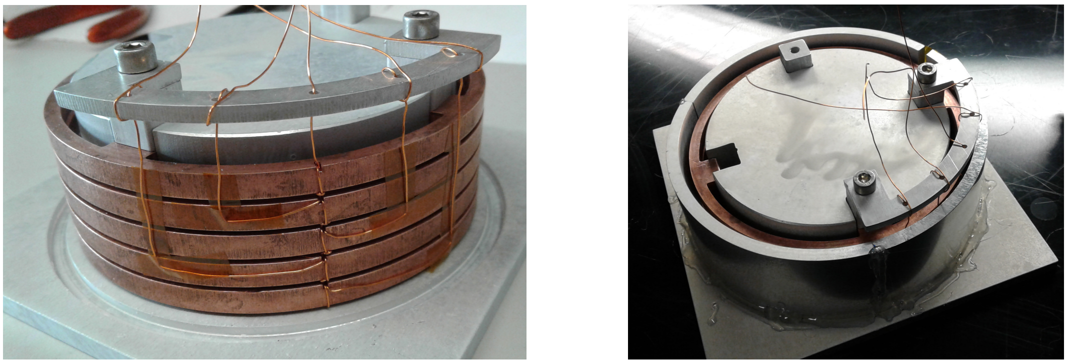

(a) (b)

Figure 11.8: The setup to produce the epoxy version of the field cage. In (a) the wiring is shown before the outer shell of the mould is placed. The wires are fixed to the rings by knotting to a hole in the ring. To avoid contacts where the wire passes the other rings polyimide tape is placed between the wires and the rings. The wires are then fixed with a holder to the positions of the contacts on the PCB. In (b) the mould is closed; the outer shell consists of three parts allowing for a better removal later. Hot glue was used to close all gaps in the outer shell of the mould.

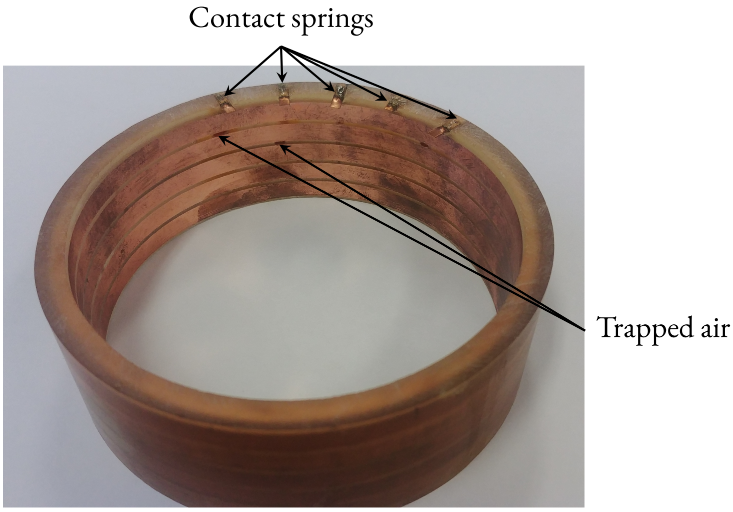

Figure 11.9: Finalised version of the epoxy field cage. As epoxy, Araldite Ay 103-1 was used. The contact springs for connection to the PCB can be seen at the top centre. Also, two bubbles of trapped air can be observed in the picture.

different shells. To fix the wires electrically and mechanically to the field cage rings each ring has a hole drilled into it with a groove to the outside on both sides. The thin copper wires ($D = 0.3$ mm) are knotted through this hole and then fixed with a dowel made from thicker copper wire. The wire is then guided through a small hole in the first shell downwards to a small hole in the second shell where the contact spring is mounted. The contact spring also has a small hole at the same position so the wire passes through the second shell and the contact spring. On the outside of the second shell, the wire will then go upwards a bit since for the assembly some extra length of wire is necessary. Then the third shell is added finishing the field cage. To allow for a proper gas flow, the gas in- and out-lets need to pass

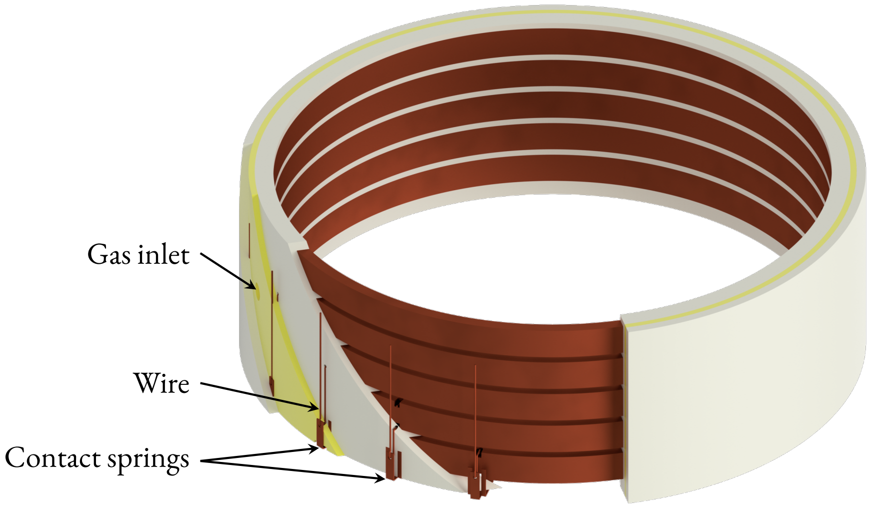

Figure 11.10: Cut view of the PTFE field cage. The second PTFE layer is coloured yellow for better differentiation. Looking on the cut the different stages of the wiring can be seen as well as the use case of the three shells. The innermost first shell holds and separates the copper rings and isolates the wire from the other copper rings. The second shell holds the contact springs, while the third layer isolates the contact springs and the wire from the drift ring. In the second shell on the left the hole for the gas inlet is visible.

through the field cage. For this, a 3 mm hole is drilled through all layers of the field cage. It is positioned such that the gas enters the detector through the centre of the third field cage ring. The manufacturing of this field cage was unproblematic and since it can be disassembled, fixtures are easy. High-voltage tests showed good results, hence the design was chosen for the detector.

In comparison, both versions of the field cage have their advantages and disadvantages. The epoxy field cage is more sturdy and has a more precise outer diameter. However, trapped air between the field cage rings introduced electrical contacts between them and the fixture of the contact springs was very imprecise and delicate. The PTFE field cage, since the layers are not fixed to each other, can accidentally be shoved apart destroying the wire. But it can be disassembled to fix the wires and the positioning of the contact springs is easy and can be modified. For both field cages, the positioning for the gas in- and outlet needs to be precisely matched with the drift ring and the contact pads on the PCB allowing only one orientation of the drift ring after manufacturing.

11.2.4 Anode

The anodes produced for the detector described in chapter 10 were produced from standard PCB material. This material (FR4) is known not to be radiopure. Since the anode is necessary and cannot be produced as a polyimide PCB since this would not be stiff enough, a combination of PTFE and copper had to be produced. Thus, a PTFE sheet was placed in a vacuum metallisation oven and then coated with copper through vapour deposition. First, two test samples with copper thicknesses of 200 nm and 400 nm were produced to see how sturdy the copper layer is. A cleaning test with a soft cloth and alcohol was performed. The result is shown in figure 11.11. It is visible that a 200 nm layer is not sufficient. For 400 nm the result of the wipe test was satisfactory, hence a thickness of 400 nm was chosen.

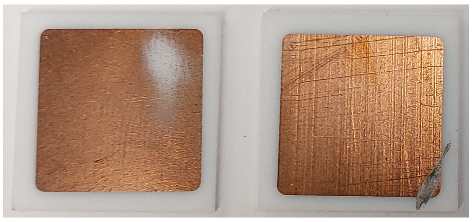

200 nm 400 nm

Figure 11.11: Test samples to determine the necessary thickness of the copper plating. Both samples were lightly wiped with alcohol to simulate a cleaning of the anode. The result showed that a thickness of 200 nm is not sufficient, while at 400 nm enough copper remained.

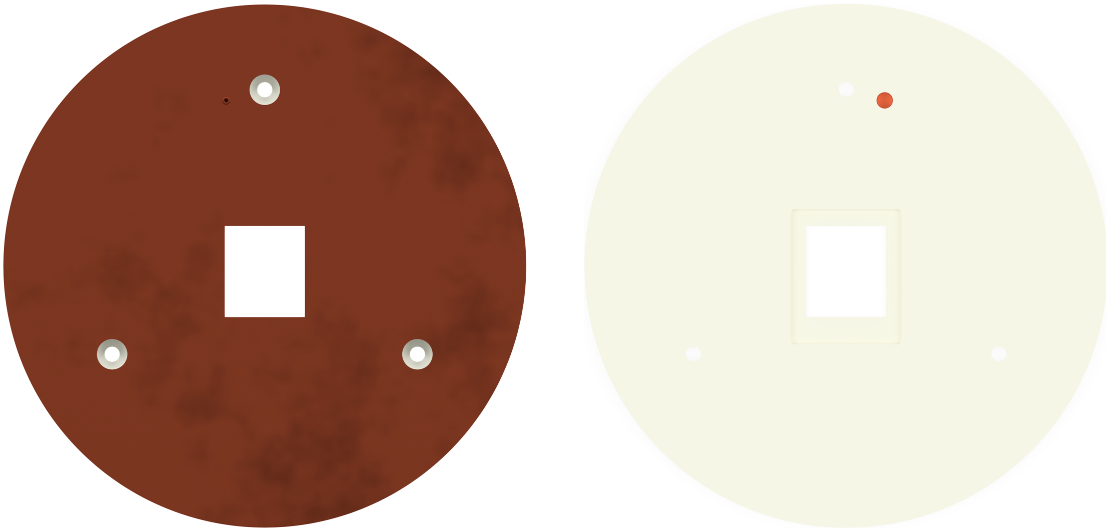

(a) Top (b) Bottom

Figure 11.12: View of both sides of the anode. The anode is made from 1.5 mm thick PTFE. The top side is completely metallised with copper and with a through contact connected to the PCB. The bottom side shows the through contact (copper rivet) and has a thinned area around the GridPix3 to allow for a closer matching of the surfaces.

The layout of the anode can be seen in figure 11.12. The anode is produced from a 1.5 mm PTFE sheet. In the centre an opening is cut out matching the GridPix3. On the bottom side around the opening the anode is milled to 0.5 mm to allow for a closer matching of the anode surface and the grid without destroying the bond wires. The anode will be fixed to the base plate via three copper screws. In order to connect the anode surface to the PCB a copper rivet is placed according to the position of the corresponding pad on the PCB.

11.2.5 Cathode

Since the detector housing consists of copper, the cathode can not be built in the same way it was done for the other detectors. To have the outer shell of the detector connected to ground potential, the cathode needs to be built in a two-layer fashion. The construction is shown in figure 11.13. The outer

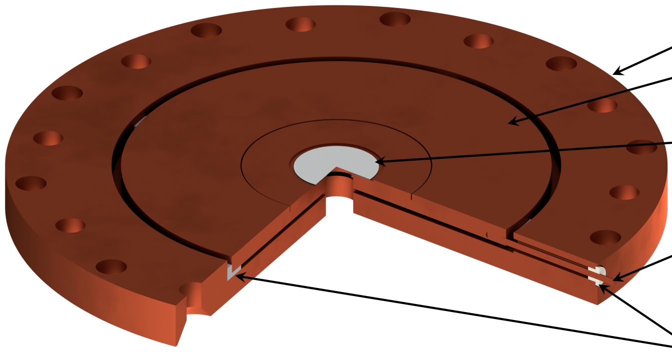

Figure 11.13: Picture of the cathode with a cut-out. The cathode consists of two main parts: the cathode housing building the outer shell which will be connected to ground potential and the cathode inside containing the window while being on high-voltage. To connect the cathode to the high-voltage a contact pin is inserted. The cathode is fixed into the cathode housing with epoxy.

shell of the cathode is the cathode housing that will seal the detector. Inside the housing, the cathode (not containing a window yet) is placed on PTFE spacers to keep it exactly in the centre and at an equal height. Then, through a hole in the side of the cathode housing, the HV contact is screwed into the cathode to electrically connect it to the outside. The pin is fixed to the centre of the hole with another PTFE spacer. The central hole for the window is then blocked with a fitting PTFE cylinder and epoxy is filled into the gap between the cathode and the cathode housing. After the epoxy is cured the PTFE cylinder is removed and the surface of the cathode is milled flat. Then the window can be placed.

During electrical tests of the cathode, two problems had to be fixed. The first problem was a too small gap between the cathode and its housing. Due to this, discharges were observed above 1 kV. After the distance was increased, still discharges could be observed. Here, the problem was that the epoxy used (Araldite Ay 103-1) was not electrically rated, hence the isolation strength was probably not sufficient for the small gaps. After changing the epoxy the cathode was successfully tested to high-voltages of 2.5 kV.

11.2.6 Sealing concept

For radiopurity reasons a new sealing concept needed to be tested as well. For this, first tests with small copper discs and gaskets made from PTFE and lead were performed. Two discs with a gasket in between formed a small test volume. The test volume was then connected to a vacuum pump and leak tested. After a successful leak test, the surfaces of the discs were inspected for marks or dents. In table 11.2

Gasket	Material	Leak-tight	Marks
Lead	Copper	Yes	No
Lead	Soft copper	Yes	No
PTFE	Copper	Yes	No
PTFE	Soft copper	Yes	No

Table 11.2: Results of the sealing tests. Soft copper describes soft-annealed copper. This was chosen since it resembles high-purity copper more closely. Leak-tight means leak rates below 10^{-11} mbar l s^{-1}.

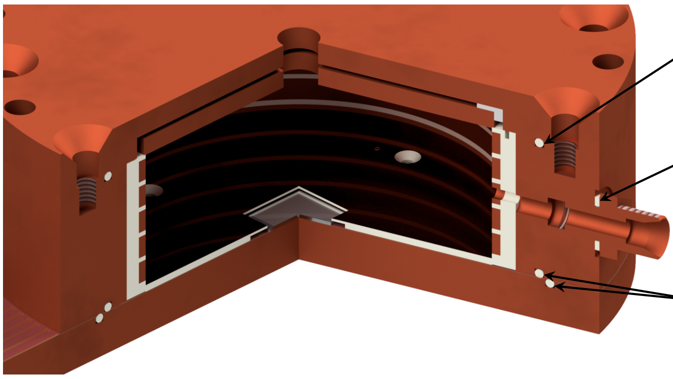

Figure 11.14: CAD view of the detector showing the different gaskets. Three gaskets are needed for the detector housing and two for the gas connectors. All gaskets are produced from PTFE.

the results are shown. Since all tests were successful, PTFE was chosen for the detector gaskets since it is the more radiopure material. For the detector five gaskets are needed: two for the gas connectors and three for the detector housing. For the gas connectors small PTFE washers are used while for the detector housing, PTFE O-rings are used. Three O-rings are necessary since the PCB needs to be sealed from the bottom and the top. This can be seen in figure 11.14. Tests with the detector housing assembled showed that the detector is sufficiently leak-tight to be operated at slight overpressure. The

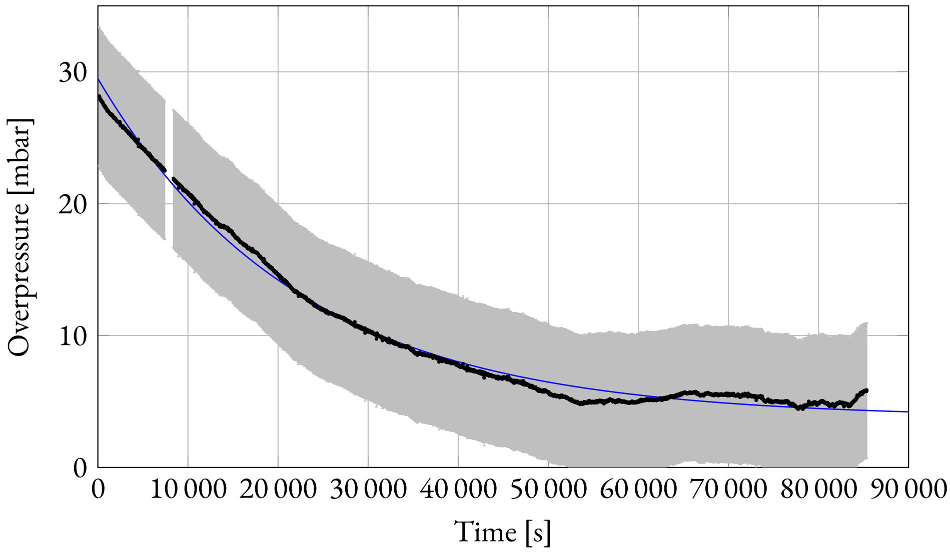

Figure 11.15: Leak test of the detector. Pressure measured with closed in- and outputs. Errors are indicated in grey. An exponential fit is shown in blue.

leak tightness was measured with the detector and is shown in figure 11.15. The data was fitted with an exponential function to calculate the time constant of the pressure decay $t_{1/2} = 15386 \pm 67$ s. However, this measurement includes the leaks of the connections to the gauges. A measurement of the leak rate without the detector failed since after dismounting the detector the leak rate was higher than with the detector. Hence, the measured leak rate can be taken as an upper bound. With the volume of the detector $V_{\mathrm{Det}} \approx 0.2\,\mathrm{l}$ the leak rate can be estimated to

$$L = \frac{V_{\mathrm{Det}}}{2t_{1/2}} = 6.6 \times 10^{-6}\,\frac{\mathrm{l}}{\mathrm{s}}. \tag{11.1}$$

This is sufficient to run the detector.

11.3 Validation of the detector

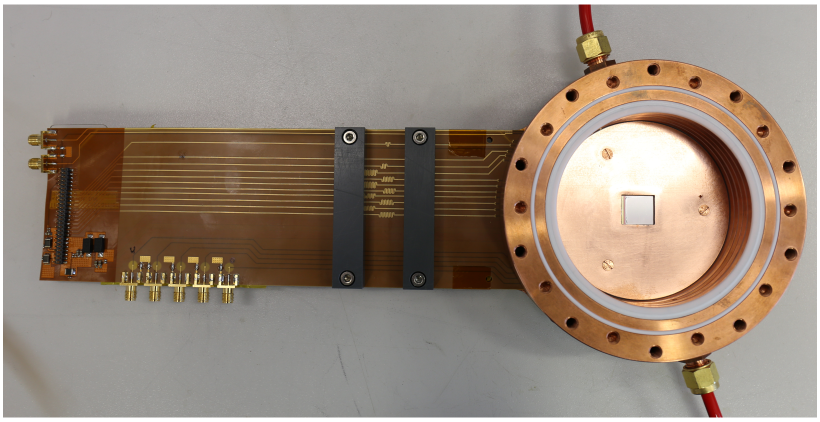

Figure 11.16: Picture of the detector with the cathode removed. The field cage, anode, and the GridPix3 are visible.

After producing all detector components, the prototype detector was set up for first tests. First, only the PCB and the chip were tested on the base plate. This already showed a first problem since one of the differential input lines was not transporting the signal properly. This was caused by a copper bridge (error from manufacturing) between the lines. After removing this, the GridPix3 was operational. Then the whole detector was mounted. A picture of the detector without the cathode is shown in figure 11.16. The anode and the GridPix3 can be seen inside the field cage. As a first test, the detector was mounted and the high-voltage system was tested with air inside. After this test, the chip was powered and tested again. Both worked fine so the gas supply was connected to perform a first measurement. After the detector was flushed with gas for several hours, the high-voltages were ramped up. During this, a breakdown of the high-voltage due to sparks could be observed. Removing the cathode and the anode again revealed that sparks occurred throughout the PCB. The result of this spark is shown in figure 11.17(a). The picture clearly shows some kind of defect on the PCB. The origin of the defect is unclear, it might be left over from the production or developed due to mishandling later. Nevertheless, after cleaning and sealing the defect with polyimide tape a second source of sparking was observed. This is shown in figure 11.17(b). The sparks between the field cage supply lines originate from a breakdown of the voltage on the uppermost supply line and the base plate through the degassing hole. This was also fixed by adding some polyimide tape. After that, one last source of sparking was identified at the cathode and solved similarly to the other problems. All these problems were only occurring with gas inside the detector hence they are attributable to Paschen's law (see section 3.5). This is shown figure 11.18. Here the breakdown voltage for a copper cathode in argon is calculated for

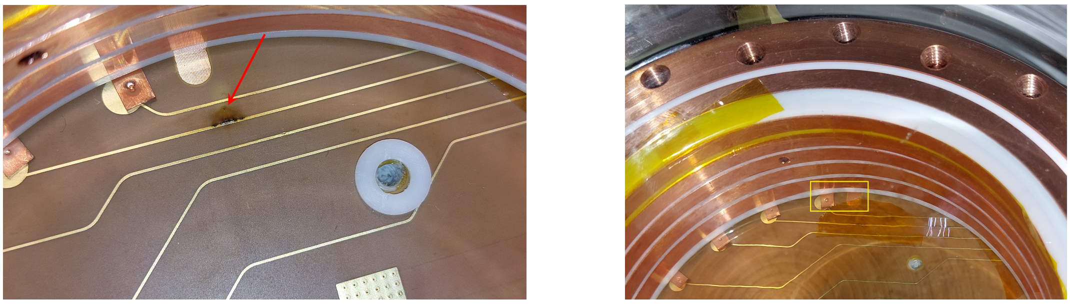

(a) (b)

Figure 11.17: Sparks observed on the PCB while operating with gas inside the detector. (a) Sparks from the field cage supply line entering a hole in the PCB (red arrow). (b) Sparks between the three field cage supply lines occur from a spark between the uppermost line and the base plate through the degassing hole (yellow rectangle).

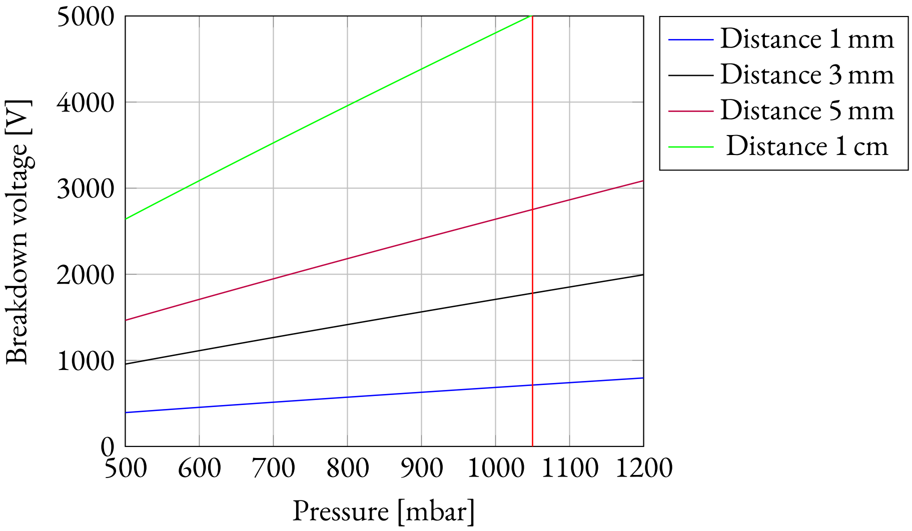

Figure 11.18: Breakdown voltage for Argon at low pressures and different distances between the cathode and the housing. The line for 1 cm is introduced to reproduce the result for argon given in [Dun88]. The red line indicates the typical used pressure 1050 mbar(a).

different gaps. The curves are fitted such that they reproduce the value given for argon at atmospheric pressure in [Dun88]. Gaps smaller than 5 mm at the cathode might lead to sparks in argon due to Paschen's law. For the other components, the gap depends on the voltage difference between them. For gaps of 1 mm or smaller voltage differences below 1 kV will already lead to sparks. After solving the problems, the detector was operational and tested, using the DAC settings described in section 10.4.2. First, the detector was calibrated. Then as a second step, a proper amplification voltage for the grid was determined. For this, different voltage settings were scanned with the ^{55}Fe source. Since the 5.9 keV photon from the Kα line should produce 224 e^{-} in argon gas the grid voltage should be set accordingly to avoid cut-offs from the threshold on one hand and to avoid additional hits from UV photons on the other hand. The results are shown in figure 11.19. It can be seen that a grid voltage of 310 V is

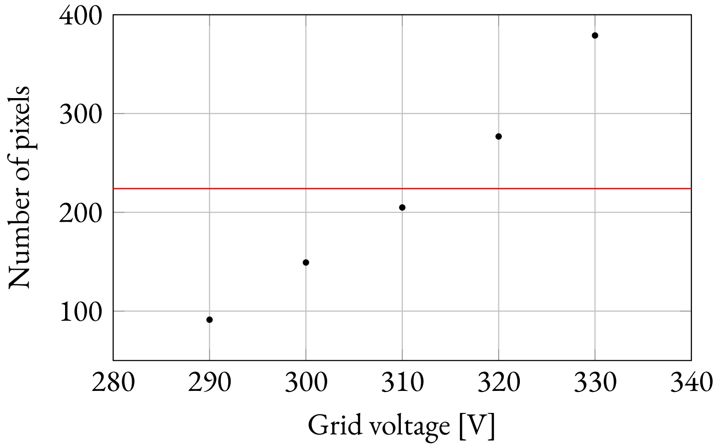

Figure 11.19: Mean from the a gaussian fit to the pixel spectrum of ^{55}Fe runs at different voltages. Error bars are to small to be visible. The expected amount of electrons produced from the ^{55} Fe Kα line is indicated in red.

slightly below the expected number of hits. Since there are always a few threshold effects, this is chosen as a sufficient value. With the grid voltage chosen, all other voltages are set to reach a drift field inside the detector of 500 V/cm. To set this, measurements are taken from the CAD model and the voltages for the drift ring are set such that the centre of each ring is on the right potential. The set voltages are

Part	Voltage in V
Grid	310
Anode	380
Ring 1	550
Ring 2	850
Ring 3	1150
Ring 4	1450
Ring 5	1750
Cathode	1925

Table 11.3: High-voltages set to the detector for operation. They are chosen such that a drift field of 500 V/cm is reached.

listed in table 11.3. With this, the detector is finally ready to take data. Since for usage at BabyIAXO or IAXO it is very important that the detector runs for long periods of time without interruptions a long term test was started with the detector. A screenshot of the monitoring of the detector can be seen in figure 11.20. It shows that the detector is running and all high-voltages show very low currents (upper left). The fluctuation between 0 nA and 40 nA is an artifact of the high-voltage module. This was tested by switching the high-voltage channels which showed no impact on the depicted current. Also, the output of the command line interface (CLI) can be seen (bottom left). Here the run time can be found as $T_{\text{run}} = 100\,\text{h}\,4\,\text{min}\,16\,\text{s}$, showing that the detector can run for more than four days without any problems. The errors printed above the run time are errors when the link FIFO on the FPGA is overflowing. These errors occurred approximately every 1.5 h. The reason for this might be small sparks produced from the grid. This is a likely scenario since the grid of the GridPix3 used was damaged. Due to charge up, a small part of the grid might move closer to the chip surface until a spark is induced, then it flips back and the procedure starts again. The pattern observed on the online monitor during these events would also fit this theory. Since a spark changes the voltage levels of the chip, the set threshold is changed for a short time. If the threshold is lowered, the pixel sends noise data. On the right part of the image online monitoring shows the current data from the detector.

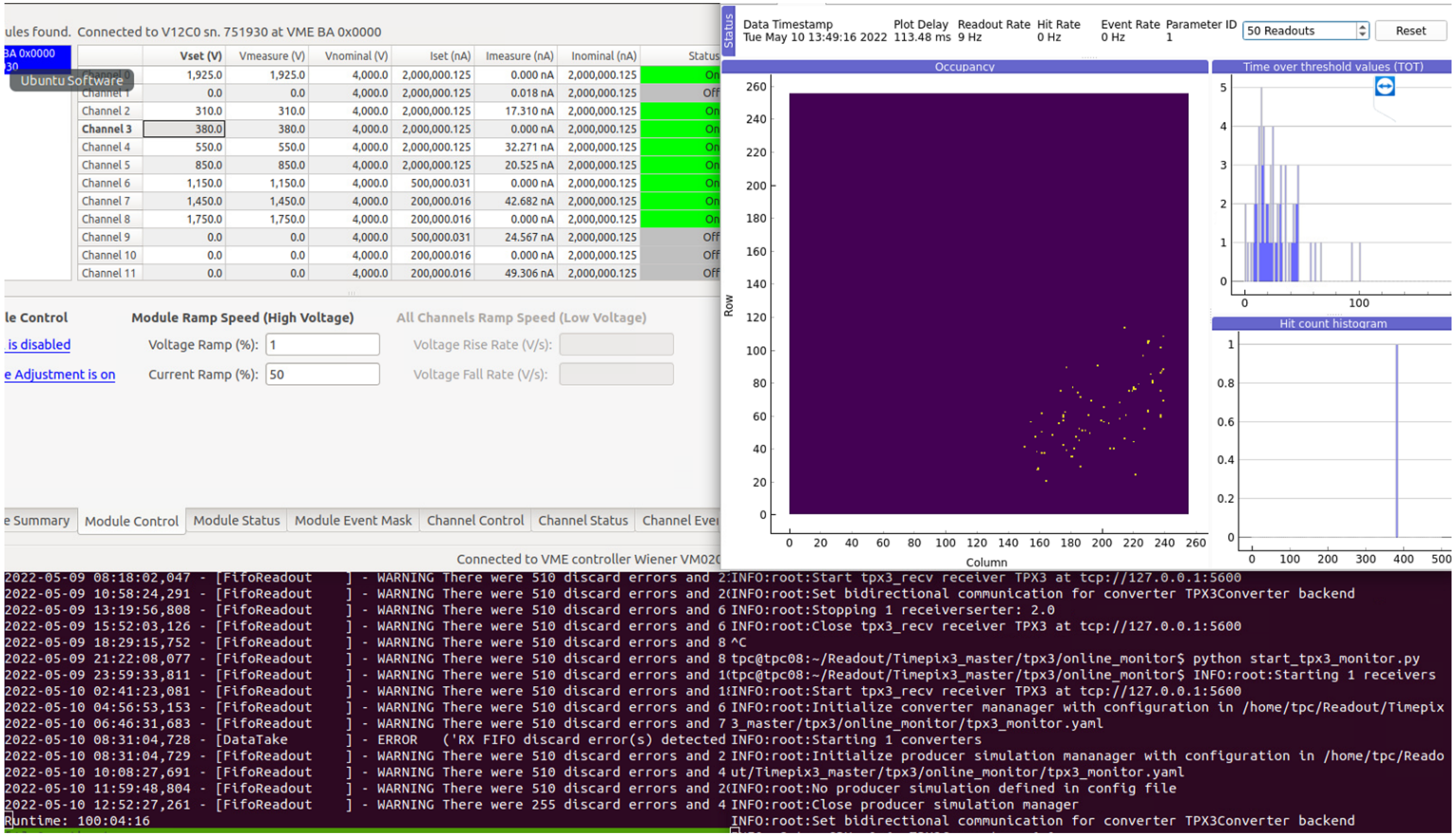

Figure 11.20: Screenshot of the monitoring of the detector. Upper left the control of the high-voltage module can be seen with all high-voltages set. Upper right an online monitor shows the data. Bottom left the CLI shows the current run time (time since the start of the run) $T_{\mathrm{run}} = 100\,\mathrm{h}\,4\,\mathrm{min}\,16\,\mathrm{s}$.

CHAPTER 12

A DETECTOR TEST STAND AT FTD

In order to have an in-house possibility to test low background detectors, a test stand is being built at the "Forschungs- und Technologie-Zentrum Detektorphysik"(FTD). For this a shallow underground laboratory is used. The laboratory is located 7 m below the surface and special low-radiation concrete is used to reduce the background. Due to the amount of concrete and earth above the laboratory, the cosmic muon flux is presumably reduced by a factor of two compared to the surface.

The test stand will feature a lead housing of $60 \times 60 \times 60\,\text{cm}^3$ surrounded by an active muon veto produced from plastic scintillators. A CAD model of the test stand is shown in figure 12.1. The lead

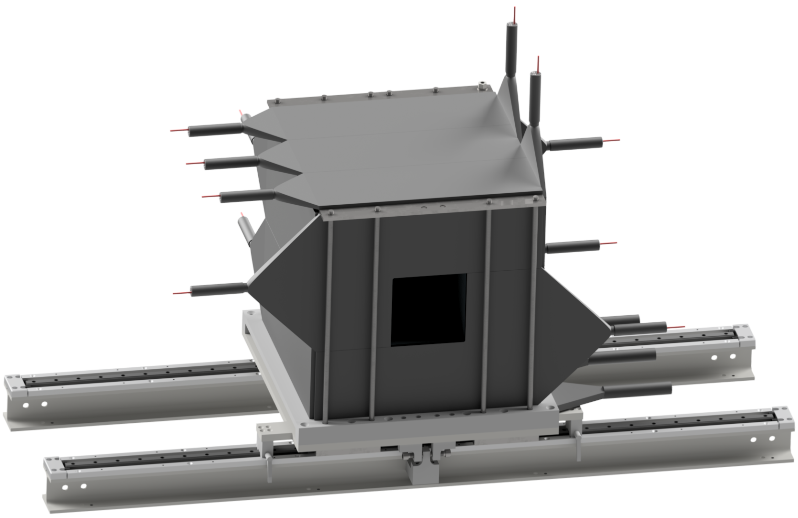

Figure 12.1: CAD render of the test stand in the closed state. The detector would be set up in the hole visible. The central stop can be seen (centre bottom). Scintillators as an active veto are arranged such that they cover almost 4π of the lead housing.

housing is mounted on a rail system such that it can be parted in the middle to allow easy access to a mounted detector. An image of the opened test stand is shown in figure 12.2. From the images, it can be seen that in the centre a hole for mounting the detector is left. The hole has a dimension of $20 \times 20 \times 35\,\text{cm}^3$. However, this can be easily adapted since the lead housing is set up from lead bricks.

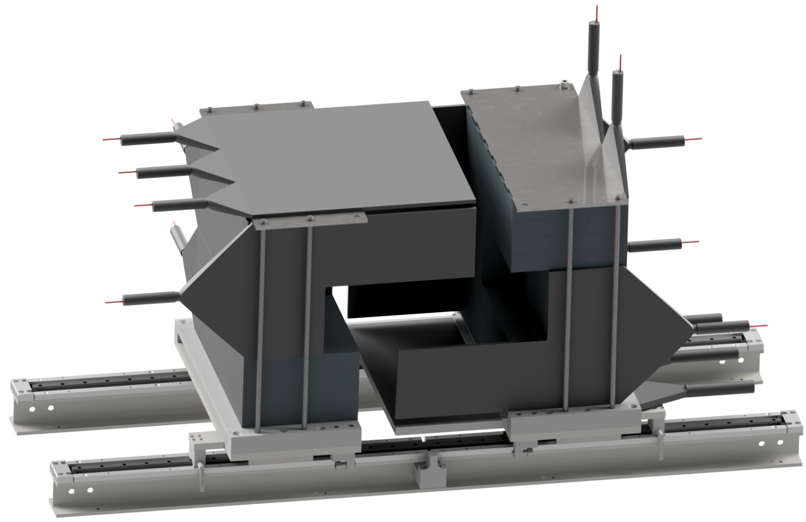

Figure 12.2: CAD render of the opened test stand, both sides can be moved individually. Scintillators are arranged such that they can be moved with the lead housing.

The scintillators of the muon veto surround the test stand by almost 4π, only in the front, a cutout of $20 \times 20\,\mathrm{cm}^2$ is left to allow the supply lines to reach the detector.

12.1 The lead housing

The lead housing consists of ≈ 2300 kg low radiation lead with an activity of 38 ± 11 Bq/kg. With this radiation level an additional background contribution of $\mathcal{O}\left(1 \times 10^{-7}\,\mathrm{counts\,cm^{-2}keV^{-1}s^{-1}}\right)$ [CL21] is expected, sufficient for first detector tests. The housing consists of standard lead bricks ($20 \times 10 \times 5\,\mathrm{cm}^3$). To adapt for different detectors also smaller lead bricks are available. The total size of the lead housing is adapted to the envisioned shielding of BabyIAXO such that test results are applicable to the final experiment. To reach for even lower background levels an additional lining of radiopure copper and PTFE might be added as shielding around the detector to absorb the emission originating from ^{210}Pb.

12.2 The rail system

The rail system is a modified version of a rail system designed for the E3 area at ELSA [Hä]. It consists of two 2 m long rails on which two wagons loaded with the lead housing will move. Each of those wagons stands on four rail gliders and will carry around 1250 kg (as a conservative approach). To ensure that the system is able to support this amount of mass some calculations on the wagons have been performed. The lead housing itself sits on a steel plate. This plate needs to support the weight without significant bending, therefore two different thicknesses of the plate were taken into account: 10 mm and 20 mm. The most important parameters are the bending stress σ_b and the total displacement f.

Following [GKM+19], the bending stress is given by

$$\sigma_\mathrm{b} = \frac{M_\mathrm{b}}{W}, \tag{12.1}$$

with the bending moment M_b, and the section modulus W given by

$$M_\mathrm{b} = \frac{Fl}{8} \text{ and } W = \frac{bh^2}{6}. \tag{12.2}$$

Here, F is the force, $l = 455.2\,\mathrm{mm}$ is the length between the two rail gliders, $b = 300\,\mathrm{mm}$ is the width, and h is the thickness of the steel plate. For the force, two values can be considered. The most conservative approach would be to take the full force of $F = 12500\,\mathrm{N}$ into account. Since the length of the lead housing (600 mm) is wider than the free length, the force acting on this length needs to be reduced to

$$F_\mathrm{red} = \frac{F}{600} 455.2 \approx 9500\,\mathrm{N}. \tag{12.3}$$

From the above, one can now give the bending stress for all four cases:

σ_b in MPa	$F = 9500\,\mathrm{N}$	$F = 12500\,\mathrm{N}$
$h = 10\,\mathrm{mm}$	108.11	142.25
$h = 20\,\mathrm{mm}$	27.03	35.56

For construction steel S235JR the maximum allowed bending stress is 160 MPa [GKM+19] for a static load and therefore all cases are good. The next step is to calculate the displacement f for the given cases, which is given by [GKM+19]

$$f = \frac{5 \cdot Fl^3}{384 \cdot EI}, \tag{12.4}$$

with E being Young's modulus (for construction steel S235JR: $E = 210\,\mathrm{GPa}$ [thy]). The second area moment I can be calculated via

$$I = \frac{bh^3}{12}. \tag{12.5}$$

From the above, we can now calculate the displacement:

f in mm	$F = 9500\,\mathrm{N}$	$F = 12500\,\mathrm{N}$
$h = 10\,\mathrm{mm}$	2.22	2.92
$h = 20\,\mathrm{mm}$	0.28	0.37

The maximum acceptable displacement is 0.5 mm [Rod]. Otherwise, the rail system might be prevented from working. Hence, the thickness needs to be at least 20 mm. Since all calculations above considered a flat steel plate without any features, a simulation with those features has been performed to confirm the result. This is shown in figure 12.3. The result of this simulation shows, that the maximum displacement is 0.06 mm and therefore even smaller than the calculated values.

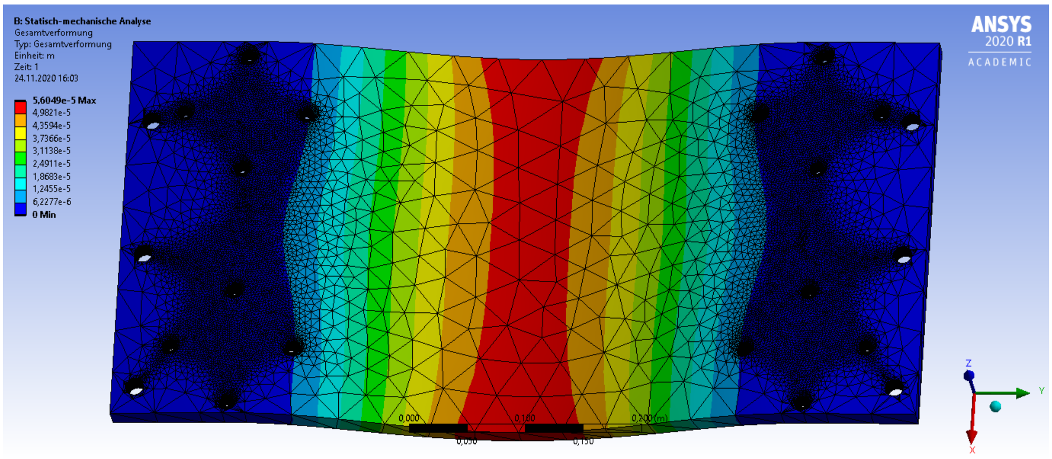

Figure 12.3: Simulation of the 20 mm thick steel plate. A force of 12500 N was applied to the surface. The maximum displacement is 0.06 mm. Simulated with ANSYS [Ans].

This steel plate is mounted on the rail gliders, where one side is fixed and one side is on floating bearings. Those bearings are made from a special plastic (iglidur® J) which has a maximum allowed surface pressure of 35 MPa [igu]. Since this pressure should not be exceeded the worst-case surface pressure on the floating bearings, meaning half the weight is sitting on one glider, will be calculated. The weight is sitting on the red surfaces shown in fig.: 12.4. The size of those is 235.6 mm for each

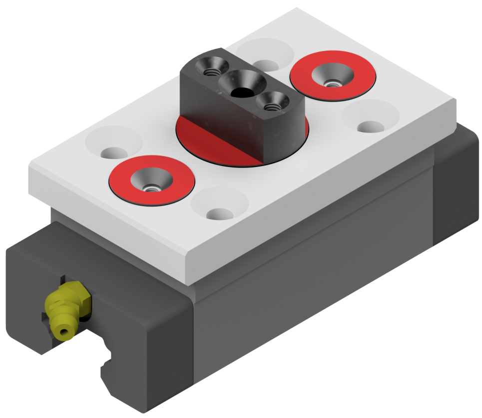

Figure 12.4: Loaded top surface (red) of the floating bearing of one of the rail gliders.

outer one and 341.6 mm for the middle bearing. Taking now a force of $F = 6500\,\mathrm{N}$ into account resting on the bearings the surface pressure p can be calculated to

$$p = \frac{F}{A} = 8.0\,\mathrm{MPa}\,, \tag{12.6}$$

with $A = 2 \cdot 235.6\,\mathrm{mm} + 341.6\,\mathrm{mm}$ as the surface of the bearing. To consider also an even worse scenario let's consider only the middle bearing being loaded. Then the surface reduced to $A = 341.6\,\mathrm{mm}$

resulting in $p = 19.0\,\mathrm{MPa}$. The opposite side of the bearings is in all cases bigger, so the bearings are also suited well.

The rail gliders (Rodriguez BRH25BL) can hold a dynamic load of 26 kN [Rod] each. This is well above everything expected to be loaded on the wagons.

The last critical part is the I-beam holding the rails. The I-beam is an IPB100-beam mounted on four concrete pillars spaced by 513.3 mm(see fig.: 12.5). For this beam again the maximal displacement

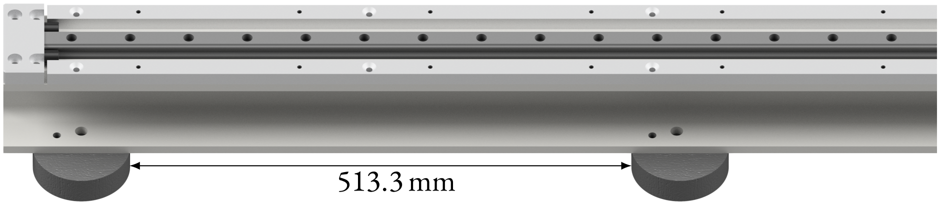

Figure 12.5: Part of the rail sitting on the concrete pillars. The free length is indicated. At the left end of the rail the stopper can be seen preventing the glider from dropping from the rail.

and the bending stress are the important parameters. For this standard beam the values for the second area moment and section modulus are tabulated: $I = 4500000\,\mathrm{mm}^4$; $W = 89900\,\mathrm{mm}^3$ [GKM+19]. To again have a worst-case scenario a point force of $F = 6500\,\mathrm{N}$ is considered to push on the beam in the middle between two concrete pillars. The bending moment M_b is in this case given by

$$M_\mathrm{b} = F\frac{l}{4} = 834.1\,\mathrm{Nm}. \tag{12.7}$$

With this the bending stress calculates to $\sigma_\mathrm{b} = 9.3\,\mathrm{MPa}$, thus considering the same steel as before the bending stress is uncritical. The displacement for this case can be calculated to

$$f = \frac{Fl^3}{48 \cdot EI} = 0.02\,\mathrm{mm}\,, \tag{12.8}$$

with $E = 210\,\mathrm{GPa}$. Again this value is well inside the margins of 0.195 mm [Rod]. Since these simple calculations do not include any cutouts or holes in the beam. To study this a FEM simulation was performed to see how the displacement changes. The simulation is shown in figure 12.6. Here, one can see that the maximum displacement is with 0.033 mm slightly bigger, which was expected due to the weakening by cutouts and holes. However, this displacement is well inside the margins.

To allow proper positioning a central stop is built into the system as well as breaks in order to fix the housing at the desired position (both seen in 12.1). At both ends of the rails stoppers are mounted to prevent the rail gliders and therefore the lead housing to drop from the rails (see fig. 12.5). Hence resulting from the calculations and simulations the rail system is feasible to move the lead housing.

12.3 Scintillators

As visible in figure 12.1 the scintillator setup consists of three shapes of scintillators. On the top and the bottom three scintillators of $20 \times 60\,\mathrm{cm}^2$ are used since there the highest muon flux will be observed.

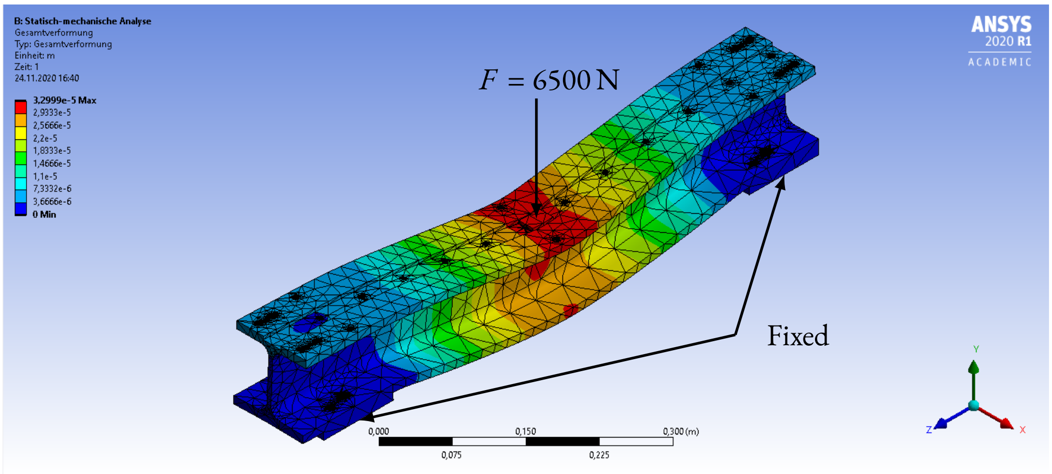

Figure 12.6: Simulation of the displacement of the I-beam under a worst-case load of 6500 N acting on a $20 \times 30\,\mathrm{mm}^2$ area in the middle of the beam. The maximum displacement is 0.033 mm. Simulated with ANSYS [Ans].

On the sides, two scintillators of $30 \times 60\,\mathrm{cm}^2$ are used and at the front two L-shaped scintillators will be mounted to allow access to the detector. All scintillators have a thickness of 15 mm and are made from BC408 [Lux]. Within a bachelor thesis [vF21], it was shown that the scintillators are able to detect $\approx 99.3\%$ of all incoming muons, hence the thickness is sufficient for a proper veto. As a next step in a bachelor [Ham22] and a master thesis [Sch24b] a readout system was developed. The system is based on a Teensy microcontroller controlling a discriminator and taking the data from the scintillators.

12.3.1 Scintillation material

The scintillation material chosen was BC408, a general-purpose plastic scintillator well suited for the efficient detection of muons. It offers a short rise time $\tau_\mathrm{r} = 0.9\,\mathrm{ns}$ and also features a rather short decay time $\tau_\mathrm{d} = 2.1\,\mathrm{ns}$ [Lux]. Thus, allowing a precise timing with a short dead time. Additionally, it was chosen to fit the rather long scintillators, hence a low light attenuation is needed. The base material of the scintillator is polyvinyltoluene. A minimal ionising muon will lose on average $\approx 2\,\mathrm{MeV/cm}$ [Par]. Thus, for 15 mm of thickness, a muon trajecting the scintillator vertically will lose 3 MeV in the scintillator. This is sufficient to detect muons reliably while providing a low noise level.

12.3.2 Readout electronics

As mentioned before the electronics were developed within two theses [Ham22, Sch24b]. As shown in figure 12.7 the setup works as follows. The signal from the photomultiplier tube (PMT) reading the scintillator is compared with the threshold produced by a DAC. If the signal of the PMT is smaller than the threshold (negative polarity) the comparator produces an output signal. The length of this output signal is the time the PMT signal is below the threshold. This signal needs to be extended to a duration the microcontroller (Teensy4.1) can process. This is done with a monostable multivibrator. Due to this, the energy information from the scintillator signal is lost, however for the use case at the test stand this information is not needed. The threshold is changeable with the microcontroller as well. Thus, a

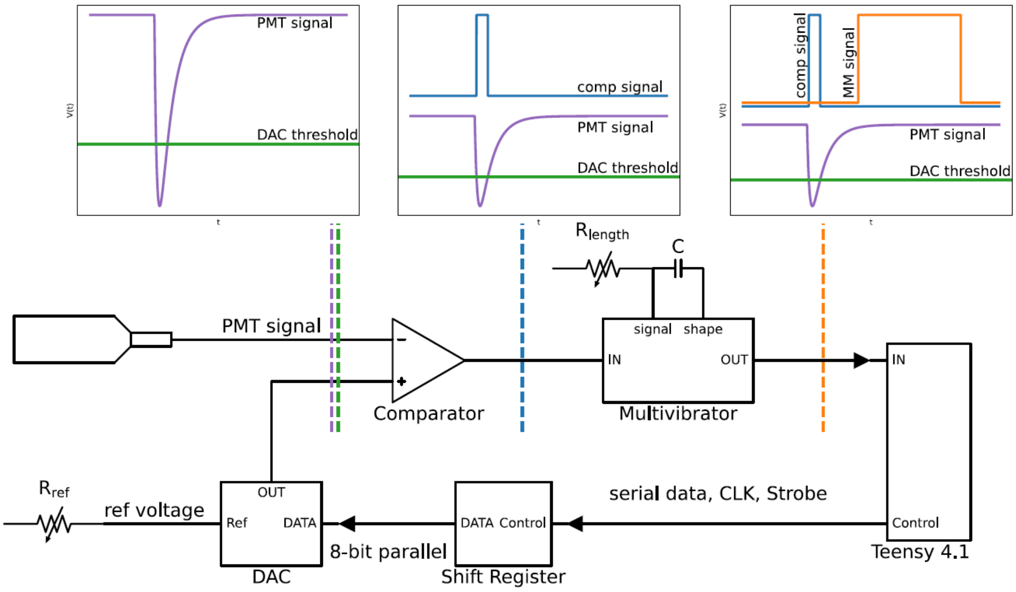

Figure 12.7: Schematic view of the setup of one discriminator channel. The Teensy controls the DAC to set the threshold for the comparator and collects the data. Since the pulse length from the comparator is too short to be measured by the Teensy a multivibrator is used to extend the pulse. Taken from [Sch24b].

fully remote controllable discriminator is set up. Since a total of 14 scintillators have to be read out and controlled for the test stand a 15-channel discriminator has been developed from this. The full system is shown in figure 12.8. Each individual channel is set up as described before. By communicating with the microcontroller the thresholds for all channels can be set and the discriminator signals are read into a 16-bit register. This register is monitored by an interrupt routine reading the register if one channel is triggered. The register is then combined with a time stamp in order to allow a combination with the data taken from the detector in the offline analysis. The time stamped register data is then pushed into a ring buffer and sent to the computer. The dead time is in the order of 100 ns. So, only a few muons should be missed. For a detailed description of the scintillator readout see [Sch24b].

12.4 Summary

A test stand was planned and the installation has started. For the test stand a rail system was designed and installed (see figure 12.9). Additionally, the lead housing is designed and the material is tested and ready for mounting. To lower the background induced by muons additionally an active scintillator veto was designed. The scintillators were tested within three theses and a remote controllable readout for the scintillators is available. Additionally in the underground laboratory, a gas cabinet was installed to enable the usage of gaseous detectors.

As the next step, the base plate to carry the lead housing has to be produced and the test stand has to be finally assembled.

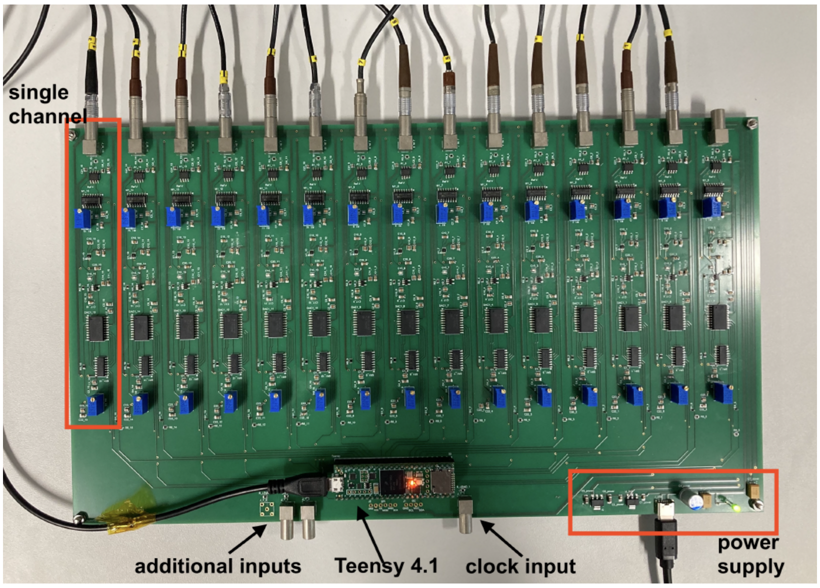

Figure 12.8: The 15-channel discriminator board. All discriminators are controlled by one microcontroller. A single channel as well as the microcontroller(Teensy4.1) are indicated. Taken from [Sch24b].

Figure 12.9: The rail system for the test stand mounted in the shallow underground laboratory of the FTD. The rails are mounted on 2 m long steel beams. Cross-beams connecting the rail gliders can be seen on which later the steel plate for the lead housing will be mounted.

CHAPTER 13

Reconstruction and measurement principles

In this chapter, the data analysis chain as well as typical parameters used within this thesis will be discussed. In section 13.1, the data preparation with the TimepixAnalysis framework will be discussed. After that, a short example of a typical signal and background event of the detector will be given. Section 13.3 presents the ^{55}Fe source typically used for calibration runs. In section 13.4 the determination of the gas gain with different methods will be discussed. Afterwards, the calculation of the energy resolution of the detector is introduced (sec. 13.5). Finally, the effective gain difference between GridPix and GridPix3 is discussed in section 13.6.

13.1 Data preparation

The data taken with the GridPix detector is interpreted and analysed within the TimepixAnalysis framework. A very detailed description of this can be found in [Sch24a, Schb]. Here, only a short overview will be given. The framework takes the raw data taken either with Timepix or Timepix3 and processes the data in multiple steps. The first step is the `raw_data_manipulation`. For Timepix this step first converts the ASCII files into a HDF5 [Theb] data structure, while at the same time removing empty frames. Also pixels with ToA/ToT values outside a predefined window can be removed in this step. For Timepix3 this step is similar. However, since the data is taken in a continuous stream and zero suppressed, no frames are recorded. Therefore, the data has to be reframed by its ToA values. Note that this means the `raw_data_manipulation` does so far not work if no ToA data is taken in data-driven mode. To define the end of a frame the difference in ToA from one hit pixel to the next must be larger than a settable number of clock cycles (typically 100) of the ToA, to avoid single events being split up.

After the `raw_data_manipulation` the steps are the same for Timepix and Timepix3 data. The next steps are performed using the `reconstruction`. The `reconstruction` first uses a cluster-finding algorithm in order to separate clusters in one frame. For this purpose two different algorithms are implemented: The default approach (used here and in [Kri18, Sch24a]) looks for neighbouring pixels in a square of length l around a pixel. If a neighbour is found this starts another square looking for neighbours. If no new neighbouring pixels found anymore the cluster is defined. The second algorithm is DBSCAN [EKS+96], which utilises a density-based approach and can therefore better distinguish between clusters in near proximity. After all clusters are found, the following geometric and time properties are calculated and saved within the file:

- `x`: The x-coordinate of each pixel in the cluster
- `y`: The y-coordinate of each pixel in the cluster
- `ToA`: The ToA Values for each pixel in the cluster
- `ToACombined`: The extended ToA values for each pixel in the cluster
- `ToT`: The ToT Values for each pixel in the cluster
- `centerX`: The centre of the cluster in x-direction in mm
- `centerY`: The centre of the cluster in y-direction in mm
- `eccentricity`: The eccentricity ϵ of the cluster
- `fractionInTransverseRMS`: The fraction of pixels within a circle of radius transverse RMS around the centre of the cluster
- `hits`: The number of hit pixels in the cluster
- `kurtosisLongitudinal`: The fourth statistical moment of the long axis of the cluster
- `kurtosisTransverse`: The fourth statistical moment of the short axis of the cluster
- `length`: The length of the long axis of the cluster
- `lengthDivRmsTrans`: The `length` of the cluster divided by `rmsTransverse`
- `rmsLongitudinal`: The RMS value of the long axis of the cluster
- `rmsTransverse`: The RMS value of the short axis of the cluster
- `rotationAngle`: The rotation angle of the long axis of the cluster
- `skewnessLongitudinal`: The third statistical moment of the long axis of the cluster
- `skewnessTransverse`: The third statistical moment of the short axis of the cluster
- `sumTot`: The total ToT of the cluster
- `toaKurtosis`: The fourth statistical moment of the ToA distribution within the cluster
- `toaLength`: The length of the cluster in time
- `toaMean`: The mean of the ToA distribution within the cluster
- `toaMin`: The minimal ToA value of the cluster
- `toaRms`: The RMS value of the ToA distribution within the cluster

- `toaSkewness`: The third statistical moment of the ToA distribution within the cluster
- `width`: The length of the long axis of the cluster

In order to calculate most of these properties the first step is to rotate the coordinate system to align the long axis of the cluster to the y-axis of the chip. With this coordinate system, the other geometric properties can be calculated. The eccentricity is defined as [Sch24a]

$$\epsilon = \frac{\max(x_{\mathrm{RMS}}, y_{\mathrm{RMS}})}{\min(x_{\mathrm{RMS}}, y_{\mathrm{RMS}})} \geq 1\,. \tag{13.1}$$

Here, the RMS is synonymously used for the standard deviation. After the `reconstruction`, calibrations can be applied to deduce further properties. For example, a charge calibration converting the ToT values into charge values can be applied for further use. Using the result of a ToT calibration scan performed for Timepix(3) a charge value can be computed for each ToT value. As a result, two new properties are applied to the HDF5 data structure:

- `charge`: The charge value for each pixel of the cluster
- `totalCharge`: The total charge of the cluster

All these properties together can be used to monitor the integrity of the recorded data. Furthermore, they can be used to apply cuts during the further analysis steps.

13.2 Typical event

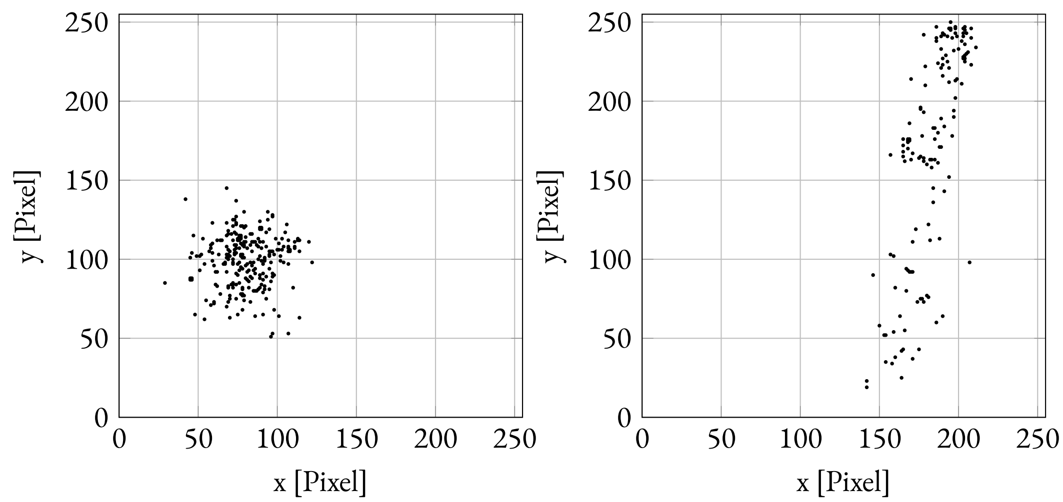

(a) X-ray-like event (b) Background-like event

Figure 13.1: An X-ray (a) and a background (b) event of the GridPix3.

A typical background event and a typical X-ray event are shown in figure 13.1. It can be seen that for a background event (cosmic muon) a track is recorded in the detector while a photon leaves a round shape. Due to these properties most of the cosmic background can be reduced by a cut on the eccentricity value. However, not all muon events will look like this. If the muon enters the detector orthogonally to the GridPix readout plane, the resulting hit distribution can mimic a photon event. These events can either be tagged by scintillators (see chapter 8) or resolved with the information from the ToA. Since a photon basically converts at one point of the detector volume, all primary electrons arrive roughly at the same time on the GridPix. The muon however traverses the detector and produces electrons along its track. These electrons will reach the amplification gap and hence the readout in a time span given by the height of the gas volume and the drift speed for the electrons in the gas. Thus, a cut on the `toaLength` parameter can be used to further reduce the background (see section 14.2).

13.3 The iron-55 calibration source

For testing and calibration purposes typically a ^{55}Fe-source is used, which decays via electron capture into ^{55}Mn. The missing electron will then be filled up from the outer shells by either releasing an Auger electron or emitting X-rays to radiate the leftover energy. The emitted Auger electrons have energies around 5 keV and will be absorbed from the encapsulation of the source or by the surrounding air [BCZC]. The energies of these emission lines can be found in table 13.1. It can be seen that four emission lines with energies above 1 keV are available: $K\alpha_1$, $K\alpha_2$, $K\beta_{1,3}$ and $K\beta_5$. Those lines amount to $\approx$ 98% of the X-ray emission [Cas]. Energies below 1 keV can be neglected since they will be absorbed by the material encapsulating the ^{55}Fe-source and by air. The $K\alpha_1$ and the $K\alpha_2$ have nearly the same

Line	Energy in keV
$K\alpha_1$	5.88765
$K\alpha_2$	5.89875
$K\beta_{1,3}$	6.49045
$K\beta_5$	6.5352
$L\alpha_{1,2}$	0.6374
$L\beta_1$	0.6488
$L\beta_{3,4}$	0.721
$L\eta$	0.5675
Ll	0.5563

Table 13.1: X-ray emissions lines from the ^{55}Fe decay. Data from [Bea67]

energy (difference of $\approx$ 10 eV) and also the $K\beta_{1,3}$ and $K\beta_5$ (difference of $\approx$ 40 eV) are very similar. Thus, in the scope of this thesis the four lines can be treated as two lines, called $K\alpha$ and $K\beta$ in the following. Regarding the ratio between $K\alpha$ and $K\beta$ different numbers are found in the literature (e.g. $\approx$ 0.115 [Yal07, Boo01] or $\approx$ 0.135 [LpPM94, BJBL01]. In the scope of this thesis, the following ratio will be used:

$$\frac{K\beta}{K\alpha} = 0.125. \tag{13.2}$$

13.4 Gas gain determination

To characterise the stability and the properties of a gaseous detector the gas gain is one of the key parameters. It is not possible to precisely determine the average gas gain for the GridPix detector due to multiple systematic effects. However, an estimate for an effective gas gain can be obtained using data sets from mono-energetic X-ray sources/lines. To monitor the stability of the GridPix detector and directly compare results of different GridPixes the effective gas gain for a single electron needs to be measured. For this purpose, three different methods of estimation were used and will be compared in the following. For the measurements, the ^{55}Fe-source described in section 13.3 is used providing two nearly mono-energetic X-ray emission lines. The data then is processed as explained in section 13.1. After this cuts on the geometric properties are applied to reduce the number of non X-ray events. First a cut on the eccentricity $\epsilon \leq 1.3$ in order to only allow X-ray-like events. Additionally, the centre of the clusters needs to be at least 50 pixels away from the borders of the pixel matrix to avoid truncated events. At last, a cut is applied allowing only clusters with more than 5 pixels active. With these cuts, the number of clusters is reduced by about 50% (non X-ray events and events close to the edges of the chip).

The first method is a classical fit of a Pólya-distribution to the charge spectrum of the pixels. The Pólya-distribution itself does not arise from the physics of gas amplification, however it describes the typical charge spectrum of Micromegas like gas amplification stages (see section 3.3). The following representation of the Pólya-distribution will be used [BRR08] to fit the measured charge distribution:

$$P(x, \theta, k, G) = \frac{k}{G} \frac{(\theta + 1)^{(\theta+1)}}{\Gamma[\theta + 1]} \left(\frac{x}{G}\right)^{\theta} \mathrm{e}^{-(\theta+1)\frac{x}{G}}, \tag{13.3}$$

where $\Gamma[z]$ is the gamma function, k is a scaling factor, θ determines the width of the function and G is the mean gas gain. The variance is given by:

$$\sigma^2 = \frac{G^2}{\theta + 1}. \tag{13.4}$$

Function 13.3 was fitted to the charge per pixel spectrum of the data as shown in figure 13.2. The data is smoothened via a running mean over the direct neighbours to smooth out local fluctuations disturbing the fit quality. The threshold of the pixel matrix was set to a value corresponding to 471 e^-, which is indicated as a red line in the figure 13.2. Due to small deviations between the pixels, this threshold is not exactly the same for all pixels. Therefore, the first five histogram bins in the charge spectrum are not taken into account for the fit. It can be seen that the fit quality is not very good since the fit is not following the data very well. First, the dip in the spectrum observed with the GridPix3 is not modelled within the Pólya-distribution. This might be just an unknown problem of the specific GridPix3 used for this test. However, the second problem, the distribution of the threshold, is valid for both, GridPix and GridPix3. Looking at the charge spectrum of a single pixel (see figure 13.3) shows that both problems do not disappear, indicating that also on the pixel level systematic influences of the threshold occur. Also, the unexpected dip in the spectrum occurs for a single pixel, pointing towards either a problem in the design of the pixels or the analog frontend of this GridPix3. Thus, it is unclear which data points should be left out of the fit. In the attempt to observe differences in the behaviour of the fit and, respectively the gas gain G a similar measurement with a GridPix was taken (see fig.: 13.4). Both detectors were operated in similar conditions with comparable thresholds. The

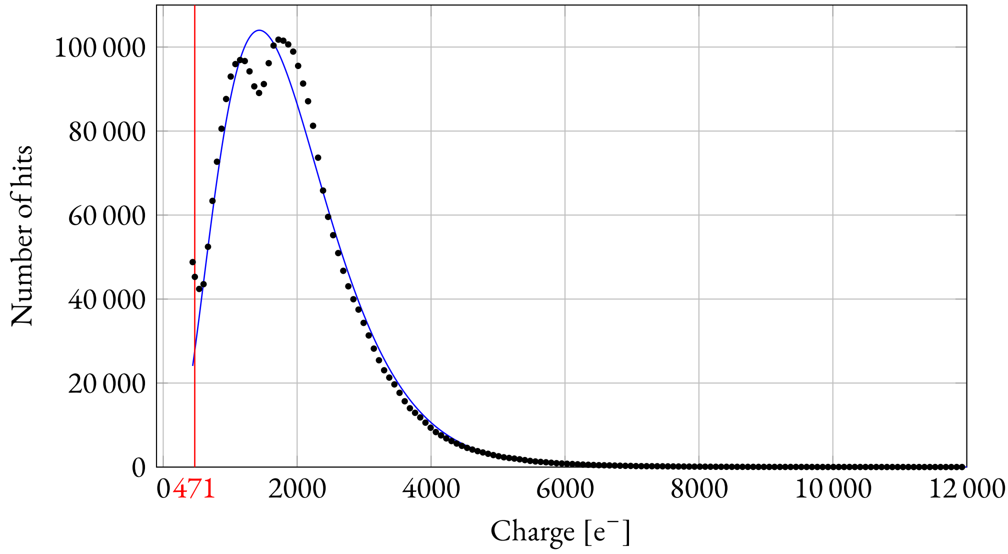

Figure 13.2: Charge per pixel histogram for a GridPix3. The set threshold is indicated in red. The fitted Pólya-distribution is shown in blue. Due to the dip in the data the function is not describing the data well. For fitting, the first five data points are not used. Errors included but not visible.

fit to the charge spectrum of the GridPix shows a better agreement. Again the threshold (455 e^-) is shown in red. The cutoff for the fit was also the first five histogram bins. As the next step, this fit was done for cutoffs from 0 to 40(90) histogram bins. The results are shown in figure 13.5. The results show that the fit strongly depends on the peak of the distribution. Therefore, any modification of the peak height and position will have a strong impact on the result. This is visible for the GridPix3 data. Here, due to the double peak, the gain determined from the fit rises after cutting out the first peak and then drops sharply after the second one. At a cut value of 5 histogram bins, which seems a value in the stable region the gain is determined to $G_{\text{pólya,TPX}} = 2811 \pm 19\,e^-$ and $G_{\text{pólya,TPX3}} = 1914 \pm 10\,e^-$ using argon(97.7%)-isobutane(2.3%) at 1050 mbar(a).

The second method to estimate the gas gain is to compare the peak positions of the total charge spectrum and the hit pixel spectrum of the data taken with the ^{55}Fe source. The spectra are obtained by calculating the total charge/hit pixels for each photon event. Both histograms are shown in figure 13.6. These histograms can be described with a double Gauss-function in the form of a convolution of the photo peak and the escape peak:

$$g(x, a, b, \mu_{\text{esc}}, \mu_{\text{pho}}, \sigma_{\text{esc}}, \sigma_{\text{pho}}) = a \cdot e^{-\frac{1}{2}\left(\frac{x-\mu_{\text{esc}}}{\sigma_{\text{esc}}}\right)^2} + b \cdot e^{-\frac{1}{2}\left(\frac{x-\mu_{\text{pho}}}{\sigma_{\text{pho}}}\right)^2} . \tag{13.5}$$

Here $\mu_{\text{esc}}, \mu_{\text{pho}}$ gives the mean of the fit and $\sigma_{\text{esc}}, \sigma_{\text{pho}}$ is the standard deviation while a and b are just scaling factors. It should be stated at this point that this is for the ^{55}Fe source, not the real fit function since the source emits photons at two energies close to each other (see section 13.3). This would in principle result in the necessity to fit four Gauss-functions to the spectrum. Two for the photo peak and two for the escape peak. For the determination of the gas gain with this method, the additional error is very small $O(0.1\%)$ and therefore negligible. Since a fit with only two Gauss-functions is also more stable it is chosen. One can take the mean values μ_{esc} and μ_{pho} of the pixel and the total charge

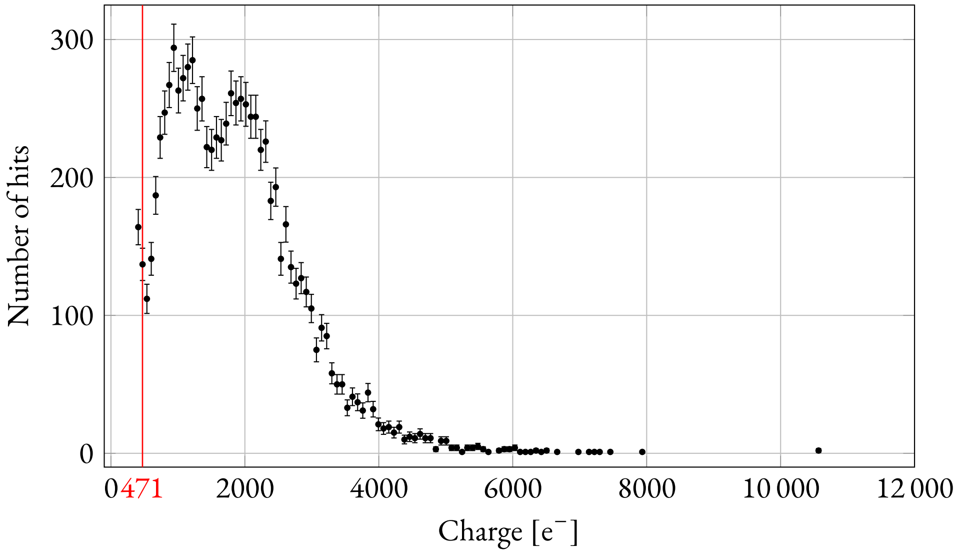

Figure 13.3: Charge histogram for the single pixel[128,128]. The set threshold is indicated in red. No clear cutoff is observable at the set threshold. The data shows the same behaviour as the full chip shown in figure 13.2.

spectrum and divide them by each other resulting in an expression for the effective gas gain $G_{\text{pho/esc}}$ for either the photo peaks (pho) or the escape peaks (esc):

$$G_{\text{pho/esc}} = \frac{\mu^{\text{charge}}_{\text{pho/esc}}}{\mu^{\text{pixel}}_{\text{pho/esc}}}. \tag{13.6}$$

From this formula and the fit parameters of the two spectra, one can then compute gain values. The parameters and the gain can be found in table 13.2. This method is already more robust than the first

	Photo peak	Escape peak
μ^{pixel}	274.4 ± 0.3	139.4 ± 0.7
σ^{pixel}	21.05 ± 0.24	16.46 ± 0.63
μ^{charge}	$506706 \pm 506\,\text{e}^-$	$257930 \pm 1173\,\text{e}^-$
σ^{charge}	$47735 \pm 381\,\text{e}^-$	$33773 \pm 1015\,\text{e}^-$
G	$1846.7 \pm 0.2\,\text{e}^-$	$1813.5 \pm 1.3\,\text{e}^-$

Table 13.2: Fit parameter from the fit to the double Gauss-function to the total charge spectrum and the pixel spectrum. The gain G is calculated from these values.

method using a fit of the Pólya-distribution. However, changes in the gain during the measurement can not be determined. In addition large statistics are necessary to get a reliable result. Overall this method overestimates the gain, since pixels with low deposited charge, below the threshold, will not show up in the histograms and therefore one has an overall higher charge per pixel. Also, if two electrons enter one hole a higher charge will be measured by the pixel below, adding to the overestimation. This behaviour

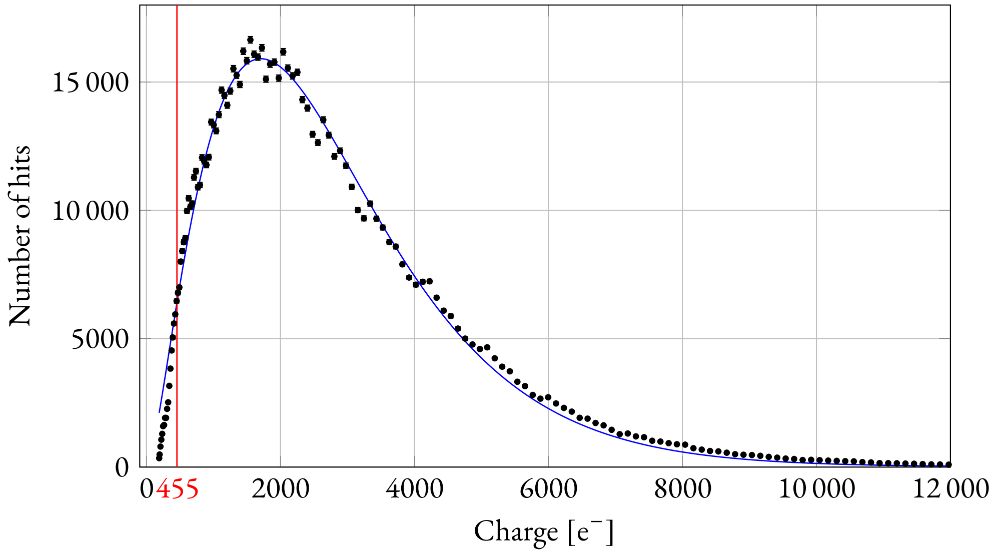

Figure 13.4: Charge histogram for a GridPix. The set threshold is indicated in red. The fitted Pólya-distribution is shown in blue. For fitting, the first five data points are not used. Errors included but not visible.

can be tested using a simulation developed within [Gru]. In this simulation, a photon is transported through the gas volume until it interacts with the gas. Then the corresponding primary electrons are traced until they hit the plane of the grid. For each electron the ToT of the pixel is increased by one. Thus dividing each event's total ToT by the number of hit pixels leads to the ratio of double hits. The result of the simulation can be seen in figure 13.7. It clearly shows that for low energies almost no double hits occur. This is expected since low energetic photons will be absorbed by the gas almost at the window and the corresponding events will diffuse across the full detector length. For higher energies the probability rises that the photon travels further. Hence the electrons will diffuse less. Additionally, more electrons are produced raising the chances for double hits. At 3500 eV a small kink is visible. This kink is expected due to the argon Kβ-line at 3190 eV [Boo01]. Here, the absorption probability rises again, and therefore the photons will convert closer to the window. Overall the effect of double hits is not negligible for energies above 1.5 keV. For measurements with the ^{55}Fe source, about 7% of the pixels are hit by two electrons. Another possible influence could be contributed by noisy/broken pixels but due to their random behaviour, this effect should average out.

The third method to estimate the gas gain is the calculation of the mean charge per pixel per event. This means for each event the total charge of the event is divided by the number of hit pixels of the event. Then the results are arranged as a scatter plot and a fit to a constant is performed. As an example, the first 1000 events of the calibration run are shown in figure 13.8. Fitting the mean to this distribution works already for low numbers of recorded events and therefore gives a good measure for the detector stability. The change of the gain over time will be visible in the data as also short-term changes affecting only a few 100 events, to which the previous methods are not sensitive. To reduce the influence from outliers a Gauss-function can be fitted to the histogram of all events and then everything outside of the $n\sigma$ region can be cut away. The result of such cuts is shown in figure 13.8. After the cuts, the mean can be calculated on the reduced data sets. It has to be stated that the fit of the Gauss-function needs

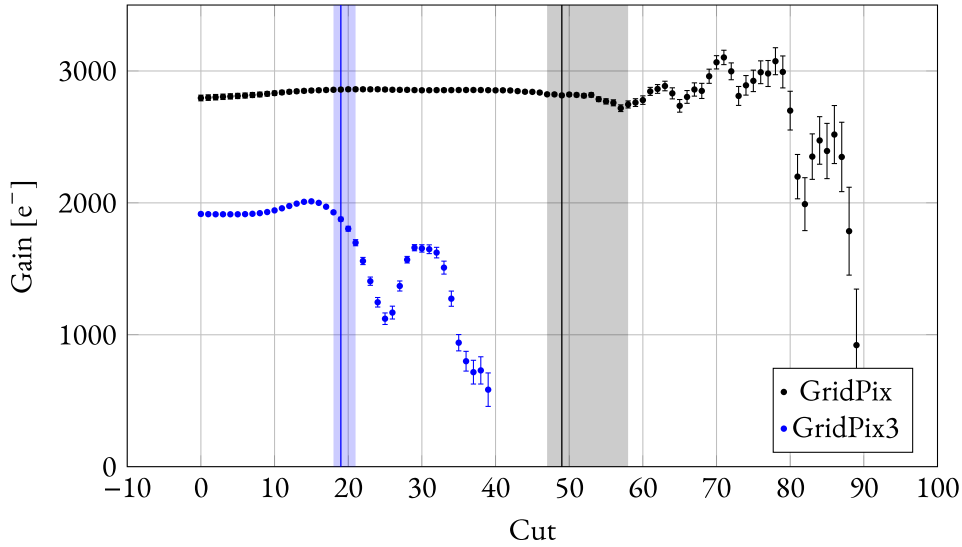

Figure 13.5: Gain from the Pólya-distribution for different data cuts. The cut value gives the number of data points cut away from the beginning of the distribution. The shaded areas indicate the positions of the highest peak of the distributions with the solid line indicating the highest value of the peak.

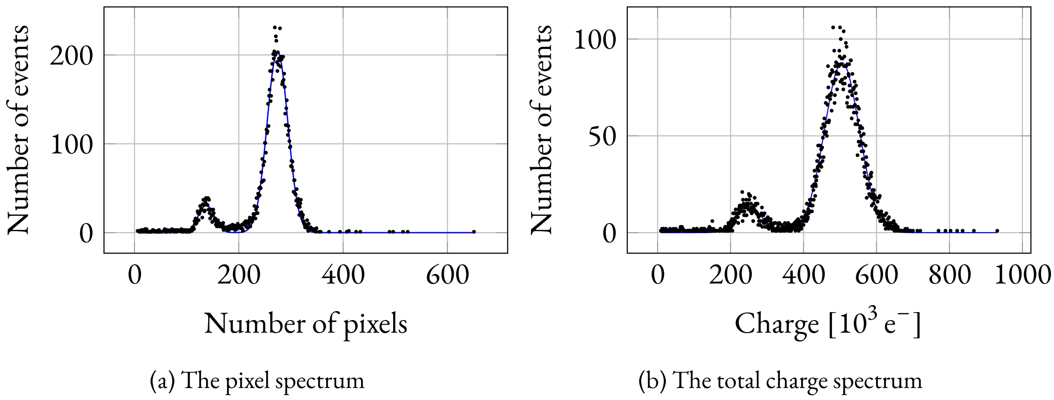

Figure 13.6: The pixel (a) and the charge spectrum (b) of the GridPix3 calibration run with ^{55}Fe. Errors are not indicated for higher visibility. The gaussian fits (blue) are also shown.

a larger set of events to produce proper results and therefore is not suited for online monitoring of the detector. To see if the data shows an overall slope a linear function can also be fitted to it. For the presented case the slope is $(-1.88 \pm 0.35) \times 10^{-3}\,e^-$, hence the gain can be considered stable. The results for the four data sets are listed in table 13.3. It can be seen that except for the cut to 1σ the results for the different cuts are compatible within two standard deviations. This shows the reliability of the method. However, it also overestimates the gain due to the inability to tackle the loss of low charge hits cut by the threshold and double electron counting effects. But it is the most robust one since the fit is very stable and relies on the smallest data set to get an estimate. Additionally, it will show changes in the gas gain even for small time windows, thus having the best properties for online monitoring of the detector.

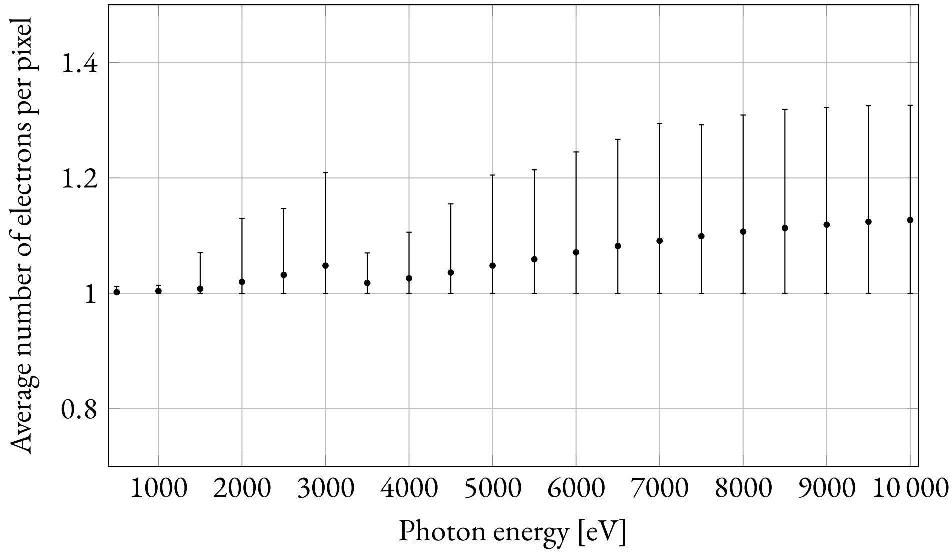

Figure 13.7: Average number of electrons per pixel for different photon energies. Simulation with 10000 photons per energy. It can be seen that for low energies almost no double hits (two electrons enter one pixel) occur. For higher energies, the number of double hits reaches almost 13%. The kink at 3500 eV is due to the argon Kβ-line raising the absorption.

G_{full}	$1832.6 \pm 1.2\,e^-$
$G_{3\sigma}$	$1829.4 \pm 1.0\,e^-$
$G_{2\sigma}$	$1830.1 \pm 1.0\,e^-$
$G_{1\sigma}$	$1839.2 \pm 0.7\,e^-$

Table 13.3: Gain from the mean charge per pixel per event method. The gain for the complete data as well as for the reduced data is shown.

A comparison of the results from all methods is shown in figure 13.9. It can be seen that the two later methods provide results within a 2σ interval while $G_{\text{pólya}}$ is far off towards higher gains. This shows that the estimation via the Pólya-distribution does not provide a conclusive result since the other methods already yield an overestimation of the gain. Therefore, the result of using the Pólya-distribution should be lower than all other cases. Since the results of the other methods coincide, the mean charge per pixel per event, as it has the most robust fit, will be used within this thesis if not otherwise stated.

The effect of the overestimation due to the threshold cut can be demonstrated by a set of measurements at different thresholds, to then interpolate to a threshold of zero. The results for such a measurement at three different voltages and 14 different thresholds can be seen in figure 13.10. It can be seen that a linear fit describes the data well. The results from the fits are listed in table 13.4. From the parameter b one can read the resulting effective gain. But as it is the effective gain the cutoff due to the pixel size needs to be taken into account. Also, it shall be stated that a linear fit is not a proper description for the data, since the threshold as a gaussian distribution cuts with rising thresholds more and more into the gas gain distribution. Due to the unknown parameters of the gaussian distribution and the partly unknown shape of the gas gain distribution, no further modeling is possible.

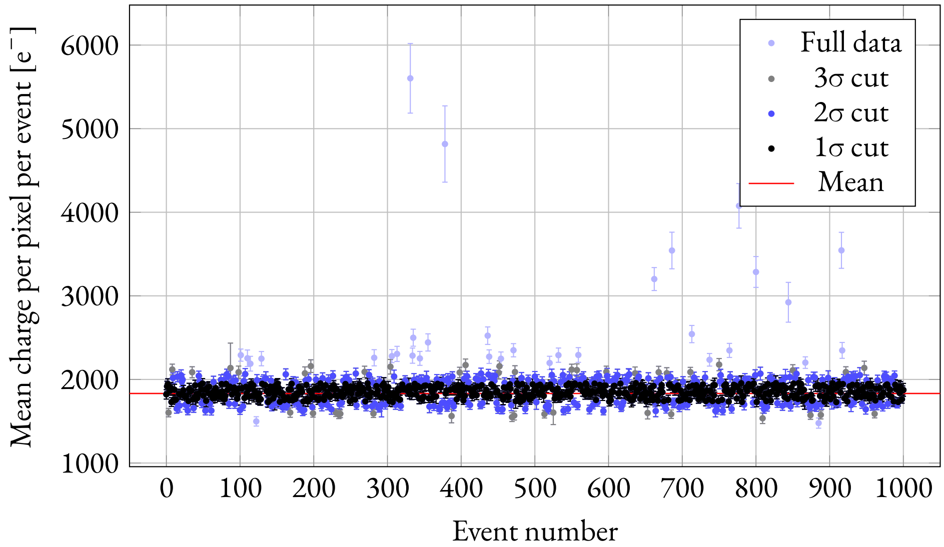

Figure 13.8: Distribution of the mean charge per pixel per event shown for the first 1000 events of the used GridPix3 run. In different colours also sets for different cuts around a Gauss-function fitted to the histogram of all events are shown.

Voltage in V	a	b in e^-	χ^2/n.d.o.f.
310	0.766 ± 0.008	1327.03 ± 9.51	3.06
315	0.786 ± 0.011	1527.19 ± 13.61	5.87
320	0.667 ± 0.014	1991.12 ± 17.12	12.62

Table 13.4: Results of the linear fit $f(x) = ax + b$ for the measurement shown in figure 13.10. It can be seen that the effective gain b rises with the grid voltage.

13.5 Energy resolution

The energy resolution is an important feature of the detector. For a given energy E it can be determined by a gaussian fit to the corresponding peak in the energy or pixel spectrum (see fig. 13.6). From the fit, the mean μ_{peak} and the width σ_{peak} then lead to the energy resolution ϵ_E via:

$$\epsilon_E = \frac{\sigma_{\text{peak}}}{\mu_{\text{peak}}} . \tag{13.7}$$

For example, for the calibration run data this can be determined from either the photo or the escape peak. The mean and the width for the fits can be found in table 13.2. However, the fit uses only one instead of two gaussian functions per peak representing the two close-by lines of the ^{55}Fe source. Therefore a comparison with fits containing two gauss functions per fit has to be performed. The full

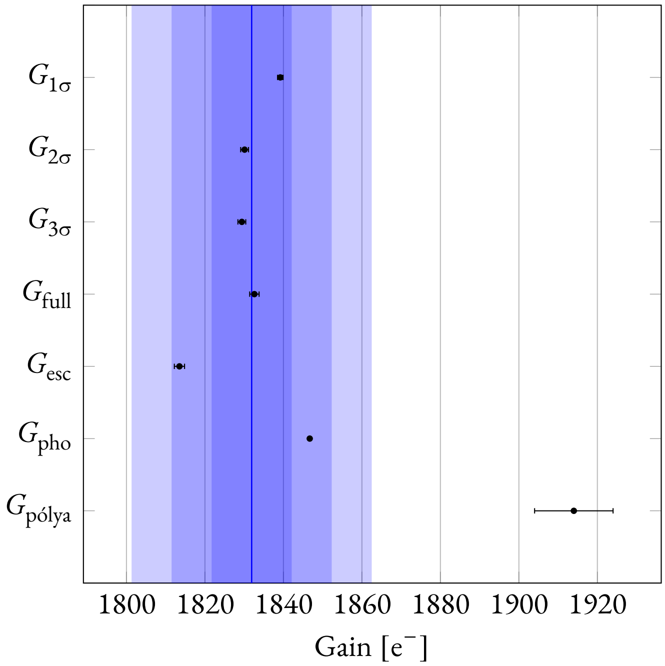

Figure 13.9: Comparison of the results for the gain from the different methods. Mean and standard deviation were calculated without the $G_{\text{pólya}}$ data. All values coincide within a 2σ confidence interval, except for the determination from the Pólya-distribution (see blue shaded regions for 1, 2, and 3σ).

representation for this fit would be a convolution of four gaussian functions:

$$g(x, a, b, c, d, \mu_{\text{K}\alpha,\text{esc}}, \mu_{\text{K}\beta,\text{esc}}, \mu_{\text{K}\alpha,\text{pho}}, \mu_{\text{K}\beta,\text{pho}}, \sigma_{\text{K}\alpha,\text{ esc}}, \sigma_{\text{K}\beta,\text{ esc}}, \sigma_{\text{K}\alpha,\text{ pho}}, \sigma_{\text{K}\beta,\text{ pho}}) =$$
$$a \cdot \mathrm{e}^{-\frac{1}{2}\left(\frac{x-\mu_{\text{K}\alpha,\text{ esc}}}{\sigma_{\text{K}\alpha,\text{ esc}}}\right)^2} + b \cdot \mathrm{e}^{-\frac{1}{2}\left(\frac{x-\mu_{\text{K}\beta,\text{ esc}}}{\sigma_{\text{K}\beta,\text{ esc}}}\right)^2} + c \cdot \mathrm{e}^{-\frac{1}{2}\left(\frac{x-\mu_{\text{K}\alpha,\text{ pho}}}{\sigma_{\text{K}\alpha,\text{ pho}}}\right)^2} + d \cdot \mathrm{e}^{-\frac{1}{2}\left(\frac{x-\mu_{\text{K}\beta,\text{ pho}}}{\sigma_{\text{K}\beta,\text{ pho}}}\right)^2} . \tag{13.8}$$

The result of such a fit will be very unstable and dependends on the start parameters. To reduce the number of free parameters the known characteristics of the ^{55}Fe source (see section 13.3) can be used. Especially the relation between the peak positions and the peak height

$$\frac{b}{a} = \frac{d}{c} = \frac{\text{K}\beta}{\text{K}\alpha} = 0.125\,,\ \xi_{\text{esc}} = \frac{\mu_{\text{K}\beta,\text{ esc}}}{\mu_{\text{K}\alpha,\text{ esc}}} = \frac{3.548\,\text{keV}}{2.938\,\text{keV}}\,,\ \xi_{\text{pho}} = \frac{\mu_{\text{K}\beta,\text{ pho}}}{\mu_{\text{K}\alpha,\text{ pho}}} = \frac{6.505\,\text{keV}}{5.895\,\text{keV}} \tag{13.9}$$

can be used for this. Additionally, the width σ of the emission lines can be assumed to be the same for the Kα and the Kβ-line, leading to a simplified expression:

$$g(x, a, c, \mu_{\text{K}\alpha,\text{esc}}, \mu_{\text{K}\alpha,\text{pho}}, \sigma_{\text{esc}}, \sigma_{\text{pho}}) =$$
$$a\left(\cdot\mathrm{e}^{-\frac{1}{2}\left(\frac{x-\mu_{\text{K}\alpha,\text{ esc}}}{\sigma_{\text{esc}}}\right)^2} + \frac{\text{K}\beta}{\text{K}\alpha}\cdot\mathrm{e}^{-\frac{1}{2}\left(\frac{x-\xi_{\text{esc}}\mu_{\text{K}\alpha,\text{ esc}}}{\sigma_{\text{esc}}}\right)^2}\right) + c\left(\cdot\mathrm{e}^{-\frac{1}{2}\left(\frac{x-\mu_{\text{K}\alpha,\text{ pho}}}{\sigma_{\text{pho}}}\right)^2} + \frac{\text{K}\beta}{\text{K}\alpha}\cdot\mathrm{e}^{-\frac{1}{2}\left(\frac{x-\xi_{\text{pho}}\mu_{\text{K}\alpha,\text{ pho}}}{\sigma_{\text{pho}}}\right)^2}\right), \tag{13.10}$$

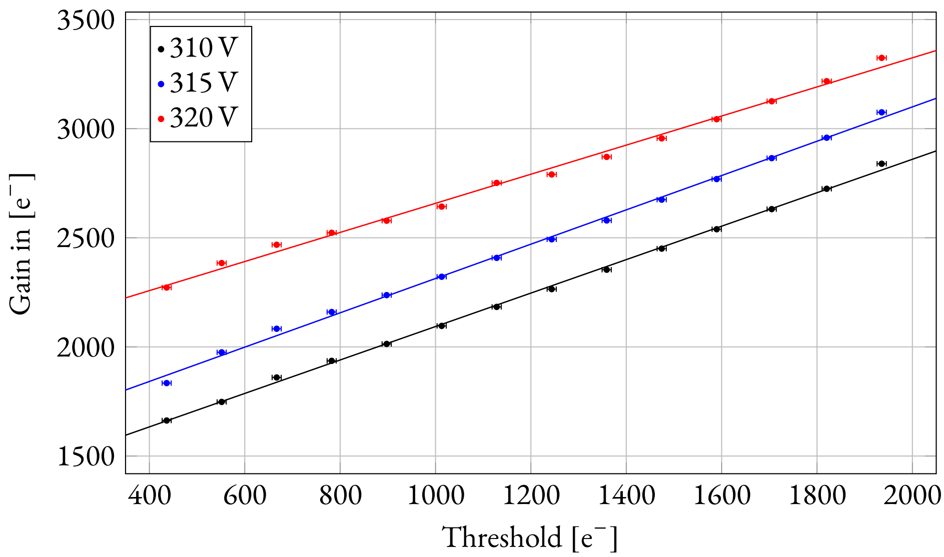

Figure 13.10: Measurement to extrapolate the effective Gain. Data and linear fits are shown for three different voltages.

with now only six free parameters. Since the ratio $\frac{K\beta}{K\alpha}$ has different values from the literature and the detector efficiency varies with the energy of the incoming particle another fit can be performed including the ratio as a free parameter. The results can be seen in figure 13.11 and are summarised in table 13.5. Figure 13.11 shows that the double gauss fit is performing slightly worse compared to the

Spectrum	Fit	χ^2/n.d.o.f.	ϵ_E
Pixel	Double Gauss	2.116	7.67 ± 0.02%
	Quad Gauss fix	1.980	7.05 ± 0.02%
	Quad Gauss var	1.978	7.16 ± 0.06%
Charge	Double Gauss	1.137	9.4 ± 23.9%
	Quad Gauss fix	1.059	9.0 ± 25.9%
	Quad Gauss var	1.054	8.8 ± 80.5%

Table 13.5: Energy resolution for three different fits: a double gauss, a quadruple gauss where the ratio $\frac{K\beta}{K\alpha}$ is fixed and a quadruple gauss where the ratio $\frac{K\beta}{K\alpha}$ is a free parameter. All are fitted for both, the pixel and the charge spectrum. The results are very close to each other. However, the errors for the values from the charge spectrum are very large.

other two. This can also be observed from the χ^2/n.d.o.f. values are given in table 13.5. For the two different ways to fit the quadruple gauss function, it can be seen that both agree very well and also the fitted parameter $\frac{K\beta}{K\alpha}$ is in the order of the literature value:

$$\left(\frac{K\beta}{K\alpha}\right)_{\text{pixel}} = 0.097 \pm 0.001\,, \quad \left(\frac{K\beta}{K\alpha}\right)_{\text{charge}} = 0.185 \pm 0.003\,. \tag{13.11}$$

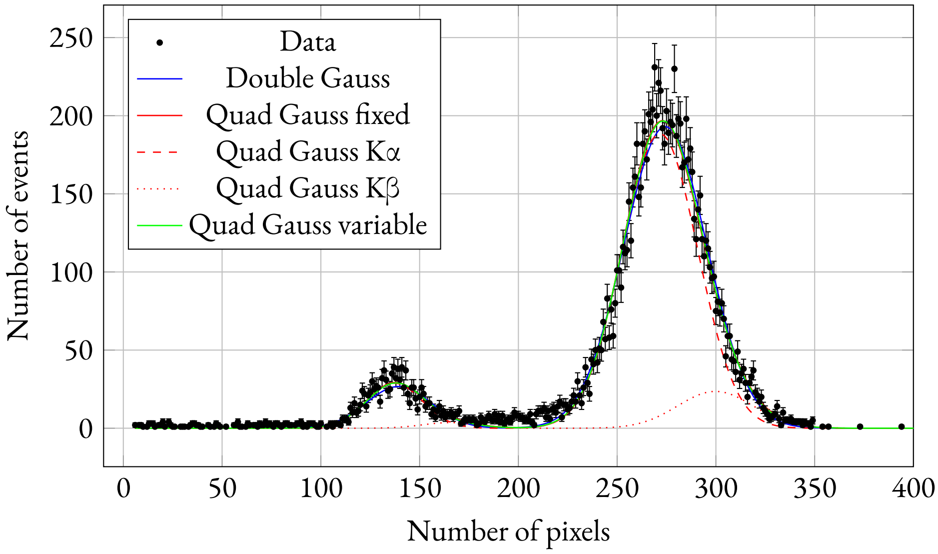

Figure 13.11: The pixel spectrum with three different Gauss fits: a double gauss (blue), a quadruple gauss where the ratio $\frac{K\beta}{K\alpha}$ is fixed (red) and a quadruple gauss where the ratio $\frac{K\beta}{K\alpha}$ is variable (green). Additionally, for the fixed quadruple gauss fixed fit (red line) the composition from the Kα(dashed) and Kβ(dotted) lines is shown. The fits agree very well, however the double gauss fit performs slightly worse.

The value for the fit to the charge spectrum is given for comparison. Regarding the values for the energy resolution ϵ_E, for all methods they agree within 0.5% with the absolute resolution. This is a good result which benefits to stability measurements over time. In order to get a quantitative value for the energy resolution the quadruple gauss fit with fixed values would be the preferred method since the relative difference is in the order of $(5 - 10)\%$. Hence for monitoring of the detector, the double gauss would be sufficient, while for comparison of the energy resolution, the quadruple gauss approach has to be used. Since the stability of the fit is not changed by the two approaches the quadruple gauss will be used for all determinations of the energy resolution.

13.6 Collection efficiency for Timepix and Timepix3

One of the key differences between the Timepix and the Timepix3 is their pixel pad size (see section 4.3). This measure can directly influence the measured gas gain for GridPix or GridPix3 detectors. To quantify this effect a dedicated setup with two detectors was built and both detector run parameters were tuned to result in a comparable operation. The setup consisted of two similar detectors, a GridPix and a GridPix3 detector, connected to one gas supply in a row. In the middle of the measurement, the gas inlet and outlet were switched from Setup1 to Setup2, shown in figure 13.12, in order to change the ordering of the detectors and therefore reduce systematic errors. First, the minimal threshold was determined for both detectors. Then the detector with the lower minimal threshold was set as close to the value as possible of the other detector. Thus leading to a threshold of 455 e^- for the GridPix detector and 471 e^- for the GridPix3 detector. After that the grid voltage was set to 310 V and data was taken with the ^{55}Fe source. The data taking was performed in the following order:

1. 30 min GridPix

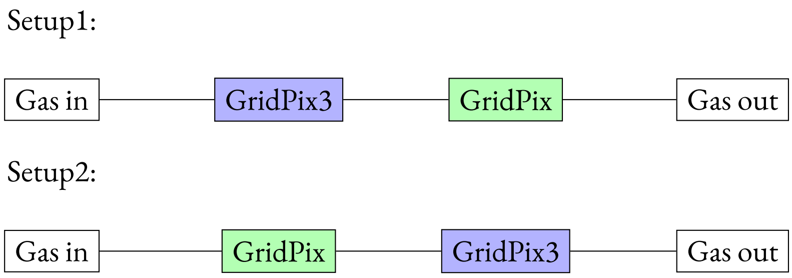

Figure 13.12: The two setups for the gain measurement. Both detectors are connected in a row. At Gas in a flow meter was installed, at Gas out a pressure controller. For Setup1 the GridPix3 detector was in the first position while for Setup2 the GridPix detector was in the first position.

2. 30 min GridPix3
3. 30 min GridPix

After that Setup1 was switched to Setup2 and the measurement was repeated. The reason for doubling the measurement time with the GridPix detector is that due to the frame-based readout, the dead time is very large and therefore fewer events can be recorded within the same time. For these six measurements the gas gain results are shown in table 13.6. From the results, it can be seen that the gain is always

Setup	Measurement	Gas gain in e^-
	GridPix	2211.4 ± 6.2
Setup1	GridPix3	1865.4 ± 2.1
	GridPix	2110.7 ± 6.4
	GridPix	2344.9 ± 5.1
Setup2	GridPix3	1597.8 ± 1.8
	GridPix	2377 ± 6.1

Table 13.6: Gas gain measurement for the GridPix and the GridPix3.

lower for the detector in the second position. A possible effect causing this behaviour could be the plastic tube connection between the detector introducing humidity to the gas and thus reducing the gas gain. However, the combination of the measurements should minimise this effect. To get the result we calculate the gain ratio of the GridPix3 with respect to the GridPix ϵ_{pix}:

$$\epsilon_{\text{pix}} = \frac{\left(G_{\text{GridPix3, Setup1}} + G_{\text{GridPix3, Setup2}}\right)/2}{\left(G_{\text{GridPix, Setup1}} + G_{\text{GridPix, Setup1}} + G_{\text{GridPix, Setup2}} + G_{\text{GridPix, Setup2}}\right)/4} = 76.6 \pm 0.1\,\%\,. \tag{13.12}$$

Thus, resulting in the effective gas gain for GridPix3 being approximately $76.6 \pm 0.1\%$ of the gas gain for the GridPix. This corresponds also to the difference in pixel size and a gaussian distributed electron cloud from the amplification of a 1σ width of 11 µm due to pure diffusion [Gru18]. Hence, the pixel pad of GridPix (20 µm) would be 1.81σ and GridPix3 (12 µm) would be 1.09σ. This would result in a difference of approximately 77%. Thus the difference in pad size could lead to the measured difference due to the change in the number of electrons hitting the pad. Nevertheless, to get a proper theoretical value the inductance towards the pixel's weighting field needs to be simulated.

This loss in the effective gain can be compensated by a slightly higher grid voltage.

CHAPTER 14

Preliminary estimation of the background levels of the GridPix3 detectors

To approve the feasibility of the detectors presented in chapters 10 and 11 for BabyIAXO, a measurement campaign with each detector was performed to validate the long-term stability and to have a first look at the background rates achievable with these detectors. Especially for the IAXO prototype detector this will give a first hint on possible future background levels. For the analysis, TimepixAnalysis [Schb] was used. In the following, first, a short introduction to the used methods shall be given (section 14.1). After this, in section 14.2 the advantage of the time of arrival (ToA) measurement shall be discussed, focusing on the usage to reduce the background. Then in section 14.3 the long-term stability of the detectors will be evaluated. Before the background levels will be discussed in section 14.4.

14.1 Method

After preparing the data as described in section 13.1 using TimepixAnalysis the background spectrum of the detectors shall be calculated. This is done via a likelihood method implemented in TimepixAnalysis. The likelihood method compares a set of parameters to distinguish between signal or background like events. The set of parameters was already used within the analysis in [Kri18, Sch24a]. Within these theses it was shown that a good set of variables from the ones presented in 13.1 are:

- `eccentricity` called ϵ in the following
- `fractionInTransverseRMS` called f in the following
- `lengthDivRMSTrans` called l in the following

All three are geometric properties and, albeit being highly correlated, show a good separation power between signal and background. However, to use these parameters within the likelihood the properties of signal-like (X-ray) events have to be known. This data was gained for both detectors from the calibration runs with the ^{55}Fe-source. However, since this data is depends on the energy of the X-ray, one can only produce parameter sets for two energies. A calibration with more energies would be necessary. Since this data is not available for GridPix3 detectors another method had to be developed.

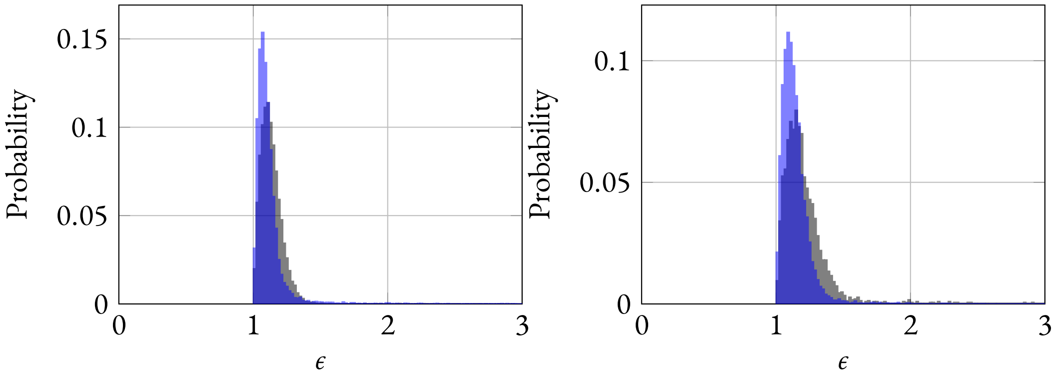

(a) (b)

Figure 14.1: Probability densities of the `eccentricity` ϵ of simulated GridPix3 data (blue) and data from the ^{55}Fe-source (black). Shown for (a) the 6 keV photo peak and (b) the 3 keV escape peak.

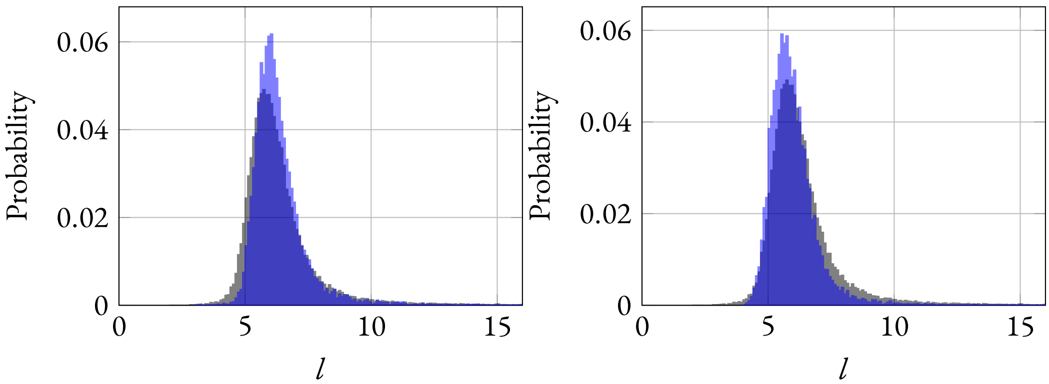

(a) (b)

Figure 14.2: Probability densities of the `lengthDivRMSTrans` l of simulated GridPix3 data (blue) and data from the ^{55}Fe-source (black). Shown for (a) the 6 keV photo peak and (b) the 3 keV escape peak.

One approach is the usage of simulated data. In order to validate the simulated data the probability densities used for the likelihood need to be compared to data. This is done by comparing the simulation with the data taken with the ^{55}Fe-source. This leads to the comparisons shown in figure 14.1 for the `eccentricity`, in figure 14.2 for the `lengthDivRMSTrans` and in figure 14.3 for the `fractionInTransverseRMS`. It can be seen that for all three values the results fit for the photo peak and for the escape peak. Only for figure 14.3(b) a slightly larger difference can be seen. However, the data from the escape peak is systematically biased due to the difference in the mean free path of a real 3 keV X-ray photon. Hence, 3 keV X-ray photons are absorbed earlier by the gas resulting in a larger diffusion of the cluster changing the properties presented. Thus, simulated data can be used for the likelihood approach to calculate a preliminary background estimate (implemented in [Scha]).

Another approach is to reuse the data taken for the seven GridPix detector shown in chapter 9 and modify it such that the data fits to the measured two energies of the ^{55}Fe-source. This was performed by matching the escape peak to the data taken with the aluminium target and the photo peak to the

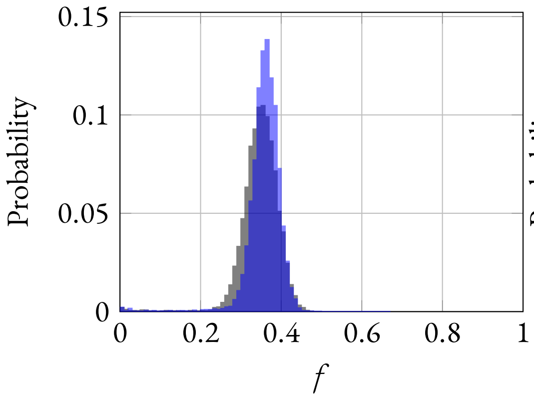

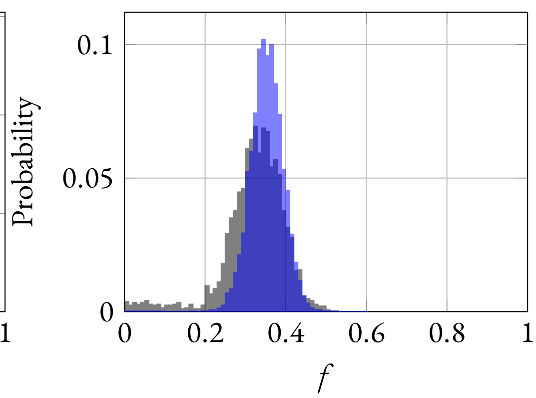

Figure 14.3: Probability densities of the `fractionInTransverseRMS` f of simulated GridPix3 data (blue) and data from the ^{55}Fe-source (black). Shown for (a) the 6 keV photo peak and (b) the 3 keV escape peak.

data taken with the manganese target. To do this the CDL distribution is rebinned via:

$$x_{\mathrm{i,new}} = (x_{\mathrm{i}} - x_1)\frac{y_{\mathrm{n}} - y_1}{x_{\mathrm{n}} - x_1} + y_1 \,. \tag{14.1}$$

This is example-wise shown for the `eccentricity` at the energy of the photo peak in figure 14.4. It can be seen that after the morphing both distributions agree very well. For all three relevant properties, factors were calculated to fit the spectra to each other. With a linear interpolation between the two data sets the rest of the CDL data was adjusted. The drawback of this approach is that it is based on Timepix data, therefore no information on the time of arrival (ToA) is available. Here x are the histogram bins of the CDL data reaching from 0 to n and y denotes the histogram bins for the distribution from the ^{55}Fe data. For the ^{55}Fe data, a cut on y_{n} is performed such that both distributions overlay as well as possible. With these adjusted values one can now properly define the likelihood as

$$L(\epsilon, f, l) = P_\epsilon(\epsilon) \cdot P_f(f) \cdot P_l(l) \,, \tag{14.2}$$

with $P_x(x)$ being the probability densities of parameter x corresponding to the value (x). The probability densities can be calculated using the reference histograms from the morphed CDL data and normalising them. With this one can calculate the likelihood value for each event. For numerical stability, to avoid the function getting very small this is done via a negative log likelihood

$$-\ln\left(L(\epsilon, f, l)\right) = -\ln\left(P_\epsilon(\epsilon)\right) - \ln\left(P_f(f)\right) - \ln\left(P_l(l)\right) . \tag{14.3}$$

Calculating this for all events from the CDL data and filling them in a histogram leads to the likelihood distribution $\mathcal{L}$ for a given energy E. With the likelihood distribution one can now finally define a cutoff value L_{cut} to define signal-like events if

$$L_{\mathrm{event}} \leq L_{\mathrm{cut}}. \tag{14.4}$$

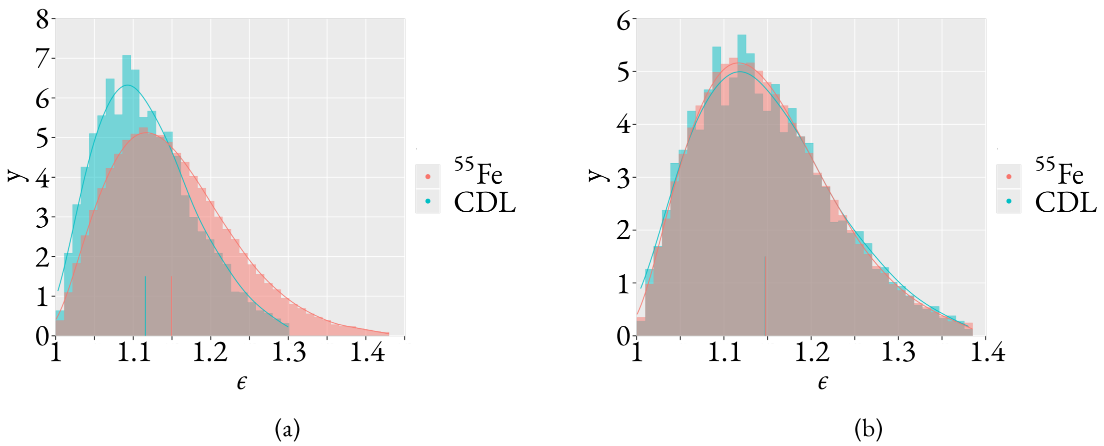

Figure 14.4: Comparison of the CDL data (blue) with the ^{55}Fe photo peak (red) for the `eccentricity` for the unmorphed case (a) and the final morphed case (b). The means of the distributions are indicated as lines. It is clear that the morphed distribution fits very well to the ^{55}Fe photo peak data after the morphing. In collaboration with [S.].

To calculate L_{cut} one needs to define an efficiency ϵ_{eff} of the cut and calculate,

$$\epsilon_{\text{eff}} = \frac{\int_0^{L_{\text{cut}}} \mathcal{L}(L)\mathrm{d}L}{\int_0^{\infty} \mathcal{L}(L)\mathrm{d}L} . \tag{14.5}$$

Thus, the value L_{cut} defines the cut where the percentage given by ϵ_{eff} of all events from the CDL data is classified as signal events. To now calculate the background spectrum one just has to calculate the likelihood value of an event and compare it with L_{cut}. Every event smaller than L_{cut} is presumed to be a signal. Here it shall be mentioned that with GridPix3 a fourth very interesting variable `toaLength` comes into play for the likelihood cut since it shows a strong discrimination power (see section 14.2).

14.2 ToA length as a likelihood variable

As mentioned in section 14.1 the ToA as a variable has a very good separation power between background-like and X-ray-like events. This comes from the fact that an X-ray is basically producing all primary electrons at the interaction point. Thus, the `toaLength` (the difference between the latest and earliest timestamp in the cluster) is just dependent on the longitudinal diffusion through the detector. For background-like events (muons), this is different since they produce electrons along a track through the detector. Consequently, as soon as the track is tilted with respect to the GridPix3 surface the `toaLength` will rise due to the different drift times the electrons need to reach the grid. In the special case of a muon traversing the detector perpendicular to the GridPix3 mimicking geometrically a photon event will have a much larger `toaLength` mainly determined by the drift time through the detector. The difference in the spectrum of the `toaLength` between a background run and an X-ray run with the ^{55}Fe-source is shown in figure 14.5. Here no cuts are applied to the data, thus also the ^{55}Fe X-ray data contains background events. However, already from these raw events the discrimination strength can be seen, since beyond 20 clock cycles basically only background data is found. Regarding a typical

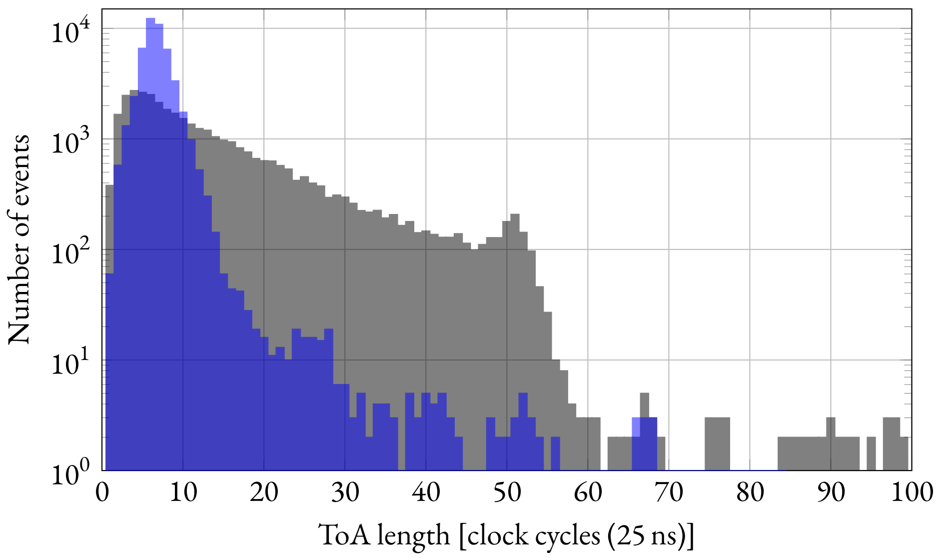

Figure 14.5: Histogram of the `toaLength` of GridPix3 events without any cuts applied. In black a background run is shown, while in blue an X-ray run with the ^{55}Fe-source is shown. The difference of X-ray and background data can be clearly seen.

photon event, converting close to the grid, the one sigma time span within the event should be due to diffusion

$$t_{\text{diff}} = 2\frac{D_\text{l}\sqrt{l}}{u} = \frac{249.32\,\frac{\mu\text{m}}{\sqrt{\text{cm}}}\sqrt{3\,\text{cm}}}{22.98\,\frac{\mu\text{m}}{\text{ns}}} = 37.6\,\text{ns}. \tag{14.6}$$

Using the longitudinal diffusion D_l, drift velocity u (see table 3.1), and the length of the drift volume l this results in approximately two clock cycles for the one sigma region, even the full event should be much narrower than 20 clock cycles in its `toaLength`. In the background data a peak at 50 clock cycles (1.25 µs) is visible. The peak is expected and relates to the perpendicular muons since the time t_{drift} an electron needs to drift from the cathode to the GridPix is given by

$$t_{\text{drift}} = \frac{l}{u} = \frac{3\,\text{cm}}{22.98\,\frac{\mu\text{m}}{\text{ns}}} = 1305.3\,\text{ns}. \tag{14.7}$$

This time corresponds to $1305.3\,\text{ns}/25\,\text{ns} = 52$ clock cycles, agreeing very well with the peak position. Therefore, by cutting on the `toaLength` those events will be removed. To use this within the likelihood we have to get `toaLength`-distributions for different energies. In the best case, those would come from a measurement similar to the one taken at the CDL. As already mentioned this does not exist for the GridPix3, but one can simulate these events. This was done for 20 energies in the range of 0.5–10 keV.

From the result of the simulation, the probability densities were calculated. The results for seven selected energies are shown in figure 14.6. It can be seen that towards higher energies the spectrum gets wider, which is expected due to the larger amount of electrons and therefore a larger impact from longitudinal diffusion. It can also be clearly seen that a cut on `toaLength` can be performed below 12 clock cycles thus having an even better discrimination. To compare the simulation with real data a cut

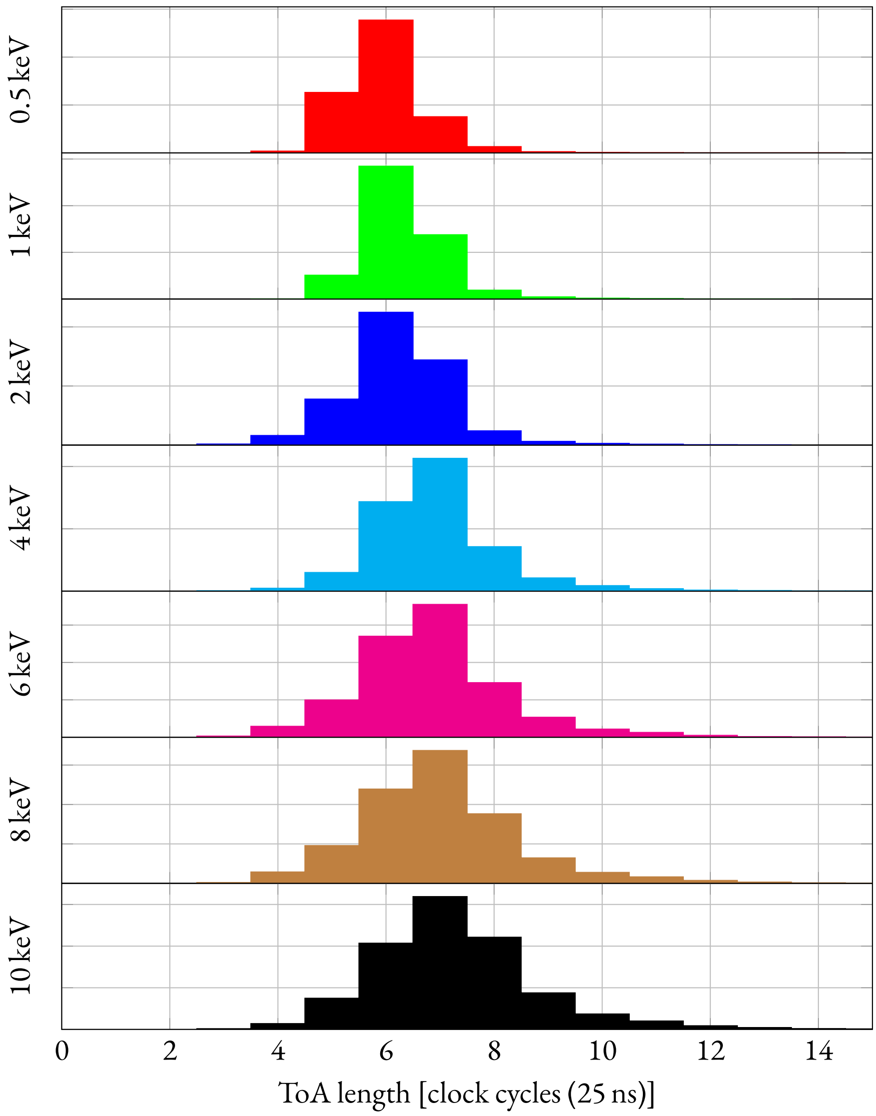

Figure 14.6: Probability densities of the `toaLength` of simulated GridPix3 data for seven selected energies. It can be observed that towards higher energies the spectrum gets wider.

on the photo peak ($\approx$ 5.9 keV) has been performed for one of the calibration runs to be compared with simulation data.

In figure 14.7 the comparison of the probability densities of the simulated data for 6 keV and the data from the photo peak is shown. It can be seen that the shape is similar but shifted by two clock cycles. Consequently, the probability densities need to be shifted by two clock cycles. In figure 14.8 the same is shown for the escape peak at 3 keV. Again a shift of two clock cycles needs to be applied to bring the distributions into agreement. The shift is expected since the data from the calibration run suffers from an influence of the so-called time walk, an effect that depending on the pulse height induced into the pixel, the ToA value differs due to the steepness of the slope. A correction for this

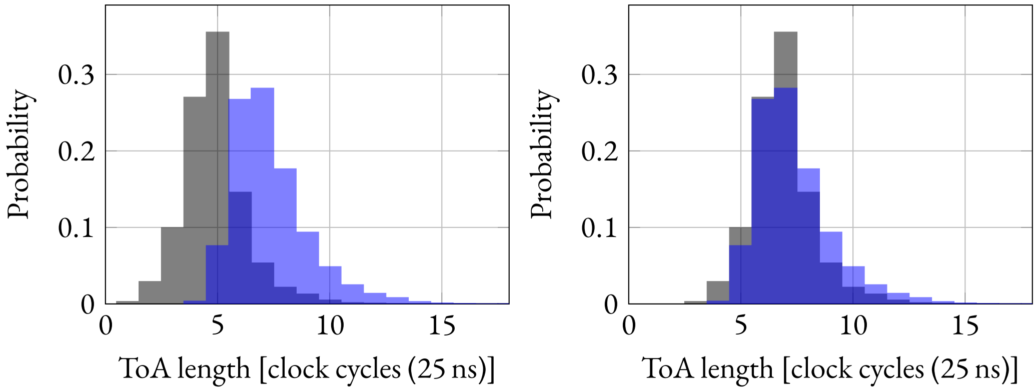

(a) (b)

Figure 14.7: Probability densities of the `toaLength` of simulated GridPix3 data at 6 keV (black) and data from the ^{55}Fe-source cut to the photo peak. (a) The original data, (b) simulated data shifted by two clock cycles.

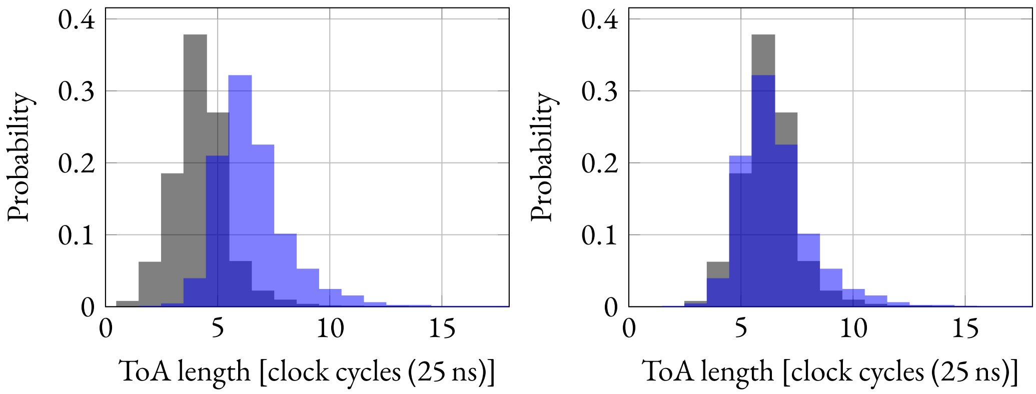

(a) (b)

Figure 14.8: Probability densities of the `toaLength` of simulated GridPix3 data at 3 keV (black) and data from the ^{55}Fe-source cut to the escape peak. (a) The original data, (b) simulated data shifted by two clock cycles.

was at the time of the data taking not implemented, thus cannot be applied. Also, the simulation is not taking the gas amplification below the grid into account, therefore missing another addition to the time spread. After the shift, the data agrees quite well with the simulated distribution. Thus, a cut at 12 clock cycle can be applied to the data or the shifted probability density $P_t(t)$ can be added to the likelihood to determine X-ray-like events in a better fashion. This results in

$$L(\epsilon, f, l, t) = P_\epsilon(\epsilon) \cdot P_f(f) \cdot P_l(l) \cdot P_t(t). \tag{14.8}$$

14.3 Stability of the detectors

For the two background measurements of the two detectors every weekday a calibration run with the ^{55}Fe-source was taken. From this data, the effective gain and also the peak position of the photo peak and the energy resolution are parameters to observe for the detector stability. In the following the evolution of these parameters over time will be discussed for both detectors.

14.3.1 GridPix3 detector

For the GridPix3 detector presented in chapter 10 a data set of 14 days was taken with ten calibration runs. The results of the calibration runs for each day are shown in figure 14.9. The data shows that the

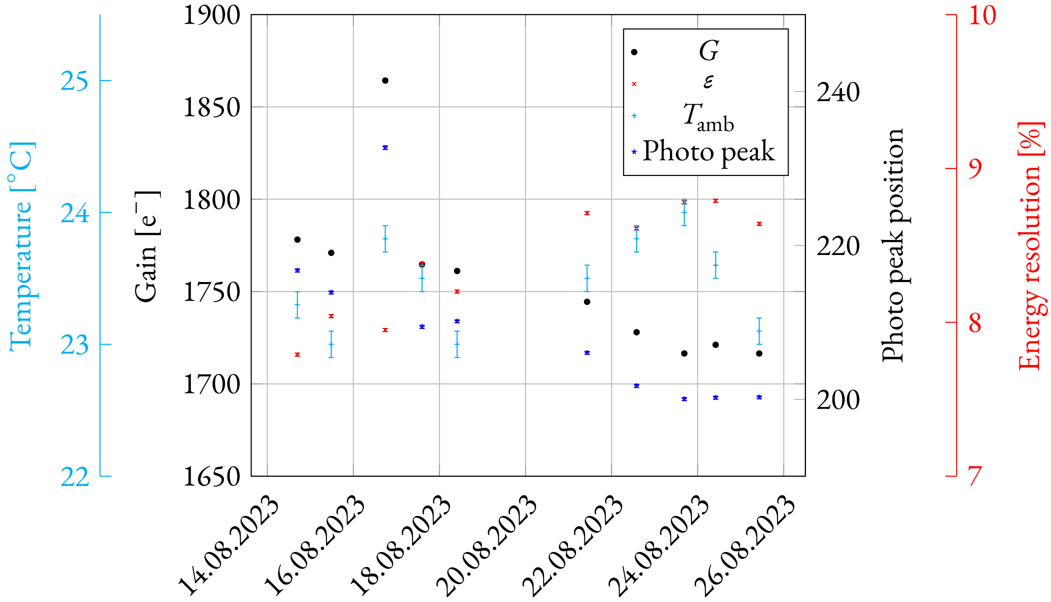

Figure 14.9: Data on the time evolution of the ten calibration runs of the GridPix3 detector. The effective gain (G), the position of the photo peak, and the energy resolution (ε) are given. In addition, the room temperature is shown. The data shows that the temperature has no effect on the given parameters, however they are changing.

detector is not influenced by the ambient temperature. In the first week of measurements 14th–18th of August, the gain seems to follow the temperature (higher temperature, larger gain), but in the second week this behaviour is not observed, hence for the GridPix3 detector a direct connection between the ambient temperature and the gain cannot be stated. This is expected since the GridPix3 is not thermally coupled to the ambient air. As visible in figure 10.4 the GridPix3 on its carrier is mounted on a PMMA holder and mostly surrounded by the detector gas, thus having a very bad thermal coupling to the outside. However, changes in the effective gas gain are still observed. Except for the outlier at the 16th of August the difference over the measurement is in the order of 2%, which is tolerable for a measurement campaign. It can be seen that the position of the photo peak is following the gas gain as expected, thus monitoring only one of these parameters will be sufficient. The energy resolution is staying stable within 7.8–8.8%. From this data, the detector can be stated to be operating stable.

Within the data taking campaign also for this detector measurements of more than 100 hours have been successfully recorded showing that also long continuous data taking campaigns are feasible.

14.3.2 IAXO prototype

With the IAXO prototype detector data was taken for 34 days, within these 18 calibration runs were performed to monitor the stability of the detector. The results for the three mentioned parameters are shown in figure 14.10. From the figure it can be seen that the detector was basically running stable.

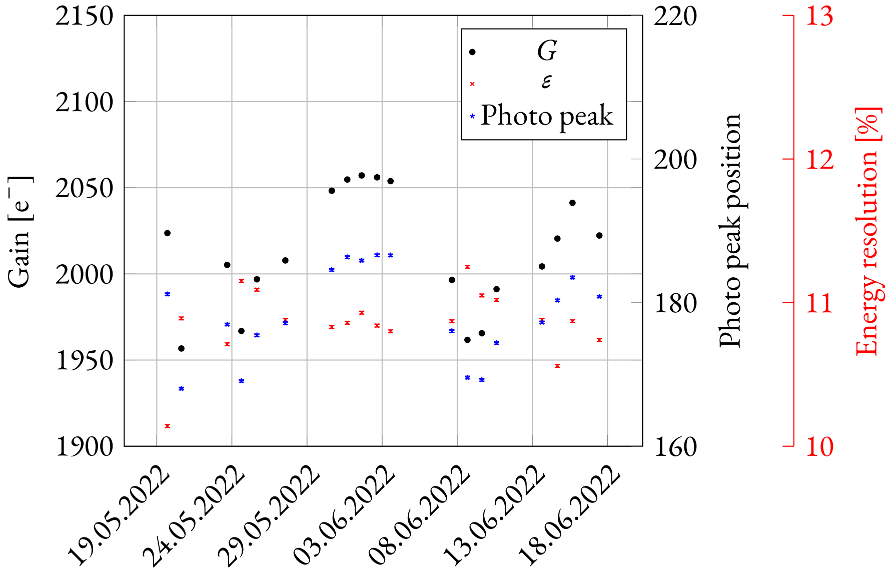

Figure 14.10: Data on the time evolution of the 18 calibration runs of the IAXO prototype detector. The effective gain (G), the position of the photo peak, and the energy resolution (ε) are given.

The monitored chip temperature was constantly at 44–45 °C, thus very stable. The effective gas gain was changing in the order of 100 e$^-$ and the photo peak position is again proportional to the effective gas gain. This is comparable with the results from the GridPix3 detector shown in figure 14.9. Since data on the ambient temperature is not available for the measurement a comparison is not possible. However, due to the similarities, the ambient temperature was either very stable or does not affect the detector. However, the latter is not very probable since the chip is directly coupled to the surroundings via the copper base plate (see section 11.2). The energy resolution is stable within 1%. The photo peak position is with $\approx$ 180 hits rather low compared with the data shown in figure 14.9. This is due to a very high threshold of the used GridPix3 of 1914 e$^-$. This also explains why for a higher gas gain in comparison to figure 14.9 the amount of hit pixels in the photo peak is lower due to the threshold cut off. The high threshold also shows that the used GridPix3 is of bad quality since the typical threshold should be in the order of 500 e$^-$.

Method	Remaining cluster photon data	Remaining cluster background data
CDL	6912	41
CDL + ToA cut	6899	40
Sim	6650	43
Sim + ToA cut	6636	41
ToA in lnL	6410	15

Table 14.1: Validation of the five methods using a small data set of background data and a small data set of photon data, both taken with the IAXO prototype detector.

14.4 Background levels

With the methods presented one can now calculate the background rates of the detectors. The explained cuts are applied to the data and the remaining clusters are binned in a histogram. For both detectors, five different methods are used and compared. The first two methods use the morphed CDL data for the calculation of the likelihood. For the second method, a cut on the `toaLength` at a value of 12 is performed. The next two methods use the simulated data for the likelihood. Again one time with and one time without the cut on the `toaLength`. The last method uses the extended likelihood adding the `toaLength` as a parameter. In order to have the background rate comparable with [Kri18, Sch24a] it is also calculated for the so-called gold region (the innermost $5 \times 5\,\mathrm{mm}^2$) of the active GridPix3 area. All background rates presented in the following are calculated with a software efficiency $\epsilon_{\mathrm{eff}} = 80\%$ for the likelihood.

Before using the old and the newly developed methods on the long background runs taken with both detectors, first all methods needed to be verified. For this, a X-ray data set from a run with the ^{55}Fe-source and a short background run both taken with the IAXO prototype detector were used. Using the methods should not change the number of remaining clusters in the photon data, while the number of remaining clusters for the background data might change. The results of this test are shown in table 14.1. It can be seen that indeed the number of remaining clusters in the photon data set is not drastically changing while for the background data, especially for the method adding the `toaLength` to the likelihood a reduction by more than a factor of two can be expected.

14.4.1 The likelihood distributions

The distribution of the overall likelihood values for all events from calibration and background data sets is shown in figure14.11 for the likelihood method using the simulated X-ray data and in figure 14.12 for the likelihood with the additional usage of the `toaLength`. The distributions for both methods look comparable and show a good separation between background and calibration data. The distribution of the values for the calibration run looks as expected, thus real photons have a low $-\ln(L)$ value. The behaviour of the background values is hard to determine however the prominent spikes in the distributions are not expected. A probable origin might be reoccurring noise events. Interestingly, the sharp peaks seem to smear out by using the `toaLength` within the likelihood, thus the similarities seem to appear mostly within the event geometry, pointing towards events with very few pixels close to each other. One problem with the addition of the `toaLength` into the likelihood is the low number of bins in the probability histograms. Especially at low energies like 1 keV the ToA probability histogram (see fig. 14.13(b)) shows only three populated bins, therefore for these energies, the likelihood values

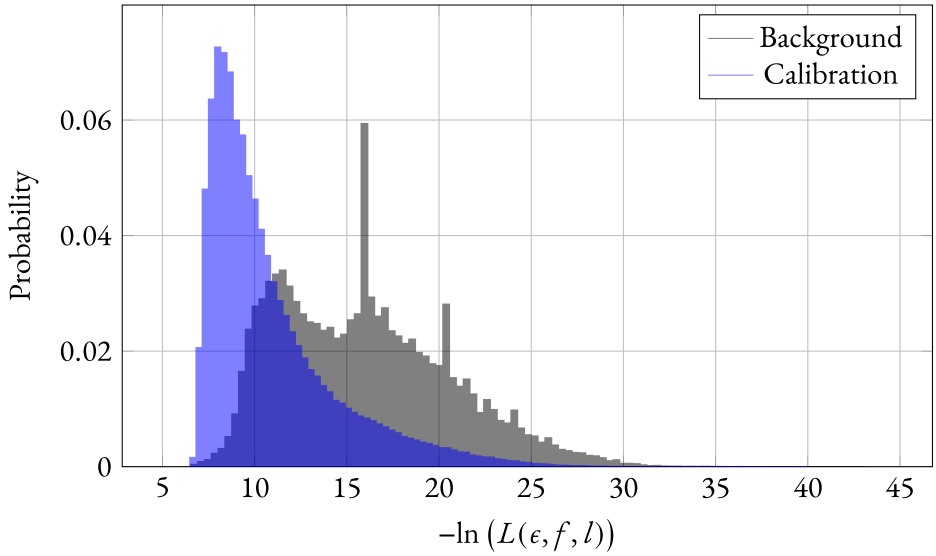

Figure 14.11: Comparison of the calculated likelihood values for background and calibration data using simulated data for the likelihood of the data taken with the IAXO prototype detector.

show a discretisation as seen in figure 14.13(a). This leads to the problem that with the efficiency cut at 80%, events with a `toaLength` outside the two main bins are cut, even if the other properties would classify it as a very X-ray-like event. This means that depending on the `toaLength` background-like events might be kept while X-ray-like events might be cut off. The only way to avoid this is to raise the number of bins in the reference histogram. Since for the `toaLength` already every possible value is used as a bin this is only possible with a better time resolution. The Timepix3 can provide this with the fineToA extension. This would allow for 16 times more time bins, smoothing out the distribution. Consequently, for further data takings, the fine ToA should be used to allow for a better discrimination of background and photon data via the `toaLength`.

14.4.2 GridPix3 detector

For the estimation of the GridPix3 detector over 14 days a background data set of 318 hours was taken. The detector was placed on a lab table with the window pointing upwards. No additional shielding was used. During the measurement, ten calibration runs using the ^{55}Fe-source were performed as shown in figure 14.9 showing that the detector was running stable.

To analyse the achievable background of the detector first the data was reconstructed and then a likelihood cut was performed using five different methods.

The results for the first two methods using the morphed CDL data as an input for the likelihood are shown in figure 14.15. The background rate shows that except for the first two bins it looks expectable. The peak at 8 keV originates from the copper fluorescence line (Cu Kα_1 = 8.047, 8 keV [Boo01]). However, the high background rate at low energies especially at the first two bins can not be easily explained. To ensure that this background level is not originating from a spark region the distribution of the remaining cluster centres, shown in figure 14.14, was inspected. It reveals a homogeneous distribution of the cluster centres within the used gold region (red square) thus an induced artificial background due to sparks can be excluded. The typical rise of photon like cluster centres towards the

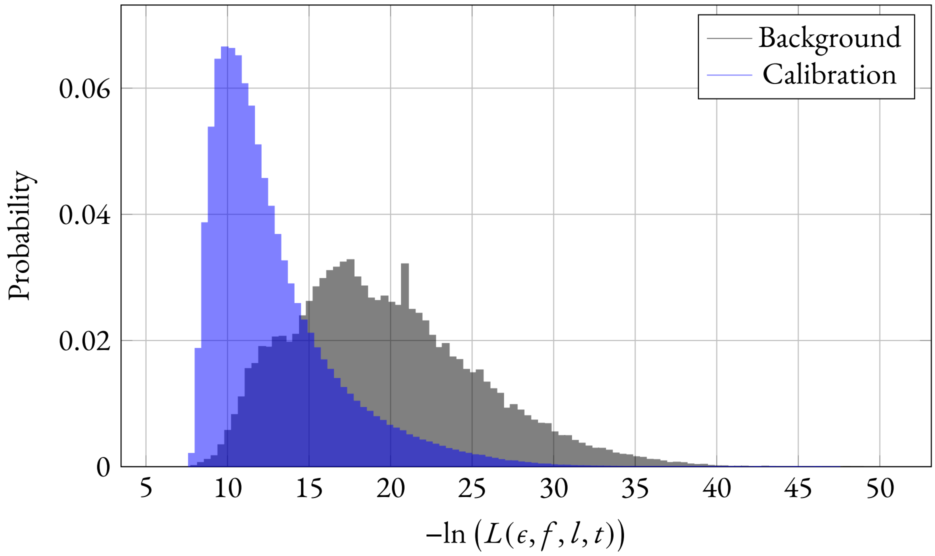

Figure 14.12: Comparison of the calculated likelihood values for background and calibration data using the likelihood method including the `toaLength` for the data taken with the IAXO prototype detector.

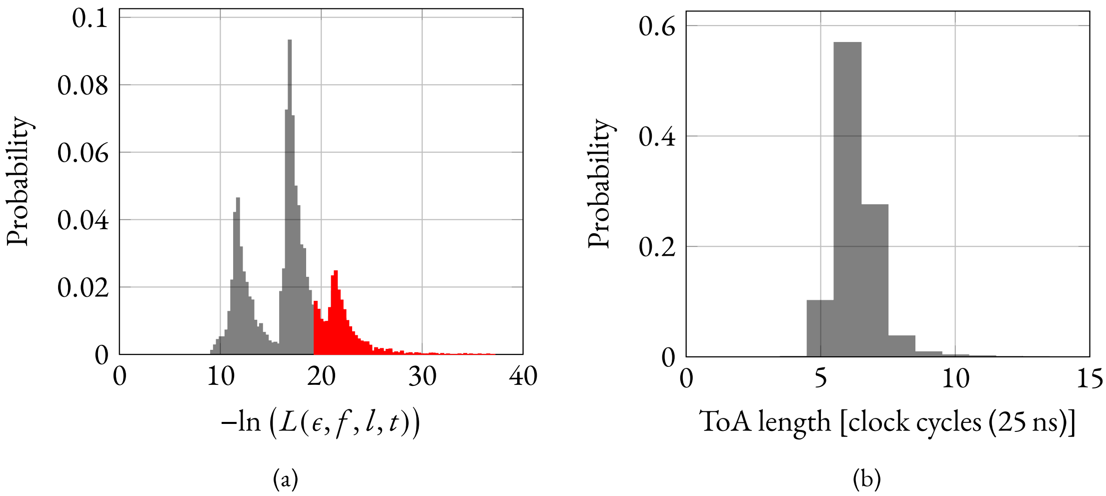

Figure 14.13: Comparison of (a) the $-\ln\left(L(\epsilon, f, l, t)\right)$ and (b) the reference distribution for the `toaLength` taken from the simulated data, both at 1 keV. Due to the low number of bins a prominent substructure can be observed in (a) reproducing the three populated bins in (b). The cut at 80% efficiency is shown in red.

corners (see [Kri18, Sch24a]) originates from truncated muon tracks mimicking a X-ray-like cluster while only passing the corner of the GridPix. Thus, the high rate at low energies seems not to originate from sparks. An explanation could be that the morphed CDL data fits at low energies not very well to the taken data. Since no real photon data at low energies is available for this detector a proof of this cannot be given here. Investigating the difference between the two spectra concerning the cut on the `toaLength`, it can be observed that (even being very conservative) already impacts the background level in the interesting region between 1–7 keV.

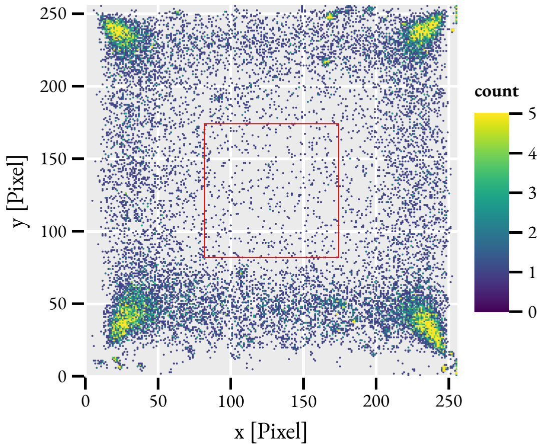

Figure 14.14: Distribution of the background cluster centres using the morphed CDL data for the likelihood. The distribution is homogeneous in the centre and no clustering areas are visible within the gold region marked in red. The strong rise of cluster centres towards the corners of the GridPix is expected due to cutoff muon tracks mimicking a X-ray-like event.

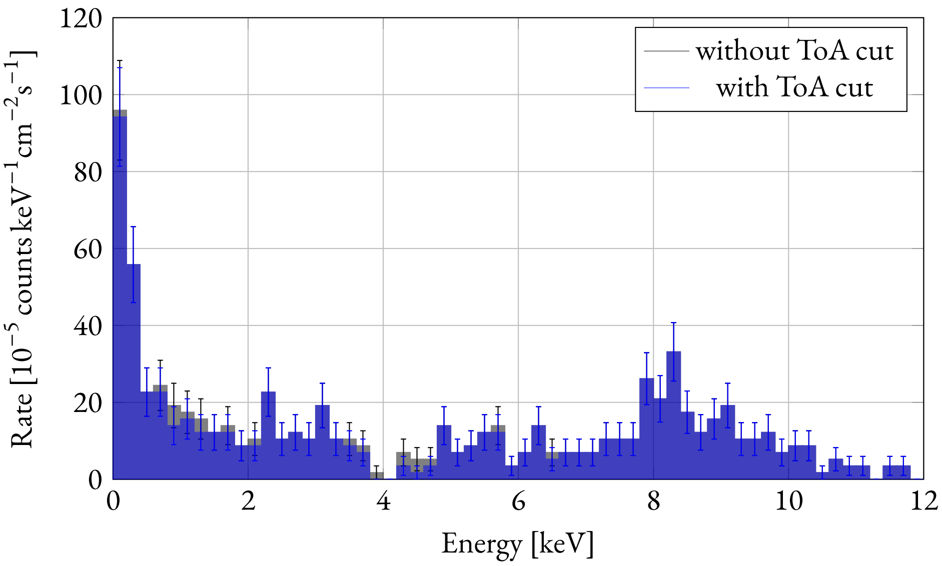

Figure 14.15: Background rate using the morphed CDL data with and without ToA cut at ToA = 12.

In figure 14.16 the background rates for the likelihood approach using the simulated data can be seen. Here the behaviour is similar to the behaviour with CDL data. Again the copper fluorescence is visible as a peak in the data and the rise towards low energies can be observed. The total background level except for the first two bins is slightly lower but not significantly and the impact of the cut on the `toaLength` behaves similarly as in the case for the likelihood based on the CDL data. This is a good result since it generally shows that both likelihood approaches work comparably. However, a few differences between the two methods need to be discussed. The first one is the high rate in the first bin.

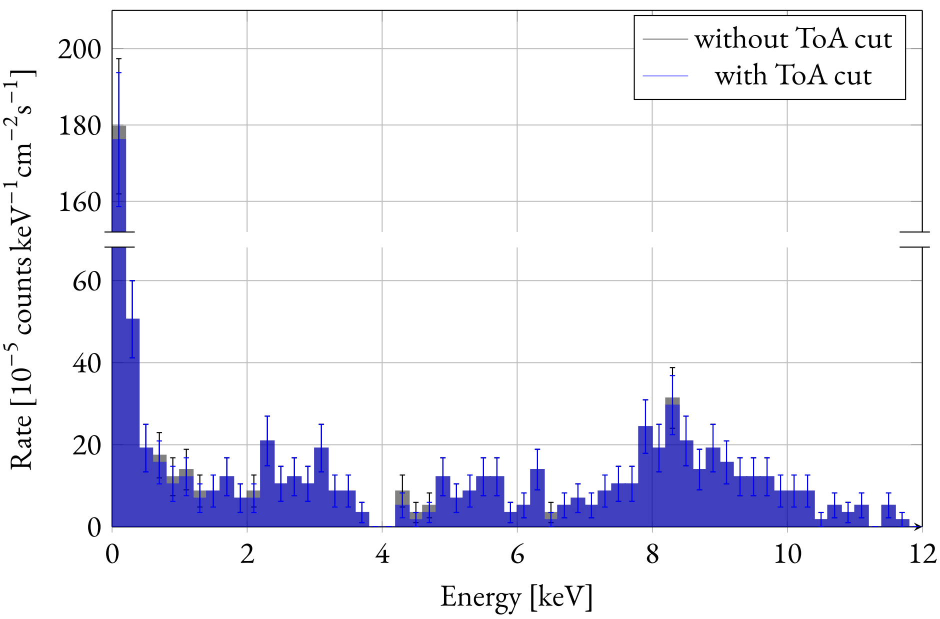

Figure 14.16: Background rate using the simulated data for the likelihood with and without ToA cut at ToA = 12.

Here the simulated data seems to perform even worse, which could hint into the direction of bad fitting likelihood distributions at the very low energies, since for the simulated data the lowest reference energy is 0.5 keV while for the CDL data it is 0.277 keV. Thus, the linear interpolation towards lower energies will yield a more realistic result the lower the last measured energy is. Hence, for the lowest energies the method using CDL data will perform better while for higher energies due to more available data sets the method using the simulated data will perform better, which can be seen from figures 14.15 and 14.16.

The last method is the in section 14.2 described extension of the likelihood with the `toaLength`. For this obviously, only the simulated data can be used since the CDL data taken with a Timepix ASIC does not contain ToA data, thus the likelihood distributions cannot be computed from this data using the `toaLength` addition. The results can be seen in figure 14.17. The most obvious reduction is in the first two bins here the background is drastically reduced. A reason for this behaviour might arise from the difference that the usage of the `toaLength` within the likelihood method removes clusters on both ends of the `toaLength` distribution, while the ToA cut only removes high `toaLength` values. Also for the first time, the Argon fluorescence line ($\approx$ 3 keV) is visible. Of course, also the copper fluorescence can be seen. Both lines are expected within the spectrum. The rest of the background is slightly lower but comparable with the results from the other methods. Hence, using the `toaLength` as a parameter within the likelihood reduces the background and seems to especially tackle parts that are overseen by the geometrical properties.

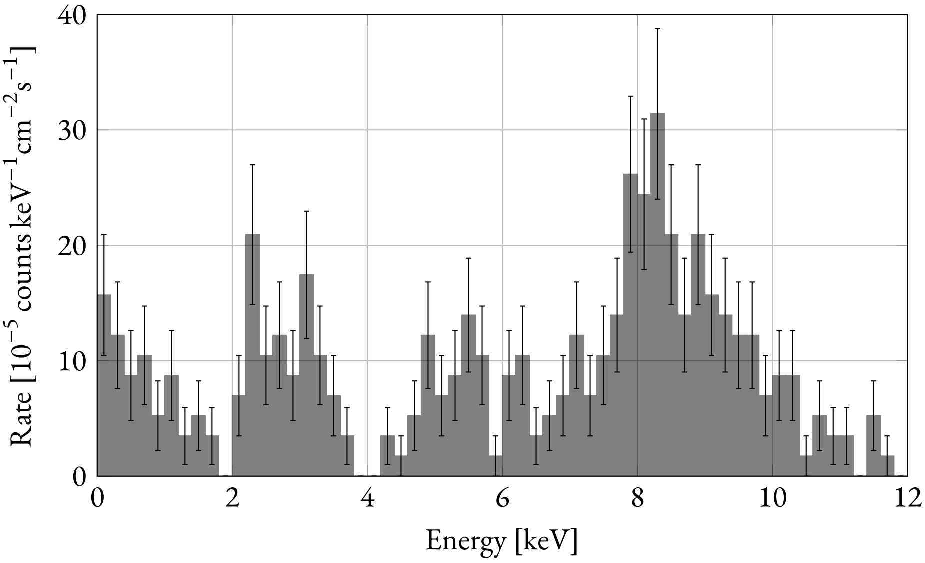

Figure 14.17: Background rate using the likelihood method including the `toaLength`.

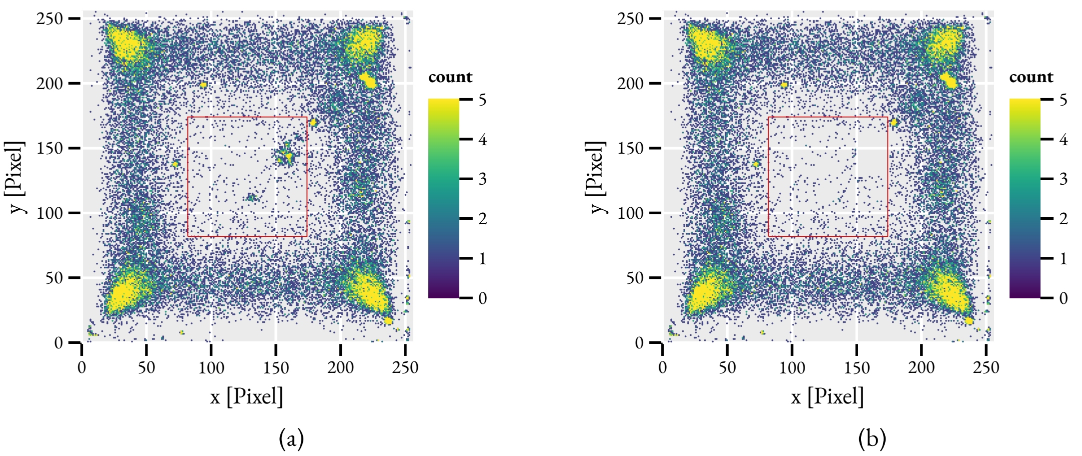

Figure 14.18: Comparison of the distribution of background cluster centres using the likelihood method with stretched CDL data. In (a) without any cuts on the pixel matrix a very noisy area can be observed. These are removed in (b) since it would raise the measured background level artificially. The gold region used for the background estimates is indicated in red.

14.4.3 IAXO prototype

Similar to the GridPix3 detector also with the IAXO prototype detector a background data set was taken. For this again the detector was operated without any additional shielding on a lab table, the window pointing upwards. For this detector, a data set of 750 hours of background data was taken within 34 days. Within these 34 days, 18 calibration runs with the ^{55}Fe-source were taken showing, as presented in figure 14.10, that the detector did run stable. The data was then also first processed using the likelihood method based on the CDL data. As shown in figure 14.19 a very high background rate

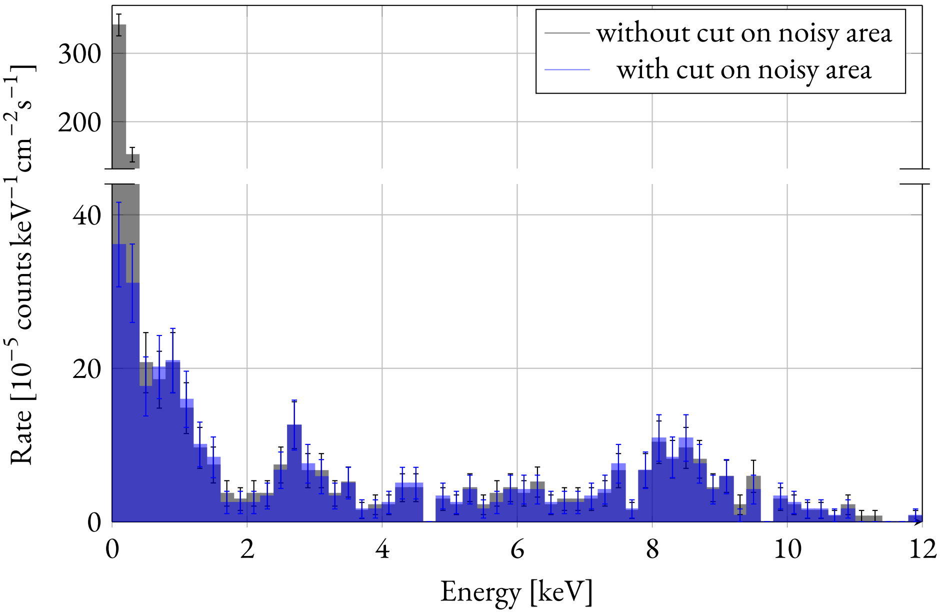

Figure 14.19: Comparison of the background rate using a cut on the noisy area of the GridPix3. This cut reduces the artificial background events, especially in the first two bins.

within the first two bins was observed again. Again the cluster centre distribution can be used for a first investigation of the behaviour. As seen in figure 14.18(a) clearly two active areas can be observed within the gold region and a few more outside. These regions originate from a hole in the grid and probably from some dust particles stuck in a hole. Since this is inducing artificial noise to the chip and therefore producing an artificial background rate, those areas need to be removed from the gold region to produce a proper estimate of the background rate. The cluster centres after the removal can be seen in figure 14.18(b) showing a homogeneous distribution over the remaining gold region. Calculating the background rates for the remaining shows a significant reduction in the first two bins, thus (see fig. 14.19), for the prototype detector, the high background rate in the first two bins is mostly artificial due to bad chip areas. For the further background rate estimations this cut on the bad areas will always be used.

First, again the background level using the likelihood with the CDL data shall be investigated. The result is shown in figure 14.20. In comparison with the result from the GridPix3 detector, it can be easily seen that the overall background is lower. Also, both fluorescence lines argon and copper can be seen as peaks in the background rate. Again a rise towards very low energies is observed however the first two bins are not as prominent as they were for the GridPix3 detector. The cut on the `toaLength` shows a good additional reduction of the background in the range between 1 keV and 8 keV, consequently being really useful in the interesting range for axion searches.

The results shown in figure 14.21 use the simulated data for the likelihood. Here an overall reduction of the background rate can be observed. With the cut on the `toaLength` the background is reduced even further for energies above 1 keV. Below 1 keV a reduction of the background can be observed compared to the background rate achieved using the morphed CDL data within the likelihood calculation. Still, at low energies, the background is too prominent to be seen as non-artificial.

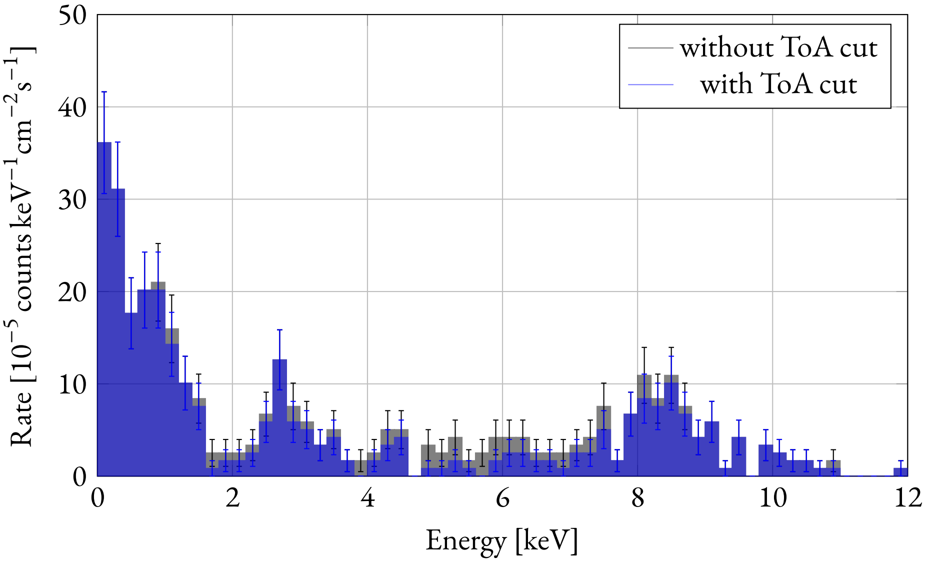

Figure 14.20: Background rate using the morphed CDL data with and without ToA cut at ToA = 12.

The last method is again the likelihood including the `toaLength` as a parameter. The background rate is shown in figure 14.22. Here a significant reduction of the overall background is visible. Both fluorescence lines are visible and a small leftover peak at energies below 2 keV can be observed. Overall the reached background rate for a non-shielded detector is very promising and comparable with the rates achieved within a lead shielding from the detectors used at CAST [Kri18, Sch24a].

14.4.4 Comparison of the results

To compare the results obtained in sections 14.4.2 and 14.4.3 a calculation of an average background rate over a certain energy range will be used. For comparison four energy ranges will be used. The overall background (0–12 keV), the rate interesting for an overall solar axion search 0–8 keV, the rate for the search for solar axions originating from the Primakov effect 2–7 keV, and the range for axion-electron coupling 0.5–5 keV. The result is shown in table 14.2. The table reveals that the IAXO prototype detector is outperforming the GridPix3 detector in every scenario, even if not being built from radiopure material and using a not optimally working GridPix3. Hence, with a radiopure version of this detector using an optimal GridPix3 even lower rates should be achievable, maybe already reaching $\mathcal{O}(10^{-6}\text{counts keV}^{-1}\text{cm}^{-2}\text{s}^{-1})$ without an additional lead shielding.

Having a look at the different scenarios it can be seen that for the energy ranges relevant for the solar axion searches (2–7 keV and 0.5–5 keV) the overall background rate is the lowest which occurs from the fact that both ranges ignore the copper fluorescence peak. Thus, the detector seems to be well suited for such searches. Comparing the GridPix3 detector with the IAXO prototype detector in these ranges reveals that the IAXO prototype has a factor of 3–4 lower background than the GridPix3 detector. The reason for this large difference is probably the usage of a polyimide PCB in the prototype detector instead of a standard PCB made from FR4 as used for the GridPix3 detector. FR4 is known to have a fairly high radioactivity (see [Heu95, ABB+13]) in the scope of radiopure materials. Therefore, it will spoil the detector with additional background. Comparing the result of the prototype detector using

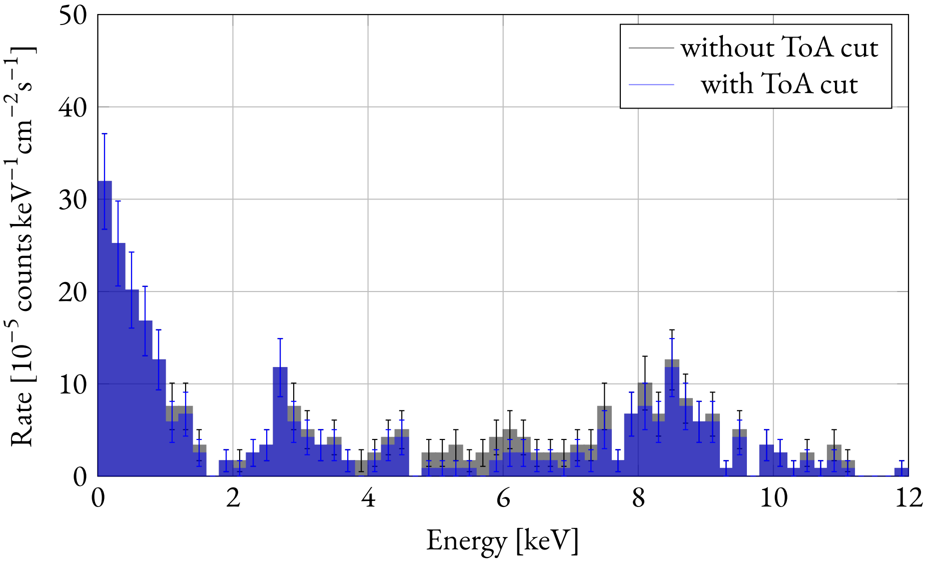

Figure 14.21: Background rate using the simulated data for the likelihood, with and without ToA cut at ToA = 12.

Method	Rate in counts keV^{-1}cm^{-2}s^{-1} for E in range 0–12 keV	0–8 keV	2–7 keV	0.5–5 keV
GridPix3 detector				
CDL + ToA cut	$1.247(60) \times 10^{-4}$	$1.430(78) \times 10^{-4}$	$8.931(789) \times 10^{-5}$	$1.054(90) \times 10^{-4}$
Sim + ToA cut	$1.305(61) \times 10^{-4}$	$1.496(81) \times 10^{-4}$	$8.233(758) \times 10^{-5}$	$9.071(839) \times 10^{-5}$
ToA in lnL	$9.187(517) \times 10^{-5}$	$9.114(630) \times 10^{-5}$	$8.373(764) \times 10^{-5}$	$7.288(752) \times 10^{-5}$
IAXO prototype detector				
CDL + ToA cut	$5.083(267) \times 10^{-5}$	$6.343(365) \times 10^{-5}$	$2.789(306) \times 10^{-5}$	$5.713(462) \times 10^{-5}$
Sim + ToA cut	$4.396(248) \times 10^{-5}$	$5.230(331) \times 10^{-5}$	$2.520(291) \times 10^{-5}$	$4.182(395) \times 10^{-5}$
ToA in lnL	$2.618(192) \times 10^{-5}$	$2.688(238) \times 10^{-5}$	$2.151(269) \times 10^{-5}$	$2.352(296) \times 10^{-5}$

Table 14.2: Averaged background rates for different energy ranges for the two tested detectors and three methods. The IAXO prototype detector outperforms the GridPix3 detector in all ranges.

the extended likelihood method with those of the detectors used at CAST using a lead shielding around the detector (data taking 2014/15 achieved a background rate of $\sim 2.9 \times 10^{-5}$ counts keV^{-1}cm^{-2}s^{-1}, data taking 2017/18 achieved a background rate of $(2.124 \pm 0.097) \times 10^{-5}$ counts keV^{-1}cm^{-2}s^{-1} for the energy range from 0 to 8 keV [Sch24a]) it can be seen that the results are comparable, thus the prototype detector seems also to outperform the so far used GridPix detectors.

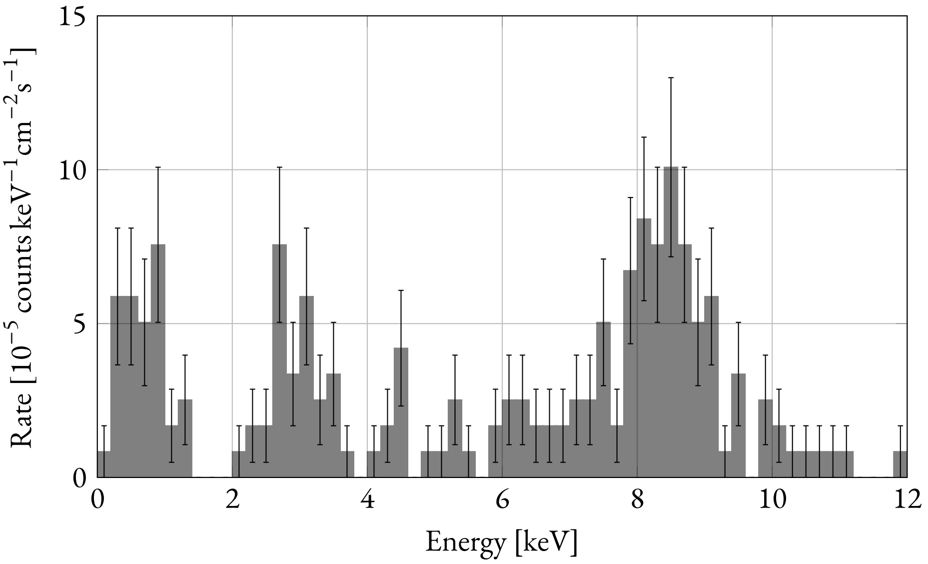

Figure 14.22: Background rate using the likelihood method including the `toaLength`.

CHAPTER 15

Outlook

For the search for solar axions further and novel detector developments are necessary to allow to reach into physically interesting and not yet excluded regions in the phase space. Towards this, in section 15.1 a new detector concept shall be presented allowing to reach the energy range of the plasmon-axion conversion (1 eV–200 eV) and consequently a first insight towards this part of the solar axion spectrum. Then, in section 15.2 some ideas for the further development of the radiopure IAXO prototype detector will be given.

15.1 The UV-enhanced detector

To measure very low energetic X-rays ($\mathcal{O}(100\,\text{eV})$) a problem arises with gaseous detectors. Since the average energy needed to produce an electron-ion pair, e.g. from argon, is around 26 eV, only very few electrons will be created and measured by the GridPix. This leads to the problem that noise pixels are hard to identify and additionally can spoil the measurement by large amounts. Thus, in order to reduce the probability of interpreting noise as hits, the concept of the UV-enhanced detector was conceived. While operating a GridPix detector UV-photons are a nearly non-avoidable effect, which raises the number of hit pixels. Depending on the field strength underneath the grid and therefore the grid voltage the number of produced UV-photons rises with the gain. Normally, to reduce this effect a quencher gas is added. However, at low concentrations, it can be observed that UV-photons still have a strong impact on the number of hits per event. As shown in figure 15.1 this was already measured within a master thesis [Gru18]. From the figure, it can be seen that for low quantities of added quencher, the number of hits per cluster rises significantly even at moderate grid voltages. Marked with red circles for example, measurements with 2% added quencher gas, showing about two or three times more active pixels than expected. With most of those additional hits accounted to UV-photons the impact can already be clearly seen.

Simulating the UV-photons below the grid reveals, see figure 15.2, that most of the UV photons will hit the grid within a short distance of the incident avalanche position. Also, it can be seen that due to the pillars supporting the grid, several regions are excluded due to shadowing. From the simulated distribution, it can be stated that within a radius of a few pixels, most UV-photons will hit the grid. Hitting the grid allows, due to the photoelectric effect, the production of a new electron. This electron will then be accelerated towards the chip starting another avalanche. This can then activate another

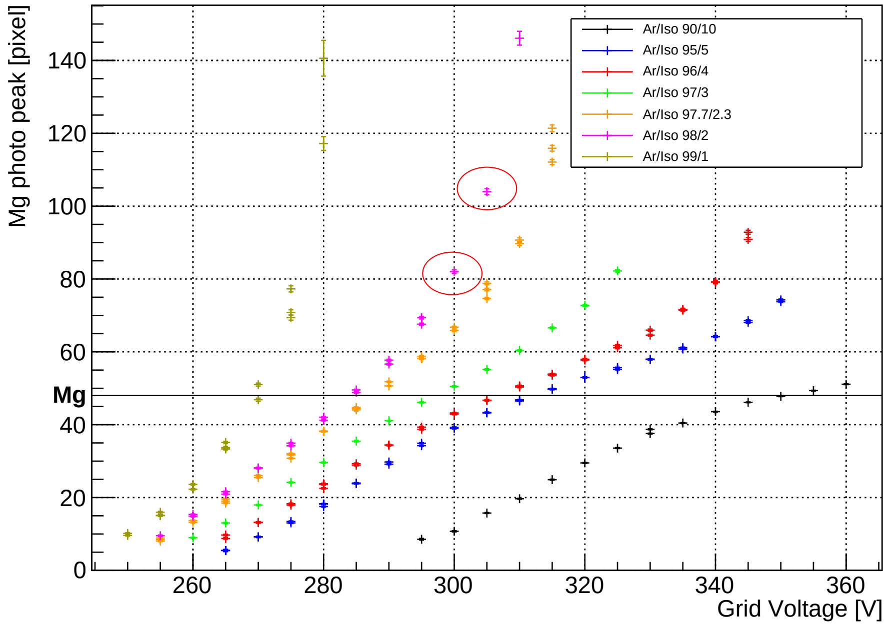

Figure 15.1: A measurement of the magnesium Kα-line a different grid voltages for different amounts of quencher. Marked in red are two measurements where UV photons probably dominate the pixel spectrum. This should lead to small clusters within the spectrum reassembling the expected 48 pixels. Adapted from [Gru18].

pixel. Since these pixels are in a close vicinity to each other a small-scale clustering should be able to combine those recreating the correct number of primary electrons.

To test this, an additional small-scale clustering with a search radius of three pixels was implemented to reanalyse the data marked in the red circles of figure 15.1. The results can be seen for both data sets in figure 15.3. The figure reveals that the base idea is working, so after the clustering, the number of isolated pixels and clusters reproduces the expected number of primary electrons. The number of clusters found within each event is additionally shown. This number shows that about 50% of the hits within an event originate from small clusters.

With this knowledge, the UV-enhanced detector seems feasible. In order to produce a proper UV-enhanced detector a few things should be kept in mind. First, the detector needs to be temperature and pressure stabilised to keep the gas gain constant. Then, the gain has to be adjusted to a point where as many clusters as possible are produced. Note that this only works to a certain point before a gas discharge sets in. The primary electrons should arrive with a certain distance to each other at the grid such that the emerging clusters do not overlap. This is typically given for the drift length of 3 cm and a mixture of argon and isobutane used so far since very low energetic X-rays convert very close to the entrance window. Thus, their mean distance from the conversion point will be

$$\sigma_t = D_t\sqrt{3\,\mathrm{cm}} = 1.15\,\mathrm{mm} = 21\,\mathrm{pixels}\,. \tag{15.1}$$

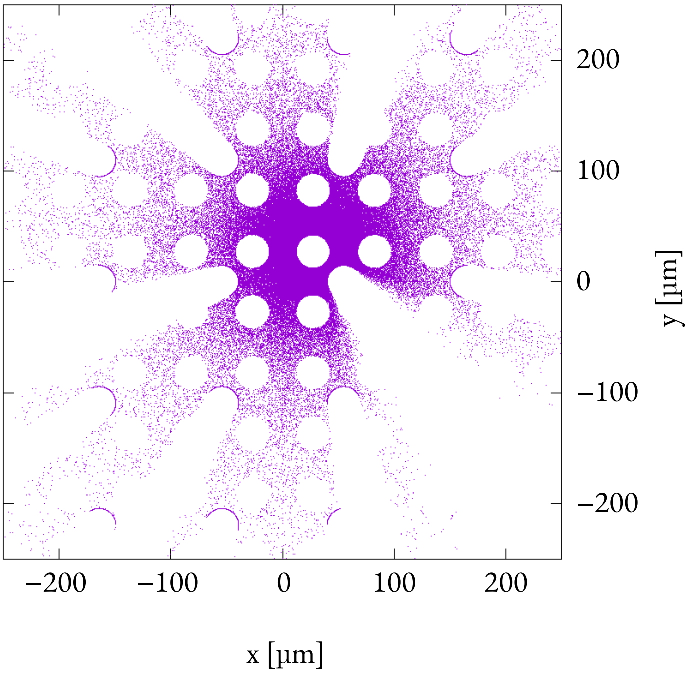

Figure 15.2: Simulation of the UV-photons underneath the grid. Purple dots mark the places where the photons were stopped by the grid and by the pillars. Photons stopped by the Timepix are ignored since they will not produce avalanches. It is clearly visible that most photons reach the grid within a few pixels.

Hence, for only a few primary electrons the chances that two clusters are too close to each other are reasonably small. This can also be deduced from figure 13.7. The lower the energy of the incident photon the lower the chance that two electrons enter the same grid hole.

Overall it could be shown that already with a not optimised detector 50% of the primary electron hits are clusters. To measure at the lowest energies the base idea would be to recluster the events and either just count the clusters or to additionally use the isolated pixels. This has to be tested for very low energies. With this one should be able to measure at least energies to about 100 eV. Reaching this energies would allow for the first time to measure axions arising from plasmon-axion conversions which are increasing the model independent flux tremendously. This is getting more interesting with the availability of ultra-thin windows as shown in figure 15.5, showing in the range of 50 eV to 100 eV transparencies of ~ 30%. Exactly where the solar flux from the plasmon-axion conversions peaks (see figure 15.5).

15.2 The radiopure GridPix3 detector

For the next generation of radiopure IAXO detector, a few things should be changed in order to achieve an even lower background level. First of all, as learned from the seven GridPix detector the usage of a ring of six veto chips around the central one allows for a major reduction of background, not only at the chip edges but also in the centre. As shown in [Sch24a] from the outer chips additional vetoes can be defined to find isolated clusters remaining from charged particle tracks (see figure 15.4(a),(b)).

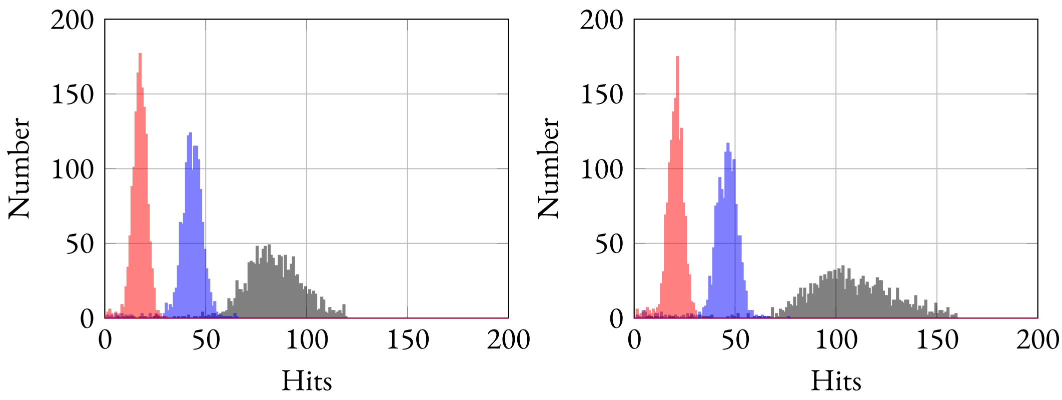

Figure 15.3: Test of a small-scale clustering (three pixels search radius) within two data sets with high numbers of hit pixels per event. The magnesium Kα-line is expected to be at 48 hits. The unclustered distribution —all hit pixels in the event— is shown in black. In blue close-by pixels are clustered and counted only once, while in red only the number of clusters is shown without isolated pixels. It can be clearly seen the blue histograms reproduce the expected 48 hits in a good manner. (a) a data set was used with about double the amount of expected pixels and (b) a data set with approximately three times the amount of active pixels.

These vetoes will be way more effective due to the additional usage of the ToA. Since this allows also a time-wise correlation of charged particle tracks on the outer chips and events on the central one, leading to a higher efficiency of these vetoes. Using the ToA information a third veto can be implemented reducing the number of argon fluorescence photons. If the central GridPix shows a X-ray-like event and another event on the outer GridPixes in a coincident time window, the photon is likely to be a argon fluorescence photon induced by the event on the outer GridPixes as sketched in figure 15.4(c).

For the ToA measurement the fine ToA should be activated. This will enhance the efficiency of the likelihood cut including the `ToAlength` of the event. This might reduce the background further. Also using a neural network approach, shown to be very successful [Sch24a], should be tested with the addition of the ToA information. Interpolating from the already achieved results, this could lead to a background level in the envisioned region of 10^{-7} counts $\mathrm{keV}^{-1}\mathrm{cm}^{-2}\mathrm{s}^{-1}$.

From the mechanical point of view, the detector performed fine during the test run except for the sparking problem. Especially the cathode should be redesigned to fulfill the necessary gap sizes following Paschen's law. Regarding the PCB a new version is available but yet untested. For the ultra-thin windows already progress was made towards even thinner windows. The next generation of those windows will have a thickness in the order of 100 nm–170 nm depending on the diameter of the window. For these new windows two different diameters have been chosen in order to reflect the different focal spot size of the two optics planned for BabyIAXO.

The expected transparencies of the two different windows are shown in figure 15.5. It can be seen that especially below 1 keV a significant rise in the transparency is reached. With this, a better signal to background rate can be reached. This is particularly interesting for the axion-electron coupling, peaking at low energies as well as for searches for axions from the plasmon-axion conversion.

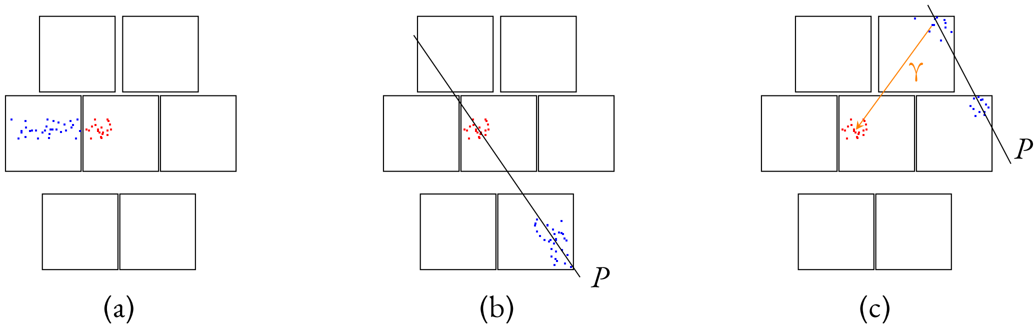

Figure 15.4: Sketches of the three vetoes possible with the veto ring made from six GridPixes. The central X-ray-like event is indicated in red. In blue the additional information from the veto ring is indicated. Black lines give the trajectory of a particle *P*. The vetoes (a), a truncated path of a charged particle, and (b), a path with low density (a large gap), have already been implemented for the seven GridPix detector (see [Sch24a]). Veto (c) is not used. Here, an argon ion produces an X-ray (orange) which travels to the central GridPix producing a signal. Due to the usage of ToA a coincidence can be used to identify those signals. This could reduce the argon fluorescence peak.

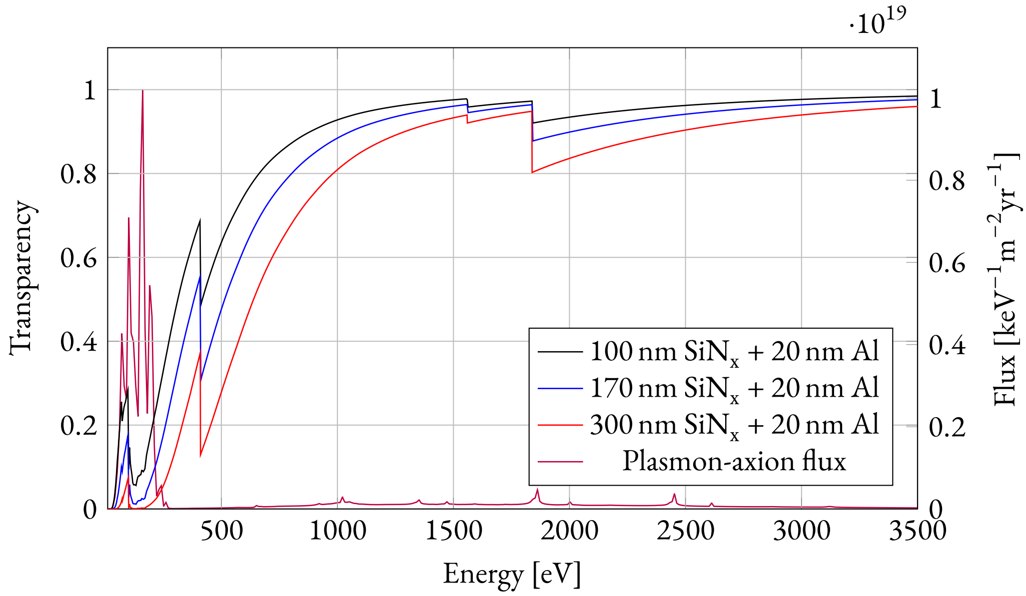

Figure 15.5: Preliminary transparencies of the next generation SiN_x windows for an energy range from 10 eV to 3500 eV. For comparison also the transparency of a 300 nm window as described in chapter 7 is shown. Expected transparencies from [Gul], plasmon-axion flux from [vO23].

CHAPTER 16

Conclusion

In this thesis the developments towards a GridPix3 detector for the upcoming BabyIAXO experiment were shown. Starting with the seven GridPix detector as an IAXO prototype used at CAST, a new veto system was implemented, as well as a cooling device and new ultra-thin windows in order to raise the efficiency of the detector. The new veto system uses a ring of six GridPixes surrounding the central GridPix to reject background. To reduce the additional heat of these six GridPixes a cooling device was developed assuring stable operation of the detector. Additionally, a system of scintillator vetoes was implemented. Furthermore, the signal of the grid from the central GridPix was included in the veto system. It was used to time stamp the signals from the scintillators and as a trigger leading to a better duty cycle of the detector.

To use the Timepix3 for the GridPix detector readout, a new readout system was developed and commissioned. For this first the PCBs were designed and a detector housing based on the design of the detectors used at CAST. Then the firm- and software were developed. The software includes a UI featuring both a CLI and a GUI to allow intuitive usage of the readout. With the full detector assembly first scans to find the best DAC settings for the Timepix3 were performed. After this optimisation the detector was operational and a data set of 350 hours of background data was taken. Here the long-term stability of the detector could be proved.

For BabyIAXO the anticipated background levels are lower than the results achieved so far with GridPix detectors at CAST. It is known that one of the major components of the background is the intrinsic background of the detector material. To solve this problem, a unique detector was developed consisting only of materials known to be radiopure. A prototype of this detector was built —using partly non-radiopure materials— and tested. The studies in this thesis prove that the detector is fully functional. Additionally, the stability within a 750 hour background run was demonstrated. Within these tests problems could be identified and solved towards the next generation detector.

The data of both mentioned background runs was analysed and used to compare different approaches of using the time of arrival parameter to improve the background rejection. The comparison showed that the usage of the time length of the clusters within the likelihood cut significantly reduces the observed background rates. The comparison of the two tested detectors shows that the prototype detector, even not being built entirely from radiopure materials, outperforms the CAST-like detector. This led to a background rate of $(2.151 \pm 0.269) \times 10^{-5}$ counts $\mathrm{keV}^{-1}\mathrm{cm}^{-2}\mathrm{s}^{-1}$ in the energy range of 2–7 keV. This is a significant improvement compared to the CAST-type detectors, for which similar rates could be achieved within a lead shielding of 5–10 cm.

Bibliography

[AAA+07a] P Abbon, S Andriamonje, S Aune, T Dafni, M Davenport, E Delagnes, R de Oliveira, G Fanourakis, E Ferrer Ribas, J Franz, et al. The micromegas detector of the cast experiment. *New Journal of Physics*, 9(6):170, 2007.

[AAA+07b] P Abbon, S Andriamonje, S Aune, T Dafni, M Davenport, E Delagnes, R de Oliveira, G Fanourakis, E Ferrer Ribas, J Franz, T Geralis, A Giganon, M Gros, Y Giomataris, I G Irastorza, K Kousouris, J Morales, T Papaevangelou, J Ruz, K Zachariadou, and K Zioutas. The micromegas detector of the cast experiment. *New Journal of Physics*, 9(6):170, jun 2007.

[AAA+10] S Andriamonje, S Aune, D Autiero, K Barth, A Belov, B Beltrán, H Bräuninger, JM Carmona, S Cebrián, JI Collar, et al. Search for solar axion emission from 7li and d (p, γ) 3he nuclear decays with the cast γ-ray calorimeter. *Journal of cosmology and astroparticle physics*, 2010(03):032, 2010.

[AAA+15] V. Anastassopoulos, M. Arik, S. Aune, K. Barth, A. Belov, H. Bräuninger, G. Cantatore, et al. Search for chameleons with cast. *Physics Letters B*, 749:172–180, 2015.

[AAA+21] M Aker, K Altenmüller, JF Amsbaugh, M Arenz, M Babutzka, J Bast, S Bauer, H Bechtler, M Beck, A Beglarian, et al. The design, construction, and commissioning of the katrin experiment. *Journal of Instrumentation*, 16(08):T08015, 2021.

[AAA+22] CM Adair, K Altenmüller, V Anastassopoulos, S Arguedas Cuendis, J Baier, K Barth, A Belov, D Bozicevic, H Bräuninger, G Cantatore, et al. Search for dark matter axions with cast-capp. *Nature Communications*, 13(1):6180, 2022.

[AAAC+21] A Abeln, K Altenmüller, S Arguedas Cuendis, E Armengaud, D Attié, S Aune, S Basso, L Bergé, B Biasuzzi, PTC Borges De Sousa, et al. Conceptual design of babyiaxo, the intermediate stage towards the international axion observatory. *Journal of High Energy Physics*, 2021(5):1–80, 2021.

[AAAC+24] K. Altenmüller, V. Anastassopoulos, S. Arguedas-Cuendis, S. Aune, J. Baier, K. Barth, H. Bräuninger, G. Cantatore, et al. New upper limit on the axion-photon coupling with an extended cast run with a xe-based micromegas detector. *Physical Review Letters*, 133(22):221005, 2024.

[AAB+14a] M. Arik, S. Aune, K. Barth, A. Belov, et al. Search for solar axions by the cern axion solar telescope with ^{3}He buffer gas: Closing the hot dark matter gap. *Phys. Rev. Lett.*, 112:091302, Mar 2014.

[AAB+14b] E Armengaud, FT Avignone, M Betz, P Brax, Pierre Brun, Giovanni Cantatore, JM Carmona, GP Carosi, Fritz Caspers, S Caspi, et al. Conceptual design of the international axion observatory (iaxo). *Journal of Instrumentation*, 9(05):T05002, 2014.

[AAB+17] V Anastassopoulos, S Aune, K Barth, A Belov, G Cantatore, JM Carmona, JF Castel, SA Cetin, F Christensen, JI Collar, et al. New cast limit on the axion–photon interaction. *Nature Physics*, 13(6):584–590, 2017.

[AAB+19] E Armengaud, D Attié, S Basso, P Brun, N Bykovskiy, JM Carmona, JF Castel, S Cebrián, M Cicoli, M Civitani, et al. Physics potential of the international axion observatory (iaxo). *Journal of cosmology and astroparticle physics*, 2019(06):047, 2019.

[AAB+21] Nancy Aggarwal, Odylio D Aguiar, Andreas Bauswein, Giancarlo Cella, Sebastian Clesse, Adrian Michael Cruise, Valerie Domcke, Daniel G Figueroa, Andrew Geraci, Maxim Goryachev, et al. Challenges and opportunities of gravitational-wave searches at mhz to ghz frequencies. *Living reviews in relativity*, 24:1–74, 2021.

[AÁMAC+23] Saiyd Ahyoune, Alejandro Álvarez Melcón, Sergio Arguedas Cuendis, Sergio Calatroni, Cristian Cogollos, Jack Devlin, Alejandro Díaz-Morcillo, David Díez-Ibáñez, Babette Döbrich, Javier Galindo, et al. A proposal for a low-frequency axion search in the 1–2 μev range and below with the babyiaxo magnet. *Annalen der Physik*, 535(12):2300326, 2023.

[ABB+13] V Alvarez, I Bandac, A Bettini, FIGM Borges, S Carcel, J Castel, S Cebrián, A Cervera, CAN Conde, T Dafni, et al. Radiopurity control in the next-100 double beta decay experiment: procedures and initial measurements. *Journal of Instrumentation*, 8(01):T01002, 2013.

[ABC+85] R Apsey, D Baynham, P Clee, D Cragg, N Cunliffe, R Hopes, and R Stovold. Design of a 5.5 metre diameter superconducting solenoid for the delphi particle physics experiment at lep. *IEEE Transactions on Magnetics*, 21(2):490–493, 1985.

[ABC+07] D Autiero, B Beltrán, JM Carmona, S Cebrián, E Chesi, M Davenport, M Delattre, L Di Lella, F Formenti, IG Irastorza, et al. The cast time projection chamber. *New Journal of Physics*, 9(6):171, 2007.

[ACC+15] F Aznar, J Castel, FE Christensen, T Dafni, TA Decker, E Ferrer-Ribas, JA Garcia, I Giomataris, JG Garza, CJ Hailey, et al. A micromegas-based low-background x-ray detector coupled to a slumped-glass telescope for axion research. *Journal of Cosmology and Astroparticle Physics*, 2015(12):008, 2015.

[ACD+14] S Aune, JF Castel, T Dafni, M Davenport, G Fanourakis, E Ferrer-Ribas, J Galán, JA Garcia, A Gardikiotis, T Geralis, et al. Low background x-ray detection with micromegas for axion research. *Journal of Instrumentation*, 9(01):P01001, 2014.

[ADF+09] S Aune, T Dafni, G Fanourakis, E Ferrer Ribas, J Galán Lacarra, T Geralis, I Giomataris, FJ Iguaz, IG Irastorza, K Kousouris, et al. An ultra-low-background detector for axion searches. In *Journal of Physics: Conference Series*, volume 179, page 012015. IOP Publishing, 2009.

[AG96] K Azar and JE Graebner. Experimental determination of thermal conductivity of printed wiring boards. In *Twelfth Annual IEEE Semiconductor Thermal Measurement and Management Symposium. Proceedings*, pages 169–182. IEEE, 1996.

[AGGB98] G Auday, Ph Guillot, J Galy, and H Brunet. Experimental study of the effective secondary emission coefficient for rare gases and copper electrodes. *Journal of applied physics*, 83(11):5917–5921, 1998.

[Aka] Akasa. Specifications of tt12-80. "https://akasa.co.uk/update.php?tpl=product/product.detail.tpl&no=181&type=Accessories&type_sub=Thermal%20Interface&model=AK-TT12-80, [Accessed: 2023-01-11]".

[ÁMACB+21] Alejandro Álvarez Melcón, Sergio Arguedas Cuendis, Justin Baier, Klaus Barth, Heinrich Bräuninger, Sergio Calatroni, Giovanni Cantatore, Fritz Caspers, JF Castel, SA Cetin, et al. First results of the cast-rades haloscope search for axions at 34.67 µev. *Journal of High Energy Physics*, 2021(10):1–16, 2021.

[AMDL+11] Kerstin Avila, David Moxey, Alberto De Lozar, Marc Avila, Dwight Barkley, and Björn Hof. The onset of turbulence in pipe flow. *Science*, 333(6039):192–196, 2011.

[AMSM18] Jean-Luc Autran, Daniela Munteanu, T Saad Saoud, and Soilihi Moindjie. Characterization of atmospheric muons at sea level using a cosmic ray telescope. *Nuclear Instruments and Methods in Physics Research Section A: Accelerators, Spectrometers, Detectors and Associated Equipment*, 903:77–84, 2018.

[Ans] Ansys Inc. Ansys. "https://www.ansys.com/, [Accessed: 2022-03-18]".

[BBE+24] J Bilicki, P Bongratz, F Edzards, F Iguaz Gutierrez, C Menneglier, S Mertens, L Schönfeld, D Siegmann, J Beteta, K Urban, C Wiesinger, and M Willers. Sdd x-ray detection efficiency measurement at soleil status. IAXO detector meeting, 2024.

[BCZC] M.J. Berger, J.S. Coursey, M.A. Zucker, and J Chang. Estar, pstar, and astar: Computer programs for calculating stopping-power and range tables for electrons, protons, and helium ions. "http://physics.nist.gov/Star, [Accessed: 2024-12-03]".

[Bea67] Joyce Alvin Bearden. X-ray wavelengths. *Reviews of Modern Physics*, 39(1):78, 1967.

[BFA+11] L Baudis, AD Ferella, A Askin, J Angle, E Aprile, T Bruch, A Kish, M Laubenstein, A Manalaysay, T Marrodan Undagoitia, et al. Gator: a low-background counting facility at the gran sasso underground laboratory. *Journal of Instrumentation*, 6(08):P08010, 2011.

[BGS+16] Marco Barbera, Fabio Gastaldello, Luisa Sciortino, Simonpietro Agnello, Gianpiero Buscarino, Alfonso Collura, Nicola La Palombara, Ugo Lo Cicero, Nicola Sartore, Andrea Tiengo, et al. The thin and medium filters of the epic camera on-board xmm-newton: measured performance after more than 15 years of operation. *Experimental Astronomy*, 42:179–197, 2016.

[Bia] S Biagi. Magboltz - transport of electrons in gas mixtures. "https://magboltz.web.cern.ch/magboltz/, [Accessed: 2024-01-20]".

[Bil] Y. Bilevych. Courtesy of Yevgen Bilevych.

[BJBL01] Christiane Bonnelle, Philippe Jonnard, Marie-Martine Bé, and Marie-Christine Lépy. Emissions xk du manganèse: comparaison entre les spectres du métal et d'une source de 55fe. *Bulletin du Bureau national de métrologie*, pages 7–16, 2001.

[Boo01] X-Ray Data Booklet. X-ray data booklet. *Laboratory, Univ. California*, 2001.

[BRR08] Walter Blum, Werner Riegler, and Luigi Rolandi. *Particle detection with drift chambers*. Springer Science & Business Media, 2008.

[BRW+94] M Bona, L Rossi, L Walckiers, F Rodriguez-Mateos, A Siemko, P Sievers, E Acerbi, R Perin, and D Leroy. Performance of the first cern-infn 10 m long superconducting dipole prototype for the lhc. Technical report, CERN, 1994.

[BS18] Hans-Jürgen Bargel and Günter Schulze. *Werkstoffkunde*. Springer-Verlag, 2018.

[C.] Margalejo C. Courtesy of Cristina Margalejo Blasco.

[CAB+11] William W Craig, HongJun An, Kenneth L Blaedel, Finn E Christensen, Todd A Decker, Anne Fabricant, Jeff Gum, Charles J Hailey, Layton Hale, Carsten B Jensen, et al. Fabrication of the nustar flight optics. In *Optics for EUV, X-Ray, and Gamma-Ray Astronomy V*, volume 8147, pages 151–164. SPIE, 2011.

[Cas] P Cassette. Lne – lnhb/cea table de radionucléides. "http://www.lnhb.fr/nuclides/Fe-55_tables.pdf, [Accessed: 2024-12-03]".

[CDFR+11] S Cebrián, T Dafni, E Ferrer-Ribas, J Galán, I Giomataris, H Gómez, FJ Iguaz, IG Irastorza, G Luzón, R De Oliveira, et al. Radiopurity of micromegas readout planes. *Astroparticle Physics*, 34(6):354–359, 2011.

[CG] S. Cebrián Guajardo. privat communication.

[CL21] S Cebrián and G Luzón. Radiopurity low background techniques. 8. IAXO Technical Coordination Meeting, 2021.

[Com20] The Dow Chemical Company. Dowsil se 4445 cv gel technical data sheet, 2020.

[CPG+25] P Carenza, JA Pascual, M Giannotti, IG Irastorza, M Kaltschmidt, A Lella, A Lindner, G Lucente, A Mirizzi, and MJ Puyuelo. Detecting supernova axions with iaxo. *arXiv preprint arXiv:2502.19476*, 2025.

[D.] D. Arnold et al. Messungen des gehalts natürlicher radionuklide in blei und glas. https://www.ptb.de/cms/ptb/fachabteilungen/abt6/forschungsnachrichtenabt6/nachrichten-2006.html.

[DCLVKK99] D De Chambure, R Lainé, K Van Katwijk, and P Kletzkine. Xmm's x-ray telescopes. *ESA bulletin*, 100:30–42, 1999.

[DFS81] Michael Dine, Willy Fischler, and Mark Srednicki. A simple solution to the strong cp problem with a harmless axion. *Physics letters B*, 104(3):199–202, 1981.

[DH82] Moshe Deutsch and Michael Hart. Wavelength, energy shape, and structure of the cu k α 1 x-ray emission line. *Physical Review B*, 26(10):5558, 1982.

[DLGG+22] Luca Di Luzio, Javier Galan, Maurizio Giannotti, Igor G Irastorza, Joerg Jaeckel, Axel Lindner, Jaime Ruz, Uwe Schneekloth, Lukas Sohl, Lennert J Thormaehlen, et al. Probing the axion–nucleon coupling with the next generation of axion helioscopes. *The European Physical Journal C*, 82(2):120, 2022.

[Dun88] William G Dunbar. Design guide: Designing and building high voltage power supplies. volume 2. *Interim Report*, 1988.

[EAA+23] A Elersich, P Agnes, I Ahmad, S Albergo, IFM Albuquerque, T Alexander, AK Alton, P Amaudruz, M Atzori Corona, M Ave, et al. Study of cosmogenic activation above ground for the darkside-20k experiment. *Astroparticle Physics*, 152:102878, 2023.

[EEC+19] Aldo Ejlli, Damian Ejlli, Adrian Mike Cruise, Giampaolo Pisano, and Hartmut Grote. Upper limits on the amplitude of ultra-high-frequency gravitational waves from graviton to photon conversion. *The European Physical Journal C*, 79(12):1032, 2019.

[EKS+96] Martin Ester, Hans-Peter Kriegel, Jörg Sander, Xiaowei Xu, et al. A density-based algorithm for discovering clusters in large spatial databases with noise. In *kdd*, volume 96, pages 226–231, 1996.

[FLB+09] L Fleischmann, M Linck, A Burck, C Domesle, S Kempf, M Rodrigues, A Pabinger, C Pies, JP Porst, H Rotzinger, et al. Physics and applications of metallic magnetic calorimeters for particle detection. In *Journal of Physics: Conference Series*, volume 150, page 012013. IOP Publishing, 2009.

[FMM22] Gabriele Franciolini, Anshuman Maharana, and Francesco Muia. Hunt for light primordial black hole dark matter with ultrahigh-frequency gravitational waves. *Physical Review D*, 106(10):103520, 2022.

[fZuMI] Fraunhofer-Institut für Zuverlässigkeit und Mikrointegration (IZM). Courtesy of IZM Berlin.

[GC17] Rebecca Grinham and Andrew Chew. A review of outgassing and methods for its reduction. *Applied Science and Convergence Technology*, 26(5):95–109, 2017.

[Ger62] ME Gertsenshtein. Wave resonance of light and gravitional waves. *Sov Phys JETP*, 14:84–85, 1962.

[GGC81] Kuldip C Gupta, Ramesh Garg, and Rakesh Chadha. Computer aided design of microwave circuits. *NASA STI/Recon Technical Report A*, 82:39449, 1981.

[GHI+20] Shao-Feng Ge, Koichi Hamaguchi, Koichi Ichimura, Koji Ishidoshiro, Yoshiki Kanazawa, Yasuhiro Kishimoto, Natsumi Nagata, and Jiaming Zheng. Supernova-scope for the direct search of supernova axions. *Journal of Cosmology and Astroparticle Physics*, 2020(11):059, 2020.

[GI22] Igor Garcia Irastorza. An introduction to axions and their detection. *SciPost Physics Lecture Notes*, page 045, 2022.

[GKM+19] Roland Gomeringer, Roland Kilgus, Volker Menges, Stefan Oesterle, Thomas Rapp, Claudius Scholer, Andreas Stenzel, Andreas Stephan, and Falko Wieneke. *Tabellenbuch Metall*. Europa-Lehrmittel, 2019.

[Gru] M. Gruber. Markus Gruber, dissertation in preparation.

[Gru18] M. Gruber. Study of ionisation and amplification processes in gridpix detectors, December 2018.

[Gul] E. Gullikson. X-ray interactions with matter. "https://henke.lbl.gov/optical_constants/, [Accessed: 2024-05-03]".

[Ham22] P. Hamacher. Installation des myon-veto-systems eines detektorstandes für babyiaxo, August 2022.

[HCC+13] Fiona A Harrison, William W Craig, Finn E Christensen, Charles J Hailey, William W Zhang, Steven E Boggs, Daniel Stern, W Rick Cook, Karl Forster, Paolo Giommi, et al. The nuclear spectroscopic telescope array (nustar) high-energy x-ray mission. *The Astrophysical Journal*, 770(2):103, 2013.

[Heu95] G Heusser. Low.-t dioactivity background techniques. *Annu. Rev. Nucl. Part. Sci*, 45:543–90, 1995.

[HJT21] Sebastian Hoof, Joerg Jaeckel, and Lennert J Thormaehlen. Quantifying uncertainties in the solar axion flux and their impact on determining axion model parameters. *Journal of Cosmology and Astroparticle Physics*, 2021(09):006, 2021.

[HKS+15] D Hengstler, M Keller, C Schötz, J Geist, M Krantz, S Kempf, L Gastaldo, A Fleischmann, T Gassner, G Weber, et al. Towards fair: first measurements of metallic magnetic calorimeters for high-resolution x-ray spectroscopy at gsi. *Physica Scripta*, 2015(T166):014054, 2015.

[Hä] P. Hänisch. privat communication.

[IAXa] IAXO Collaboration. Iaxo webpage. "https://iaxo.desy.de/, [Accessed: 2024-08-12]".

[IAXb] IAXO magnet group. Private communication.

[igu] igus GmbH. iglidur j - werkstoffdaten. "https://www.igus.de/gleitlager/werkstoffe/dauereinsatz/iglidur-j-werkstoffdaten, [Accessed: 2024-12-03]".

[IH05] Kent D Irwin and Gene C Hilton. Transition-edge sensors. *Cryogenic particle detection*, pages 63–150, 2005.

[IMMD06] Mourad Idir, Pascal Mercere, Thierry Moreno, and Aurélien Delmotte. Technical report: Metrology and test beamline at soleil. *Synchrotron Radiation News*, 19(4):18–23, 2006.

[Ino74] Mitio Inokuti. Introduction to the symposium on the jesse effect and related phenomena. *Radiation Research*, 59(2):343–349, 1974.

[IR18] Igor G Irastorza and Javier Redondo. New experimental approaches in the search for axion-like particles. *Progress in Particle and Nuclear Physics*, 102:89–159, 2018.

[J.C] J.C. Loach et al. radiopurity.org. https://www.radiopurity.org/.

[JLA+01] F Jansen, D Lumb, B Altieri, J Clavel, M Ehle, C Erd, C Gabriel, M Guainazzi, P Gondoin, R Much, et al. Xmm-newton observatory-i. the spacecraft and operations. *Astronomy & Astrophysics*, 365(1):L1–L6, 2001.

[Jou18] Karl Jousten. *Handbuch Vakuumtechnik*. Springer-Verlag, 2018.

[JS55] William P Jesse and John Sadauskis. Ionization by alpha particles in mixtures of gases. *Physical Review*, 100(6):1755, 1955.

[KAB+09] Jason E Koglin, HongJun An, Kenneth L Blaedel, Nicolai F Brejnholt, Finn E Christensen, William W Craig, Todd A Decker, Charles J Hailey, Layton C Hale, Fiona A Harrison, et al. Nustar hard x-ray optics design and performance. In *Optics for EUV, X-Ray, and Gamma-Ray Astronomy IV*, volume 7437, pages 107–114. SPIE, 2009.

[KBC+07] M Kuster, H Bräuninger, S Cebrián, M Davenport, C Eleftheriadis, J Englhauser, H Fischer, J Franz, P Friedrich, R Hartmann, et al. The x-ray telescope of cast. *New Journal of Physics*, 9(6):169, 2007.

[KCG+16] M Karuza, Giovanni Cantatore, A Gardikiotis, DHH Hoffmann, Yannis K Semertzidis, and K Zioutas. Kwisp: An ultra-sensitive force sensor for the dark energy sector. *Physics of the Dark Universe*, 12:100–104, 2016.

[Kim79] Jihn E Kim. Weak-interaction singlet and strong cp invariance. *Physical Review Letters*, 43(2):103, 1979.

[KKLD17] C Krieger, J Kaminski, M Lupberger, and K Desch. A gridpix-based x-ray detector for the cast experiment. *Nuclear Instruments and Methods in Physics Research Section A: Accelerators, Spectrometers, Detectors and Associated Equipment*, 867:101–107, 2017.

[KKVD18] Christoph Krieger, Jochen Kaminski, Theodoros Vafeiadis, and Klaus Desch. Energy dependent features of x-ray signals in a gridpix detector. *Nuclear Instruments and Methods in Physics Research Section A: Accelerators, Spectrometers, Detectors and Associated Equipment*, 893:26–34, 2018.

[KPGA20] Alain E Kaloyeros, Youlin Pan, Jonathan Goff, and Barry Arkles. Silicon nitride and silicon nitride-rich thin film technologies: state-of-the-art processing technologies, properties, and applications. *ECS Journal of Solid State Science and Technology*, 9(6):063006, 2020.

[Kri18] Christoph Krieger. *Search for solar chameleons with an InGrid based X-ray detector at the CAST experiment*. PhD thesis, University of Bonn, 2018.

[Kru91] F. Krummenacher. Pixel detectors with local intelligence: an ic designer point of view. *Nuclear Instruments and Methods in Physics Research Section A: Accelerators, Spectrometers, Detectors and Associated Equipment*, 305(3):527–532, 1991.

[KSB22] Ruslan Khubbutdinov, Martin Seyrich, and Kai Bagschik. Soft x-ray grating monochromators as a source of spatial coherence degradation: A wave-optical approach. *Journal of Physics: Conference Series*, 2380(1):012072, dec 2022.

[KW16] Hermann Kolanoski and Norbert Wermes. *Teilchendetektoren*. Springer, 2016.

[KW19] Hans-Joachim Kretzschmar and Wolfgang Wagner. D2. 1 thermophysikalische stoffwerte von wasser. In *VDI-Wärmeatlas*, pages 201–218. Springer, 2019.

[LBC+07] X. Llopart, R. Ballabriga, M. Campbell, L. Tlustos, and W. Wong. Timepix, a 65k programmable pixel readout chip for arrival time, energy and/or photon counting measurements. *Nuclear Instruments and Methods in Physics Research Section A: Accelerators, Spectrometers, Detectors and Associated Equipment*, 581(1):485–494, 2007. VCI 2007.

[LCC+16] JC Loach, J Cooley, GA Cox, Z Li, KD Nguyen, and AWP Poon. A database for storing the results of material radiopurity measurements. *Nuclear Instruments and Methods in Physics Research Section A: Accelerators, Spectrometers, Detectors and Associated Equipment*, 839:6–11, 2016.

[LCD+02] X. Llopart, M. Campbell, R. Dinapoli, D. San Segundo, and E. Pernigotti. Medipix2: A 64-k pixel readout chip with 55-/spl mu/m square elements working in single photon counting mode. *IEEE Transactions on Nuclear Science*, 49(5):2279–2283, 2002.

[LKLT20] Klaus Langeheinecke, André Kaufmann, Kay Langeheinecke, and Gerd Thieleke. *Thermodynamik für Ingenieure*. Springer, 2020.

[LL05] Michael A Lieberman and Allan J Lichtenberg. *Principles of plasma discharges and materials processing*. John Wiley & Sons, 2005.

[Llo] X. Llopart. Private communication.

[Llo06] X. Llopart. Timepix manual v1.0, 2006.

[LP92] Yu-Ran Luo and Philip D Pacey. Effects of alkyl substitution on ionization energies of alkanes and haloalkanes and on heats of formation of their molecular cations part 2.* alkanes and chloro-, bromo-and iodoalkanes. *International journal of mass spectrometry and ion processes*, 112(1):63–77, 1992.

[LP15] X. Llopart and T. Poikela. Timepix3 manual v2.0, 2015.

[LpPM94] MC L py, J Plagnard, and J Morel. Radiative auger effect: an explanation for discrepancies between theoretical and experimental k?/k? x-ray emission probability ratios? *Nuclear Instruments and Methods in Physics Research Section A: Accelerators, Spectrometers, Detectors and Associated Equipment*, 339(1-2):241–247, 1994.

[LSC91] HW Lefevre, RMS Schofield, and DR Ciarlo. Thin si3n4 windows for energy loss stim in air. *Nuclear Instruments and Methods in Physics Research Section B: Beam Interactions with Materials and Atoms*, 54(1-3):47–51, 1991.

[LSC+92] DM Lazarus, GC Smith, R Cameron, AC Melissinos, G Ruoso, Yannis K Semertzidis, and FA Nezrick. Search for solar axions. *Physical Review Letters*, 69(16):2333, 1992.

[Lup16] Michael Lupberger. *The Pixel-TPC: A feasibility study*. PhD thesis, University of Bonn, 2016.

[Lux] Luxium Solutions. Bc-400,bc-404,bc-408,bc-412,bc-416 datasheet. "https://luxiumsolutions.com/radiation-detection-scintillators/plastic-scintillators/bc400-bc404-bc408-bc412-bc416, [Accessed: 2024-12-03]".

[MÍ] MÉTROLOGIE Beamline. MÉtrologie beamline website. "https://www.synchrotron-soleil.fr/en/beamlines/metrologie, [Accessed: 2024-05-03]".

[MBC+05] J Morales, B Beltran, JM Carmona, S Cebrian, E Garcia, IG Irastorza, H Gómez, G Luzón, M Martínez, A Morales, et al. The canfranc underground laboratory. present and future. In *The Identification of Dark Matter*, pages 447–452. World Scientific, 2005.

[MBK+20] Susanne Mertens, Tim Brunst, M Korzeczek, M Lebert, D Siegmann, A Alborini, K Altenmüller, M Biassoni, L Bombelli, M Carminati, et al. Characterization of silicon drift detectors with electrons for the tristan project. *Journal of Physics G: Nuclear and Particle Physics*, 48(1):015008, 2020.

[MCC+18] Alejandro Álvarez Melcón, Sergio Arguedas Cuendis, Cristian Cogollos, Alejandro Díaz-Morcillo, Babette Döbrich, Juan Daniel Gallego, Benito Gimeno, Igor G Irastorza, Antonio José Lozano-Guerrero, Chloé Malbrunot, et al. Axion searches with microwave filters: the rades project. *Journal of Cosmology and Astroparticle Physics*, 2018(05):040, 2018.

[Med] Medipix collaboration. Medipix collaboration. "https://medipix.web.cern.ch/home, [Accessed: 2024-03-28]".

[ML11] Y Ménesguen and M-C Lépy. Characterization of the metrology beamline at the soleil synchrotron and application to the determination of mass attenuation coefficients of ag and sn in the range $3.5 \leq e \leq 28$ keV. *X-Ray Spectrometry*, 40(6):411–416, 2011.

[MLTZ20] Mainak Mukhopadhyay, Cecilia Lunardini, FX Timmes, and Kai Zuber. Presupernova neutrinos: directional sensitivity and prospects for progenitor identification. *The Astrophysical Journal*, 899(2):153, 2020.

[MMN+98] Shigetaka Moriyama, Makoto Minowa, Toshio Namba, Yoshizumi Inoue, Yuko Takasu, and Akira Yamamoto. Direct search for solar axions by using strong magnetic field and x-ray detectors. *Physics Letters B*, 434(1-2):147–152, 1998.

[NAG+24] S Navas, C Amsler, T Gutsche, C Hanhart, JJ Hernández-Rey, C Lourenço, A Masoni, M Mikhasenko, RE Mitchell, C Patrignani, et al. Review of particle physics. *Physical Review D*, 110(3):030001, 2024.

[Nor] Norcada Inc. Norcada. "https://www.norcada.com/, [Accessed: 2022-03-18]".

[O'H20] Ciaran O'Hare. cajohare/axionlimits: Axionlimits. https://cajohare.github.io/AxionLimits/, July 2020.

[OPT] OPTO DIODE CORPORATION. Ird axuv100 datasheet. "https://optodiode.com/pdf/AXUV100GDS.pdf, [Accessed: 2024-05-14]".

[OSH20] T Okajima, Y Soong, and T Hayashi. Development of the xrism x-ray mirror assembly. In *American Astronomical Society Meeting Abstracts# 235*, volume 235, pages 373–06, 2020.

[Par] Particle Data Group. Muons in polyvinyltoluene. "https://pdg.lbl.gov/2017/AtomicNuclearProperties/MUE/muE_polyvinyltoluene.pdf, [Accessed: 2024-12-03]".

[Pea18] William Burling Peatman. *Gratings, mirrors and slits: beamline design for soft X-ray synchrotron radiation sources*. Routledge, 2018.

[Pfe13] Pfeiffer Vacuum GmbH. *The vacuum technology book*, volume 2. Pfeiffer Vacuum GmbH, 2013.

[PG17] Denys Poda and Andrea Giuliani. Low background techniques in bolometers for double-beta decay search. *International Journal of Modern Physics A*, 32(30):1743012, 2017.

[Pla55] Robert L Platzman. Subexcitation electrons. *Radiation Research*, 2(1):1–7, 1955.

[PPW+14] Timepix Poikela, J Plosila, T Westerlund, M Campbell, M De Gaspari, X Llopart, V Gromov, R Kluit, M Van Beuzekom, F Zappon, et al. Timepix3: a 65k channel hybrid pixel readout chip with simultaneous toa/tot and sparse readout. *Journal of instrumentation*, 9(05):C05013, 2014.

[PQ77a] Roberto D Peccei and Helen R Quinn. Constraints imposed by cp conservation in the presence of pseudoparticles. *Physical Review D*, 16(6):1791, 1977.

[PQ77b] Roberto D Peccei and Helen R Quinn. Cp conservation in the presence of pseudoparticles. *Physical Review Letters*, 38(25):1440, 1977.

[Qui] A. Quintana. Private communication.

[RC20] Elisa Ruiz Chóliz. *Ultra-low background Micromegas X-ray detectors for Axion searches in IAXO and BabyIAXO*. PhD thesis, Universidad de Zaragosa, 2020.

[Red13] Javier Redondo. Solar axion flux from the axion-electron coupling. *Journal of Cosmology and Astroparticle Physics*, 2013(12):008, 2013.

[Rod] Rodriguez GmbH. Produktkatalog profilschienenführungen. "`https://www.rodriguez.de/fileadmin/4_downloads/3_kataloge/01_lineartechnik/rodriguez_profilschienen_03-2024_web.pdf`, [Accessed: 2024-12-03]".

[RSET21] Andreas Ringwald, Jan Schütte-Engel, and Carlos Tamarit. Gravitational waves as a big bang thermometer. *Journal of Cosmology and Astroparticle Physics*, 2021(03):054, 2021.

[S.] Schmidt S. Courtesy of Sebastian Schmidt.

[Scha] Tobias Schiffer. `TimepixAnalysis ToA extension`. "`https://github.com/Vindaar/TimepixAnalysis/pull/63`, [Accessed: 2025-01-06]".

[Schb] Sebastian Schmidt. `TimepixAnalysis`. "`https://github.com/Vindaar/TimepixAnalysis`, [Accessed: 2024-12-17]".

[Sch14] T. Schiffer. Erweiterung der optischen strahldiagnose an der elektronen-stretcher-anlage elsa, November 2014.

[Sch19a] L. Scharenberg. Studies on the thermal behaviour of gridpix-based detectors, February 2019.

[Sch19b] H. Schmick. Characterization of an improved gridpix detector for solar axion search at cast, Jule 2019.

[Sch24a] Sebastian Schmidt. *Search for solar axions using a 7-GridPix IAXO prototype detector at CAST*. PhD thesis, University of Bonn, 2024.

[Sch24b] G. Schmieden. Development and characterisation of the 14 scintillator readout for the iaxo detector teststand at ftd, June 2024.

[SGRK+22] Norbert Schartel, Rosario González-Riestra, Peter Kretschmar, Marcus Kirsch, Pedro Rodríguez-Pascual, Simon Rosen, Maria Santos-Lleó, Michael Smith, Martin Stuhlinger, and Eva Verdugo-Rodrigo. *XMM-Newton*, pages 1–38. Springer Nature Singapore, Singapore, 2022.

[Sik83] Pierre Sikivie. Experimental tests of the" invisible" axion. *Physical Review Letters*, 51(16):1415, 1983.

[Sik21] Pierre Sikivie. Invisible axion search methods. *Reviews of Modern Physics*, 93(1):015004, 2021.

[SiL] SiLab Bonn. "https://github.com/SiLab-Bonn/basil, [Accessed: 2022-03-18].

[SIR] SIRIUS Beamline. Sirius beamline website. "https://www.synchrotron-soleil.fr/en/beamlines/sirius, [Accessed: 2024-05-03]".

[SOL] SOLEIL. Soleil website. "https://www.synchrotron-soleil.fr/en, [Accessed: 2024-05-03]".

[Spa19] Roland Span. D2. 2 thermophysikalische stoffwerte von trockener luft. In *VDI-Wärmeatlas*, pages 219–237. Springer, 2019.

[SPW90] F Sarvar, NJ Poole, and PA Witting. Pcb glass-fibre laminates: Thermal conductivity measurements and their effect on simulation. *Journal of electronic materials*, 19(12):1345–1350, 1990.

[SS96] Peter J Serlemitsos and Yang Soong. Foil x-ray mirrors. *Astrophysics and Space Science*, 239:177–196, 1996.

[SVZ80] Mikhail A Shifman, AI Vainshtein, and Valentin I Zakharov. Can confinement ensure natural cp invariance of strong interactions? *Nuclear Physics B*, 166(3):493–506, 1980.

[T$^+$20] XRISM Science Team et al. Science with the x-ray imaging and spectroscopy mission (xrism). *arXiv preprint arXiv:2003.04962*, 2020.

[TGH$^+$18] Masaharu Tanabashi, Particle Data Grp, K Hagiwara, K Hikasa, Katsumasa Nakamura, Y Sumino, F Takahashi, J Tanaka, K Agashe, Giulio Aielli, et al. Review of particle physics. *Physical Review D*, 98(3), 2018.

[Thea] The GTK Team. GTK. https://www.gtk.org/.

[Theb] The HDF Group. Hierarchical Data Format, version 5. https://www.hdfgroup.org/HDF5/.

[thy] thyssenkrupp. Material data sheet 235jr. "https://ucpcdn.thyssenkrupp.com/_legacy/UCPthyssenkruppBAMXFrance/assets.files/product_pdf/carbon_flat_steel_/plates_and_slabs_carbon_steel/s235jr_1_0038_11_2016_engl.pdf, [Accessed: 2024-12-03]".

[TKK21] Jason Tang, Fabian Kislat, and Henric Krawczynski. Cadmium zinc telluride detectors for a next-generation hard x-ray telescope. *Astroparticle Physics*, 128:102563, 2021.

[TKM+16] Tadayuki Takahashi, Motohide Kokubun, Kazuhisa Mitsuda, Richard Kelley, Takaya Ohashi, Felix Aharonian, Hiroki Akamatsu, Fumie Akimoto, Steve Allen, Naohisa Anabuki, et al. The astro-h (hitomi) x-ray astronomy satellite. In *Space Telescopes and Instrumentation 2016: Ultraviolet to Gamma Ray*, volume 9905, pages 212–228. SPIE, 2016.

[TKS+14] Pekka T Törmä, Jari Kostamo, Heikki Sipilä, Marco Mattila, Pasi Kostamo, Esa Kostamo, Harri Lipsanen, Christian Laubis, Frank Scholze, Nick Nelms, et al. Performance and properties of ultra-thin silicon nitride x-ray windows. *IEEE Transactions on Nuclear Science*, 61(1):695–699, 2014.

[TME+11] J Toledo, H Muller, R Esteve, J M Monzó, A Tarazona, and S Martoiu. The front-end concentrator card for the RD51 scalable readout system. *Journal of Instrumentation*, 6(11):C11028–C11028, nov 2011.

[TRI22] TRISTAN group. Conceptual design report: Katrin with tristan modules, 2022.

[TSM+13] Pekka T Törmä, Heikki J Sipilä, Marco Mattila, Pasi Kostamo, Jari Kostamo, Esa Kostamo, Harri Lipsanen, Nick Nelms, Brian Shortt, Marcos Bavdaz, et al. Ultra-thin silicon nitride x-ray windows. *IEEE Transactions on Nuclear Science*, 60(2):1311–1314, 2013.

[UAE+21] D Unger, A Abeln, C Enss, A Fleischmann, D Hengstler, S Kempf, and L Gastaldo. High-resolution for iaxo: Mmc-based x-ray detectors. *Journal of Instrumentation*, 16(06):P06006, 2021.

[VBMMR89] K Van Bibber, PM McIntyre, DE Morris, and GG Raffelt. Design for a practical laboratory detector for solar axions. *Physical Review D*, 39(8):2089, 1989.

[vdG07] Harry van der Graaf. GridPix: An integrated readout system for gaseous detectors with a pixel chip as anode. *Nucl. Instrum. Meth. A*, 580:1023–1026, 2007.

[vF21] A. von Faber. Test eines szintillationszählers zum bau des myon-veto-systems eines detektorteststandes für babyiaxo, August 2021.

[vO] J. von Oy. Johanna von Oy, dissertation in preparation.

[vO23] Johanna von Oy. SolarAxionRayTracing, 2023.

[Wei78] Steven Weinberg. A new light boson? *Physical Review Letters*, 40(4):223, 1978.

[Wie] C. Wiesinger. Private communication.

[Wil78] Frank Wilczek. Problem of strong p and t invariance in the presence of instantons. *Physical Review Letters*, 40(5):279, 1978.

[Wil19] Philip Willmott. *An introduction to synchrotron radiation: techniques and applications*. John Wiley & Sons, 2019.

[Wol52] Hans Wolter. Spiegelsysteme streifenden einfalls als abbildende optiken für röntgenstrahlen. *Annalen der Physik*, 445(1-2):94–114, 1952.

[Yal07] P Yalçın. Measurement of relative k x-ray intensity ratio following radioactive decay and photoionization. *Nuclear Instruments and Methods in Physics Research Section B: Beam Interactions with Materials and Atoms*, 254(2):182–186, 2007.

[ZAA+99] Konstantinos Zioutas, CE Aalseth, D Abriola, FT Avignone Iii, RL Brodzinski, JI Collar, R Creswick, DE Di Gregorio, H Farach, AO Gattone, et al. A decommissioned lhc model magnet as an axion telescope. *Nuclear Instruments and Methods in Physics Research Section A: Accelerators, Spectrometers, Detectors and Associated Equipment*, 425(3):480–487, 1999.

[ZAA+05] Konstantinos Zioutas, S Andriamonje, V Arsov, S Aune, D Autiero, FT Avignone, K Barth, A Belov, B Beltrán, H Bräuninger, et al. First results from the cern axion solar telescope. *Physical review letters*, 94(12):121301, 2005.

[Zhi80] AP Zhitnitskii. Possible suppression of axion-hadron interactions. *Sov. J. Nucl. Phys.(Engl. Transl.);(United States)*, 31(2), 1980.

List of Figures

List of Tables

Danksagung

Zuerst möchte ich mich bei Klaus Desch bedanken, für die Vergabe des spannenden Themas und für die Unterstützung über die Jahre.

Mein besonderer Dank gilt Markus und Basti, ohne euch wäre diese Arbeit sich nicht zu dem geworden, was sie ist. Vielen Dank!

Desweitern, gilt mein Dank all den vielen lieben Kollegen aus dem Büro und aus der Arbeitsgruppe! Ohne euch hätte es sicher weniger Spaß gemacht. Ein besonderer Dank gilt meinen Freunden Christoph und Olli. Danke für all die interessanten Gespräche!

Basti, Christoph, Johanna, Markus, Patrick, Thomas und Vlad möchte ich auch für das Korrekturlesen danken.

Auch meinen Freunden aus der ELSA Gruppe möchte ich danken für die Kaffeepausen, Tipps und Gespräche. Danke Dennis, Dennis, Florian und Thomas!

Ebenso möchte ich mich bei Hubert Blank und Michael Brock bedanken, die wertvolle Hilfe beim Bau der Detektoren geleistet haben. Auch Philipp Hänisch gilt mein Dank für die vielen Diskussionen zu mechanischen Problemen.

Alex Fassbender und der AG Linden möchte ich für die Beschichtung der Anoden danken.

Ebenfalls möchte ich mich bei der gesamten IAXO Mannschaft bedanken, für die schöne Zeit und die vielen anregenden Gespräche.

Mein größter Dank gilt jedoch meinen Eltern, ohne eure Unterstützung wäre ich sicher nie soweit gekommen. Vielen vielen Dank!